Reflection Anisotropy Spectroscopy and Scanning Probe Microscopy Studies with Applications to Liquid Crystal Alignment Layers

by

Brian Fraser Macdonald

Submitted for the degree of Doctor of Philosophy

The University of Edinburgh

2002

Acknowledgements

I am indebted to Dr R. J. Cole who proved to be not only an excellent supervisor who never turned me away and always made a huge effort to help but who is also a good friend. This work would not have been possible were it not for his input and assistance, his enthusiasm in proof reading this thesis and the subsequent comments are particularly appreciated.

Like all experimental projects, this one had its fair share of breakdowns and problems throughout. I am grateful to Mr A. Garrie who has provided technical support and advice over the past three years to ensure these setbacks were minimised and the equipment was operational again as soon as possible.

I would like to thank Dr W. Zheng for the part he played in the experiments involving the polymer alignment layers, Dr D. S. Martin for his assistance with the vicinal copper surfaces and alkane experiments and Dr V. Koutsos for his help with the dodecane on graphite AFM analysis. General thanks go out many members of staff within the School of Physics, both academic and non-academic, for their assistance throughout.

I acknowledge the financial support of the Engineering and Physical Sciences Research Council who have funded me for the past three years.

Last but by no means least is the unending support and encouragement from my family and friends, in particular Rebecca who also had the unenviable task of proof reading most of this thesis. I hope I have always showed my appreciation in the past to each and every one of you.

Abstract

Homogeneous alignment of liquid crystal (LC) molecules is fundamental to the fabrication and optimum operation of LC devices. As a consequence of employing alignment layers with directional properties, the alignment of LC molecules is promoted. The most commonly used technique to fabricate LC alignment layers is by mechanically rubbing polymer films. However, reductions in production costs and further advancements in LC technology are now being hindered by the rubbing technique and so either a new technique or monitoring of the current technique is required. In these studies, a monitor of the rubbing technique and of the potential replacement techniques is demonstrated.

By constructing a surface sensitive technique, traditionally a monitor of semiconductor growth, and applying it to alignment layers, the first uses of reflection anisotropy spectroscopy (RAS) to monitor the fabrication of LC alignment layers are presented. This technique, in conjunction with atomic force microscopy (AFM), has been successfully used to study a number of variables of the rubbing technique and as a real-time monitor of the photoalignment and atomic beam etching techniques. Of these, the latter has shown the most potential to replace mechanical rubbing yet it is probably the least understood. The results are interpreted using stratified media simulations and molecular alignment models

An interesting by-product of these alignment layer studies has been the introduction of an extension to the normal RAS technique. By using examples such as doubly rubbed alignment layers and double sided rubbed alignment layers, angular dependent RAS (ADRAS) has been shown to be capable of isolating and monitoring optical anisotropy from multiple sources within a single system.

To increase understanding of the etching technique, the complex polymer surfaces were replaced by a model system: a copper single crystal. The complexity of these studies was later increased by the introduction of vicinal surfaces and the adsorption of chiral molecules onto the Cu (110) surface. Both of these changes alter the characteristic spectra but the latter also has potential to allow further uses of ADRAS as the chiral molecule is known to lie at a specific angle to the rows of copper atoms.

To further the understanding of the interactions between LC molecules, polymer layers and surfaces, an AFM study of a model system, dodecane on highly ordered pyrolytic graphite, was carried out, from which observations about the dewetting of surfaces have been made.

Contents

Chapter 1: Introduction

'Anyone who has never made a mistake has never tried anything new'
Albert Einstein (1879 - 1955)

Summary

The motivation of this project concerns liquid crystal displays and so in this first chapter a general introduction into the construction and operation of liquid crystal displays is given. Also included is a brief overview of the project, highlighting the areas studied, the motivation for the work and the some of the results.

Liquid Crystal Displays

Historical View of Liquid Crystal Displays

For many decades now, flat panel displays have been developed with the ultimate goal of replacing cathode ray tube (CRT) displays. The development of rival technologies has been limited over the years due to the exceptional success of the CRT which provides high performance at a relatively low cost. However, for large displays (over 40 inches diagonally), the CRT becomes too bulky, heavy and expensive for many applications. Similarly for portable applications, the size and power consumption of the CRT has prevented it from being widely used [1.1].

In the last decade or so, liquid crystal displays (LCDs) have begun to reduce the market share of the CRT. In particular, the LCD now dominates both large scale (e.g. projection displays) and small scale (e.g. watches, calculators and portable computers) applications. Although recent advances in LCD technology have resulted in relatively large, high resolution displays with a colour quality exceeding that of CRTs, the CRT has retained the bulk of the displays market. A major factor in this is the higher selling price of LCDs, resulting from increased manufacturing cost caused by high levels of waste created during the fabrication process. Commercially, the fabrication process of LCDs includes a rubbing procedure used to create alignment layers. It is this process which is responsible for the majority of the waste and needs to be replaced, possibly by non-contact techniques, or to be monitored more effectively. Either of these options will reduce the level of waste and help to lower the cost of producing LCDs [1.2]. The ideal solution would be to have an effective monitor of a non-contact technique.

The future of the display industry, and in particular LCDs, seems to be tending towards flexible displays. Unless the limitations created as a result of the alignment process are solved, future technologies will suffer from exactly the same problems.

Liquid Crystals

There are many different types of liquid crystals (LCs) and it is their unique properties which enable LCDs to operate. By definition, as well as having fluid properties, LCs also posses long range order similar to that in a crystalline solid. These molecules appear elongated (rod shaped) and can align parallel to each other, gaining anisotropic electrical and optical properties, enabling applications to displays [1.3]. For display purposes it is the cyanobiphenyl compound, shown in *Figure 1.1*, which is normally used. To help describe the orientation of the LC molecules a unit vector, called the director (***n***), is defined in the direction of the long axis of the molecule.

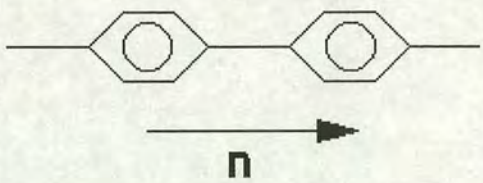

Figure 1.1 *The cyanobiphenyl compound commonly used in LCDs.*

Classes of Liquid Crystals [1.4]

LCs are characterised by their properties when in physical states between the crystalline and liquid phases. The crystalline phase (K) has a regular structure and posses both long range positional and long range orientational order. The liquid or isotropic phase (I) has random atomic or molecular positioning and orientation. In the liquid phase, the position and orientation of one molecule provides no information about other molecules in that phase, unlike a crystal. The phases of LCs which are of importance to LCDs are described below.

The nematic phase (N), shown in *Figure 1.2 (a)*, is similar to the isotropic phase in that the molecules have a random position. In the ideal N phase, which excludes thermal fluctuations, the shape of the molecules cause a layered structure in which the directors of the molecules lie parallel.

The cholesteric or chiral nematic phase (Ch or N*), shown in *Figure 1.2 (b)*, like the N phase, has random molecular positioning, with the directors aligned parallel forming layers parallel to the plane of the director. Unlike the nematic phase however, the directors have a spiral structure as they rotate from layer to layer in the bulk. The N phase can be considered a special case of the Ch phase.

The smectic *A* phase (S_A), shown in *Figure 1.2 (c)*, is similar to the N phase as it is characterised by parallel alignment of the molecular director. In this case though, there is also some positional order, resulting in the molecules forming layers with the director parallel to the layer normal.

The smectic C (S_C) phase is similar in structure to the S_A phase. The difference is that the molecular directors are tilted at a constant angle to the layer normal. In the chiral smectic C (S_C*) phase, shown in *Figure 1.2 (d)*, the presence of chiral (optically active) molecules causes the director to rotate from layer to layer.

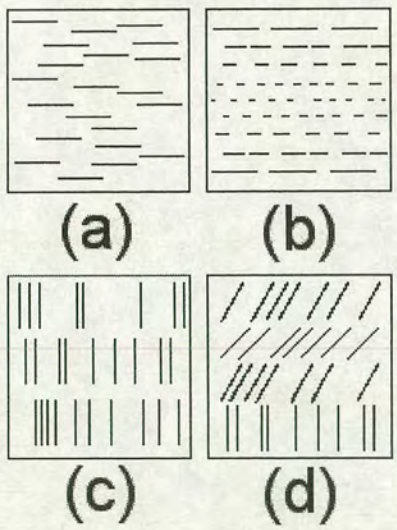

Figure 1.2 *The (a) nematic, (b) cholesteric, (c) smectic A and (d) chiral smectic C phases of liquid crystals.*

Twisted Nematic Liquid Crystal Displays [1.1]

The most commonly used LCDs are made using the twisted nematic (TN) cell as shown in *Figure 1.3*. The cells are made from two glass plates which are coated with a transparent conductor on one side, usually indium tin oxide (ITO). The ITO layer is coated with a thin layer of polymer which is then treated, usually by rubbing, to encourage the LC molecules to align parallel to the rubbing direction. The cell is constructed with the polymer layers facing inwards and with the alignment directions perpendicular. The LC molecules, which are sandwiched between these layers, undergo a 90° twist from one plate to the next. Polarisers are applied to the top and bottom surfaces of the cell, with the polarisation directions parallel to the alignment direction.

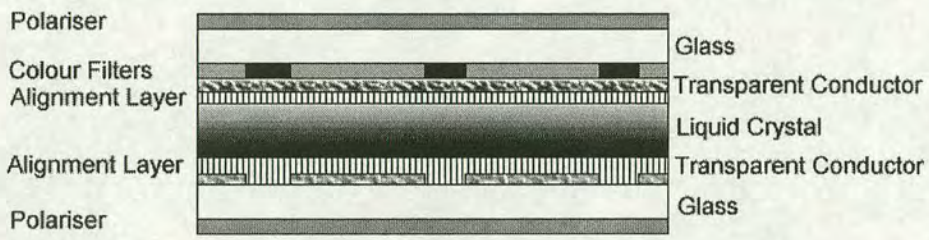

Figure 1.3 Construction of Twisted Nematic LCDs.

These cells are non-emissive and normally use a back-light. An alternative lighting arrangement is to construct the cells using a reflective silicon back plate and a single glass plate on top. In this case a light source is directed into the cell from the side and is reflected back out of the front of the cell. LC cells modulate the incident light and use colour filters to enable full colour images. When unpolarised light is incident on the cell it becomes linearly polarised. As it is transmitted through the LC layer, when in the undriven and relaxed state, the light undergoes a 90° rotation in polarisation and leaves the cell through the exit polariser (*Figure 1.4 (a)*). When a high enough electric field is applied across the cell (the driven state), the LC molecules align themselves in the direction of the field. Light incident on the cell in this state does not undergo a rotation and is absorbed by the exit polariser (*Figure 1.4 (b)*). These cells are 'switched' between states by an AC voltage applied across the cell and have a typical response time of 30 ms. Higher resolution displays are possible but at the

cost of the response time. This is done using a 'super twisted nematic' cell, which uses a twist of 180° - 270° instead of 0° - 90°.

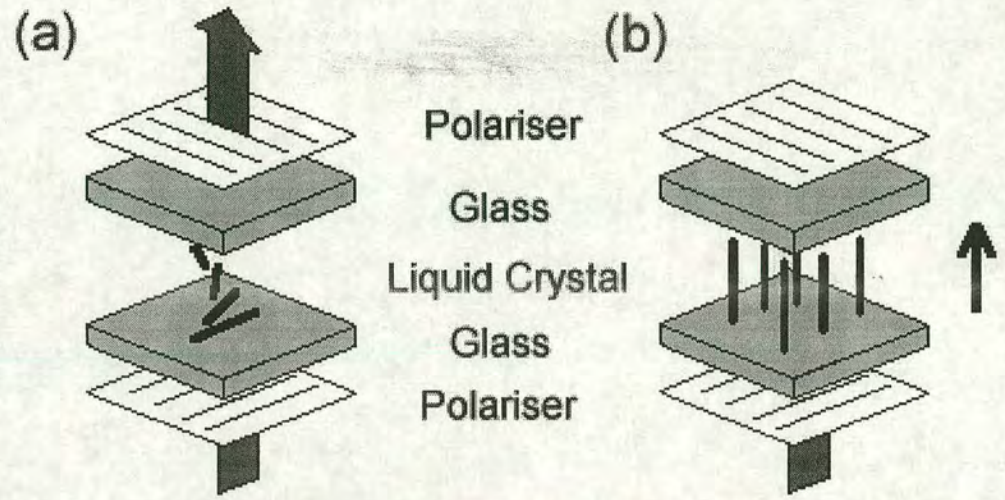

Figure 1.4 *Twisted nematic liquid crystal cells in (a) the on state and (b) the off state.*

Ferroelectric Liquid Crystal Displays [1.5]

Some S_C^* phases exhibit ferroelectric properties, they have domains which are electrically polarised in specific directions, and so can be used in LCDs. The construction of ferroelectric LCDs is similar to a TN cell except that the cells are thinner and the rubbing directions of the polymer alignment layers lie parallel instead of perpendicular to each other as before. The ferroelectric liquid crystals (FLCs) fill the cell with their molecular directors in planes parallel to the glass plates and at an angle to the plane of the layer. These molecules are bistable and can be switched between the two states by applying a DC pulse of the correct polarity. The use of crossed polarisers gives these devices bright and dark appearances respectively due to the birefringence of the LC, as shown in *Figure 1.5*.

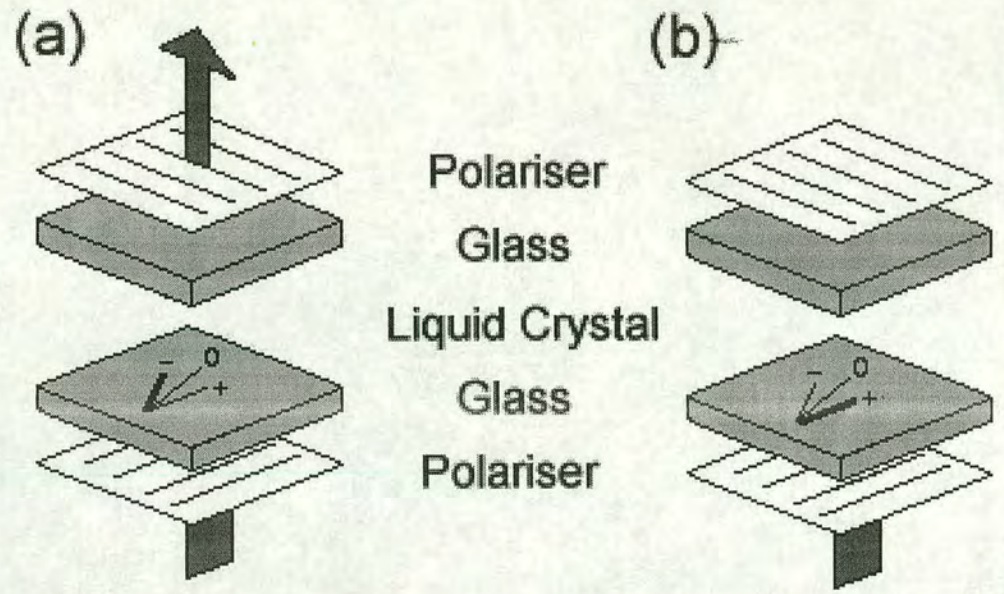

Figure 1.5 *Ferroelectric liquid crystal cells in (a) the on state and (b) the off state.*

To make ferroelectric LCDs, a polariser is placed on the front surface of the cell with its optical axis parallel to the molecular axis of one of the FLC states. Another polariser is placed behind the cell with its optical axis perpendicular to the optical axis of the first polariser. If the directors of the molecules within the cell are parallel to the first polariser, no light will pass (*Figure 1.5 (b)*). If the directors of the molecules are switched to the other direction, any light transmitted through the first polariser will have its polarisation changed as it passes through the liquid crystals. Therefore, the polarisation of the light as it exits the cell is not aligned perpendicularly to the second polariser and so some is transmitted (*Figure 1.5 (a)*).

As the FLC pixels are bistable, each responds only to its most recent voltage pulse and does not decay over time as with the TN pixels. This allows ferroelectric LCDs to be operated in a simpler manner than the TN display which reduces production costs. Additionally, switching times of a few microseconds can be achieved (which is a hundred to a thousand times faster than the TN cell) allowing other applications, such as fast optical shutters.

Project Scope

As previously mentioned, the commercial development of LCDs is being hindered by problems associated with the polymer alignment layer. The technique most commonly used to create these alignment layers is a dirty and somewhat unreliable technique which results in large amounts of waste, thus increasing the fabrication costs of LCDs. The aim of this project is to investigate alignment layers using novel techniques with the goal of understanding more about these layers and the possible introduction of a suitable monitoring technique.

Chapter 2 gives background information regarding the main experimental techniques used throughout the project and *Chapter 3* contains a full description of the construction and operation of the apparatus used. The first experimental results are presented in *Chapter 4* which gives details of a study of polymer alignment layers by reflection anisotropy spectroscopy (RAS) and atomic force microscopy (AFM). A range of different materials and techniques has been examined to obtain a complete study of the alignment layer fabrication process. In general, it was found that the information obtained by RAS, and in some cases backed up by AFM, could be used to monitor the fabrication of the alignment layers. Simulations based upon a molecular alignment model have been used to understand the origin of the optical anisotropy induced by the rubbing process. Ion beam etching has been shown to be a suitable non-contact alternative to rubbing for the production of alignment layers, this technique has also been monitored by RAS. The use of RAS in these ways is a novel application of the technique and an interesting by-product of these studies, angular dependent RAS (ADRAS), is discussed in *Chapter 5*.

The results of the alignment layer studies have shown the creation of alignment layer to be an extremely complicated situation which could not be fully explained. The same techniques were therefore applied to simpler systems from where it may be possible to build towards an understanding of the complex systems of before. In *Chapter 6*, details of experiments on the well understood Cu (110) surface are given. This surface, as well as more complex vicinal surfaces, is studied by RAS under a

variety of surface processing techniques. Of particular interest, after considering the findings of the previous chapters, is the etching of the surfaces using an ion beam. *Chapter 7* studies the effect of evaporating molecules on the copper surfaces and is a further step towards the initial system involving the polymer alignment layers. By studying a chiral molecule on the copper surface it has been possible to extend the applications of ADRAS (the angular technique first introduced in *Chapter 5*). The earlier chapters have shown the necessity of having a uniform surface to aid the LC alignment. Even prior to any processing some structure can be found on the polymer surfaces which probably results from drying. The final experimental chapter, *Chapter 8*, is an AFM study of dodecane on highly ordered pyrolytic graphite (HOPG). In a similar way to the previous RAS measurements, this system is used as a simplified version of the alignment layer and allows a study of the structures formed as a result of the dewetting and drying mechanisms. *Chapter 9* is the final chapter and gives a summary of the conclusions of the work and suggestions for further work in these areas.

Chapter 2: Experimental Techniques

'There are three principal means of acquiring knowledge... observation of nature, reflection and experimentation. Observation collects facts, reflection combines them; experimentation verifies the results of that combination'
Denis Diderot (1713 - 1784)

Summary

This is a descriptive chapter used to give an introduction into the main experimental techniques used in this project. The techniques covered in this chapter are scanning tunnelling microscopy (STM), atomic force microscopy (AFM), low energy electron diffraction (LEED) and reflection anisotropy spectroscopy (RAS). Of these, AFM and RAS are the most frequently used.

Scanning Tunnelling Microscopy

Historical View of the Scanning Tunnelling Microscope

Scanning tunnelling microscopy (STM) is probably the most basic technique of the selection of scanning probe microscopy (SPM) technologies currently available. It is also the oldest, the one that gives the highest resolution with least effort and is therefore very commonly used. The technique was first introduced by Gerd Binnig and Heinrich Rohrer in 1981 at IBM Zurich [2.1]. Their discovery earned them a Nobel prize five years later in 1986.

Introduction to the Scanning Tunnelling Microscope [2.2 - 2.4]

The STM is operated by moving a sharpened conducting tip over the surface of a conducting sample. A bias is applied to both the tip and sample to create a potential difference across the gap between them. When the size of the gap between the tip and sample is brought below ~1 nm, a current will flow. As the tip rasters the surface of the sample, a two dimensional map of the surface is constructed using the values of current at each point of the surface. Using an exponential relationship between the current and the relative height of the tip, a topographical image with very high sensitivity in the z-direction can be formed.

The movement of the tip in the x, y and z directions is controlled by piezoelectric crystals. Use of this method allows very accurate movement of the tip with relatively low hysteresis. As the scan proceeds it may be necessary to alter the distance between the tip and sample. To allow this, the z-piezo is connected to a feedback loop that responds to the topography of the surface. If the tunnelling current exceeds a pre-set value (indicating the tip is too close to the sample), the z-piezo is activated to retract the tip until the tunnelling current returns below a pre-set value. Similarly if the tip becomes too far from the sample, the piezo will move the tip closer.

Figure 2.1 illustrates the situation, in terms of energy, when the distance between the tip and sample is large (greater than ~1 nm). The air gap between the tip and sample acts as a dielectric and does not allow electrons to pass through. Any electrons in the

tip travelling towards the sample are either reflected back from the boundary or are transmitted into the air but will decay after a short time prior to reaching the sample. *Figure 2.2* illustrates the situation when the distance between the two metals is small enough (less than ~1 nm) to allow quantum mechanical tunnelling. As before, electrons travelling through the tip towards the sample are either reflected back or transmitted into the air gap. Now the gap is small enough such that the electrons can reach the other side before they decay away. In general, if the gap between the tip and sample is too big, the barrier between the metals is too large for electrons to overcome and so no electrons will be able to tunnel through.

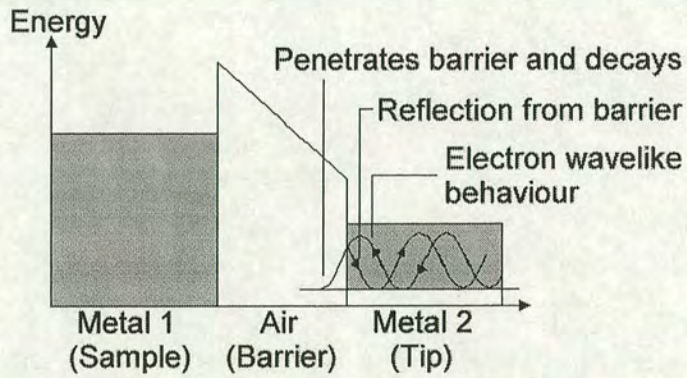

Figure 2.1 *Energy diagram showing the behaviour of electrons when the distance between the tip and sample is large.*

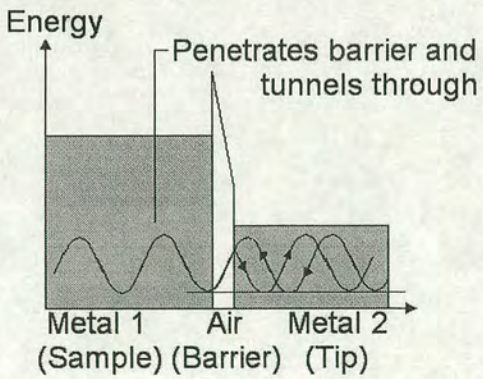

Figure 2.2 *Energy diagram showing the behaviour of electrons when the distance between the tip and sample is small.*

To briefly summarise the two available modes of operation, constant height mode has a high scan speed and should not be used to image rough surfaces. Constant current mode is suitable to be used on rough surfaces but has a lower scan speed.

Atomic Force Microscopy [2.3, 2.5, 2.6]

Historical View of the Atomic Force Microscope

In 1986, Binnig and Quate developed the atomic force microscope (AFM) as a method to measure forces as small as 10^{-18} N [2.7]. This technique is, in the words of Binnig and Quate, 'a combination of the principles of the scanning tunnelling microscope and the stylus profilometer' [2.7]. The original application of the AFM was to study the surfaces of insulators on an atomic scale, something that STM could not do. A little over a year later, the first images of a non-conductor were published [2.8], these images showed monatomic steps of NaCl and was followed shortly by the first atomic resolution image of a non-conductor [2.9]. Since then the use of AFM and the number of applications has increased dramatically. With the addition of intermittent contact imaging techniques to the AFM, applications involving biological and polymer samples have become commonplace.

Introduction to the Atomic Force Microscope

The AFM probes surfaces using a sharp tip mounted on a flexible reflective cantilever. As the cantilever is rastered over the surface, Van der Waals forces cause it to deflect following the topography of the sample. The deflection of the cantilever is detected optically by reflecting a laser beam off the top surface of the cantilever into a four-segment photodiode, as shown in *Figure 2.3*. The use of a four-segment detector allows twists in the cantilever, as a result of friction, to be detected as well. The voltage output from the photodiode is converted into topographic data by the SPM controller and SPM software.

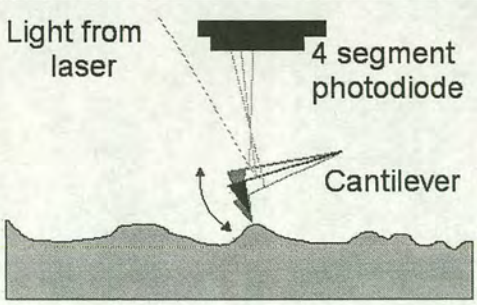

Figure 2.3 *Optical detection of cantilever deflection in an AFM.*

Atomic Force Microscope Cantilevers

The cantilevers are part of a larger holder, as shown in *Figure 2.4* and are microfabricated from a Si (110) single crystal or from Si_3N_4. A full description of the microfabrication technique is given in [2.10]. A typical cantilever has a length of 100 - 200 μm and a tip diameter of ~10 nm, although these values vary depending on the particular type of cantilever; therefore allowing many different applications. By increasing the sharpness of the tip it is possible to obtain higher resolution images. The number of applications can be increased further by varying the dimensions of the cantilevers to obtain a range of spring constants (C) and resonant frequencies (f) which can be found using *Equations 2.1 & 2.2* (which exclude the mass of the tip). T, W & L are the thickness, width and length of the cantilever, E is the modulus of elasticity (Young's modulus) and ρ is the density of the material used to make the cantilevers.

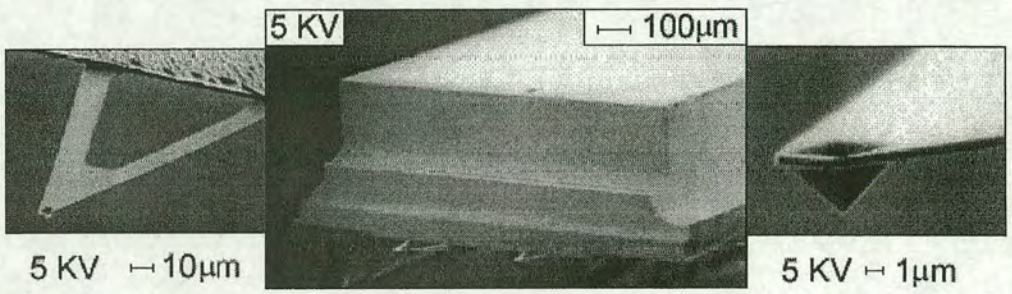

Figure 2.4 *Scanning electron microscopy images of AFM cantilevers [2.11].*

$$C = \frac{E}{4}\frac{W \cdot T^3}{L^3} \qquad \textit{Eq. 2.1}$$

$$f = 0.162 \cdot \sqrt{\frac{E}{\rho}\frac{T}{L^2}} \qquad \textit{Eq. 2.2}$$

Forces

The AFM operates by measuring the forces between the cantilever and sample. These forces are mainly dependent on the separation between the tip and sample, any contamination, the type of sample and the type of tip. The relationship between the

separation and the force felt by the cantilever can be seen in *Figure 2.5*. At high separation the net force is attractive but is relatively weak as it is mainly due to long range Van der Waals forces. As the atoms of the tip and sample are brought closer together, the attractive force grows until the electron clouds of the atoms repel each other and cancel out the attractive force. With further reduction in separation the repulsive force becomes dominant.

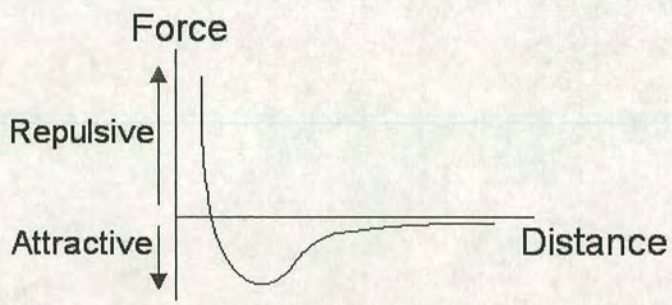

Figure 2.5 *The forces between the tip and sample as a function of separation.*

Modes of Operation

Contact Mode

The main mode of operation of the AFM is contact mode, in which the tip is held a few Angstroms above the surface of the sample. In this mode the AFM operates in the repulsive regime, the steep part of the curve shown in *Figure 2.5*, and generally uses cantilevers which have relatively low spring constants (lower than the effective spring constant between the atoms of the sample). As there is a strongly repulsive force between the tip and sample, any pressure on the tip results in a bend of the cantilever rather than reducing the separation between the tip and sample. By monitoring the deflection of the cantilever as it passes over a surface, it is possible to build up a topographic image of the sample. If a force large enough to overcome the repulsive force is applied to the sample via a stiff cantilever, nanolithography of the sample will result.

The deflection of the cantilever and therefore the force felt by the cantilever as a function of distance from the surface can be seen in *Figure 2.6*. Point *A* shows the repulsive force on the tip due to the close proximity of the tip to the sample. At point *B*, where the tip begins to feel the repulsive force of the sample, the attractive long range force is beginning to be neutralised by the repulsive atomic force. Also at point *B*, when the cantilever is retracted from the sample, a capillary force is felt by the tip due to the contamination (water) layer on the surface of the sample. The apparent size of the adhesion shown on force-distance curves will depend on the stiffness of the cantilever and the amount of contamination. Point *C* shows the attractive long range force from the sample felt by the cantilever

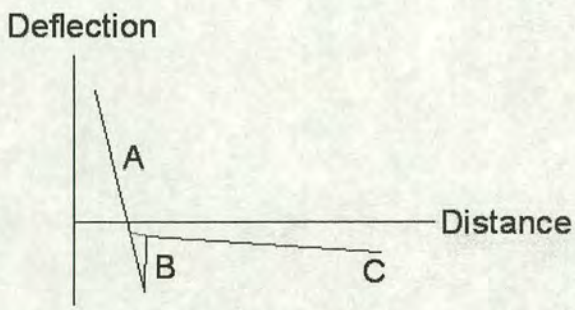

Figure 2.6 *A 'Force - Distance' curve.*

Intermittent Contact Mode

A disadvantage of contact mode AFM occurs when trying to image soft samples or samples which are loosely bound to the substrate as these may be damaged during imaging. These problems occur frequently when imaging biological samples and cannot be solved by simply using softer cantilevers.

One solution is to use an alternative imaging technique in which the cantilever contacts the surface intermittently. Instead of being dragged along the surface as in contact mode, the tip bounces over the surface. The result is an imaging technique which applies less force to the surface and therefore causes less damage. This technique has several names such as 'Tapping mode' and 'Acoustic mode' and it operates by forcing the cantilever to resonate (the resonant frequency of the cantilever can be determined using *Equation 2.2*). This is normally done using a

transducer, which when supplied with a voltage, vibrates the cantilever at the desired frequency and amplitude. An alternative method is to resonate a magnetically coated cantilever in an AC magnetic field.

All intermittent contact techniques operate using the same basic principles. *Figure 2.7* shows the motion of the cantilever and how topographical information is extracted whilst in intermittent contact mode. As the cantilever is oscillated at its resonant frequency, the tip softly contacts (taps) the surface on the bottom part of the oscillation. The amplitude of the cantilevers oscillation varies depending on the tip to sample distance and therefore on the surface topography. By comparing the measured oscillation with the vibrational movement applied to cantilever, it is possible to extrapolate the surface topography.

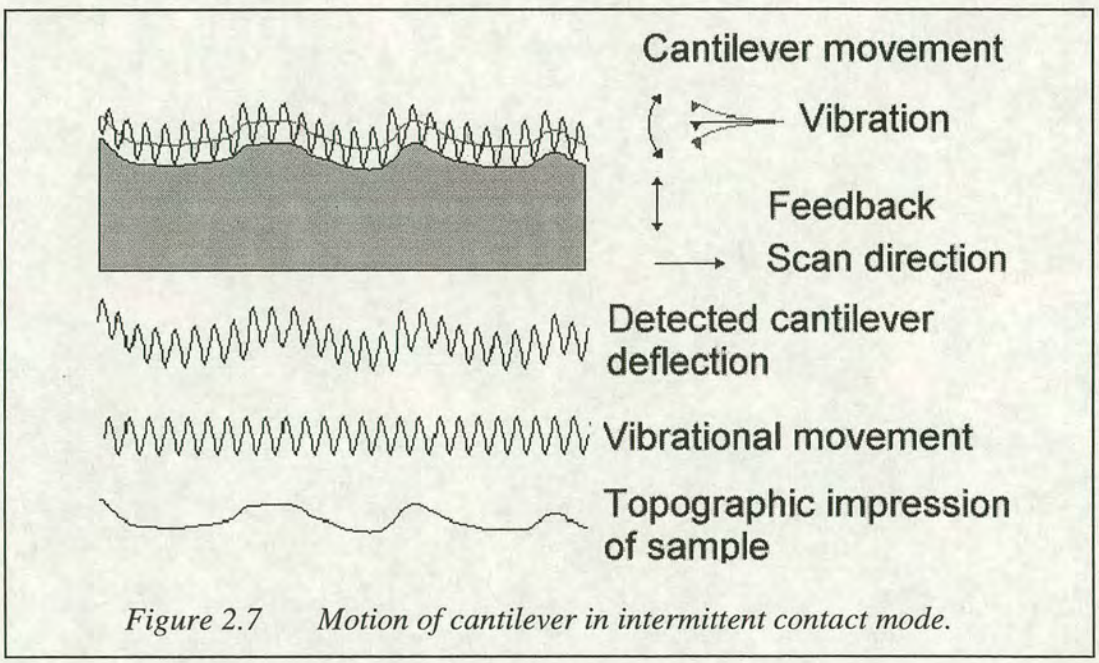

Figure 2.7 Motion of cantilever in intermittent contact mode.

Low Energy Electron Diffraction [2.12, 2.13]

Historical View of Low Energy Electron Diffraction

The primary developments in the technique of low energy electron diffraction (LEED) date back over a century to 1897. In this year, J. J. Thomson discovered cathode rays were comprised of electrons. Some 30 years later Davisson and Germer performed the first electron diffraction experiment to confirm the de Broglie hypothesis of electrons behaving like waves.

For this technique, the usual definition of 'low energy' is between 1 and 1000 eV. At low energies such as these, the penetration of the incident electrons through crystals is limited to the first few atomic layers of the surface. It is for this reason that the state of the surface strongly modifies the diffraction process. To overcome this problem and to allow electrons to probe further into samples, higher energies were used. It took about another 30 years, until the 1960's, before LEED was developed much more. At this time, techniques had been developed to clean (ion bombardment) and anneal samples plus the advent of ultra high vacuum (UHV) systems meant samples could be kept 'clean' in chambers for hours instead of seconds.

The initial weakness of LEED, of only being able to probe the surface of a sample, is now its major strength. LEED is now the principle technique used to determine the periodicity and condition of surfaces. The information gathered using LEED is in the form of a diffraction pattern. From the position of the spots, information about the size, symmetry and rotational alignment of the unit cell of the sample can be found. Similarly, from the intensities of the spots, information about atomic positioning can be found. This is done by recording the intensities as a function of incident electron beam energy, generating an I - V curve, which is then compared to theoretical values.

Introduction to Low Energy Electron Diffraction

In the operation of LEED, electrons are fired at a sample from an electron gun. Elastically scattered electrons from the sample contribute to the diffraction pattern formed. In *Figure 2.8* a typical LEED experimental arrangement is shown. The

energy and quantity (i.e. the current) of electrons fired at the sample is controlled by the electron gun. The grids are used to filter out lower energy electrons and the diffraction pattern is displayed on the fluorescent screen. In order to generate a back-scattered electron diffraction pattern, the sample must be a single crystal with a well-ordered surface.

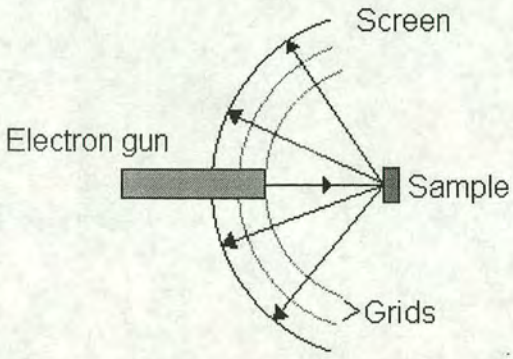

Figure 2.8 A typical LEED experimental arrangement.

The principles of operation of LEED are very much dependent on diffraction theory. From the fundamentals of wave-particle duality, the electrons incident on the sample may be regarded not only as a stream of particles but also as a stream of waves. These waves will be scattered by the surface atoms as they encounter regions of highly localised electron density. The atoms can therefore be considered to act as point scatterers.

When a wavefront strikes a crystal surface in which the layers of atoms are separated by a spacing d, there is a path-difference in the distance the reflected beam has to travel from the scattering centres to the detector. The path difference is $d \sin\theta$, where θ is related to the angle of incidence. This must be equal to an integral number of wavelengths for constructive interference to occur at the detector (screen). It can be found that all surface diffraction patterns show symmetry reflecting that of the surface structure and are centrally symmetric. The scale of the pattern shows an inverse relationship to the size of the surface unit cell and to the incident electron energy.

Figure 2.9 (a) shows an anisotropic *fcc* (110) crystal surface in which the spacing between the atoms horizontally is greater than the spacing vertically. *Figure 2.9 (b)* and *Figure 2.9 (c)* show two different diffraction patterns typical of the *fcc* (110) surface. In these, the spots seen (representing the atoms) have a greater spacing vertically than horizontally. Therefore, the observed LEED pattern is a scaled representation of the reciprocal lattice of the surface structure. The difference between the two diffraction patterns is the energy of the incident electrons. By increasing the energy, the distance between spots appears reduced.

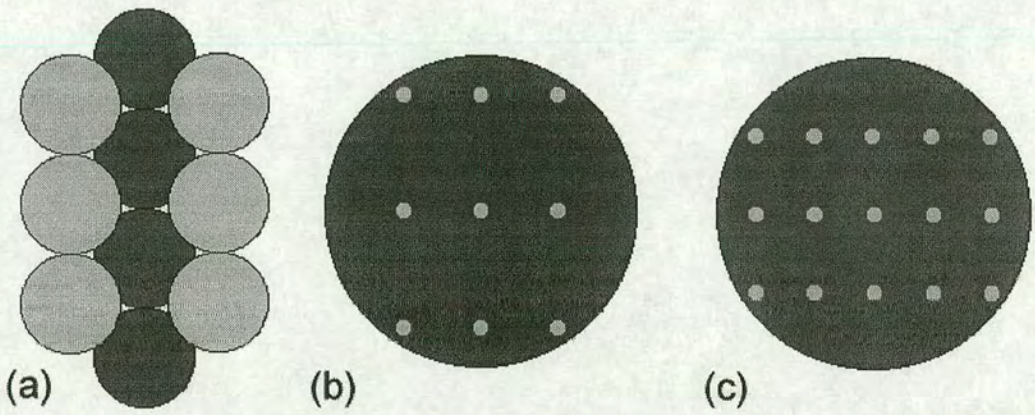

Figure 2.9 *(a) fcc (110) crystal plane. LEED images of the fcc (110) surface at (b) low energy and (c) higher energy.*

Reflection Anisotropy Spectroscopy

Historical View of Reflection Anisotropy Spectroscopy

Reflection anisotropy spectroscopy (RAS) is a linear optical experimental method used to probe surface anisotropy as a function of photon energy incident upon a sample. The difference between the reflectivity for light linearly polarised along two perpendicular directions (x & y) at normal incidence is measured (Δr).

The origins of reflection anisotropy (RA) measurements can be traced back to Cardona who in 1968 studied Si (110) using 'Rotoreflectance' [2.14]. Then in 1971, McIntyre and Aspnes showed the change in normalised reflectivity can be used to gain direct information about the physical properties of a system [2.15]. More than a decade later in 1985, Aspnes and Studna reported their studies of the optical anisotropy of cubic semiconductors and highlighted the potential of optical anisotropic techniques in studies of surfaces and interfaces [2.16]. Within two years, the technique was being used to measure the changes in optical reflectance as an *in-situ* monitor of molecular beam epitaxy (MBE) [2.17, 2.18]

RAS in its current format, using a photoelastic modulator (PEM), was developed by Aspnes *et al.* in 1988 [2.19] to study the growth of semiconductors by MBE and in particular under UHV conditions. The use of a PEM negates the use of the previously used rotating analyser giving the advantage of a higher signal to noise ratio [2.20]. They later gave an analysis of several reflectance difference (RD) configurations with MBE applications in mind [2.20]. Since then RAS has been developed by several other groups and now has many uses in addition to monitoring semiconductor growth. Borensztein *et al.* reported the first use of RAS on a single metal crystal [2.21] using Ag (110). This was closely followed by Richter *et al.* studying the RA of a Cu (110) single crystal [2.22]. Examples of other studies are molecular adsorbates [2.23], catalysts [2.24], Langmuir-Blodgett films [2.25], solid-liquid interfaces [2.26] and surface-induced stress [2.27].

Reflection and Transmission

The fundamental rules of reflection are governed by Snell's law which states the ratio of the sine of the angles of reflection and refraction (both measured from the normal) is equal to the inverse ratio of the refractive indices. Here we define the refractive index as the ratio of the speed of light in a vacuum and the speed of light in a medium. The complex refractive index (N) is given below,

$$N = n - ik \qquad \textit{Eq. 2.3}$$

where n is the refractive index and k the extinction coefficient. These optical constants are related to the electrical properties of a medium, in particular the dielectric constant.

$$N = \sqrt{\varepsilon} = \sqrt{\varepsilon' - i\varepsilon''} \qquad \textit{Eq. 2.4}$$
$$\varepsilon' = n^2 - k^2 \qquad \textit{Eq. 2.5}$$
$$\varepsilon'' = 2nk \qquad \textit{Eq. 2.6}$$

Here ε' and ε'' are the real and imaginary coefficients of the dielectric function. Although Snell's law can be used to describe the angles of reflection and refraction, for information about the intensity and amplitude it necessary to turn to the Fresnel reflection and transmission coefficients. A derivation of these can be found in *Appendix A*. By considering the electric field (E) with its vector parallel and then perpendicular to the plane of incidence and by applying boundary conditions, it is possible to obtain a relation for the ratio of the reflected (E_{0r}) and incident (E_{0i}) electric field amplitudes. Similarly this can be done for the ratio of the transmitted (E_{0t}) and incident (E_{0i}) electric field amplitudes, resulting in the Fresnel equations (*Equations 2.7 & 2.8* and *Equations A.6 & A.7* from *Appendix A*) which give the reflection (r) and transmission (t) coefficients for any non-magnetic material at normal incidence.

$$r_{12} = \frac{E_{0r}}{E_{0i}} = \frac{N_1 - N_2}{N_1 + N_2} \qquad \textit{Eq. 2.7}$$

$$t_{12} = \frac{E_{0t}}{E_{0i}} = \frac{2N_1}{N_1 + N_2} \qquad \textit{Eq. 2.8}$$

The reflectance (R) and the transmittance (T) are related to these and for an interface which has air as one of the mediums, N_2=1, they can be written:

$$R = |r|^2 = \frac{(n_1 - 1)^2 + k_1^2}{(n_1 + 1)^2 + k_1^2} \qquad \textit{Eq. 2.9}$$

$$T = |t|^2 = \frac{4(n_1^2 + k_1^2)}{(n_1 + 1)^2 + k_1^2} \qquad \textit{Eq. 2.10}$$

The equivalent Fresnel reflection coefficient of a three phase system (*Equation 2.11* and *Equations A.9 & A.17* from *Appendix A)* can be obtained by using the three phase model [2.28] or the matrix methods, also described in *Appendix A*.

$$r_{123} = \frac{r_{12} + r_{23}(1 - 2i\beta_2)}{1 + r_{12}r_{23}(1 - 2i\beta_2)} \qquad \textit{Eq. 2.11}$$

Epioptics

There are several optical probes which are used to gain surface and interfacial information, these are collectively known as epioptic techniques. Optical experimental methods have the advantage over other probes as they offer a 'non-destructive' probe that can be used in a vast range of conditions from UHV to ambient and above. These techniques can offer real time *in-situ* monitoring of systems with sub-micron resolution [2.29].

The application of epioptic probes to surface science has complications. Due to the large penetration depth of light incident upon a sample, it is hard to isolate the optical response of the surface from that of the bulk. For particular materials (namely single crystals with cubic symmetry), it is possible to overcome this problem by utilising the bulk isotropic and surface anisotropic properties. In this situation, any measured RA must be due solely to the surface and not the bulk [2.30]. Using these principles

it is possible to have an optical technique which is not only surface sensitive but is surface specific. An example of this is RAS in which the difference in the reflection of near-normal incidence linear polarised light is measured along two perpendicular axes. The result (*Equation 2.12*) is given by the ratio of the difference in the sample's reflectivity along each of the two axes (r_x & r_y) and the average reflectivity (r).

$$\frac{\Delta r}{r} = 2\frac{(r_x - r_y)}{(r_x + r_y)} \qquad \textit{Eq. 2.12}$$

Surfaces studied by RAS can be thought of as a three phase system (see *Appendix A*). They have an ambient layer (medium 1), a very thin anisotropic surface layer (medium 2) and then the isotropic bulk of the sample (medium 3). By applying the Fresnel reflection coefficient of this three phase system (*Equation 2.11*) to *Equation 2.12*, a relation can be found which describes the experimentally measured quantities of RAS in terms of the dielectric properties of the sample. This relation is given in *Equation 2.13*. Note the subscript '*123*' on r in the following equations has been dropped for simplicity.

$$\frac{\Delta r}{r} = \frac{2i\omega d}{c}\frac{N_{2x}^2 - N_{2y}^2}{N_3^2 - 1}$$

$$\therefore \frac{\Delta r}{r} = \frac{2i\omega d}{c}\frac{\varepsilon_{2x} - \varepsilon_{2y}}{\varepsilon_3 - 1} \qquad \textit{Eq. 2.13}$$

$$\therefore \frac{\Delta r}{r} = \mathrm{Re} - i\,\mathrm{Im} = \frac{2i\omega d}{c}\frac{\Delta\varepsilon_2^{'} + i\Delta\varepsilon_2^{''}}{\varepsilon_3 - 1}$$

When split into its real and imaginary components gives,

$$\mathrm{Re}\left[\frac{\Delta r}{r}\right] = -\frac{2\omega d}{c}\frac{\Delta\varepsilon_2^{'}}{\varepsilon_3 - 1} \qquad \textit{Eq. 2.14}$$

$$\mathrm{Im}\left[\frac{\Delta r}{r}\right] = \frac{2\omega d}{c}\frac{\Delta\varepsilon_2^{''}}{\varepsilon_3 - 1} \qquad \textit{Eq. 2.15}$$

which are the equations relating the reflection anisotropy to the dielectric properties of the sample.

Although RAS has been designed primarily as a surface technique which utilises the isotropic features of the bulk of a sample to obtain anisotropic surface information, it can also be used on samples which are anisotropic throughout. A sample such as this can be created by mechanically stretching copper foil for example. The preliminary results of an experiment where the RA and the force applied to a sample are measured as a function of sample elongation can be seen in *Figure 2.10*. Both the force and the RA increase with elongation until fracture occurs at which point they drop off dramatically. As expected, the RA shows evidence of plastic deformation in the sample as the anisotropy at the end of the experiment is greater than the initial value.

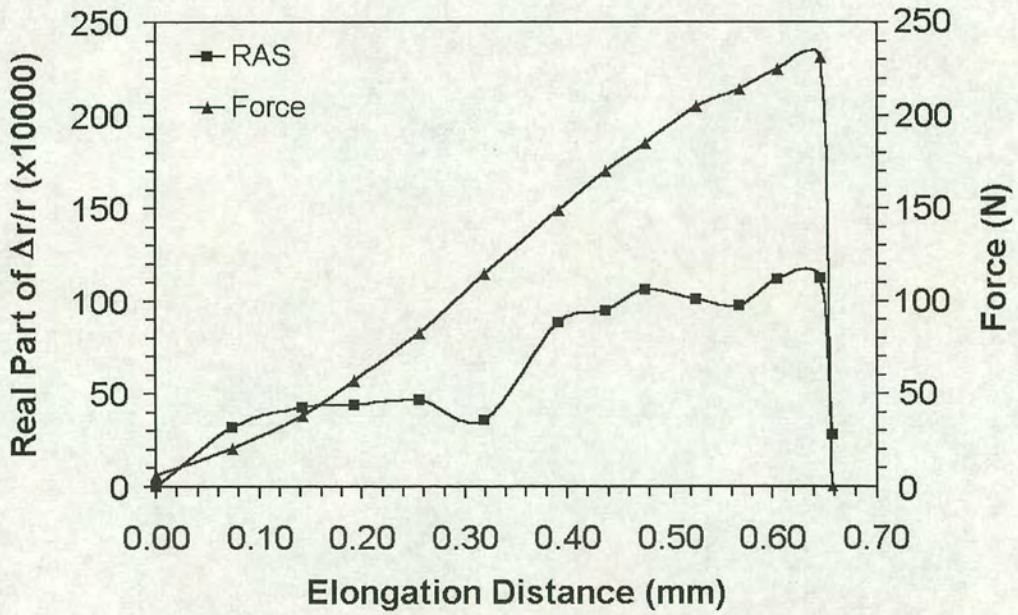

Figure 2.10 *RA at 4.1 eV and force as a function of elongation as polycrystalline copper foil is mechanically stretched.*

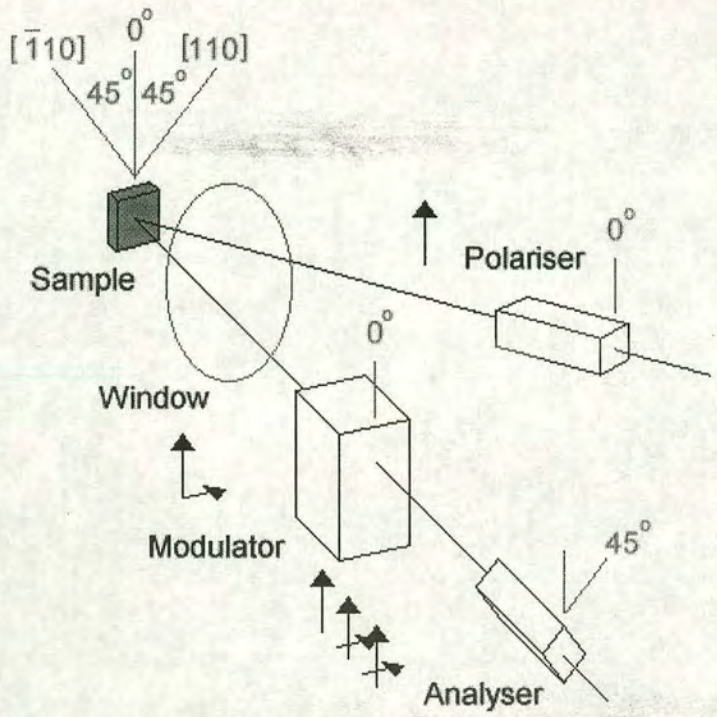

Figure 2.11 Typical RAS equipment including a PEM.

The most commonly used RA spectrometer is that of the design by Aspnes [2.19] which is shown in *Figure 2.11*. A xenon lamp provides the source of light and is aimed towards the sample. Before reaching the sample the light passes through a Rochon prism which transmits the ordinary ray of light undeviated but deflects the extraordinary ray by a few degrees. Sending unpolarised or circularly polarised light into the prism results in an output of linearly polarised light. The direction of polarisation will depend on the orientation of the prism. In the frame of reference of this example, the light is vertically polarised (0°). Depending on the use of the system, the light may next pass through a window into a vacuum chamber. Typically for these purposes, the window will be made of low strain quartz and ideally it would not alter the polarisation state of the transmitted light. To simplify the description of the operation of the spectrometer it is necessary to define another set of axes which lie in the same directions as the crystal axes of the sample. The [110] axis will be defined as being at +45° to the vertical and the [$\bar{1}$10] axis will be defined as being at -45° to the vertical. The vertically polarised light incident on the sample can be

considered to be comprised of two components of equal magnitude perpendicular to each other and at ±45° to the vertical. Anisotropy in the surface of the sample may cause the two components of light to be reflected differently and so the magnitude (or phase) of one component may not be the same as the other after reflection. The reflected light may be returned with elliptical polarisation.

The analysis and collection of the reflected light begins with the PEM. As the light is transmitted through the PEM, the phase of the light is modulated at $\omega \sim 50$ kHz. This causes the transmitted light to switch between two elliptically polarised states. In this system the optic axis of the PEM is aligned with the polariser in the vertical position. The light then passes through an analyser, which is another Rochon prism, where it is then converted from a phase modulated signal to an amplitude modulated signal. By having the analyser at 45° to the vertical, aligned with either [110] or $[\bar{1}10]$direction, the light transmitted through the analyser will be a modulated signal switching between two linearly polarised states. The difference in amplitude of the two states is a measure of the anisotropy of the sample and the average amplitude of the two states is related to the average reflectivity of the sample. These values can be extracted using a lock-in amplifier operating with the modulation frequency as a reference. The signal into the lock-in is an AC voltage which has a DC voltage offset. The AC voltage is related to the anisotropy and the DC to the reflectivity. The measured quantity ($\Delta V/V$) is directly related to the ratio of the modulated and unmodulated components of the light intensity ($\Delta I/I$).

By considering the *Jones matrices* of the optical components in the spectrometer [2.30, 2.31], it is possible to obtain the relation shown in *Equation 2.16* which relates the experimentally measured quantities to the optical and dielectric properties of the sample. In this equation, (-45° + ΔP), θ_1, θ_2, (+45° + ΔM) and (0° + ΔA) are the reference angles of the polariser, light incident on the window, light reflected back through the window, modulator and analyser [2.20] in the samples frame of reference. ΔP, ΔM and ΔA are the misalignments associated with the polariser, modulator and analyser [2.20]. δ_1, δ_2 and δ_{PEM} are the retardation effects on the light

as it is incident on the window, as it is reflected back through the window and as it passes through the modulator [2.20], in this case $\delta_{PEM} = \delta_{PEM_0} \sin(\omega t)$. The defects in the polariser and analyser prisms are given by ($x + ia_P y$) and ($x + ia_A y$), J_1 (δ_{PEM}) and J_2 (δ_{PEM}) are Bessel functions [2.20].

$$\frac{\Delta I}{I} = 2\left[-\mathrm{Im}\left(\frac{\Delta r}{r}\right) + \delta_1 \cos 2\theta_1 + \delta_2 \cos 2\theta_2 - 2a_P\right] J_1(\delta_{PEM}) \sin \omega t + 2\left[\mathrm{Re}\left(\frac{\Delta r}{r}\right) + 2\Delta P + 2\Delta M\right] J_2(\delta_{PEM}) \cos 2\omega t \qquad \textit{Eq. 2.16}$$

$$\mathrm{Re}\left(\frac{\Delta r}{r}\right) = -2\Delta P - 2\Delta M + \frac{\Delta I}{I} \frac{1}{2J_2(\delta_{PEM}) \cos 2\omega t} \qquad \textit{Eq. 2.17}$$

$$\mathrm{Im}\left(\frac{\Delta r}{r}\right) = -2a_P + \delta_1 \sin 2\theta_1 + \delta_2 \sin 2\theta_2 - \frac{\Delta I}{I} \frac{1}{2J_1(\delta_{PEM}) \sin 2\omega t} \qquad \textit{Eq. 2.18}$$

The above equations (*Equations 2.16 - 2.18*) show that the real and imaginary parts of the initial equation can be separated by their frequency dependencies [2.20]. Also shown is that the misalignments of the polariser and modulator (ΔP & ΔM) generate offsets in Re ($\Delta r/r$). Whilst the misalignment of the analyser does not appear in this first order dependency it is known to affect only the DC component [2.20]. The retardation effect of the window (δ_1 & δ_2) and defects in the polariser (a_P) contribute only to Im ($\Delta r/r$) and the defects in the analyser (a_A) do not appear as they are a second order effect [2.20].

In more general terms, excluding offsets in the system, the amplitude of the electric field detected by the RA spectrometer is,

$$A \propto \begin{bmatrix} 1 & 0 \\ 0 & 0 \end{bmatrix} \begin{bmatrix} \cos\left(\frac{\Gamma}{2}\right) & i\sin\left(\frac{\Gamma}{2}\right) \\ i\sin\left(\frac{\Gamma}{2}\right) & \cos\left(\frac{\Gamma}{2}\right) \end{bmatrix} \begin{bmatrix} r_{xx} & r_{xy} \\ r_{yx} & r_{yy} \end{bmatrix} \begin{bmatrix} 1 \\ 1 \end{bmatrix}$$

$$A \propto \cos\left(\frac{\Gamma}{2}\right)\left(r_{xx} + r_{xy}\right) + i\sin\left(\frac{\Gamma}{2}\right)\left(r_{yx} + r_{yy}\right) \qquad \textit{Eq. 2.19}$$

where the contribution from the sample (the 2 x 2 r matrix) now has non-zero off-diagonal elements to allow for sample rotation in the azimuth. By summing the averages of the diagonal and off-diagonal elements and by summing the differences of the diagonal and diagonal elements,

$$\Sigma_{AV} = \frac{r_{xx} + r_{yy}}{2} + \frac{r_{xy} + r_{yx}}{2}$$
$$\Sigma_{DIFF} = (r_{xx} - r_{yy}) + (r_{xy} - r_{yx})$$

therefore,

$$r_{xx} + r_{xy} = \Sigma_{AV} + \frac{\Sigma_{DIFF}}{2}$$
$$r_{yx} + r_{yy} = \Sigma_{AV} - \frac{\Sigma_{DIFF}}{2}$$

and *Equation 2.19* can be rewritten as,

$$A \propto \cos\left(\frac{\Gamma}{2}\right)\left(\Sigma_{AV} + \frac{\Sigma_{DIFF}}{2}\right) + i\sin\left(\frac{\Gamma}{2}\right)\left(\Sigma_{AV} - \frac{\Sigma_{DIFF}}{2}\right)$$

The intensity of the light reaching the detector is therefore,

$$I = AA^* = |\Sigma_{AV}|^2 \left\{ \begin{array}{l} 1 + \frac{1}{4}\left|\frac{\Sigma_{DIFF}}{\Sigma_{AV}}\right|^2 + \frac{\cos(\Gamma)}{2|\Sigma_{AV}|^2}\left(\Sigma_{AV}\Sigma_{DIFF}^* + \Sigma_{AV}^*\Sigma_{DIFF}\right) + \\ i\frac{\sin(\Gamma)}{2|\Sigma_{AV}|^2}\left(\Sigma_{AV}\Sigma_{DIFF}^* - \Sigma_{AV}^*\Sigma_{DIFF}\right) \end{array} \right\}.$$

By expanding the trigonometric functions using Bessel functions, J, with $J_0(\delta_{PEM_0}) = 0$, the quantity measured is,

$$\frac{\Delta I}{I} = \frac{2J_1(\delta_{PEM_0})\mathrm{Im}\left(\frac{\Sigma_{DIFF}}{\Sigma_{AV}}\right)}{1+\frac{1}{4}\left(\frac{\Sigma_{DIFF}}{\Sigma_{AV}}\right)} + \frac{2J_2(\delta_{PEM_0})\mathrm{Re}\left(\frac{\Sigma_{DIFF}}{\Sigma_{AV}}\right)}{1+\frac{1}{4}\left(\frac{\Sigma_{DIFF}}{\Sigma_{AV}}\right)}$$

$$\frac{\Delta I}{I} \approx 2J_1(\delta_{PEM_0})\,\mathrm{Im}\left(\frac{\Sigma_{DIFF}}{\Sigma_{AV}}\right) + 2J_2(\delta_{PEM_0})\mathrm{Re}\left(\frac{\Sigma_{DIFF}}{\Sigma_{AV}}\right)$$

which is similar to *Equation 2.16*. The real component can be rewritten as,

$$\mathrm{Re}\left(\frac{\Sigma_{DIFF}}{\Sigma_{AV}}\right) \approx \frac{\Delta I}{I}\frac{1}{2J_2(\delta_{PEM_0})} \qquad \textit{Eq 2.20}$$

where,

$$\frac{\Sigma_{DIFF}}{\Sigma_{AV}} = 2\frac{r_{xx} - r_{yy} + r_{xy} - r_{yx}}{r_{xx} + r_{yy} + r_{xy} + r_{yx}} = \frac{\Delta r}{r} \qquad \textit{Eq. 2.21}$$

which is the generalised RA and is a function of both energy and azimuthal angle.

Chapter 3: Construction of Apparatus

'And many strokes, though with a little axe, hew down and fell the hardest-timbered oak'
Shakespeare (1564 - 1616)
King Henry VI Part III Act 2 Scene 1

Summary

This chapter is used to describe the construction and operation of the experimental equipment used throughout this project and is split into two major parts: the vacuum system and the reflection anisotropy spectrometer. There is also a final short section concerning the scanning probe microscope. Each section contains a discussion of the major components which includes the operation of each item individually and as part of the system and any known errors associated with each component.

Part I: Vacuum System

Vacuum Chamber

The vacuum chamber used here can be split into three major sections: the main chamber, the pumping chamber and the transfer chamber. Each of these are capable of UHV pressures and can be completely isolated from one another. Measurements are taken in the main chamber where the samples are held. Connected to the base of this section is the pumping chamber which houses a liquid nitrogen trap and links the diffusion pump to the main chamber. Attached to a port on the side of the main chamber, separated by a valve, is the transfer chamber which has been designed to allow samples to be changed rapidly without exposing the entire system to ambient conditions. Photographs of the vacuum chamber are shown in *Figures C.1 & C.2* of *Appendix C.*

The primary function of this vacuum system is to allow *in-situ* monitoring, by RAS, of samples and sample processing. At present 'sample processing' refers to the use of either an ion bombardment sample cleaning source, a sample heater or molecular sublimation apparatus. However, the chamber has been designed to accommodate many other attachments giving extra flexibility in the positioning of current equipment and to allow for expansion in the future. All of the ports on the main chamber are angled towards the centre of the chamber where samples are held in a sample manipulator. To optimise the monitoring of the sample by RAS, the light enters and exits the chamber through a low strain quartz window allowing the transmission of higher levels of UV light and reducing birefringence effects. Careful positioning of all ports is crucial as it is desirable to be able to monitor as many processes as possible, simultaneously, by RAS. The quartz window is positioned in the centre of one side of the main chamber and is surrounded by the other ports as can be seen in *Figure 3.1.*

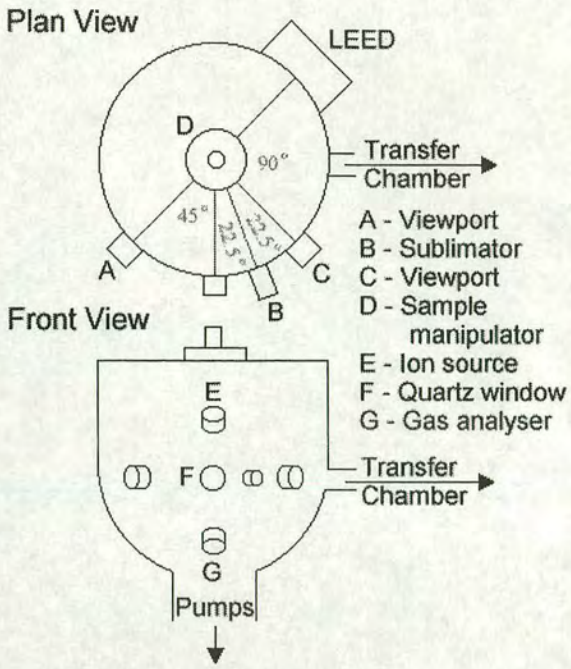

Figure 3.1 *Main chamber of the vacuum system.*

The metal crystal samples are held in a custom designed holder, *Figure 3.2*, which can be inserted into the manipulator using the mechanism contained in the transfer chamber. Two clips are used to attach samples to the holder by either pressing down on the top of the sample or by using slots cut into the sample. The sample manipulator is made of three main components allowing accurate positioning of the sample within the chamber. A RD2 rotary motion drive from Vacuum Generators allows two degrees of angular freedom and is mounted on the second component, a standard *x-y-z* stage. The third component is a custom made flexible flange from which the sample holder hangs and the other components of the manipulator are mounted. The flange has been reinforced using three variable length supports. By adjusting the length of any of the supports, the angle of the entire manipulator can be altered.

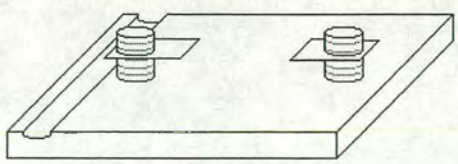

Figure 3.2 *Custom designed sample plate which has dimensions of 2 cm x 3 cm.*

The main component of the transfer chamber is a magnetically coupled transfer arm, as shown in *Figure 3.3*. When it is necessary to change the sample, the valve between the main chamber and the transfer chamber is opened and the arm extended towards the sample manipulator. The sample holder can be moved into the grooved jaw of the arm, which is then retracted before the two sections are isolated again by closing the valve. To remove the sample it is necessary to expose only the transfer chamber to ambient conditions. Using a rotary pump and a turbo pump dedicated to this part of the system it is possible to obtain a suitable vacuum in the transfer chamber after venting, such that it may safely be exposed to the main chamber within ~30 minutes.

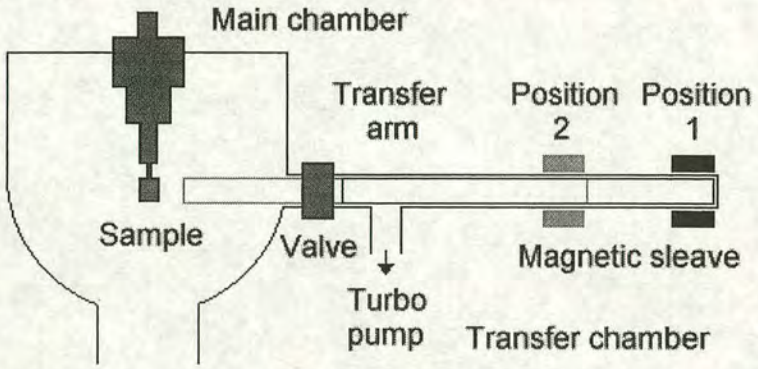

Figure 3.3 *Connection of the transfer chamber to the main chamber.*

The molecular evaporator has been custom made and consists of a filament wrapped around a tube which contains the material to be sublimated, all of which is held within the vacuum chamber. The power source for the filament is the same as used for the sample heater. The advantage of this apparatus over other methods is that the thermocouple allows the temperature to be precisely controlled and higher temperatures can be obtained as a result of the heating components being housed within the vacuum chamber.

An additional component which has been added to the transfer chamber (not shown in *Figure 3.3*) allows liquid to be dropped onto a clean sample without exposing the sample to ambient conditions. This component is a solid flange with a small hole (1 mm diameter) drilled in the centre. When operating under normal (UHV) conditions, the hole is covered by a smaller solid blank flange, creating a seal. To deposit liquid

onto the surface of a sample, the sample must be held in the transfer arm, in the transfer chamber and isolated from the main chamber. The transfer chamber is flooded with argon until a pressure several times greater than atmospheric is achieved. When the seal is removed to expose the drilled hole, air is prevented from entering the chamber by the outward flow of argon. A syringe can be used to drop liquid onto the surface. After the seal is replaced, the argon can be removed using the turbo pump and the sample replaced into the main chamber. Although this technique prevents contaminants from ambient conditions from reaching the surface, it has not proved to be totally effective. The argon used has a purity of 99.99%, the remaining 0.01% however is enough to react with the clean surface of the sample and contaminate it slightly. This method has been found to be much cleaner than simply depositing the liquid on the surface in ambient conditions.

Pumping System and Gauges

A pressure of $1x10^{-11}$ mbar can be obtained in the main chamber by using a combination of a rotary pump, a diffusion pump, a ST22 titanium sublimation pump (Vacuum Generators) and a liquid nitrogen trap. In the transfer chamber a pressure of $1x10^{-7}$ mbar is normal and is achieved using a single turbo pump backed by a rotary pump. The pressure in each chamber is measured using ion gauges, IGC 26 & IGC 11 (Vacuum Generators) and Pirani gauges at each of the rotary pumps.

As protection for the filaments and electronic components used within the vacuum chamber, a pressure switch is used. The switch will be tripped if the pressure in the main chamber rises above a set level, cutting the power to all the electrical equipment, except the pumps. In the event of a pump failure, to prevent oil flooding the chamber, an electrical circuit has been implemented which is designed to isolate the diffusion pump and deactivate all the pumps.

Low Energy Electron Diffraction

LEED is a technique used to gain information about the crystal structure of the surface of a sample. A more detailed description of the technique can be found in *Chapter 2*. The LEED equipment used was purchased from Vacuum Generators.

Sample Cleaning Ion Source

Samples are cleaned in the vacuum chamber using a model ISI3000 Ion Source (PSP Vacuum Technology). The ion source has an operating pressure of $5x10^{-6}$ mbar and is variable energy (100 - 3000 eV) giving a typical beam current of about 15 μA. Surface material is removed from samples by impacting energetic ions into the surface. The ions are created by leaking an inert gas into a discharge chamber and are then focused onto the sample.

Sample Heater

A P.I.D. heater (PSP Vacuum Technology) is used to heat and anneal samples within the vacuum chamber. The heater is mounted on the sample manipulator and incorporates a 2116 PID temperature controller (Eurotherm Controls). The heating element is a tungsten filament which acts as a low voltage resistive heater giving a maximum temperature of approximately 750° C.

Bake Out Unit

The Bake-out control unit and Bake-out heaters (PSP Vacuum Technology) use four 1 kW heaters to heat the vacuum chamber. When covered by an insulating hood, temperatures up to 200° C can be obtained. A thermocouple is used to ensure a constant temperature.

Part II: Reflection Anisotropy Spectrometer

Introduction

The RA spectrometer used to acquire the data presented in this thesis has been custom built in Edinburgh. The design of the system was largely based upon spectrometers previously constructed elsewhere, namely in Liverpool and Berlin. Although the design and components are essentially the same, much time has been spent to ensure the set up and performance of the Edinburgh spectrometer is optimal. The following section gives a relatively detailed description of the construction of the system, the operation of individual components involved and the errors involved with the system. The spectrometer can be thought of in two main sections, the electronic and optical parts, the following descriptions have been split up in the same way. The optical components of the spectrometer are used to obtain information from the sample and to process the reflected light, allowing the information contained within the light to be retrieved and presented by the electronics. Although most RA spectrometers are built as depicted in *Figure 2.11*, to allow the principal axes of the samples to be aligned horizontally and vertically, the polariser, PEM and analyser are rotated by 45° in the spectrometer built here. Photographs of the spectrometer are shown in *Figures C.3 & C.4* of *Appendix C*.

Optics

Positioning

RA spectrometers are built to be used both in conjunction with a vacuum chamber and stand-alone. For measurements in ambient conditions the sample is mounted in a holder which can be rotated through 360° in the position shown in *Figure 3.4*. Similarly, for studies in vacuum, the spectrometer must be aligned next to the vacuum chamber with the incident light beam directed into the low-strain window. All of the optical components are mounted on a single optical breadboard which has adjustable legs allowing height and angle adjustments to be made easily.

Ideally, the position of each component would match exactly the calculated positions (see *Focussing Mirrors* section later in this chapter) but due to size constraints it is not always possible. The actual positions are as close to the calculated positions as possible. In this spectrometer, the length of each polariser is 40 mm, the thickness of the PEM is 10 mm and the focal lengths of the mirrors are 200 mm and 150 mm. The longer focal length mirror being positioned closest to the lamp. The distances between the components, not including the dimensions of the components, are shown in *Figure 3.4* and are given in *Table 3.1*. The total distance between the lamp and sample is 1160 mm and the total distance between the sample and monochromator is 1045 mm. Both compare well to the calculated distances of 1134 mm & 1056 mm, as discussed later.

	a	*b*	*c*	*d*	*e*	*f*	*g*	*h*
Size (mm)	*230*	*240*	*370*	*280*	*330*	*70*	*145*	*170*

Table 3.1 *Distances corresponding to Figure 3.4.*

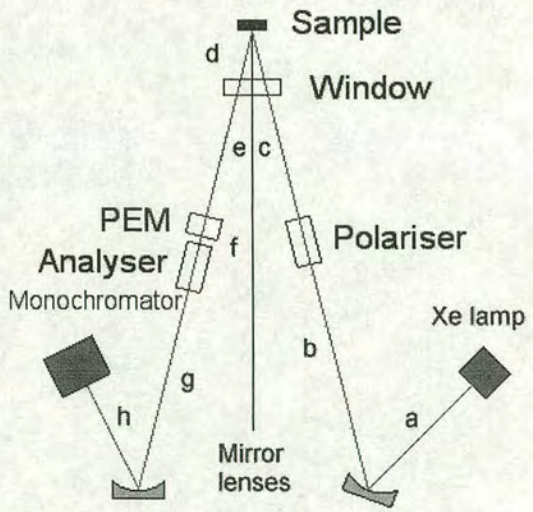

Figure 3.4 *Positions of each component in the RA spectrometer (sizes given in Table 3.1).*

Near normal incidence of light is crucial in RAS although small angles are permitted. The equations described in *Chapter 2* use this assumption. The angle of incidence is measured for this spectrometer using the positions of the analyser and the polariser as shown in *Figure 3.5*. As the distance between the sample and each of the

components is not equal (630 mm compared to 650 mm), an average of the two calculated angles is found. The distance between the prisms is measured from the near side of one prism to the far side of the other and is found to be 25 mm. The measured angle of incidence in the spectrometer built here is $2.37° \pm 0.06°$.

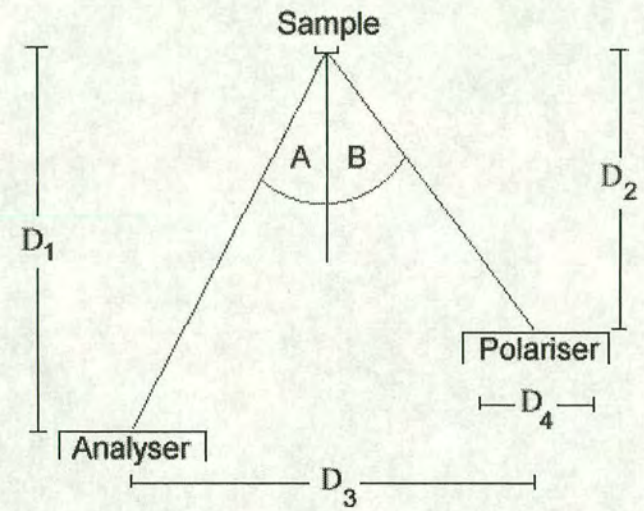

Figure 3.5 *Diagram showing the difference in angle between the incident and reflected beams.*

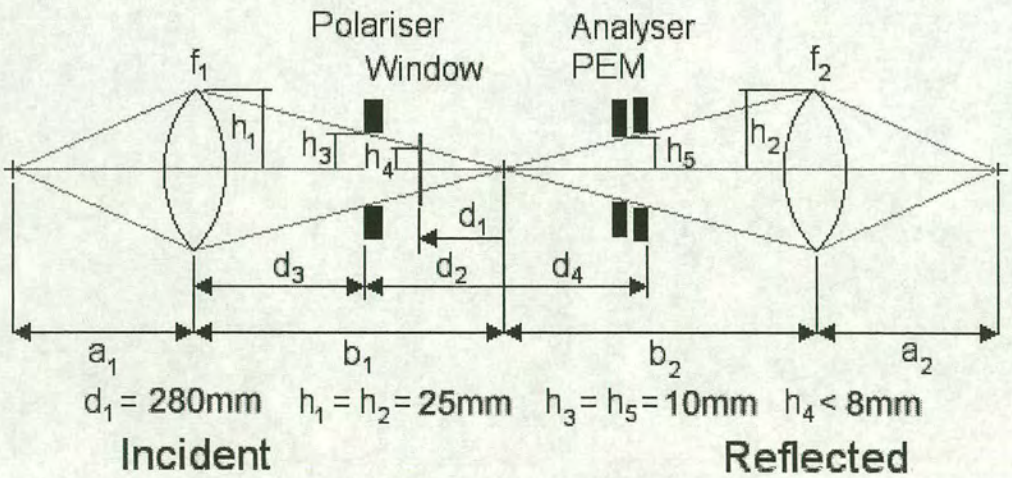

Figure 3.6 *Definition of lengths used to calculate the focal lengths of the mirrors.*

Approximate values of the required focal lengths of the mirrors were calculated using predefined criteria and the dimensions of some of the components in the system. From these estimated values, approximate positions of the mirrors, polarisers, lamp and monochromator with respect to the sample can be calculated. The focal lengths are calculated using distances defined in *Figure 3.6*.

The aim of the following calculations is to roughly find f_1 and f_2 and then to use these values to approximately find a_1, a_2, b_1 and b_2. This is done by firstly defining some criteria and then considering the 'incident' system on its own. Initially the criteria are that the light hitting the sample must be maximised, the magnification must be less than 4 and the radius of the light as it passes through the window must be less than 8mm.

$$\frac{d_2}{h_3} = \frac{d_1}{h_4} \Rightarrow d_2 > 350mm$$

$$\frac{d_2}{h_3} = \frac{b_1}{h_1}$$

$$\therefore b_1 > 875mm$$

Using the magnification criteria,

$$M = \frac{b_1}{a_1} \approx 4$$

$$\therefore a_1 > 219mm$$

$$\therefore f_1 > 175mm$$

Next, another requirement is defined and the 'reflected' system is considered as well. The extra criterion is that the amount of reflected light collected by the monochromator must be maximised and so the final spot size must be less than the monochromator slit size (~1 mm).

$$\frac{d_2}{h_3} = \frac{d_4}{h_5} \Rightarrow d_4 > 350mm$$

$$\frac{b_2}{h_2} = \frac{d_4}{h_5}$$

$$\therefore b_2 > 875mm$$

Assuming the spot size on the sample to be ~4 mm, based on a 1 mm source, to meet the criteria of getting all the light into the monochromator a magnification of ~0.2 would be required. Therefore,

$$\therefore a_2 > 175mm$$

$$\therefore f_2 > 145.8mm$$

Using these estimated values as guidelines and by studying the available focal lengths, the mirrors used will have focal length of 200 mm and 150 mm. By using these values for f_1 and f_2 and by meeting the criteria set, it is found that a_1 ~259 mm, a_2 ~181 mm, b_1 ~875 mm and b_2 ~875 mm. Therefore, the calculated distance between the lamp and sample is 1134 mm and the calculated distance between the sample and the monochromator is 1056 mm. By comparing these values to the measured values for the constructed spectrometer, it can be found that the distances are accurate to within 2.29% and 1.04% respectively. These errors are due to the size constraints of the components, as mentioned earlier.

Light Source

The light source is a Hamamatsu 75 W xenon lamp which outputs a constant range of wavelengths from ~180 nm to ~1 μm. As the light contains relatively high levels of UV, for safety reasons, the aperture size was reduced to 1mm to limit the amount of light given out by the lamp. When triggering the lamp, a large quantity of electromagnetic noise is generated. This could prove damaging to devices which are weak against such noise, for example computers.

Focusing Mirrors

Light from the source is focussed onto the sample and then from the sample onto the monochromator aperture using spherical concave mirrors. These mirrors (Coherent)

are 50 mm in diameter and have focal lengths of 150 mm and 200 mm. Each mirror is aluminium coated giving an average reflectivity over a wavelength range of 400-800 nm of greater than 87%. Although a significant amount of UV is not reflected, these are mirrors more suitable than conventional glass lenses. A discussion of the method used to eliminate errors due to the absorption of light can be found in *Errors* section of this chapter.

Polariser / Analyser

The spectrometer requires linearly polarised light incident on the sample and it requires the reflected beam to be split into its two polarisation components after passing through the PEM. To do this, two quartz Rochon polarisers (Comar Instruments) are used as a polariser and analyser. These prisms use double refraction (birefringence) to split an incident beam into its ordinary and extraordinary components. Each prism is made of two wedge shaped prisms which are cemented together with their optic axes perpendicular. In the first of these prisms, both the ordinary and the extraordinary beams travel through unchanged. This continues to be so for the ordinary beam after it enters the second prism as the refractive index is unchanged. However, as the extraordinary beam enters the second prism, the lower refractive index causes the beam to deviate. This effect is repeated as the light leaves the second prism. Having the ordinary beam undeviated is the main advantage of Rochon prisms over other types of polarisers, such as Glan–Thomson prisms, which deflect both the ordinary and the extraordinary components of the light. The deviation varies with wavelength and therefore the angular separation varies from 12° at 350 nm to 9° at 2.5 μm.

Photoelastic Modulator

To measure the difference in amplitude between the two polarised components of the reflected light it is necessary to separate the polarisations prior to the light entering the analyser. This is done using a PEM (Hinds PEM 90 D) to modulate the reflected light before it enters the analyser.

By mechanically stressing the block of silica within the PEM, birefringence is induced, that is, the velocities at which different polarisations of light travel through

the material varies slightly. The amount of birefringence is proportional to the stress applied and so by oscillating the stress applied to the sample, using a piezoelectric transducer, it is possible to oscillate the modulation. Modulation occurs at a frequency of approximately 50 kHz as this is a typical value of the resonant frequency of the fused silica used in this PEM.

Assuming the plane of polarisation of light incident on the PEM is at 45° to the modulator axis, the light can be affected in either of two ways. If the silica is unstressed as the light passes through, all of the polarisation components will remain unchanged. However, if the silica is stressed as the light passes through, the polarisation component parallel to the modulator axis will travel slightly faster than the vertical component. Depending on whether the silica is stretched or compressed, the horizontal component of the polarisation will either lag or lead the vertical component. As a result of this, light transmitted through the PEM will be modulated and will oscillate between left and right circularly polarised light.

Monochromator

To enable a spectroscopic study of the reflected light, it is necessary to split the light into its individual wavelengths. This is done using a monochromator (Jobin Yvon Ltd H10UV) which uses a concave holographic diffraction grating with a focal length of 10 cm. The grating has 1200 grooves/mm, a spectral range of 200-750 nm and a maximum resolution of 1 nm. By changing the angle of the diffraction grating, it is possible to select the frequency of light to be transmitted through the monochromator. The counter indicating the wavelength setting of the diffraction grating is graduated in nanometre increments and has a precision of ±0.5 nm.

A Hg/Cd/Zn lamp was used to calibrate the monochromator as the wavelengths of the transmission lines for these elements are well known [3.1]. The results of the calibration can be seen in *Figure 3.7*. Errors due to the slight difference between the two sets of values can be considered negligible as the monochromator has a more significant error associated with it which is discussed later in the *Errors* section of this chapter.

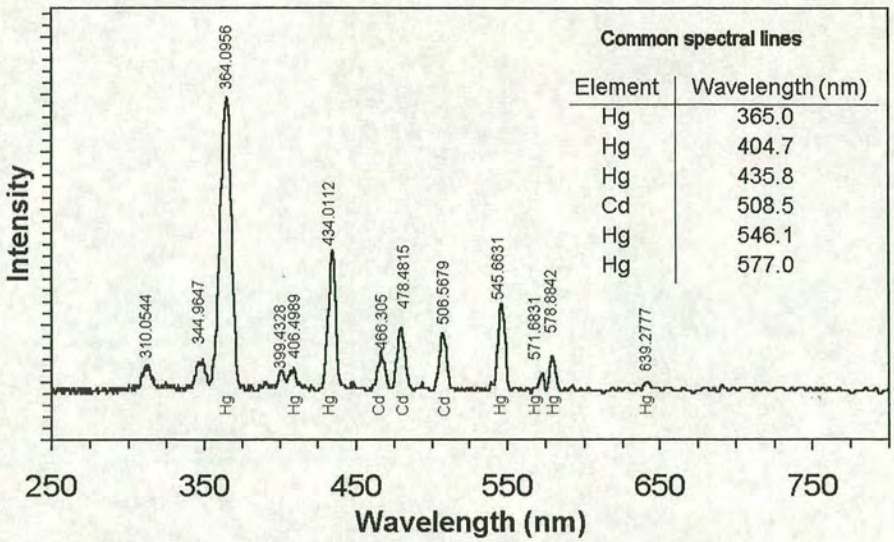

Figure 3.7 Monochromator calibration using a Hg/Cd/Zn lamp.

Electronics

The amplitude of the light, at each wavelength, is measured using a photodetector which converts the incident photons into a corresponding number of electrons. The electronic components of the spectrometer are responsible for processing the current from the detector and displaying the result. The experimental arrangement of the electronic components can be seen in *Figure 3.8*.

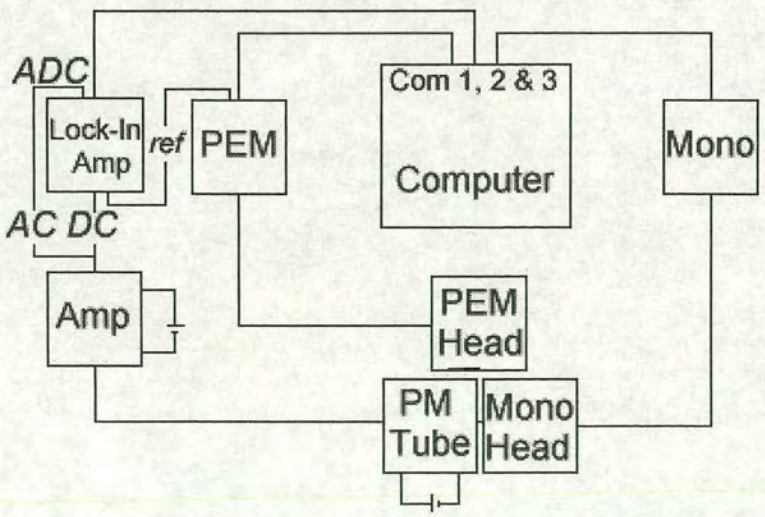

Figure 3.8 Diagram showing set up of electronic equipment.

Photomultiplier Tube

The detector used to convert the light from the monochromator into a current is a photomultiplier tube (Hamamatsu H957-08) which has a spectral range of 185 nm to 900 nm and has a typical sensitivity of 250 μA/Lm. Using a photomultiplier tube (PMT) gives very high sensitivity, nanosecond response time and low noise. The window used in the PMT is made from UV-transmitting glass which has a cut-off at ~185 nm. The power is supplied from a 15 V dual power supply (Farnell L30BT). A silicon photodiode was tested as an alternative to the PMT but was found to have a lower spectral range and so was not used.

A typical PMT consists of a photoemissive cathode, focusing electrodes, an electron multiplier and electron collector (anode) in a vacuum tube. When light hits the photocathode, photoelectrons are emitted. These photoelectrons are focused on the electron multiplier where they are multiplied by secondary emission and then collected by the anode as an output signal.

Current-Voltage Converter & Amplifier

The output signal from the PMT is a current with typical amplitude of only a few micro-amps. The signal consists of an AC component superimposed on a DC offset. The AC component is related to the anisotropy and the DC to the reflectivity. It is necessary to change both the AC and DC currents into AC and DC voltages which will then need to be amplified to be measured. These transformations are done using an electronic circuit based around an operational amplifier.

The amplification device used has been custom built for this purpose, the circuit diagram can be seen in *Figure 3.9*. Both the gain and offset are variable to allow greater control over the operation of the amplifier. The power supply needed for the operation amplifier is output +15 V, 0 V and –15 V which is supplied by the lock-in amplifier. Two different circuit diagrams are shown, *Figure 3.9* and *Figure 3.10*. The first of these is a typical circuit diagram whilst the second gives details of the wiring of the circuit to aid anyone wishing to duplicate this device in the future.

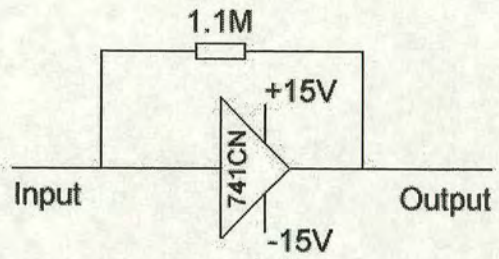

Figure 3.9 Circuit diagram of amplifier.

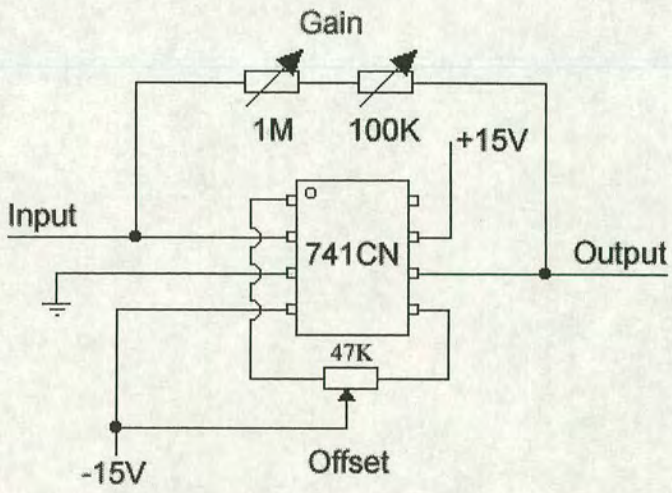

Figure 3.10 Circuit diagram of amplifier showing details of wiring.

Lock-in Amplifier

To isolate and measure both the AC and DC voltages a lock-in amplifier is needed. In this system, an EG&G 5209 (Perkin Elmer) lock-in amplifier is used. Part of the signal from the operational amplifier is sent to the analogue to digital converter (ADC) of the lock-in amplifier and part is sent to the main input. The ADC is used to measure the DC component of the signal and the AC component is phase sensitively measured by the lock-in amplifier using the modulation frequency of the PEM (~50 kHz) as a reference signal. The measured values are sent to a computer using the serial communication capability of the amplifier.

Two crucial settings of the lock-in amplifier are the sensitivity and the time constant. The value of the sensitivity chosen will depend on the amplitude of the measured signal and should be set to the highest sensitivity allowed without overloading the

lock-in amplifier. The choice of time constant is made as a compromise between sensitivity and lowering noise levels. *Figure 3.11* shows the measured RAS as a function of the sensitivity setting on the lock-in amplifier. From this figure, the offset, which is also discussed later in this section, can be seen to increase with the sensitivity setting. As *Figure 3.12* shows, by having the time constant set at a high value, the signal to noise ratio appears very good but the sensitivity of the system is sacrificed to achieve this. Alternatively, by having the time constant set at a very low value, the sensitivity of the system is very good but the signal to noise ratio is relatively poor. Therefore values of 10 ms, 30 ms or 100 ms are recommended.

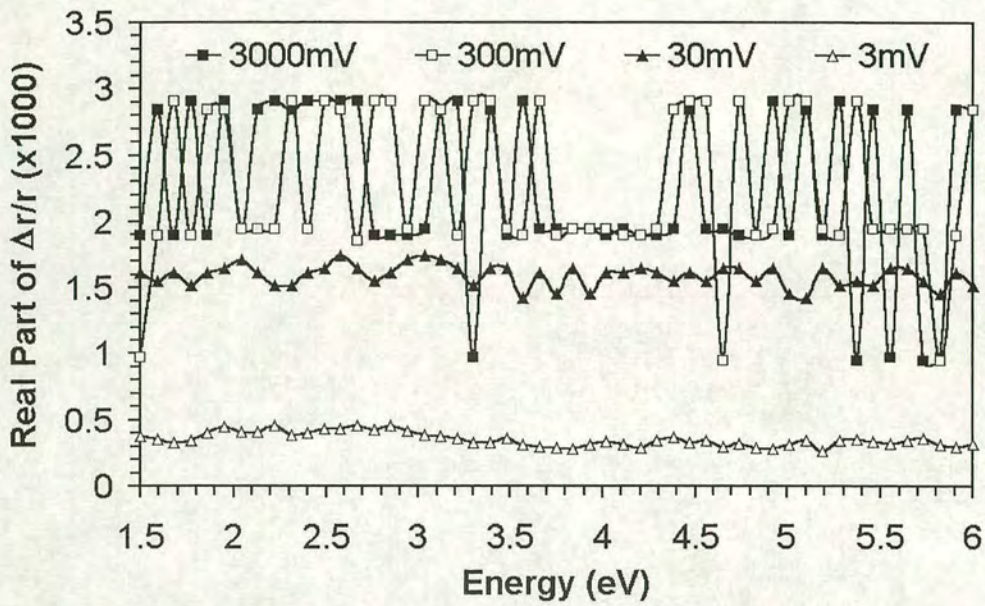

Figure 3.11 *RA spectra showing the different sensitivity settings of the lock-in amplifier with the time constant set to a constant value of 100 ms.*

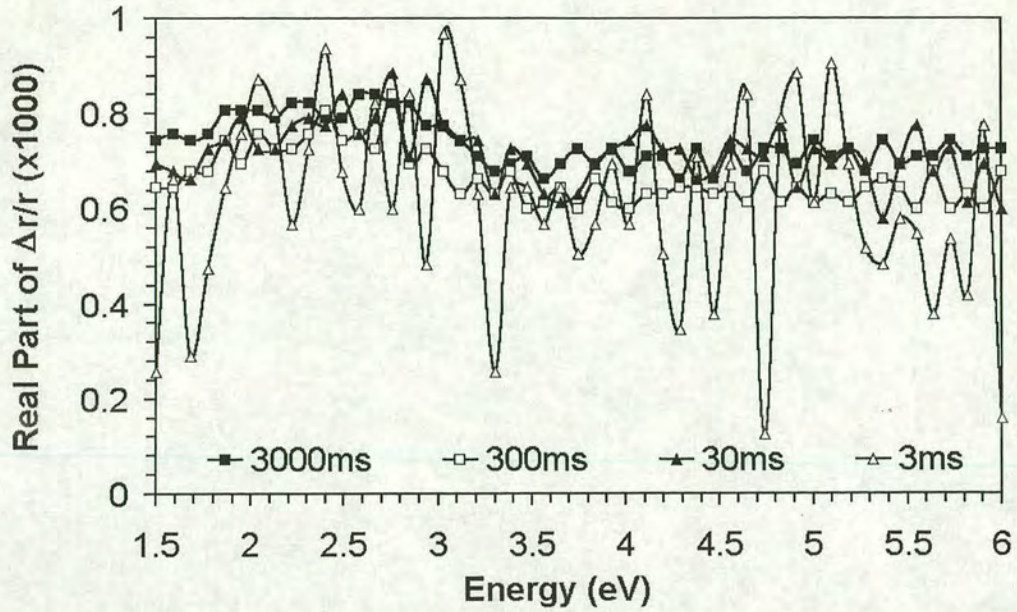

Figure 3.12 *RA spectra showing different time constant settings of the lock-in amplifier with the sensitivity set to a constant value of 10 mV.*

RS232 Communication

The computer communicates with the PEM, monochromator and the lock-in amplifier using RS232. The operating system of the computer used for RAS is software written by J Rumberg [3.2]. Some minor changes were made to the software to enable communication with the PEM-90D. Prior to the changes, the software had been set to a baud rate of 1200, the rate needed to communicate with PEM-90C. By altering the files ras.c & ras_pem.c (changing all baud rate settings corresponding to the PEM from 1200 to 9600) it is possible to communicate with PEM-90D. An extra two serial ports were added to the computer to allow serial communication with up to four devices. All the communication (com) ports were set to the values shown in *Table 3.2*.

Baud rate	9600
Data bits	8
Parity	None
Stop bits	1
Flow	Xon/Xoff

Table 3.2 *Computer communication port settings.*

Communication between the lock-in amplifier and the computer is done through an RS232 serial cable. Here, the female connector (lock-in end) is a 25 pin parallel port connection whilst the male connector (computer end) is a 9 pin parallel port connector. The pin connections are shown in *Table 3.3*. Communication between the devices can only occur if the RS232 communications controls of the lock-in amplifier are set to match those in both the software and the com port of the computer. Much time was spent trying to do this and so a full description is given here for future reference. To make changes to the RS232 settings of the lock-in amplifier, press CONFIG + SLOPE/RS232C. If the value displayed on the TUNING LCD shows '0', the Baud rate controls may now be changed. Alternatively, if the value displayed is '1', the other parameters may be set. For this configuration, it is required that the baud rate be 9600, therefore a setting of 11. Also required are 8 data bits, even parity, parity off, 1 stop bit and RS232 echo on, therefore a setting of 21. Explanations of these codes can be found in EG&G 5209 user manuals or from the Perkin Elmer website [3.3].

Female - Male	Male - Female
1-1	1-1
2-3	2-3
3-2	3-2
4-5	4-5
5-4	5-4
7-7	6-20
20-6&8	8-20

Table 3.3 RS232 cable connections.

Errors

Although the spectrometer has been optimised as much as possible, several sources of error still exist. Given in this section is a description of these errors plus a description of some other errors which have been minimised.

Normalisation of Reflectivity

The optical components in the spectrometer are not ideal transmitters and reflectors of light and so they absorb different quantities of light at different frequencies. Therefore the measured reflectivity is not a true measure of the reflectivity of the

sample. A true reflectivity value can be obtained by isolating the effect the optical components have on the light as it passes through. This can be done by using a sample of well known optical properties as a calibration standard, suitable examples are Si, Cu and GaAs. The reflectivity (R) of the calibration standard can be calculated using the refractive index (n) and extinction coefficient values (k), which may be obtained from reference [3.4]. By using *Equation 3.1*, the calculated reflectivity of the calibration standard, the measured reflectivity of the calibration standard and the measured reflectivity from any sample can be used to obtain a calculated (true) reflectivity of any sample. This method has been tested using several different samples and has resulted in spectra which appear approximately the same. These spectra, shown in *Figure 3.13*, are plots of the measured values (DC) divided by the theory (book) values for three calibration standards. The resultant spectra are graphical representations of the effect the optical components of the spectrometer have on the light as it passes through. In the case of Si and GaAs the measurements were taken in ambient conditions and although these results appear similar it is very likely both surfaces are contaminated with oxygen and hydrocarbons. In the case of Cu, the sample has been cleaned in a vacuum chamber and the reflectivity measurements are taken *in-situ*, the quartz window of the vacuum chamber must therefore be taken into consideration.

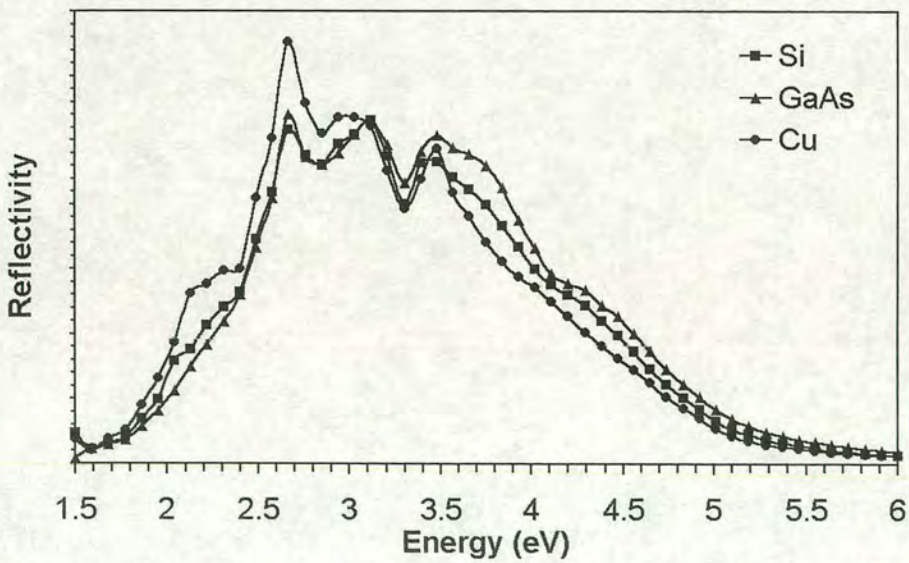

Figure 3.13 *Error spectra found by dividing the measured reflectivity by the known reflectivity.*

$$X(Theory) = X(Measured) \times \frac{Y(Theory)}{Y(Measured)} \qquad Eq.\ 3.1$$

Window Correction

Optical measurements taken from a sample within a vacuum chamber are subject to additional errors as the light will be modified as it enters and exits the vacuum chamber. Although birefringence and optical absorption effects can be minimised by the use of a low stain quartz window, a correction function is still required. The measured RA spectra can be thought to be made up of two components, one from the sample and one from the window. By using this, a correction function based upon spectra taken at perpendicular azimuthal angles can be obtained.

$$\begin{aligned} RAS(0^o) &= RAS(window) + RAS(sample) \\ RAS(90^o) &= RAS(window) - RAS(sample) \end{aligned} \qquad Eq.\ 3.2$$

The resultant effect on the RAS due to the window can be found by averaging the spectra taken at 0° and 90° (*Equation 3.2*) to give the window correction function (*Equation 3.3*). By subtracting this function from either the 0° or 90° data set, it is possible to obtain RA spectra specific to the sample.

$$WindowCorrection = RAS(window) = \frac{RAS(0^0) + RAS(90^0)}{2} \qquad Eq.\ 3.3$$

Offsets

Polariser, Analyser and Modulator

As mentioned in *Chapter 2*, the effect of misalignment of the optical components can be seen in *Equations 2.16 - 2.18*. These equations show that an offset in either the polariser or the modulator results in a offset in the real part of the measured RA. Similarly a misalignment of the analyser generates an offset in the DC [3.5]. These offsets can only be minimised by the precise alignment of the components.

Sample misalignment

The errors due to sample misalignment have been reduced significantly by the introduction of a laser alignment system. It has been found that a change in the vertical position of the light beam on the analyser, which corresponds to a very slight change in the angle of the sample, causes a significant offset in the RAS signal. It can be calculated that a 1 mm difference in the position of the light entering the polariser is due to a change of sample angle of less than 0.1°. To minimise this change, it is necessary to minimise the deviation of the angle of the sample. By having a laser diode in a fixed mounting such that the reflection of the laser beam from the sample hits a target, it is possible to accurately set the angle of the sample, with respect to the spectrometer.

Lock-In amplifier

An offset in the AC component of the signal has been found to originate from the lock-in amplifier and is dependent on the sensitivity setting and the length of time the amplifier has been switched on. As the amplifier reaches operating temperature, the AC offset is gradually reduced. The offset follows a general trend of becoming smaller as the sensitivity of the amplifier is increased. The AC offset has a constant value as a function of photon energy above 3.5 eV, below this energy the offset has a broad hump centred at 2.75 eV.

Operational Amplifier

The offset in the DC is created by the amplification of the output signal of the PMT prior to being measured by the lock-in amplifier. This offset is constant at all photon energies, is independent of all other settings, and has a value of 0.0455 V ±0.0005 V.

General

The offsets in both the AC and the DC components of the signal have been measured and isolated by recording a 'no light spectra' (the spectra measured when the aperture to the monochromator is blocked). As the DC offset appears constant, the variations in the RAS (*Figure 3.11* and *Figure 3.12*) are due to the AC component of the RAS and can be attributed to the lock-in amplifier.

The true AC and DC values are the measured AC and DC values minus the relevant AC and DC offsets. It should be remembered that the AC offset is dependent on the sensitivity setting of the lock-in amplifier which in turn is dependent on the anisotropy of the sample. To get a true RAS value it is necessary to correct both the AC and DC values by subtracting the no-light spectra value before they are used to calculate the RAS (*Equation 3.4*). It has been found that the resultant offset in the RAS due to these two offsets is negligible. From this point forward it is assumed that AC, DC and RAS refer to the true values.

$$AC(true) = AC(measured) - AC(offset)$$
$$DC(true) = DC(measured) - DC(offset) \qquad Eq.\ 3.4$$
$$RAS(true) = Const * \frac{AC(true)}{DC(true)}$$

Calibration

Monochromator

Upon initiating the software it is necessary to input the current monochromator reading. This ensures the wavelength setting of the monochromator is correlated with the wavelength recorded by the software. Over the course of many readings, the correlation between the computer and monochromator drifts. For a 50 data point scan over the range of 1.5 eV to 6.0 eV, there is a drift of ~0.05 nm. This is not considered a significant error over a small number of scans of 1.5 – 6.0 eV. However, over a significantly high number of scans or over a limited energy range the software should be brought in line with the monochromator at regular intervals to minimise these errors.

Part III: Scanning Probe Microscope

The Scanning Probe Microscope (SPM) used is a PicoSPM bought from Molecular Imaging Inc. This SPM is capable of both AFM and STM by simply changing the scanner. Different sizes of scanner are available to allow a range of scan areas. With this SPM, there is the option of using a 2 μm, 10 μm or 30 μm AFM scanner or a 10 μm STM scanner. The AFM also has the extra feature of intermittent contact mode, both magnetic and acoustic. To give optimum performance the SPM is used within an isolation chamber which reduces vibrations and noise. Diagrams of the basic SPM set-up can be seen in *Figure 3.14*.

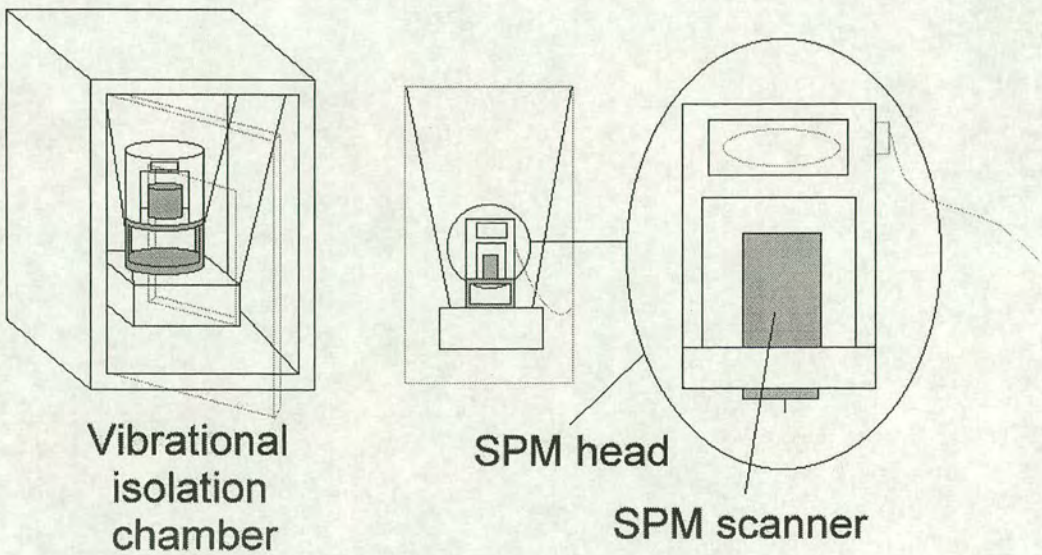

Figure 3.14 SPM configuration.

Chapter 4: Liquid Crystal Alignment Layers

'... when you have eliminated the impossible, whatever remains, however improbable, must be the truth'
Sir Arthur Connan Doyle
(1859 - 1930)

Summary

In this chapter, the first use of RAS as a tool in the study of LC alignment layers is presented. RAS is used to monitor the rubbing technique under various conditions and using various materials. It is also used to study the alternative alignment techniques of photopolymerisation and atomic beam etching. AFM and the reflectivity component of the RAS are used to gain additional information to confirm the findings. A discussion is given of the behaviour of the RA amplitude during the experiments and simulations based on the Berreman 4x4 matrices are used to interpret the data. Operational devices have been constructed to enable correlation between RAS and device properties. A large portion of this chapter has been either published or submitted for publication. Described in [4.1] are the studies of the nylon substrates, [4.2, 4.3] the polyimide substrates and [4.4] presents results relating to defects in LCDs. Atomic beam etching of alignment layer experiments are reported in [4.5], and [4.6] is a review and comparison of the all RAS experiments on LC alignment layers.

Introduction to Alignment Layers

In current LCD technology the vast majority of devices are made using the twisted nematic mode [4.7] which operates by having a layer of LC molecules sandwiched between two conductive substrates, as discussed in *Chapter 1*. When a LC molecule is placed onto a surface, it becomes anchored and no longer has an arbitrary orientation. In most LCDs, the alignment direction of the LC molecules on these surfaces is crucial to the operation of the display. Unidirectional homogeneous alignment of the LC molecules is desired and can be encouraged by using alignment layers on the inside surfaces of the conductors.

Over several decades of research into the alignment of LC molecules, many techniques have been used. Initially thin layers of long chain polymers, such as polyvinyl alcohol (PVA), and organic molecules, such as silanes, were applied to glass surfaces and then buffed [4.8]. These materials were then replaced by polyimide films giving improved results. Some examples of other techniques which have been used are the oblique evaporation of dielectrics [4.9], in particular SiO_x [4.10], photoalignment of light sensitive polymers [4.11, 4.12], Langmuir - Blodgett films [4.13, 4.14], AFM lithography of polymers [4.15, 4.16] and most recently the use of atomic beam alignment [4.17, 4.18, 4.19]. At present, rubbing remains by far the most common technique used in industry for the fabrication of alignment layers. However, this technique has many problems associated with it: the creation of surface debris, static charging and degradation of the rubbing fabric [4.20]. Each of these factors contributes to lowering the quality of the alignment layers and can result in the rejection of hundreds of displays [4.17]. This suggests either a more suitable alignment technique, a method of monitoring alignment layers or ideally both is long overdue.

The alignment of the LC molecules can be tested by constructing LC cells. These cells are typically made from two ITO coated glass substrates, each with a treated polymer surface as an alignment layer, arranged so the treated surfaces face inwards and usually with the treatment directions perpendicular. The two surfaces are

separated slightly and the gap filled with LC molecules. This enables the alignment properties of the LC molecules to be examined easily using crossed polarisers. Although this is the main technique currently used to examine the quality of alignment layers it suffers from several problems: it is difficult to isolate the effect of the individual alignment layers and the technique cannot be used in real-time during fabrication. The latter problem results from the necessity of constructing cells prior to being studied. It also generates a high quantity of waste as the completed cells, if inadequate, cannot be reused.

Several other techniques have been used to study alignment layers in the past. Although much work has been done using scanning electron microscopy (SEM) [4.21] and AFM [4.22 - 4.26], the vast majority of these are optical techniques which are non-destructive probes and can offer information on the molecular scale. Some examples are sum frequency vibrational spectroscopy [4.27, 4.28], optical second harmonic generation [4.28, 4.29] and near edge x-ray absorption fine structure spectroscopy [4.30]. Each of these techniques has disadvantages, mainly regarding the equipment used and the interpretation of the results.

Optical techniques operating in transmission mode are less suitable compared to reflection techniques because of the complication of studying *in-situ* real time situations. By using reflective techniques it is possible to isolate the reflections from multilayer systems which is not possible in transmission mode. A further discussion of the advantages of reflective techniques over transmissive techniques can be found later in this chapter. Reflection ellipsometry [4.31 - 4.34] appears to be well suited for the study of alignment layers but does not measure the exact property of interest: the lateral anisotropy.

Promotion of homogeneous alignment of LC molecules by the modification of polymer films has been suggested to result from the induced orientation of the polymer chains [4.35] which inevitably results in anisotropy within the surface layer. In general, the change in the reflectance of a material due to the modification of near nanoscale surface regions is small and therefore surface information contained within

reflectance measurements is very difficult to extract. However, by measuring ratios, much greater sensitivity can be achieved and so subtle changes can be detected. For example, ellipsometry measures the ratio of the complex Fresnel reflection amplitudes for *p* and *s* polarised light [4.36], where *p* and *s* are the polarisation components in the directions parallel and perpendicular to the electric field vector. For incidence near the Brewster angle, extremely good sensitivity to surface modification is achieved, enabling ultra-thin films and multilayers to be studied. Reflection at normal incidence provides an alternative and complementary approach which isolates anisotropic character and is surface specific rather than simply surface sensitive. For isotropic substrates when $r_s \neq r_p$, anisotropy must be present in the surface. As RAS is an experimental technique used for direct measurements of optical anisotropy with sub-monolayer surface sensitivity, it is ideally suited to the study of LC alignment layers.

In this chapter, these virtues of RAS allow the technique to be used in a similar way to its initial application of semiconductor epitaxy [4.37] by providing a real-time monitor of the alignment layer fabrication. This should allow information about alignment layers to be obtained directly rather than making inferences based on the operation of constructed devices.

Sample Preparation

The quality of the resultant alignment layer is dependent on a great number of factors. In the case of an ITO/glass substrate, both the roughness of the glass and the sputtering technique itself contribute to make the surface of the substrate relatively rough. It is possible to reduce the roughness of the substrate by chemically and mechanically polishing the surface. The surface structure and roughness of the ITO samples are found to vary depending on the supplier, as shown in *Figure 4.1*.

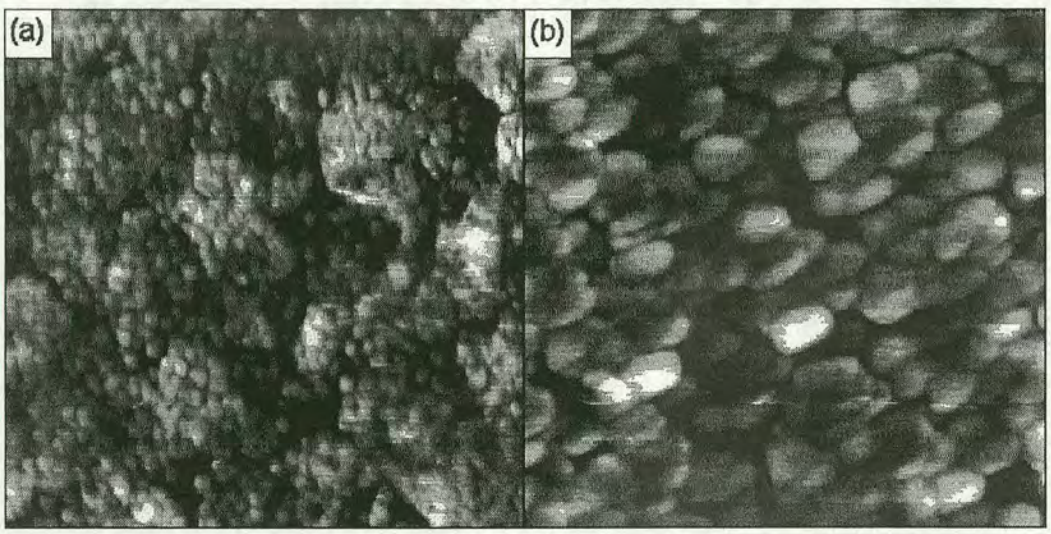

Figure 4.1 *Typical AFM images of ITO substrates purchased from a) Merck and b) Delta. Each image is ~2 x 2 μm and have height scales of 11 nm and 23 nm respectively.*

The ability of a polymer in solution to flow into low areas of the substrate leaves a flatter surface and results in better LC alignment. *Figure 4.2* shows an AFM image of an ITO/glass substrate which has been spin coated with a polymer. The image clearly shows the sample can be made smoother by coating the ITO surface with a polymer. Although, larger features, such as the trenches created on a silicon back-plane by lithography (used to create individual pixels in a LCD), cannot be covered completely. These features are very regular in shape and have a typical depth of 100 nm. However, after being polymer coated these features are reduced in depth to about ~20 nm and appear smoothed over *(Figure 4.3)*, both of which result in a flatter surface overall. The fragility of the polymer layer is also demonstrated here, in the lower half of the image the polymer has been removed by the AFM tip as the

surface is imaged. The peaks in the polymer, which occur randomly over the entire surface, are contaminants which were on the silicon surface prior to spin coating.

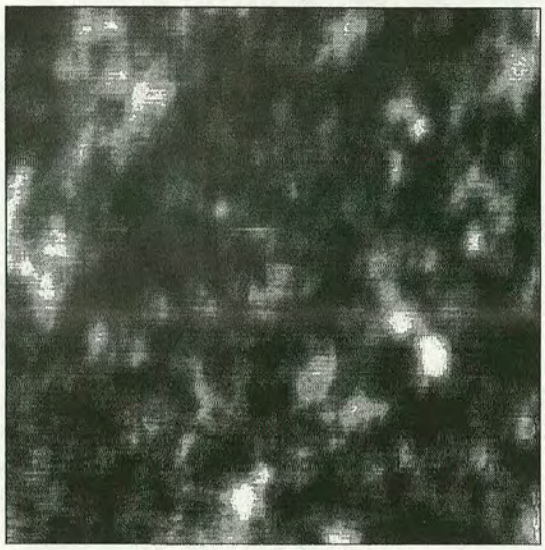

Figure 4.2 *AFM image of an ITO/glass substrate spin coated with a polymer resulting in a lower surface roughness. The image is 5 x 5 μm and has a maximum height of 5 nm.*

Figure 4.3 *AFM image of polymer coated silicon back plane demonstrating how the polymer smoothes out large features on the surface. The image size is ~30 x 30 μm and has a maximum height of 110 nm.*

For this series of experiments, several different polymers and substrates have been used. This has allowed a thorough investigation of the origin and explanation of the features presented in this chapter. All of the samples used were prepared by either Dr W. Zheng (*Samples 1, 2, 3a, 3b & 5*) or Mr C. Miremont (*Samples 3c and 4*) who were both part of the Silicon Technology Research Group in the School of Engineering at the University of Edinburgh. The values of the thickness of the polymer films given in *Table 4.1* were found using a Veeco Dektak 8000 surface profiler which measures the difference in height at the interface between a polymer coated area and an area stripped of the polymer. The error associated with the measurements of a single sample are ~5%. Through the course of these experiments it has become apparent that the intended and quoted thickness values vary from sample to sample. There are several possible explanations for the variation in film thickness but in the context of these studies it is irrelevant.

In all cases, the substrates were ultrasonically cleaned directly before spin coating. The ITO substrates used were bought from Merck and are $1cm^2$ in size, typical for all the measurements taken. The procedures used here for preparing the samples are the same as used when preparing samples for the construction of LC devices and are carried out in a clean room environment.

The preparation procedures for each different batch of samples used throughout the project are given below.

Sample 1 is prepared by dissolving PVA in distilled water to make a 3% solution and then spin coating the solution onto an ITO/glass substrate at 2000 rpm for 45 s. The coated substrates are left to dry in air.

Sample 2 is prepared by diluting 1mg of nylon 6-6 in 20 ml of m-cresol and then spin coating the solution onto an ITO/glass substrate at 3000 rpm for 1 min. The samples are then baked at 80° C for 1 hr.

Sample 3 is made using LQ 1800, a polyimide (PI) obtained from HD Microsystems Ltd. These samples were prepared by spin coating the ITO/glass substrates at 3000

rpm for 1 min with a solution of LQ 1800 dissolved in N-methyl-2-pyrrolidone (NMP). The concentration of the solution is used to vary the film thickness. For samples *3a*, *3b* and *3c* respectively, the concentrations are 3%, 15% and 1%. The samples were cured initially by soft baking at 100° C for 15-30 min followed by thermal curing at 250° C for 100 min.

Sample 4 is made using the same procedure for *sample 3a* but is made using a glass substrate.

Sample 5 is made by spin coating a 2% solution of polyvinyl cinnamate (PVCi) in chloroform onto a clean silicon substrate at 3000 rpm for 1 min. The samples are then left to dry in air.

Sample	Polymer	Substrate	Film Thickness
1	PVA	ITO coated Glass	~100 nm
2	Nylon 6-6	ITO coated Glass	~120 nm
3a	LQ 1800	ITO coated Glass	~120 nm
3b	LQ 1800	ITO coated Glass	~1.2 μm
3c	LQ 1800	Silicon wafer	~50 nm
4	LQ 1800	Glass	~120 nm
5	PVCi	Silicon wafer	~50 nm

Table 4.1 Sample types used in the study of LC alignment layers.

Rubbing

Introduction to Rubbing

It has been known for a long time that the orientation of some LC molecules can be controlled when they are placed on a solid that has been mechanically rubbed. In fact, the molecules tend to lie parallel to the rubbing direction which is crucial for display applications that require unidirectional alignment. An important and commonly used group of materials in the field of homogeneous alignment of LC molecules is polymers. By unidirectionally rubbing a polymer film with a fibrous material such as velvet, the ability of molecular alignment for certain LCs can be promoted [4.20]. A debate into the reasons for this molecular alignment was initiated by Berreman [4.38] after he proposed the alignment was due to elastic strain energy and therefore a result of the topographic features on the surface created by the rubbing process. A competing mechanism was put forward by Geary [4.35] which suggested the alignment of the molecular chains of the polymer, created by sheering the polymer chains during rubbing, was responsible for the LC alignment. Publications over the past 30 years, involving all of the techniques mentioned in the previous section and more, have been adding evidence to the argument of whether the alignment of LCs on a rubbed surface is predominantly due to topographic features or molecular orientation. Recent publications tend to favour Geary [4.27 - 4.29] although it is likely that topographical features play some part in the alignment process.

Figure 4.4 *3D AFM image of a typical rubbed polymer surface of size 10 x 10 μm and maximum height 250 nm.*

A typical rubbed polymer surface used in LC alignment, as has been reported many times before [4.21 - 4.26], can be seen in *Figure 4.4*. The machine used to rub the samples, shown in *Figure 4.5*, has been custom made by Dr W. Zheng, and is composed of a flat plate, housing the sample which passes through underneath a rotating drum. The drum is covered with a velvet material and rotates at a constant speed of 41 rpm. This speed of rotation is known from the motor manufacturers specification for 12 V applied to the motor. The velvet has fibres of diameter ~20 μm and can be seen in *Figure 4.6*. Although Mahajan *et al.* [4.25] have shown that the cloth fibres used to rub the solid is an important factor in the creation of surface topography, in this project this parameter is kept constant. The stage on which the sample is housed, passes through under the rotating drum at a pre-set speed between 1 and 60 mm/min. In these experiments, one rub is defined as one pass through under the rotating drum. For multiple rubs the sample is removed from the machine whilst it is reset to the initial position to ensure the sample passes through the same way each time the surface is treated. Here, the results obtained from rubbing several different types of polymer films are studied using both RAS and AFM. For all cases, the samples were studied with the rubbing direction in the same direction as the *x*-axis of the spectrometer (*Equation 2.12*).

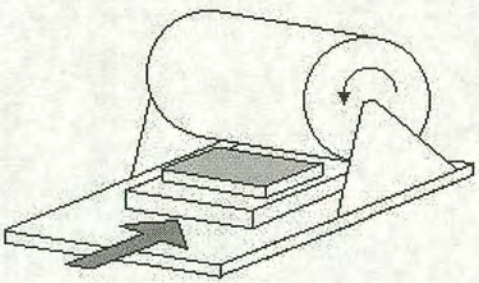

Figure 4.5 *The rubbing machine.*

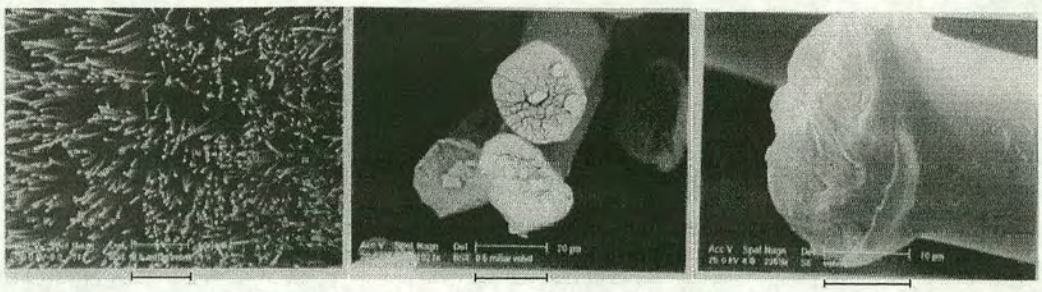

Figure 4.6 *SEM image of fibres of cloth. The scales of the images, from left to right, are 600 μm, 20 μm and 10 μm. These images were provided by Dr W. Zheng.*

Rubbing PVA

As previously mentioned, one of the first polymers to be used as a LC alignment layer was PVA. For this experiment *sample 1* is used, a description of the procedure to produce this sample can be found in the *Sample Preparation* section earlier in this chapter. AFM images (*Figure 4.7*) of the polymer after being spin coated onto an ITO/glass slide show the roughness of this sample to be greater than the ITO alone. Further AFM images were taken after the sample has been rubbed several times but do not show any grooves. RAS taken before and after rubbing shows no anisotropy and therefore no further studies were done on this surface.

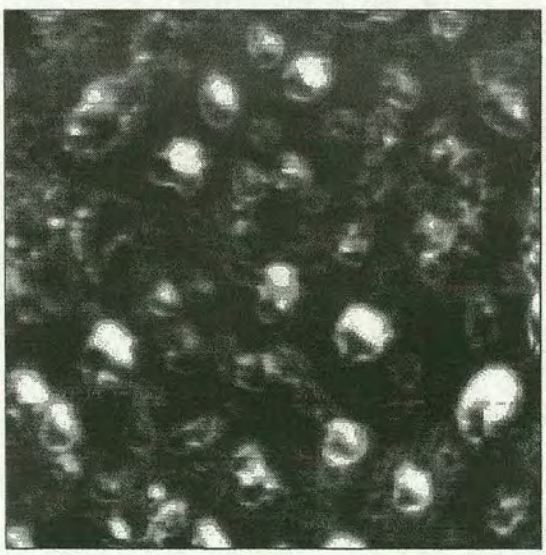

Figure 4.7 *AFM image of a PVA coated ITO on glass slide over an area of 15 x15 μm and with a maximum height of 23 nm.*

Rubbing Nylon

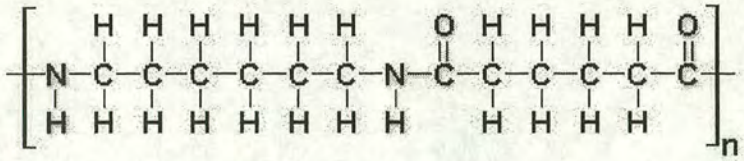

Figure 4.8 Structure of nylon 6,6.

The next set of experiments studied nylon/ITO/glass substrates (*sample 2*), the structure of the nylon is shown in *Figure 4.8*. The unrubbed nylon surface can be seen to have little optical anisotropy, *Figure 4.9 & 4.10*. AFM (*Figure 4.11 (a)*) of the unrubbed surface confirms this, as the only structure, which is thought to arise from the drying process, appears isotropic. Further RA spectra were taken after the completion each rubbing cycle at a rubbing speed of 20 mm/min. *Figures 4.9 & 4.10* show the RA to increase from zero initially to its maximum value of about 15% after a single rub and then rapidly decrease back to almost zero with subsequent rubbing.

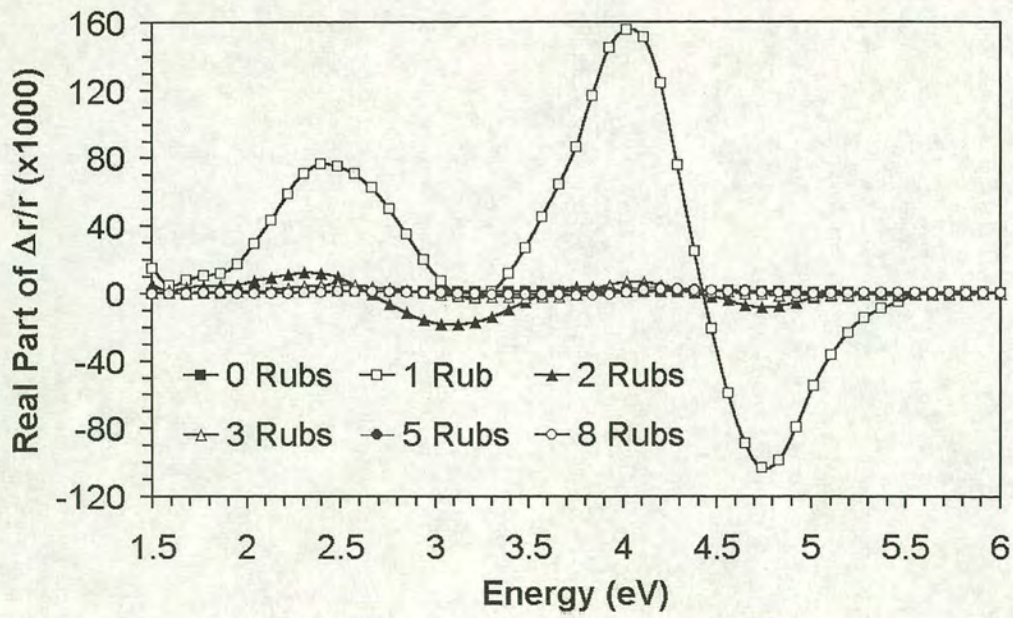

Figure 4.9 RAS versus energy of a rubbed nylon sample.

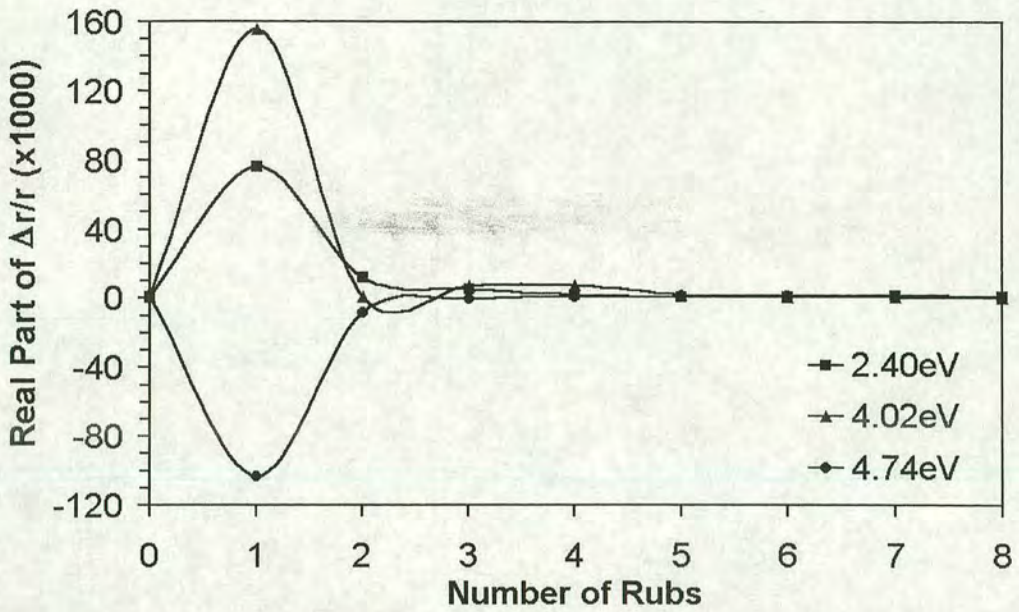

Figure 4.10 RAS versus number of rubs for a nylon sample.

The large amplitude of the RA spectra after the initial rub can be explained by considering *Figure 4.11 (b).* The surface of the sample is clearly anisotropic, having grooves at ~5° to the horizontal axis over the entire surface area. The same image shows an uneven area approximately half way up the vertical axis which runs the full length of the image. It is likely this area has been created as a result of the sample being over rubbed slightly, which for this material causes significant damage to the surface. A more detailed view of the damage done to the sample can be seen in the cross-section of the AFM image, shown in *Figure 4.12 (b),* which suggests the scale of the features created as a result of damage to the film are roughly twice the size of normal grooves. Additional rubbing reduces the RA amplitude giving further indication that more damage to the surface has occurred; *Figure 4.11 (c)* confirms this. It is apparent the nylon film is being gradually removed from the surface by continuous rubbing to the extent that the low dark areas visible on the AFM image of *Figure 4.11 (c)* are likely to be the ITO/glass substrate. From this image and the cross-sectional image (*Figure 4.12 (d)*) it is possible to gauge the thickness of the film to be ~40 nm: significantly lower than the initial thickness. The surface after 8 rubs, *Figure 4.11 (d),* appears very flat and disordered, indicating only fragments of the nylon film now remain on the ITO surface. It is apparent that as the number of rubs is increased, the roughness of the surface and the thickness of the film,

measured approximately using the AFM images, both decrease, giving further evidence the nylon film is being removed by rubbing.

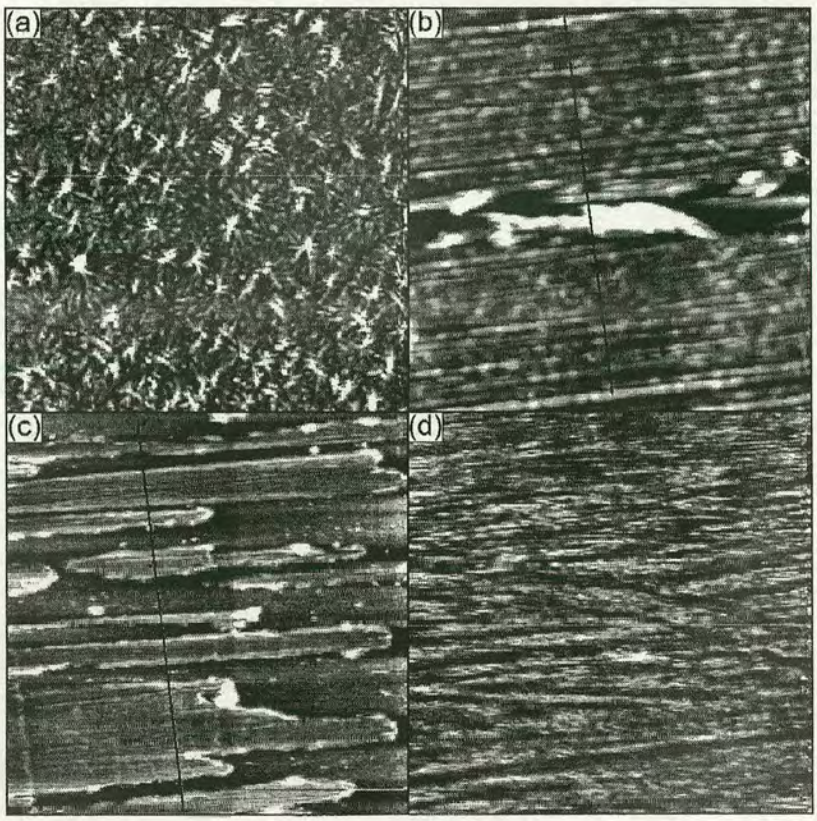

Figure 4.11 *AFM images of a nylon surface after (a) 0 rubs, (b) 1 rub, (c) 4 Rubs and (d) 8 rubs. The areas shown are 30 x 30 μm and have maximum heights of 16, 55, 50 and 9 nm.*

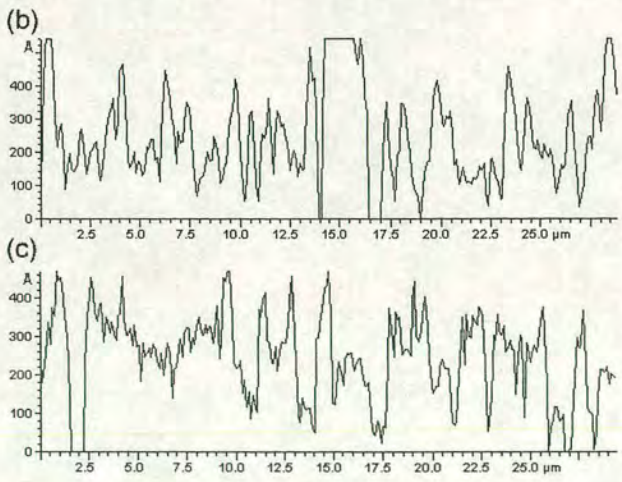

Figure 4.12 *Cross sectional AFM of rubbed nylon. (b) and (c) correspond to Figure 4.11 (b) & (c).*

Figure 4.13 shows the reflectivity of the nylon sample to increase as it is rubbed more, as does the energy position of the peaks. The overall shape of the spectra and indeed the fact that the sample is comprised of transparent thin films is very suggestive of interference effects being involved. This is true for not only the reflectivity (*Figure 4.13*) but also the RAS (*Figure 4.9*). The position and periodicity of these peaks can be predicted very approximately using the relation for constructive interference, $2Nd=m\lambda$. By using a refractive index value of N =1.53 and a film thickness of d =240 nm (120 nm each for the nylon and ITO layers), this simple relation predicts a periodicity of ~1.6 eV. Comparison of this value to the spacing of the peaks shows it is approximately correct. It is hardly surprising it lacks precision considering a single value of N was used when this is known to vary across the entire spectral range. To simulate the spectra accurately it would be necessary to use a more sophisticated model.

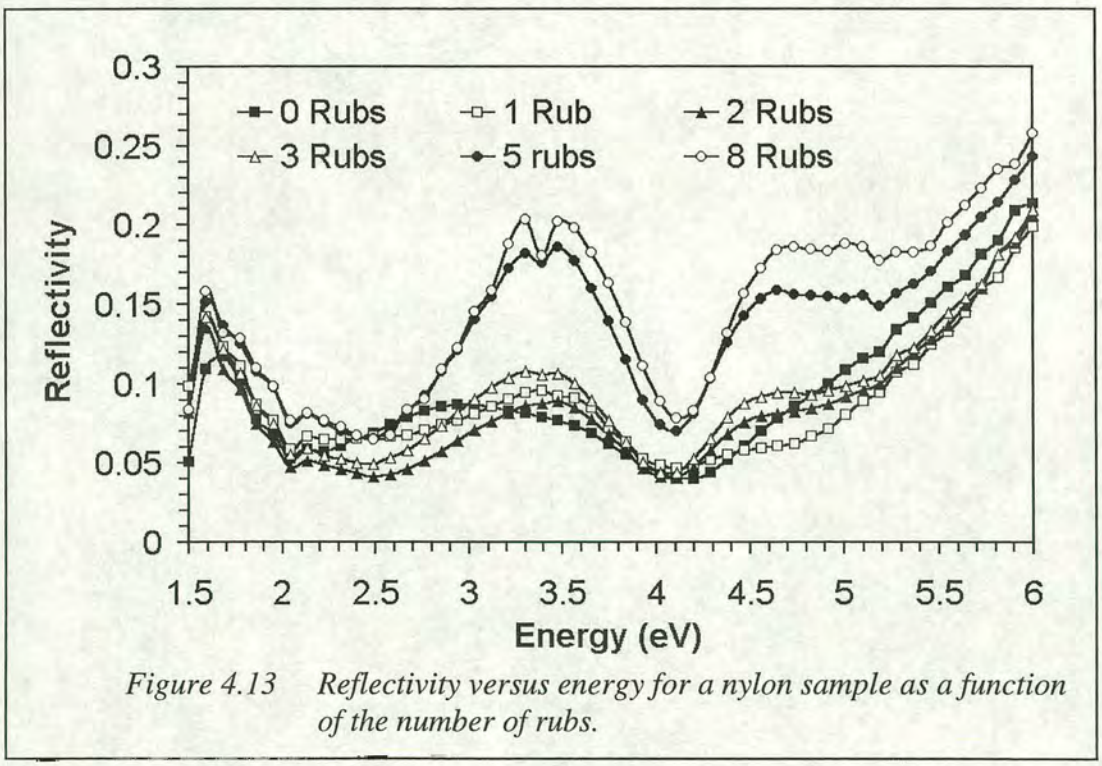

Figure 4.13 *Reflectivity versus energy for a nylon sample as a function of the number of rubs.*

The change in the reflectivity spectra as it is rubbed has two contributing factors. Firstly, as the thickness of the nylon film decreases with rubbing, a corresponding increase in energy of the position of the peaks can be predicted. Secondly, because the nylon layer is being rubbed away, more of the underlying (ITO) surface will be directly exposed to the incident light. By comparing the spectra shown in *Figure 4.13*

& *4.14*, it can be seen that the final reflectivity of the rubbed nylon sample is very similar to the reflectivity of the ITO/glass substrate.

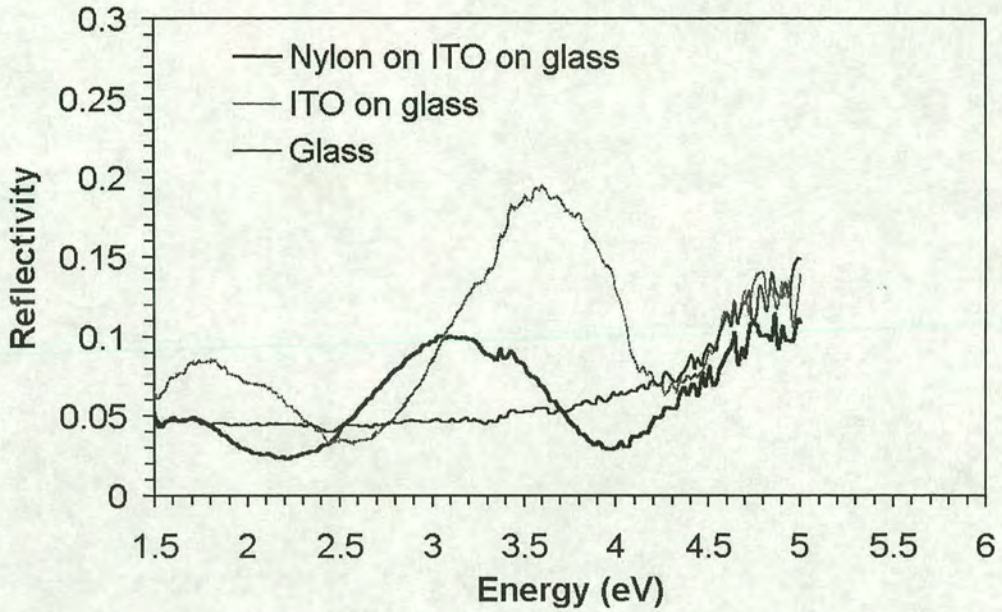

Figure 4.14 Reflectivity versus energy for nylon, ITO and glass samples which have had the back surface frosted.

Although nylon is capable of being used as an alignment layer it is not the most suitable material as in this situation the surface is very susceptible to damage by over rubbing. Additionally, the structures on the surface prior to rubbing are not conducive to good alignment. A more robust polymer, which gives a more uniform film will be studied next. A PI is the obvious choice as it is commonly used in the commercial fabrication of alignment layers.

Rubbing Polyimide

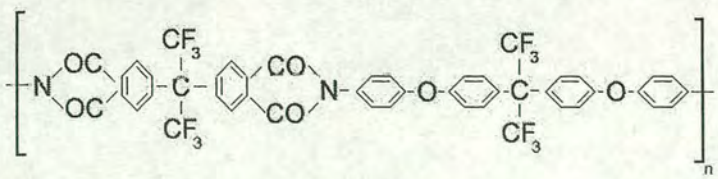

Figure 4.15 Structure of the PI molecule.

The study was continued using PI coated samples (*sample 3a*), the structure of the PI can be seen in *Figure 4.15*. The surfaces were modified using exactly the same

procedure as for the nylon samples only this time for two different rubbing speeds, 20 mm/min and 50 mm/min. This variable allows greater flexibility in the rubbing parameters and may allow the results to be applied and compared more readily to procedures used commercially. *Figure 4.16* shows the development of the RAS signal for a standard PI sample as a function of rubbing (at a speed of 50 mm/min). The rate at which a sample passes through the machine is directly proportional to the amount of surface processing the sample receives. For a high rate, such as 50 mm/min, the amount of surface processing per cycle is relatively low. Conversely, for a low rate, such as 20 mm/min, the amount of surface processing is relatively high. In general, the spectra from the PI samples appear very similar to those obtained from the nylon samples. This is because the thickness' of the samples are roughly the same and so each spectrum consists of the same three peaks created by the superposition of a multilayer interference effect onto the optical anisotropy of the sample. Although not presented here, it is possible to obtain spectra with an unusual derivative type appearance by adjusting the thickness of the samples.

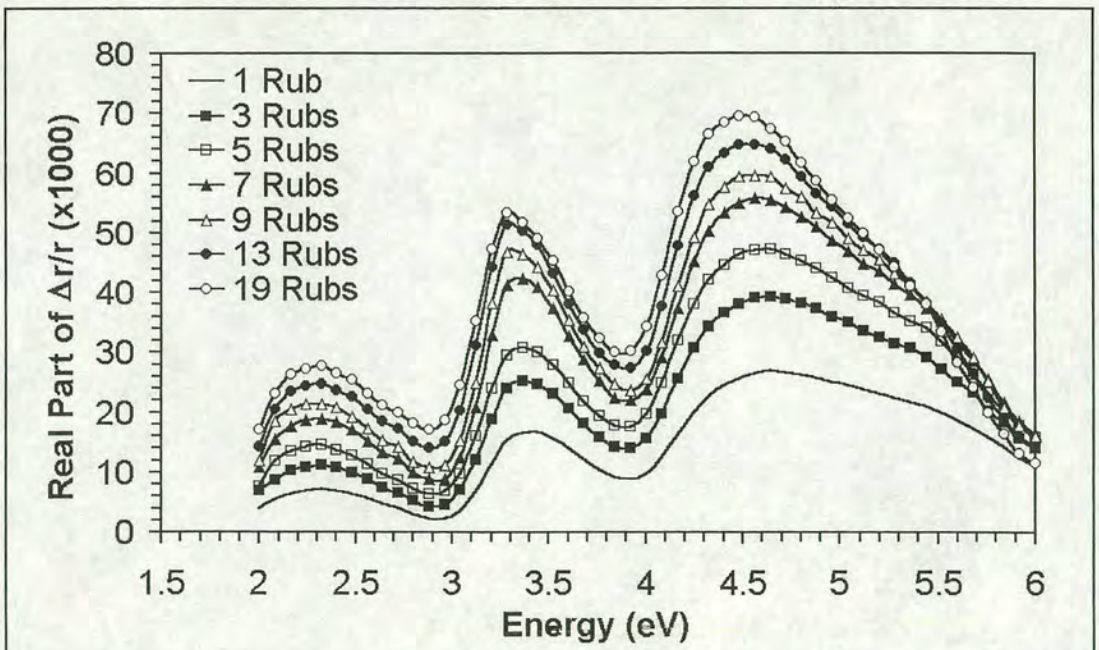

Figure 4.16 RAS versus energy for a PI sample rubbed at 50 mm/min.

As the PI is rubbed, the RA of the sample increases proportionally over the entire energy range. The 'solid triangular' data set in *Figure 4.17* shows the RA increasing as a function of rubbing but not to saturation point, even after having been rubbed twenty times, the signal still appears to be growing. *Figure 4.18* shows RA spectra

for a different PI sample which has been rubbed while passing through the machine at a slower speed of 20 mm/min. Although the shape of the RA spectra is approximately the same as the previous sample, by rubbing the samples at a different speed the RA dependence on rubbing number changes. This difference can be seen more clearly in *Figure 4.17*. At the slower processing speed, the anisotropy saturates after five rubs and decreases with further rubbing. In the previous studies of rubbed nylon alignment layers a similar effect was observed and was accounted for by damage to and the removal of the surface material. By using AFM to obtain surface profiles, this reduction in RA can also be attributed to damage being done to the polymer film as a result of the rubbing process.

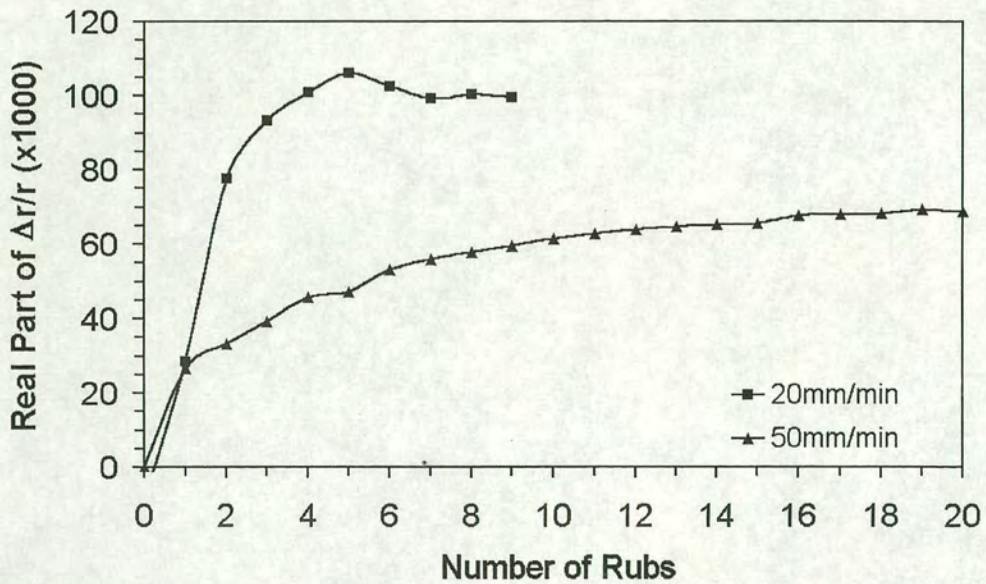

Figure 4.17 *RAS versus number of rubs for two polyimide samples rubbed at fast and slow speeds at 4.5 eV.*

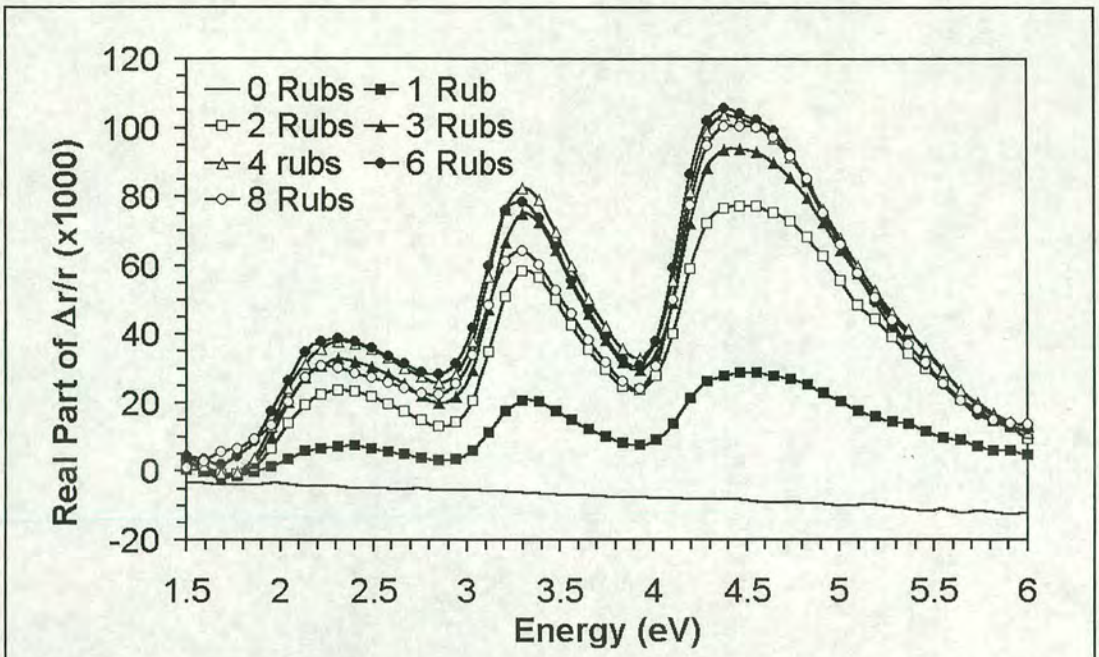

Figure 4.18 RAS versus energy for a PI sample rubbed at 20 mm/min.

AFM images of the unrubbed PI sample, *Figure 4.19 (a),* show the surface to be isotropic, corresponding to the null spectra obtained with RAS. After a single rub at 20 mm/min, the surface appears scratched and has grooves in the direction of the rubbing, *Figure 4.19 (b).* The creation of these grooves and scratches is a well-known result of rubbing a polymer film and has been reported numerous times before, for example [4.15]. After two further rubs the grooves have increased in depth and density, *Figure 4.19 (c).* The sample therefore has a more anisotropic surface than before, as found using RAS. The final AFM image, *Figure 4.19 (d),* is taken after the substrate has been rubbed five times and shows the first signs of damage being done to the surface. Further rubbing would cause more damage and would result in a lower RA due to increased scattering or the exposure of the underlying substrate.

It is apparent that although the rubbing machine is capable of producing samples which are consistently the same, it does not allow much control of the parameters which are thought to be crucial to the properties of alignment layers, i.e. the rubbing length and pressure. To allow greater flexibility in the rubbing parameters, a simpler system was employed wherein a sample was 'rubbed' by placing it face down on a velvet cloth and pushing it for a set distance. The pressure of rubbing can be varied

by placing different weights on the sample whilst being moved. Additionally, to remove the effect of the multilayer interference and perhaps give more information about the origin of the RA spectra, a silicon substrate with a thin PI film (*sample 3c*) is used.

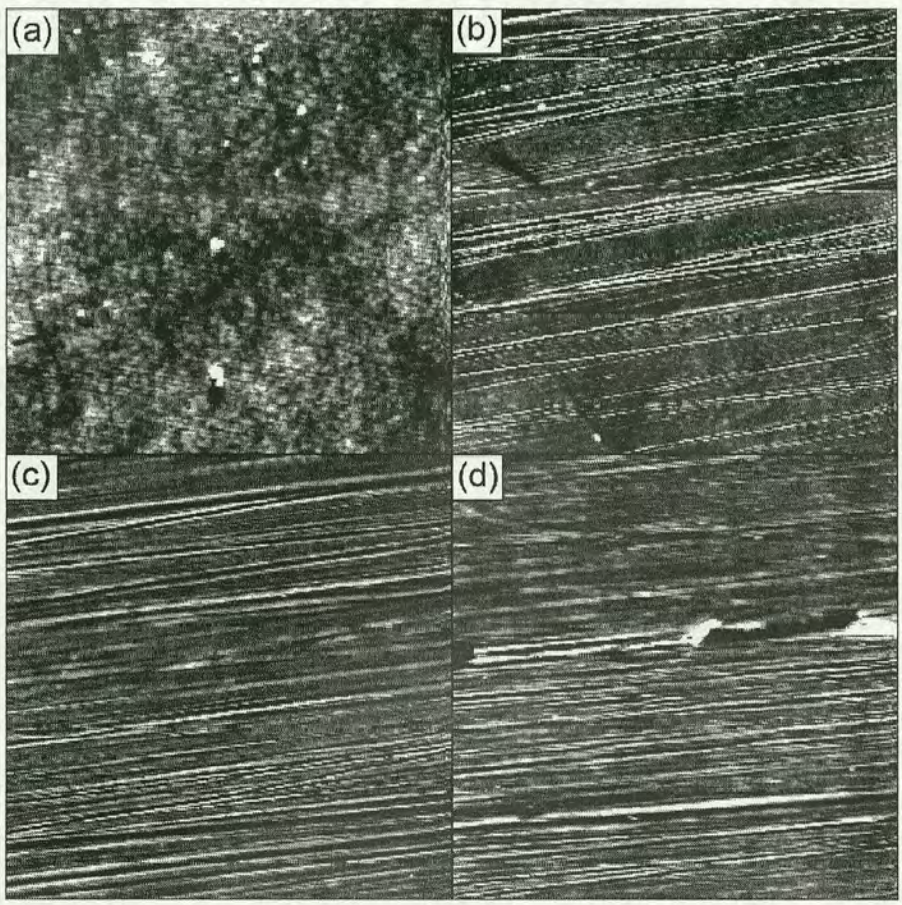

Figure 4.19 *AFM images of the PI surface rubbed at 20 mm/min after (a) 0 rubs, (b) 1 rub, (c) 3 rubs and (d) 5 rubs. The maximums heights are 5 nm, 13 nm, 30 nm and 25 nm respectively. All scans are 36 x 36 μm.*

The first of these experiments was to study the RA as a function of length under a constant pressure (always using a 2 g weight). The results can be seen in *Figure 4.20* and show the measured RA to increase with increased rubbing length. The sample was not rubbed until its saturation point and so the data presented here behaves linearly. The experiment was then repeated as a function of weight, keeping the rubbing length constant at 15 cm. As can be seen in *Figure 4.21*, the results are similar to the previous experiments as the RA increases linearly with weight. The

increased pressure on the sample will have the effect of creating deeper wider grooves. Simple trigonometry can be used to show that deeper grooves have a larger surface area and a corresponding larger contact area with the cloth fibres which results in more aligned molecules, therefore making the surface more anisotropic.

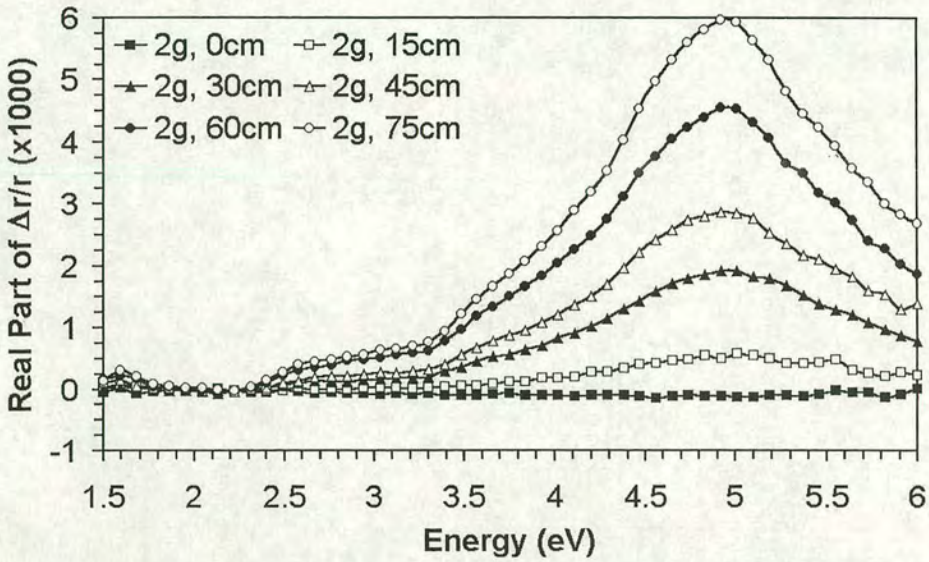

Figure 4.20 *RAS versus energy for a thin polyimide layer rubbed as a function of length.*

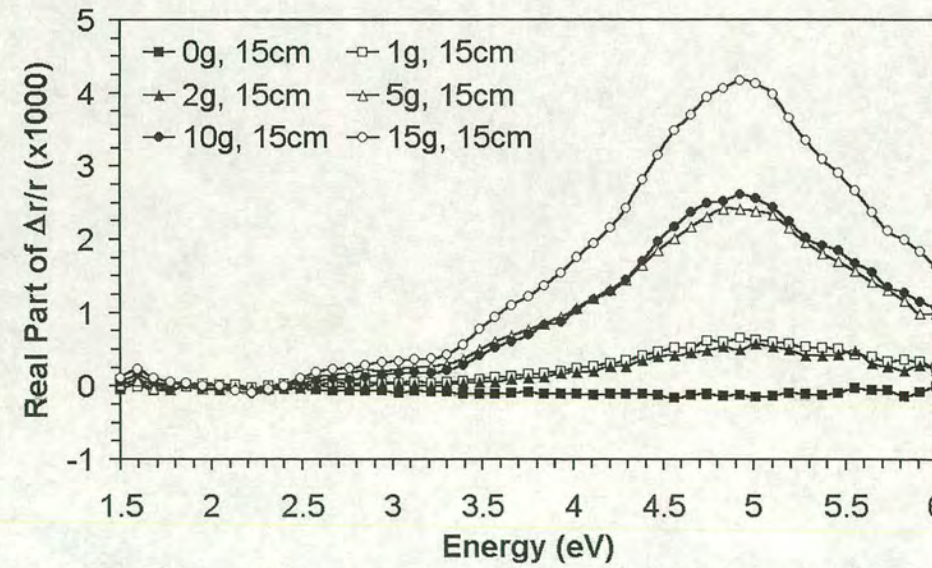

Figure 4.21 *RAS versus energy for a thin polyimide layer rubbed as a function of weight.*

The shape of the spectra measured from the thin rubbed polyimide samples is very similar to all the previous rubbing experiments if allowance of the multi-layer interference effect is made. In the most recent experiment a thin PI film is used, it is not surprising an interference pattern cannot be seen as the predicted position and periodicity of the peaks lies out-with the measured energy range. The resultant spectra is a very clear indication of what the anisotropic signal from this rubbed polymer, for any thickness and substrate, should look like without interference effects. An alternative way to obtain this information would be to use a film so thick that the periodicity of the peaks is lower than the resolution of the spectrometer. Assuming the resolution is governed by the monochromator, a maximum resolution of ~1 nm can be used. However, for a typical scan, the spectrometer covers 50 data points in 4.5 eV, therefore the interference pattern from a polymer film of over 3 μm thick would exceed the resolution governed by these parameters.

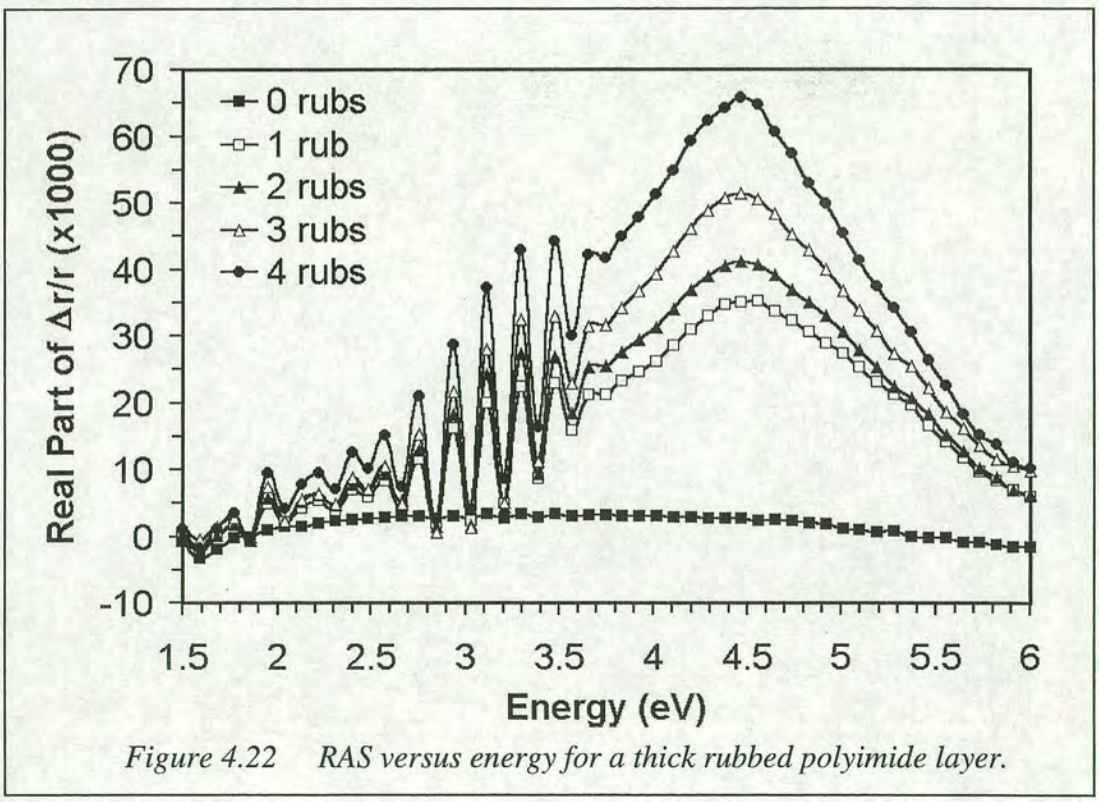

Figure 4.22 RAS versus energy for a thick rubbed polyimide layer.

Although still thin enough to show interference patterns, the next sample studied (*sample 3b*) is much thicker than previously and is rubbed at 20 mm/min. For the purposes of this experiment, it is only necessary to create an anisotropic surface to obtain an indication of the resultant RA spectra for comparative purposes. The

predicted periodicity of the interference is approximately 0.1 eV, roughly what is seen in the measured spectra from the thick sample (*Figure 4.22*). In these spectra the interference appears as a ripple in the lower energy range although the overall shape of the spectra is similar to other results, especially the thin rubbed films.

The results obtained from these rubbed polymers have so far been interpreted in an empirical fashion and have successfully shown that RAS is a viable tool for monitoring the fabrication of alignment layers in real-time. To fully utilise this tool and to possibly link the measured quantities directly to device parameters, it is necessary to understand the meaning and origin of the measured optical anisotropy.

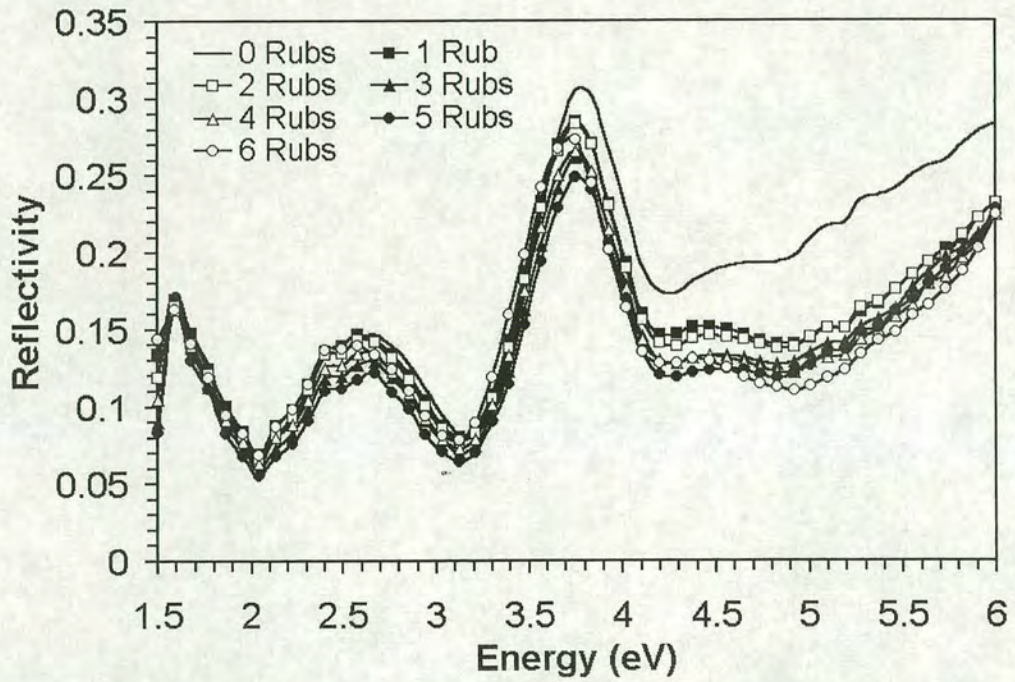

Figure 4.23 Reflectivity versus energy for standard PI/ITO/glass substrate as a function of rubbing.

The reflectivity spectra from a standard PI/ITO/glass sample (*sample 3a*) as a function of rubbing can be seen in *Figure 4.23*. This figure shows that multiple rubbing of the PI does not affect the shape of the reflectivity, indicating the PI thickness does not change significantly. This would not be true if a significant amount of damage was done to the surface as in the case of the nylon film. However, the reflectivity spectra do undergo a progressive reduction in intensity, in particular

in the UV region, as would be expected from a surface of increasing roughness. The corresponding change in the topography of the PI film as it is rubbed is illustrated in *Figure 4.19*.

Similarly, from studying all of the RA spectra, it is apparent that multiple rubbing of the surface does not alter the shape of the spectra either, unless the surface becomes severely damaged, but instead alters the amplitude. The precise reason for the increase in RA amplitude is unclear but it is highly probable that it is due to the molecules of the polymer being orientated in a single direction by the rubbing procedure. The anisotropic topography of the surface is not considered to be a significant factor as recent experiments have the shown the shape of the surface to have little effect on the retardation [4.39], and hence the RA.

From the RAS of the rubbed PI/ITO/glass samples (*Figures 4.16 & 4.18*) it is clear that the peaks observed in the spectra are not symmetrical and that the energy of RA peaks do not coincide with the peaks in the corresponding reflectivity spectra (*Figure 4.23*). The explanation of these features lies in the orientation of the polymer chains, which is believed to be in the direction of rubbing as a result of the rubbing process [4.35]. It has been found that the refractive indices of the surface, in the directions parallel and perpendicular to the rubbing directions vary by an amount Δn, typically about 0.1 [4.31, 4.40] The result of this birefringence is a slightly different optical thickness for each of the orthogonal components of polarised light giving an energy difference between the interference peaks in the reflectivity spectra. In the cases considered here, the refractive index parallel to the rubbing direction will be greater than the refractive index perpendicular to the rubbing direction, $n_x > n_y$. In addition to the energy difference between the orthogonal polarisation components, it is expected that the amplitude of reflectivity will be greater for the x component. This can be used to explain the lack of symmetry and peak positions in the measured spectra.

It has been found [4.3] that the measured RA is proportional to the first derivative of the logarithmic reflectivity when multiplied by the optical retardation in the rubbed section of the film, $d_1\Delta n$. AFM measurements, for example in *Figure 4.19*, show the

depth of the grooves and hence the size of the rubbed section to be ~10 nm. Therefore the optical retardation can be estimated at ~1 nm which is consistent with the findings of others [4.35, 4.41, 4.42]. The hollow data sets in *Figure 4.24* show the scaled derivative of the reflectivity, calculated using this optical retardation value. These are plotted against the RAS corresponding to the reflectivity for each sample. The PI film thickness' of the samples studied here are 80 nm and 1200 nm. The first sample has a significantly lower film thickness than initially thought. This corrected value (of 80 nm) was obtained from comparisons with simulations presented later in this chapter. A comparison of the experimental and calculated (from the reflectivity) spectra shown in *Figure 4.24* reveals several things. Firstly, the similarities between the two conclusively show that the features below ~4.0 eV result from interference effects in the reflectivity. Secondly, the difference between the two show that the features above ~4.0 eV are not caused by interference effects. From *Equation 5* in reference [4.3], it can be found that a large PI layer would result in a small birefringent contribution to the RAS, as illustrated by the triangular data sets of *Figure 4.24*.

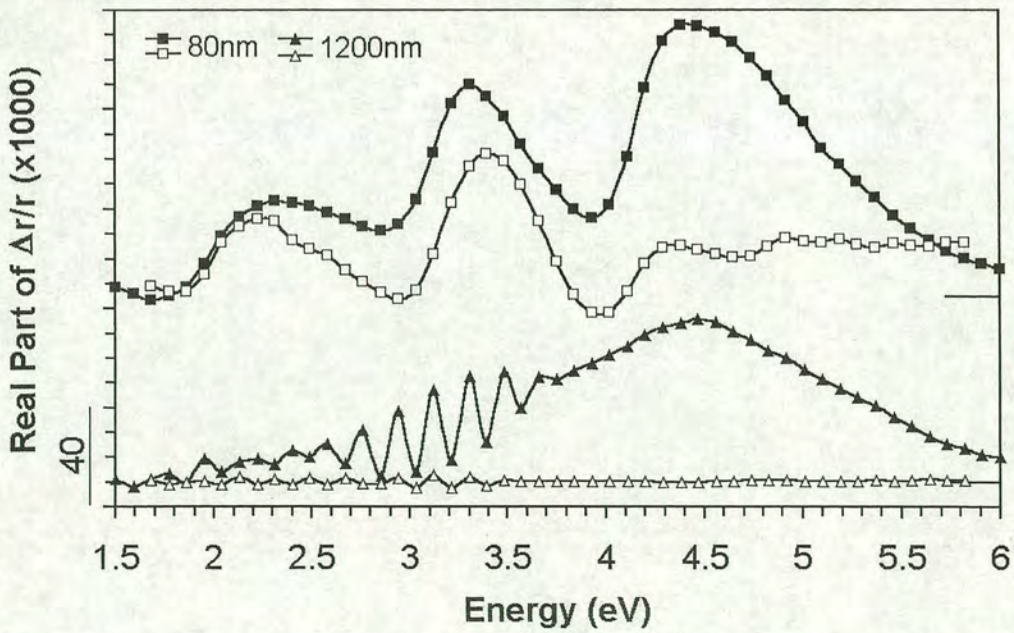

Figure 4.24 *The measured RAS is shown as the solid data sets and the derivative of the corresponding logarithmic reflectivity is shown as the hollow data sets.*

For each thickness of sample studied, a broad peak around 4.5 eV can be seen. The studies of the thicker PI sample (*Figure 4.22*) show the interference patterns to die out above ~3.5 eV because of the absorption of the polymer. The 4.5 eV peak must be therefore be attributed to the uppermost layer of the samples, which is roughly the same in each case.

Rubbing Simulations

The optical measurements taken here have been simulated using the Berreman 4x4 matrix method for stratified media [4.43]. Details of this method can be found in *Appendix A*. Firstly the reflectivity of the untreated ITO/glass surface was investigated. Simulations were run using published optical constants [4.44] initially as a function of ITO film thickness. The results in *Figure 4.25* show a good correlation between the experimental results and the simulated spectra at around 120 nm of ITO. Upon close inspection 116 nm of ITO most resembles the experimental spectra. This value ties in well with the expected value; differences in the film thickness and the spectra can easily be accounted for by the optical constants which are expected to be slightly variable [4.45]. AFM of the ITO surface reveals a surface roughness of over 10 nm (*Figure 4.1*). This roughness can be replicated in the simulations by using the Bruggeman effective medium approximation [4.46] which is used to construct a single film model of a roughened surface and substrate. Despite the age of this model it has been found to be as good as and in some cases better than other models [4.47]. In these simulations the rough surface can be regarded as a new layer and so here, both the ITO film thickness and the thickness of rough layer are varied. The best results from the various combinations investigated are shown in *Figure 4.26*. This figure reveals the roughness layer does improve the model and that the most accurate simulated spectra is obtained by using a ITO film of 110 nm with a 15 nm rough layer. The size of the simulated roughness (15 nm) corresponds well with the roughness value found from the AFM images of the ITO surface (11 nm). Interestingly, the spectra plotted all have roughly the same film thickness if the ITO thickness is added to half the roughness thickness. Also shown in *Figure 4.26*, is that as the roughness of the surface is increased, the shape of the spectra remains roughly the same except in the UV region where it is significantly reduced.

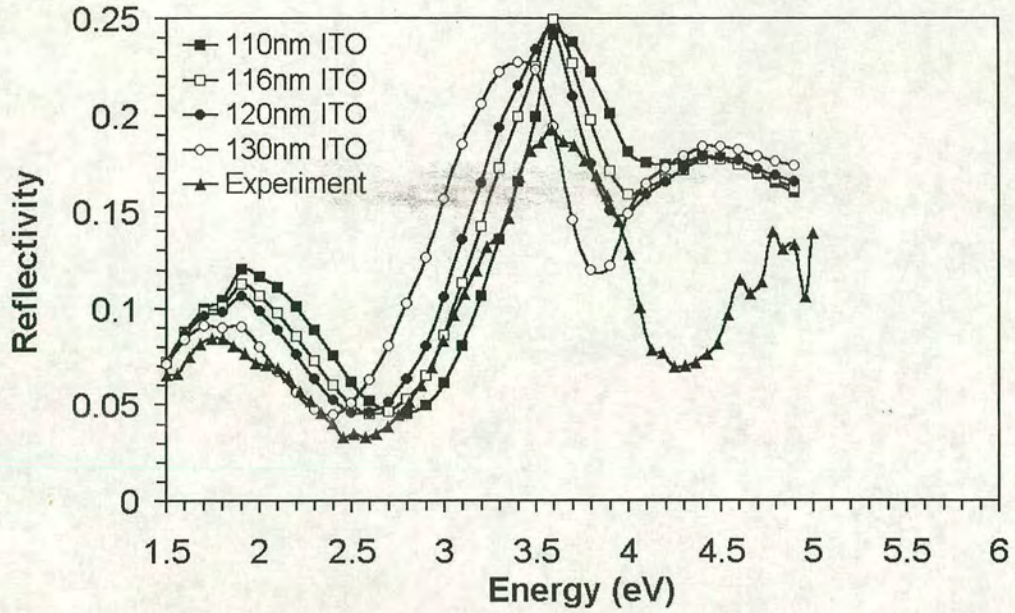

Figure 4.25 *Simulated reflectivity spectra for an ITO/glass multilayer as a function of film thickness.*

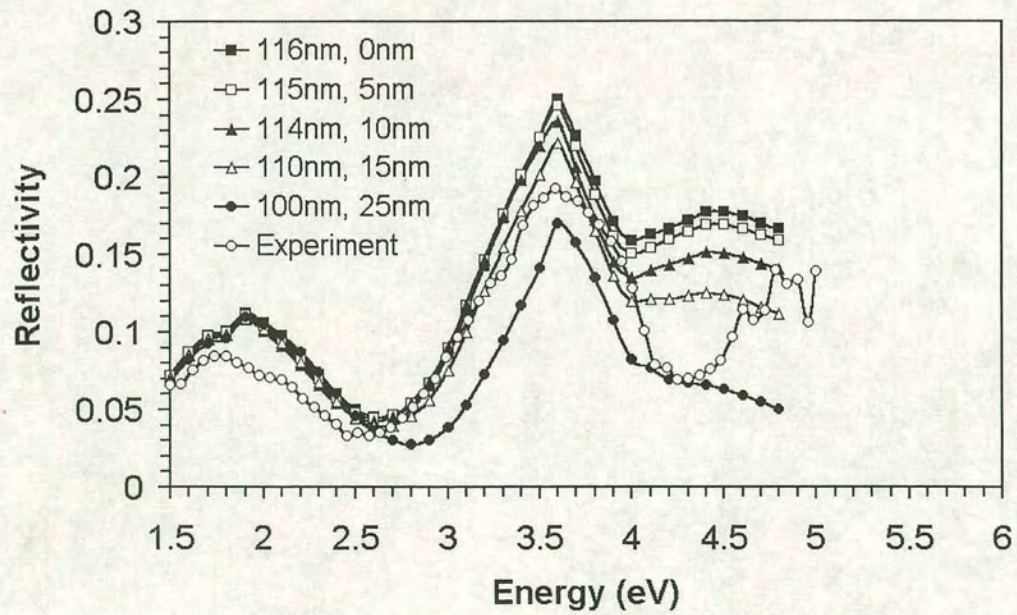

Figure 4.26 *Simulated reflectivity for an ITO/glass substrate as a function of thickness and roughness. The first number in the legend is the film thickness, the second the roughness.*

The simulations were repeated for the standard PI/ITO/glass samples that have been used throughout this chapter. As spectral values of the refractive index and extinction coefficient are not known for this PI sample, a suitable data set had to be constructed around the visible region refractive index of 1.8 and knowledge of similar materials. The optical properties are made to increase slightly across the spectral range, with the absorption highest in the UV region. As a direct consequence of estimating data for these simulations, the layers of roughness, between the PI and ITO and between the PI and ambient, were omitted. The result of the simulated reflectivity spectra for the PI/ITO/glass samples can be seen in *Figure 4.27*. The experimental spectra can be reproduced reasonably well by a PI thickness of 80 nm. Although this is thinner than the expected thickness of the PI film, considering the origin of PI data and the possible inconsistencies in the production of the samples, the result is satisfactory. For comparative purposes the 120 nm simulated reflectivity spectrum is plotted as well.

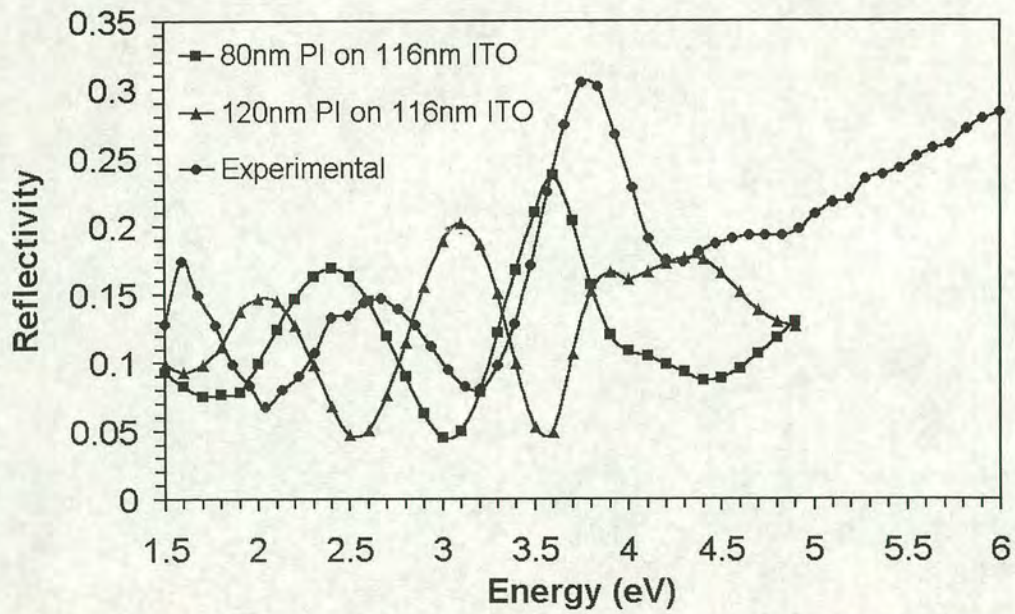

Figure 4.27 Simulated reflectivity spectra for a PI on ITO/glass multilayer as a function of PI film thickness.

The reduced spacing of the interference effect seen in the RA of the thicker samples (*Figure 4.22*) can also be seen in the measured reflectivity (*Figure 4.28*). In the same manner as the standard thickness PI samples, the reflectivity from the thick PI samples (*sample 3b*) can be modelled accurately. The results of this simulation are

shown in *Figure 4.28* and show 1200 nm of PI on 116 nm of ITO to be a good match.

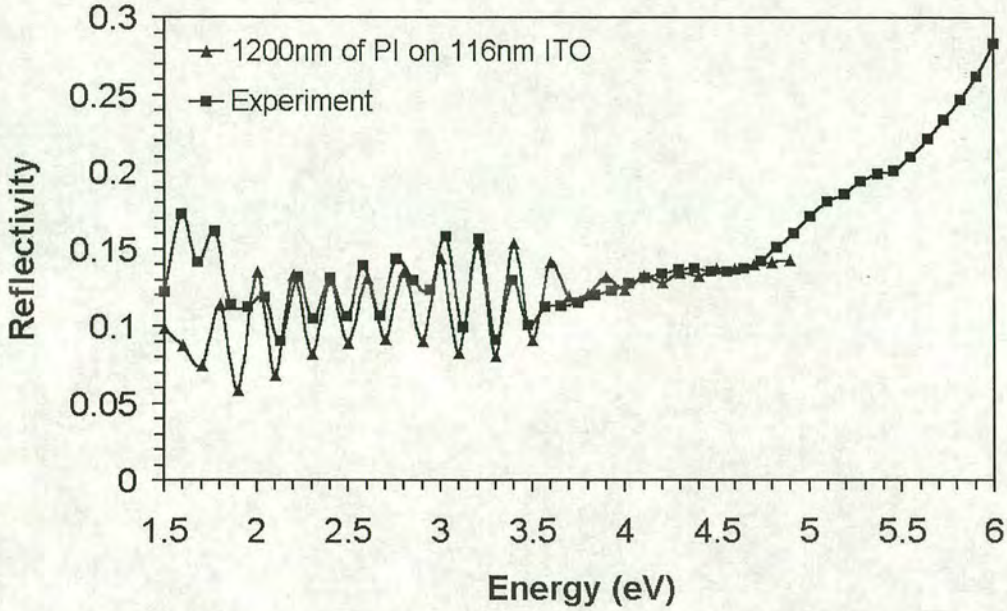

Figure 4.28 Simulated reflectivity of a thick PI/ITO/glass multilayer.

The RAS from these PI/ITO/glass samples has been simulated, again using the Berreman 4 x 4 matrices but with the structure of the samples based on a molecular orientation model. This model originates from ellipsometry studies by Hirowsawa [4.31 - 4.34] in which he demonstrated the ratio of the Fresnel reflection coefficients for *s* and *p* polarised components, measured from a rubbed PI sample, varied as function of sample orientation angle. He then simulated the results using a model that comprised an optically uniaxial medium with an orientated upper layer and a lower isotropic layer, as shown in *Figure 4.29*. For the purpose of the RAS simulations, the lower layer has a thickness d_1 and refractive index n, the upper layer has thickness d_2 in which the molecules are aligned in the rubbing direction giving a molecular birefringence, Δn. The values used are, d_2=10 nm, Δn =0.1 and n is as used in the reflectivity simulations. The result of this simulation, for PI thickness' of 80 nm and 1200 nm are shown as the solid data sets in *Figure 4.30* and show a good match with the measured values in the IR and visible regions of the spectrum but not in the UV.

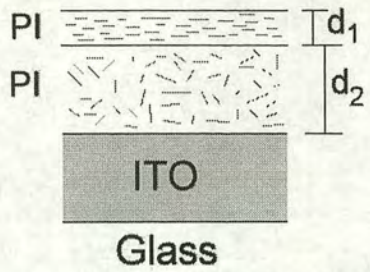

Figure 4.29 Diagrams showing the molecular model used to simulate the RA spectra.

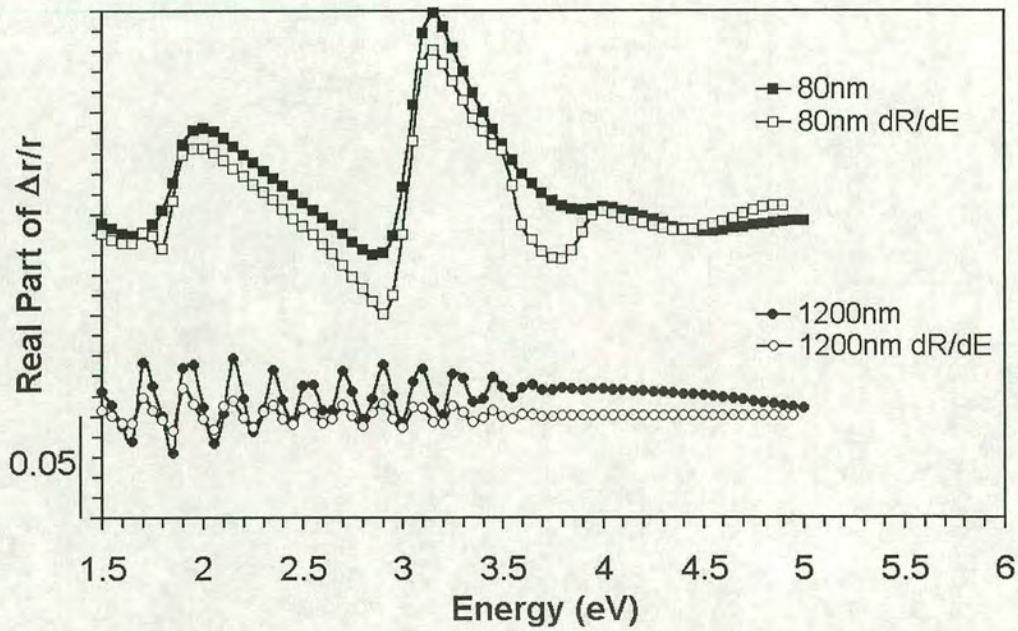

Figure 4.30 Simulations of the RA spectra of a PI/ITO/glass sample using the molecular alignment mode are shown as the solid data set. The hollow data set shows the scaled derivative of the reflectivity.

Neither the simulated or derivative spectra show evidence of the 4.5 eV feature previously seen in all of the measured RA spectra. This would be expected if this feature does not originate from the birefringence induced by the rubbing process. A possible explanation of the 4.5 eV feature could be rub-induced dichroism which would be present in the upper layer of the polymer as well as the rub-induced birefringence. Dichoric absorption was not included in the RAS simulations. Further evidence in favour of dichroism is presented with the RAS photoalignment studies.

Miller *et al.* [4.48] have previously used this mechanism to explain very similar RAS features in oriented polymer films.

Liquid Crystal Alignment

To test the alignment of the LC molecules on the rubbed polymers, LC cells are made using two pieces of ITO/glass, each of which has a treated polymer surface as an alignment layer. The cells are made with the treated surfaces facing inwards and depending on the type of cell, the treatment directions are either perpendicular or parallel. The two surfaces are separated slightly by using 2.4 μm spacers and the gap filled with LC (E49, Merck). This procedure enables the alignment properties to be studied easily by using crossed polarisers. Photomicrographs are taken of the constructed cells and can be seen in *Figures 4.31 & 4.32*. The first set of images demonstrates the quality of alignment increases with rubbing, in this case the rubbing machine was not used and so the amount the rubbing is measured in length units. In the *30 cm* image, not all the LC molecules are in domains and some of the domains themselves are relatively small. Whereas in the *120 cm* image, the domains are larger and less rugged looking, showing the LC molecules are aligned more homogeneously than before.

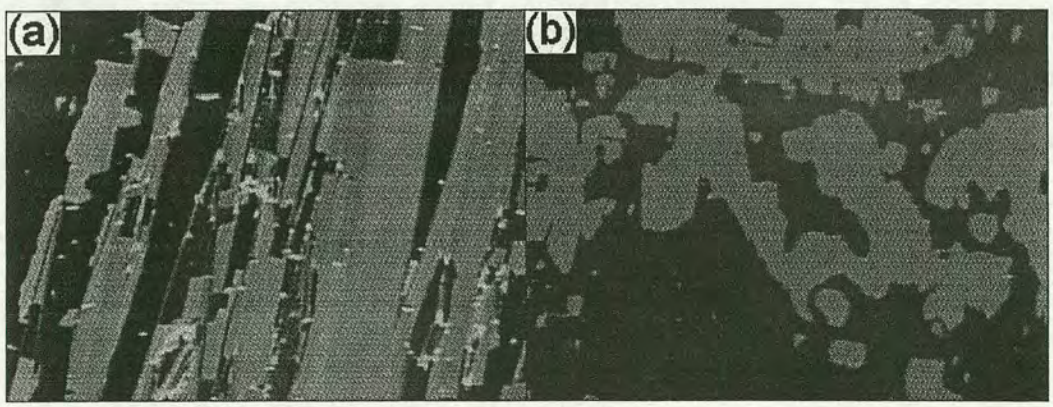

Figure 4.31 *Photos of constructed LC cells viewed through crossed polarisers showing LC alignment after (a) 30 cm and (b) 120 cm of rubbing. These cells were constructed by Mr C. Miremont who also took the photographs.*

The second set of images, illustrate that although good alignment can be obtained by rubbing the surface, *Figure 4.32 (a)*, too much rubbing can have a detrimental effect on the quality of the LC cell. In this set of images the samples were rubbed using the rubbing machine at 50 mm/min, the amount of rubbing is therefore expressed in terms of the number of rubs. Good alignment is obtained after 4 rubs, (*Figure 4.32 (a)*). As the number of rubs is increased, *Figure 4.32 (b)* shows cells after 20 rubs, *Figure 4.32 (c)* after 40 rubs, the number of defects on the surface increases proportionally, therefore decreasing the alignment quality of the LC cell. These observations suggest that in order to optimise the alignment of LCs between rubbed surfaces, a compromise must be reached between maximising the level of anisotropy and minimising the number of defects on the surface of the alignment layer. It may be necessary to find not only the minimum number of rubs required to saturate the anisotropy but to also find where the best alignment occurs in terms of a percentage of the maximum. The results presented here suggest the best results occur when the RA is at ~50% of its maximum value.

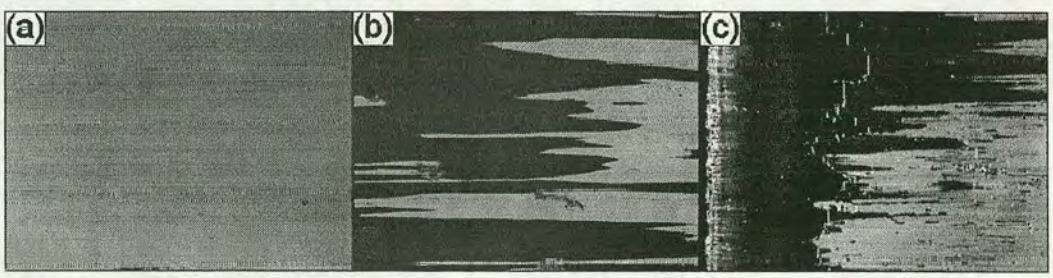

Figure 4.32 *LC cells viewed through crossed polarisers showing LC alignment after (a) 4, (b) 20 and (c) 40 rubs. These cells were constructed by Dr Zheng who also took the photos.*

Conclusion on Rubbing

The alignment of LC molecules is fundamental to the fabrication and optimum operation of LCDs. While this can be engineered by a variety of means, it is the crude process of rubbing a polymer film with a piece of fabric that dominates in the commercial displays industry. Empirical RAS measurements can be used to monitor the alignment layer fabrication in real time. Using RAS it has been possible to monitor the growth, saturation and reduction of the anisotropy of a rubbed sample. Simulations have enabled RAS features to be interpreted in terms of molecular

alignment, birefringence and dichroism. AFM has shown the reduction in anisotropy is due to a degradation of the alignment layer resulting from over rubbing. Measurements have shown RAS capable of monitoring the onset of degradation, which could be used to prevent damage to alignment layers. Increased rubbing has been found to improve the LC alignment but also give more defects on the surface, reducing device quality. Excess rubbing has been shown to damage the polymer film, reducing device quality.

Although rubbing is the preferred technique in industry for the fabrication of polymer alignment layers it has several drawbacks which include the generation of electrostatic charges and the generation of surface debris [4.20] as has been shown here. The obvious way to overcome these problems is to use a non-contact technique. In the next sections, two such techniques are investigated using RAS.

Photoalignment

Introduction to Photoalignment

As has been highlighted in the previous section, the technique of rubbing a polymer film to promote the alignment of LC molecules has several disadvantages. To avoid these problems, namely the generation of surface charge and the spreading of dirt [4.20], non-contact alignment techniques have been investigated. One technique found to be particularly effective in remedying these problems is photoalignment [4.11, 4.12 & 4.49]. This technique was first reported by Schadt *et al.* [4.50] to be suitable for the fabrication of alignment layers for use in LCDs. After polymerising photopolymers by exposure to linearly polarized light, UV dichorism and optical anisotropy are found in the surface layer [4.50]. These properties make it possible for LC molecules to align uniformly over the entire surface as the dispersive surface interaction forces align adjacent LCs parallel [4.50].

Photoalignment of a Light Sensitive Polymer

When using this technique, generally two different types of cells are made, the composite or the surface layer. The composite cell is made by mixing a UV curable polymer with LC and then putting the mixture into an empty LC cell which is then cured by exposure to linearly polarised UV light. The surface layer cell is more common and is made in a similar manner to a typical rubbed cell. That is, the substrates are coated with the polymer and then processed, in this case by exposure to linearly polarized UV light. Cells are constructed using the treated substrates which are then filled with LC.

By exposing a light sensitive polymer (in this case PVCi) to linearly polarised UV light it is possible to generate anisotropic alignment of the polymer chains on the surface of the film [4.50]. A study of photoalignment as a function of exposure time, by RAS, was carried out using *sample 5*. The spectra obtained for one exposure time at several different azimuth angles are shown in *Figure 4.33* from which it can immediately be seen that the anisotropy is approximately two orders of magnitude lower than was produced by the rubbing technique. These spectra appear similar in

shape to the RAS measurements of rubbed polymers as they each have what appears to be multilayer interference peaks in the visible region of the spectra and a larger feature at 4.5 eV. In the previous experiments it was speculated that the 4.5 eV feature was a result of rub induced dichroism. The measurements of Schadt *et al.* [4.50] agree with this as they show direct measurements of UV dichroism from photoaligned samples in the energy range of ~3.9 eV to ~4.7 eV, albeit using a slightly different polymer. For these types of samples, it is expected that the RA will vary as $\cos 2\theta$, where θ is the angle between the vertical axis of the spectrometer and the alignment direction of the sample.

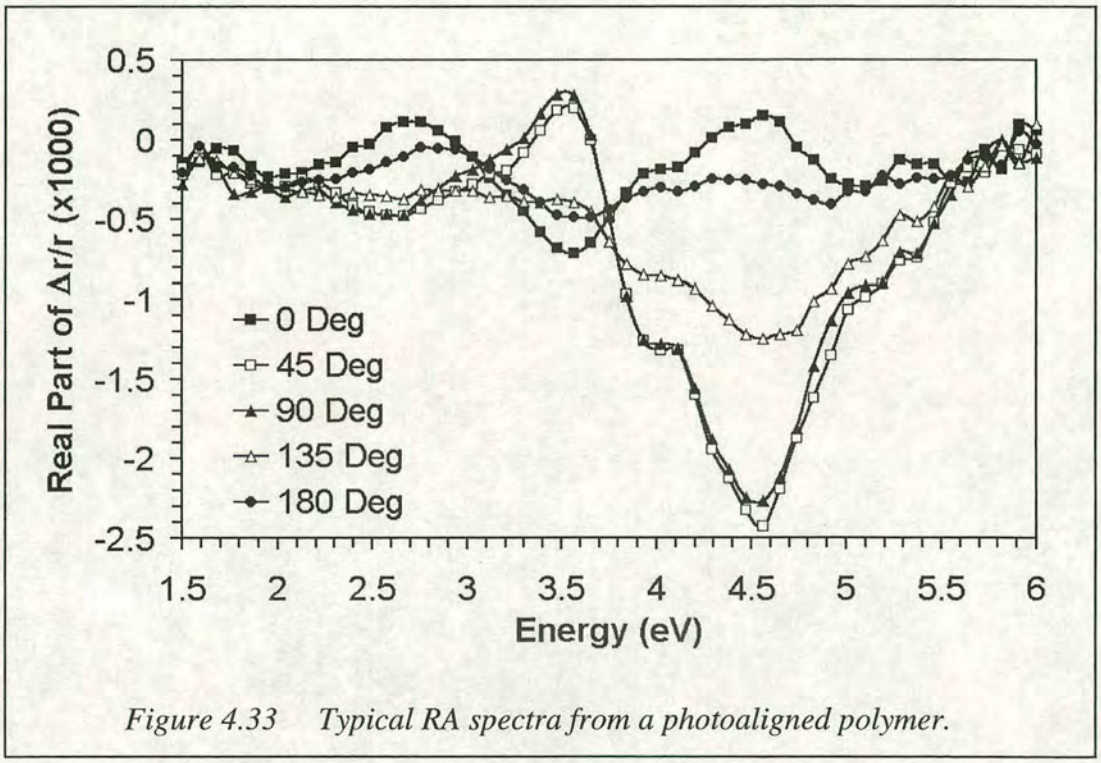

Figure 4.33 Typical RA spectra from a photoaligned polymer.

A potential hazard of this technique is the inadvertent modification of the UV sensitive polymer if a broad band light source is used. The UV component of the spectrometer light source (a 75 W broad band lamp) can be estimated to be comparable to the 10 mW UV lamp used to align the samples (with exposure times of about 1 minute), and may therefore lead to modification of the samples during data acquisition. Spectra obtained for a series of azimuthal angles are shown in *Figure 4.33*. The expected $\cos 2\theta$ dependence is not observed and in fact, all of the spectra taken after the 0° data set appear to be more negative than expected. Initially the polarisation of the light from the spectrometer is incident at 45° to the axes of the

sample and anisotropy is induced in this direction. The two competing anisotropies are thought to simply add together (after a scaling factor is considered) [4.51] resulting in an overall reduction of the measured anisotropy. Recording these spectra in the reverse order using a second sample leads to a greater RA than expected, clearly demonstrating the ongoing modification of the sample by the RAS beam.

The UV exposed PVCi film gives a clear RAS signal in the visible portion of the spectrum and so real time RAS monitoring of the UV-stimulated alignment process is possible.

Conclusions on Photoalignment

It is not completely unexpected that RAS damages the photoaligned samples as the UV exposure during data collection and during the photalignment process are similar. Therefore RAS should not be used to study the alignment layers of photoaligned polymers, unless a UV filter is used, as in this case RAS is not a non-destructive probe and interferes with the measurements. However, the shape of the measured RA spectra and the previous work of others have strengthened the case for the 4.5 eV feature seen in the rubbing spectra being due to dichroism.

Etching

Introduction to Etching

Sustained investment in the rubbing procedure has protected its dominance but with recent advances in resolution the limitations of rubbing are becoming increasingly troublesome. For example, degradation of the rubbing fabric can lead to non-uniformity of the alignment layer and streaking defects in completed displays, resulting in the rejection of entire batches i.e. hundreds of displays [4.17]. This is a problem which will only be emphasised by the steady scaling up of substrate size [4.20] and whose occurrence highlights the need for both an improved alignment strategy. The pioneering work of Sun *et al.* [4.19] has shown that argon ions, when directed with oblique incidence, can induce anisotropic surface modifications capable of providing an alignment template for LC molecules. Very recently, Chaudhari *et al.* have demonstrated this alignment technique to be well-suited to the commercial production of LCDs and to be superior in several respects to rubbing [4.17]. Here, the previous RAS studies of rubbed polymer films are extended to the study of ion beam etching of polymer films.

Ion Beam Etching of Polyimide

Before and after polymer coating, the samples (*sample 3a*) were analysed using the RA spectrometer and an AFM. In each case negligible optical anisotropy was found before and after. To create an LC alignment template samples were then exposed to a beam of argon ions with energy of 500eV and current density 15 $\mu A/cm^2$ at 45° incidence while their RA spectra were continuously measured. The alignment effect was confirmed by constructing LC cells using the nematic LC E49 (Merck) sandwiched between samples with orthogonal alignment directions which had been subjected to a dose of ~1.3 x 10^{17} ions/cm^2. *Figures 4.34 & 4.35* show dark-state photomicrographs of an etched cell and that of a similar device constructed with conventional rubbed polyimide alignment layers. As has been previously reported [4.17, 4.18] we find that the ion etched polymer layers produce more uniform devices with less debris and no evidence of streaking defects. In fact, the debris observed in the ion etched cell, *Figure 4.34,* is not intrinsic to the etching process

itself but arises primarily because of atmospheric contamination when moving the samples into and out of the ion bombarding chamber which is housed outwith of a clean-room environment.

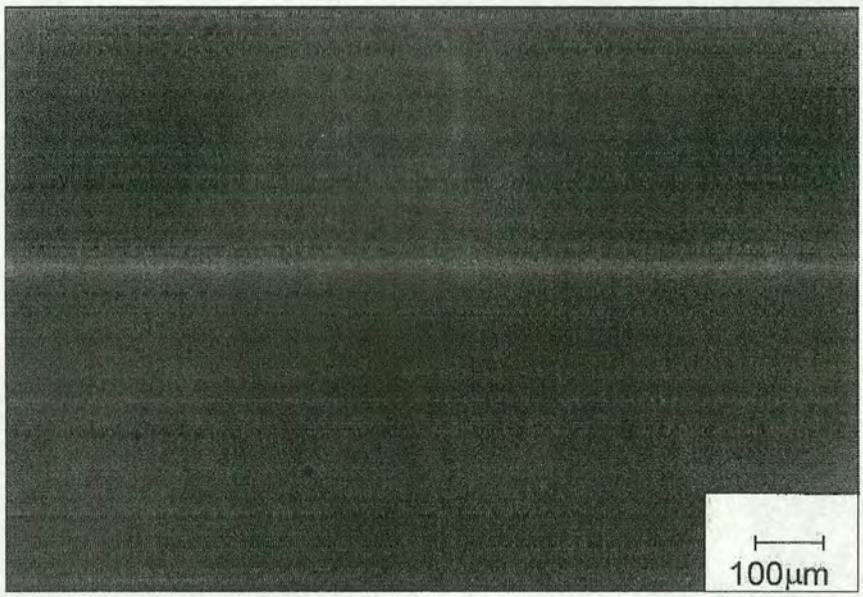

Figure 4.34 Dark state photomicrographs of an LC cell constructed using PI alignment layers prepared by ion beam etching.

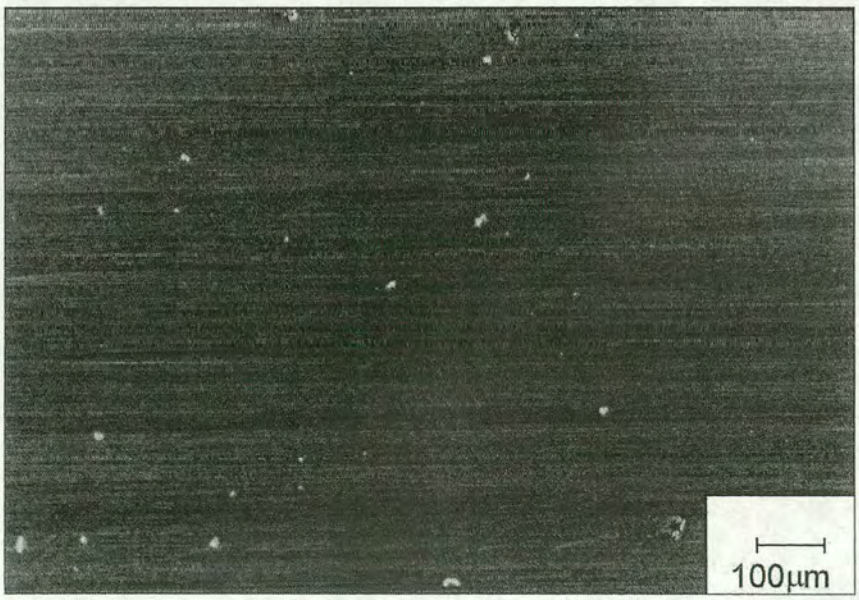

Figure 4.35 Dark state photomicrographs of an LC cell constructed using PI alignment layers prepared by rubbing.

The RA spectra measured during 20 minutes of bombardment of a sample are shown in *Figure 4.36. Figure 4.37* illustrates the optical anisotropy to initially increase before saturating after ~10 minutes, corresponding to a total dose of ~$7x10^{16}$ ions/cm^2. It appears that RAS allows clear detection of the development of the anisotropic (i.e. LC aligning) surface. Comparing the RA spectra of ion-etched and rubbed polymer alignment layers, shown in *Figure 4.18,* it is clear that the optical anisotropy of the latter is greater by approximately two orders of magnitude. This can be attributed to the depth of molecular alignment associated with the relatively deep (~10 – 30 nm) grooves created by the rubbing process. AFM cross-sections of the untreated, etched and rubbed surfaces, shown in *Figure 4.38*, illustrate the surface roughness of the ion-etched polymer to be determined essentially by the initial surface. This fact, together with our observation that the reflectivity of the sample was negligibly affected by the etching process, indicate that LC alignment on the etched polymer is promoted by surface modification at the atomic scale, in accordance with Geary *et al.* [4.35]. In the regime considered here, the collision cascade caused by the incident ions transfers energy to atoms in the near-surface region, causing some of them to be ejected. This sputtering process tends to establish a steady state in which the surface damage usually extends less than a nanometer or so into the surface. In-plane anisotropy may also be produced, giving rise to a non-zero RAS signature and the LC alignment effect in the case of etched polyimide. In general, ion beams can induce surface corrugation parallel or perpendicular to the plane of incidence [4.52], but for covalently bonded systems a simple picture in which bonds are preferentially broken in the plane of incidence of the ion beam seems appropriate [4.17]. Therefore polymer chains at the etched surface are expected to be preferentially aligned along the etching direction. Although, *Figure 4.38* shows the spectra have the same sign, which is expected as the rubbing direction was parallel to the plane of incidence of the ion beam, the spectra appear fundamentally different. However, upon closer inspection several similarities exist, in fact, the etching spectra shows signs of being an undeveloped version of the rubbed spectra. The major feature in the etching spectra is a peak at 3.1 eV, however there is a definite increase in anisotropy at 4.5 eV in additional to the formation of a shoulder around 2.3 eV. It is possible that the two lower energy features are

multilayer interference effects. Although for the etching spectra presented here one peak is distinctly more pronounced than the other, this difference in amplitude can also be seen in the RAS spectra from the rubbed samples (*Figure 4.16 and 4.18*).

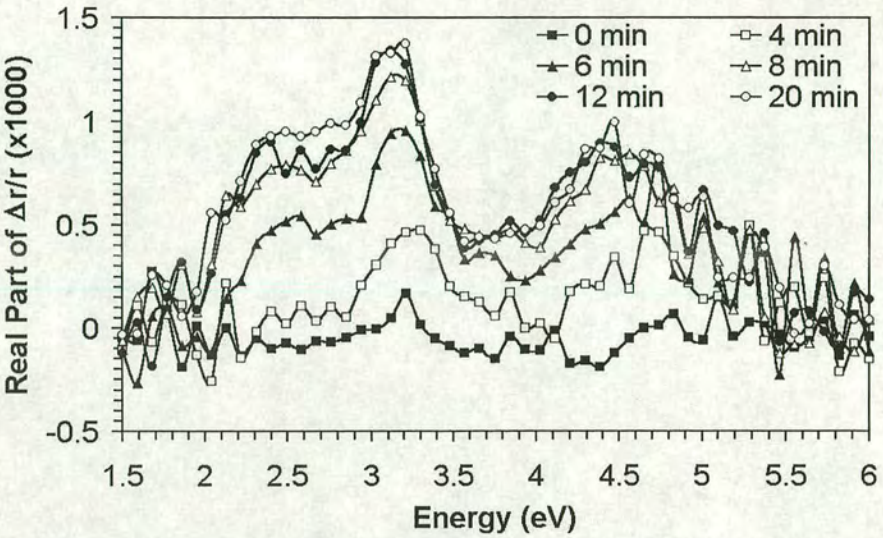

Figure 4.36 *RA spectra for an etched polyimide surface. The x-direction lies in the plane of incidence of the ion beam.*

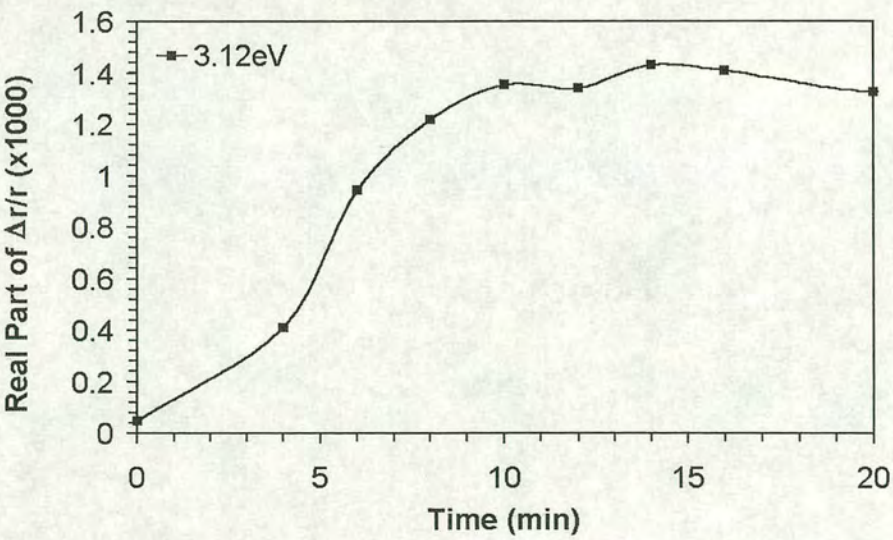

Figure 4.37 *RAS signal as a function of time for an etched polyimide surface.*

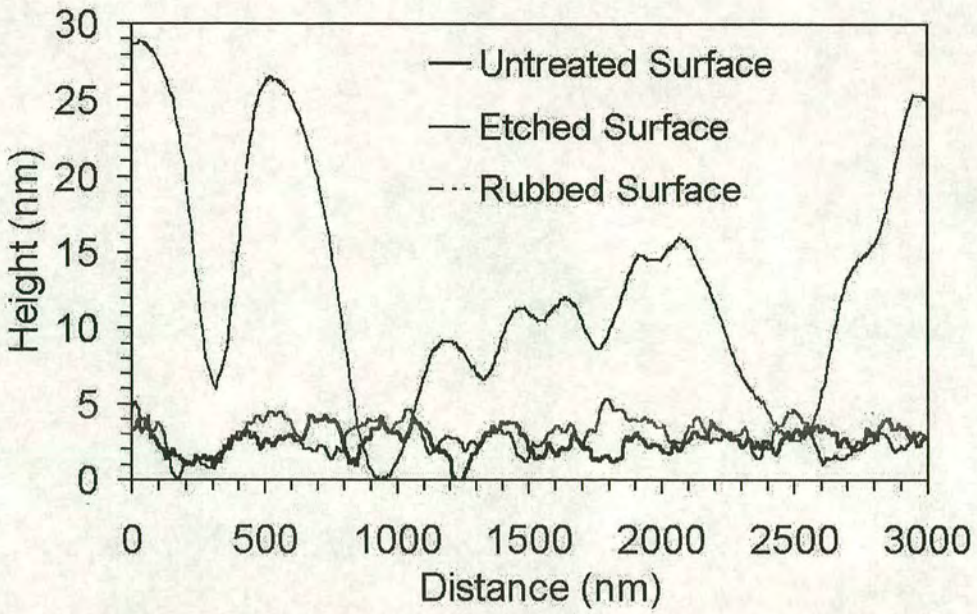

Figure 4.38 *Cross sectional atomic force microscopy images of an untreated polyimide surface, an etched polyimide surface and a rubbed polyimide surface. All cross sections are from images 3 x 3 μm.*

Conclusions on Etching

It has been shown in *Figure 4.38* that the topographical effect of etching is negligible compared to rubbing, however, corrugation of the etched surface is known to occur [4.53]. The use of a heavier element or higher energies to etch the surface would result in larger scale corrugation which may result in etching spectra more easily comparable to the rubbing spectra as the depth of molecular alignment would be greater. Nevertheless, we have found that RAS can monitor in real time the creation of ion-etched polyimide LC alignment layers.

Conclusions

It is not immediately obvious that an optical reflection technique, such as RAS, will be suitable for studying alignment layers that are in essence transparent thin films. Simulations of a standard thickness rubbed PI alignment layer, *Figure 4.39*, clearly show that although the intensity of the transmitted beam is much greater that the reflected beam, the amount of birefringence information contained within the beam is lower. In the same figure, a comparison between RAS and transmission anisotropy spectroscopy (TAS) shows the same result; RAS is more sensitive and is therefore more suited to these types of samples. In fact, although the amplitudes measured here are of the order of 10^{-1}, RAS is capable of detecting anisotropy of the order of 10^{-5}.

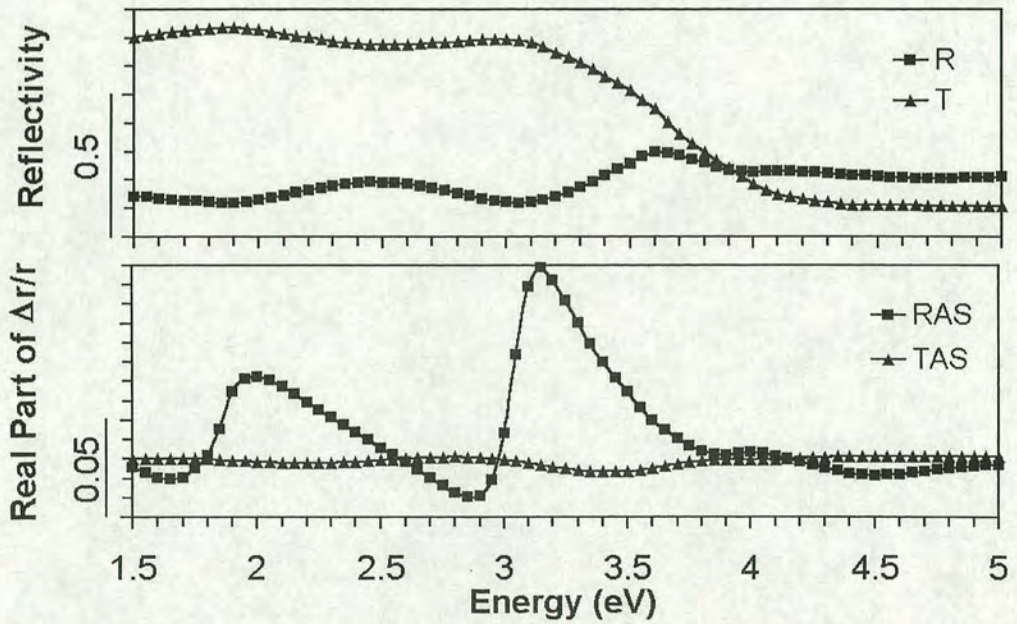

Figure 4.39 *The comparison of the reflectivity and transmittance from a PI/ITO/glass substrate is shown in the upper figure. The comparison between RAS and TAS is shown in the lower figure.*

In this chapter RAS is shown capable of monitoring the fabrication of alignment layers for most of the main commercial techniques currently used. In general, the amplitude of the measured RA from each of the samples behaves in a manner that is consistent with observations made by AFM of the topography of the processed surfaces. Simulations of the rubbed surface suggest that the optical anisotropy results from birefringence and perhaps dichroism due to the preferential alignment of the

polymer chains caused by the alignment techniques. RAS measurements of UV aligned samples show similar features to the rubbed spectra. Elsewhere, dichroism in the same energy region has been measured from similar UV aligned samples.

Operational LC cells have been constructed to demonstrate the drawbacks of the rubbing technique, namely how dirty it is. Contamination reduces the quality of the LC cells and advocates the use of non-contact fabrication techniques. Ion beam etching of a polymer is demonstrated as a superior alternative and RAS is shown to be capable of monitoring the changes in optical anisotropy of the surface which may be caused by minute topographical changes. By using RAS to monitor the fabrication, it may be possible to create a real-time quality control of the alignment layers which could result in increased production yields, lower waste and therefore lower manufacturing costs. The possibility of operating RAS in an imaging mode [4.54] may offer further advantages, for example screening for device uniformity. However, for all of the alignment techniques an important question is whether the optical anisotropy can be linked to a device property.

Clearly there is still a great deal to understand about these systems: the increased anisotropy at 4.5 eV, the contribution to the anisotropy from molecular alignment and the behaviour of surface optical properties under various conditions (i.e. etching). It seems natural to continue this investigation by studying model systems, in particular the etching technique, as it is in the ascendancy. A suitable surface is Cu (110) which has been studied in the past under etching conditions [4.54, 4.55]. Additional studies of sub-monolayer organic films adsorbed on this surface [4.56] could prove useful in future investigations into the LC/alignment interactions.

Chapter 5: Angular Dependent RAS

'Opportunity is missed by most people because it is dressed in overalls and looks like work'
Thomas A. Edison (1847 - 1931)

Summary

An interesting by-product of the previous study of LC alignment layers has been the introduction of an extension to the normal RAS technique: angular dependent RAS (ADRAS). To demonstrate the potential of this technique, three different systems are examined, a doubly rubbed alignment layer, a double sided rubbed alignment layer and an alignment layer subjected to stress. Using these examples ADRAS is found capable of isolating and monitoring optical anisotropy from different sources within a single system. Some of the work presented in this chapter has been published [5.1], and another paper, a generalised and more in-depth discussion of [5.1], has been accepted for publication [5.2].

Separation of Optical Anisotropies

Angular dependent measurements are shown to be a useful extension to the standard technique by allowing different sources of optical anisotropy to be separated experimentally. This application is demonstrated with examples which highlight the manner in which competing anisotropies contribute to the measured anisotropy and it is shown that in general, azimuth dependent RAS (ADRAS) could be used to separate different physical effects. The first example is double rubbing which has real applications to the fabrication of LCDs and so a monitor of this upcoming technique could prove invaluable. The other two examples have been contrived to demonstrate the potential of ADRAS

Double Rubbing

In the previous chapter, RAS has been shown capable of characterising thin films such as those used for polymer alignment layers in LCDs. Here, a simple extension of the standard RAS technique is shown to allow a convenient characterisation of multidirectional over-rubbed alignment layers, and hence ADRAS can disentangle optical anisotropies derived from independent mechanisms.

As discussed in *Chapter 4*, despite problems associated with charging and surface debris, rubbing is by far the dominant technique used in the commercial displays industry. Accordingly, rubbed polymers continue to attract a great deal of scientific interest. A recent development is multidirectional rubbing in which a polymer film is first rubbed in one direction and then over-rubbed in a different direction [5.3-5.6]. LC orientation on over-rubbed polymer surfaces is believed to lie between the two rubbing directions [5.3]. Recent reports suggest over-rubbing reduces the number of steps required to make multidomain displays which significantly increases viewing angle, traditionally a weakness of LCD technology [5.6].

The type of sample used in this investigation is *sample 3a*, as described in *Table 4.1* of *Chapter 4*. RAS analysis of the unrubbed samples revealed negligible optical anisotropy and corresponding topographic AFM images, *Figure 5.1(a)*, confirmed the samples to be isotropic. After mechanically rubbing the surface of the polyimide,

microgrooves were observed along the rubbing direction, as seen in *Figure 5.1(b)*. The RA spectrum after this rubbing is shown as the solid line in *Figure 5.2*.

Figure 5.1 *AFM images of (a) an unrubbed polymer sample, (b) a rubbed polymer surface, (c) a rubbed polymer surface with a single over-rub at an angle to the initial rubbing direction and (d) a rubbed polymer surface with multiple rubs at an angle to the initial rubbing direction. Each image is ~10 x 10 μm and the maximum heights are 5.5 nm, 8.0 nm, 23.5 nm and 27.0 nm respectively.*

RA spectra can, in principle, be simulated to yield material parameters such as the composition, thickness of layers and roughness [5.7]. Here however, the primary concern is with the dependence of RAS signals on the sample azimuthal angle θ, defined as the angle between the y-axis of the spectrometer and the rubbing direction

of the sample. This is shown by the curve with solid square data points in *Figure 5.3* which illustrates the RAS signal of the rubbed polymer at 3 eV as a function of azimuth angle. The same θ dependence was observed for all photon energies. From experimental results it is seen that introducing a rotation to the sample causes the RAS amplitude to vary as $\cos(2\theta)$. This observed angular dependency can be predicted by considering the Jones reflection matrix of the sample, which relates the incident and reflected field amplitudes and can be expressed in Cartesian co-ordinates as,

$$\begin{bmatrix} E_{xr} \\ E_{yr} \end{bmatrix} = \begin{bmatrix} r_{xx} & r_{xy} \\ r_{yx} & r_{yy} \end{bmatrix} \begin{bmatrix} E_{xi} \\ E_{yi} \end{bmatrix}$$

As mentioned in *Chapter 2 (Equations 2.16 & 2.20)*, the amplitude of the electric field of the light reflected from the sample being measured by the RA spectrometer can be expressed as,

$$\frac{\Delta I}{I} \approx \Re\left(\frac{\Delta r}{r}\right)$$

where from *Equation 2.21*,

$$\frac{\Delta r}{r} = 2\frac{r_{xx} - r_{yy} + r_{xy} - r_{yx}}{r_{xx} + r_{yy} + r_{xy} + r_{yx}} \qquad \textit{Eq. 5.1}$$

By applying an azimuthal angular rotation θ, such that $x \rightarrow \alpha$ and $y \rightarrow \beta$, the Jones reflection matrix becomes,

$$\begin{bmatrix} r_{xx} & r_{xy} \\ r_{yx} & r_{yy} \end{bmatrix} = \begin{bmatrix} \cos\theta & -\sin\theta \\ \sin\theta & \cos\theta \end{bmatrix} \begin{bmatrix} r_\alpha & 0 \\ 0 & r_\beta \end{bmatrix} \begin{bmatrix} \cos\theta & \sin\theta \\ -\sin\theta & \cos\theta \end{bmatrix}$$

$$\begin{bmatrix} r_{xx} & r_{xy} \\ r_{yx} & r_{yy} \end{bmatrix} = \begin{bmatrix} r_\alpha \cos^2\theta + r_\beta \sin^2\theta & r_\alpha \cos\theta \sin\theta - r_\beta \cos\theta \sin\theta \\ r_\alpha \cos\theta \sin\theta - r_\beta \cos\theta \sin\theta & r_\alpha \sin^2\theta + r_\beta \cos^2\theta \end{bmatrix}$$

By substituting the elements of this reflection matrix into *Equation 5.1*, an expression for the reflection anisotropy as a function of azimuthal angle is obtained.

$$\frac{\Delta r}{r} = 2\frac{r_\alpha - r_\beta}{r_\alpha + r_\beta}\frac{\cos 2\theta}{(1+\frac{r_\alpha - r_\beta}{r_\alpha + r_\beta}\sin 2\theta)} \qquad \textit{Eq. 5.2}$$

As $\frac{r_\alpha - r_\beta}{r_\alpha + r_\beta} << 1$, $(1+\frac{r_\alpha - r_\beta}{r_\alpha + r_\beta}\sin 2\theta) \approx 1$, and so it is clear that *Equation 5.2* simply becomes the standard RAS equation scaled by the trigonometric factor of $\cos(2\theta)$.

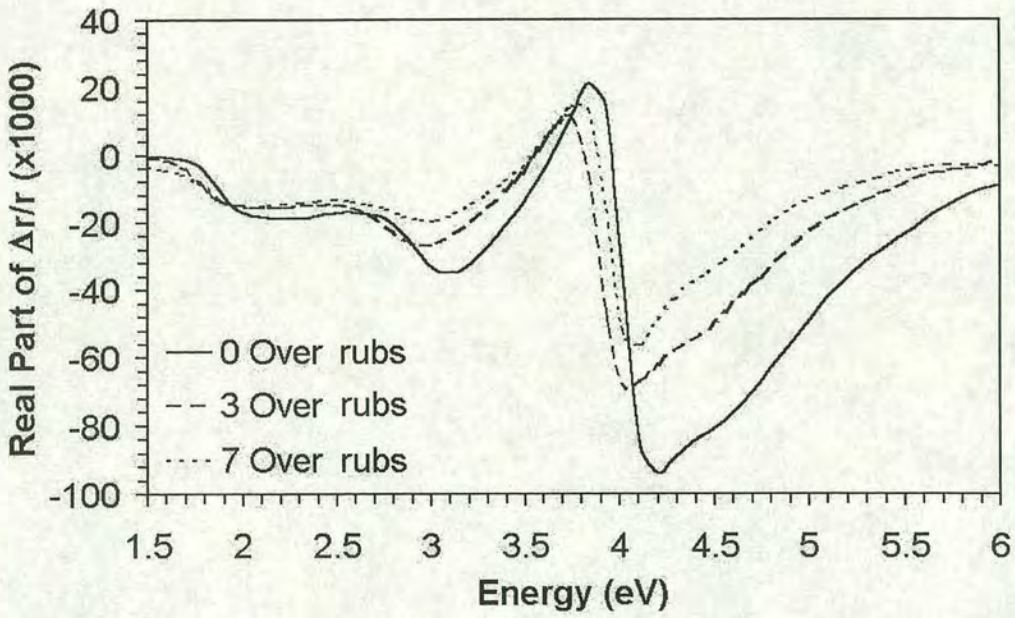

Figure 5.2 *RAS of a singly rubbed sample with 0, 3 and 7 over-rubs at angle φ to the initial rub. In each case θ=0°.*

The PI surface was then over-rubbed a number of times at an angle φ to the initial rubbing direction using the same rubbing parameters. The RA spectra after over-rubbing are shown in *Figure 5.2*. A typical AFM image of the surface after a single over-rub, shown in *Figure 5.1 (c),* appears very similar to those previously reported [5.5] and clearly shows the initial rubbing underlying the over-rubbing. The RAS lineshape is unchanged as expected but the angular dependence is modified. *Figure 5.3* shows the ADRAS maximum moving to higher θ with increased over-rubbing. If the over-rubbing completely replaces the original microgrooves, a $\cos(2(\theta-\varphi))$

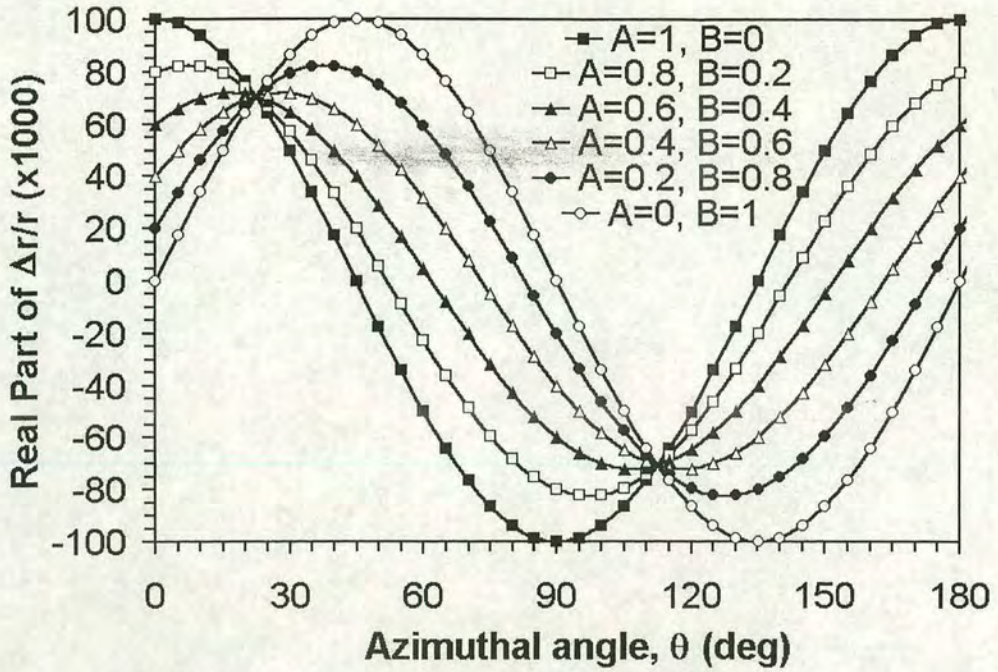

Figure 5.4 *Simulation of ADRAS based upon* $A\cos(2\theta) + B\cos(2(\theta - \varphi))$ *where* $B = 1 - A$.

Rubbing and Squeezing

In the previous example, although the sample had two sources of optical anisotropy, the spectra from each were basically identical. In general, individual contributions to a resultant anisotropy can have different spectra as well as different angular dependencies. ADRAS is now demonstrated on a sample subjected to mechanical stress applied at ~30° to the rubbing direction, the sample type used is *sample 3a*. The RA spectrum of the rubbed and squeezed sample, over a series of azimuthal angles, is shown in *Figure 5.5,* while ADRAS curves for photon energies of 3.30, 3.57 and 4.38 eV can be seen in *Figure 5.6.* The signal at 4.38 eV shows 180° periodicity while that at 3.30 eV has 90° periodicity, indicating the presence of two distinct sources of anisotropy. *Figure 5.7* clearly shows that the 4.38 eV spectra is rub-induced, as discussed in *Chapter 4*, while the 3.30 eV spectra is stress-induced birefringence (the photoelastic effect). Both mechanisms appear to contribute to the measured anisotropy at 3.57 eV which has a unique angular dependence. The 90° periodicity of the latter contribution is due to reflections from the lower surface of the sample with polarisations parallel and perpendicular to the stress (corresponding

to the fast and slow axis) combining incoherently on account of their large relative phase difference caused by the birefringence of the bulk. Confirmation of this is found by studying an identical sample under the same conditions but with the rear surface of the sample frosted to scatter light incident upon it. In this case, the angular dependency reverts to $\cos(2\theta)$. The simulation in *Figure 5.8* shows that the ADRAS curves of all photon energies can be decomposed into weighted sums of the cosine and sine-squared contributions. Conversely, a numerical fit of each ADRAS curve allows the stress-induced and rub-induced optical anisotropy spectra to be separated. For the present case this can be achieved by relieving the external stress, but usually competing mechanisms cannot be switched off. The negative sign before $\cos(2\theta)$ and the factor of $(2(\theta - 15))$ in the simulation equation result from the rubbing direction being at $\theta = 90^o$, and so the stress is actually applied at $\theta = 90^o + 2(15^o) = 120^o$.

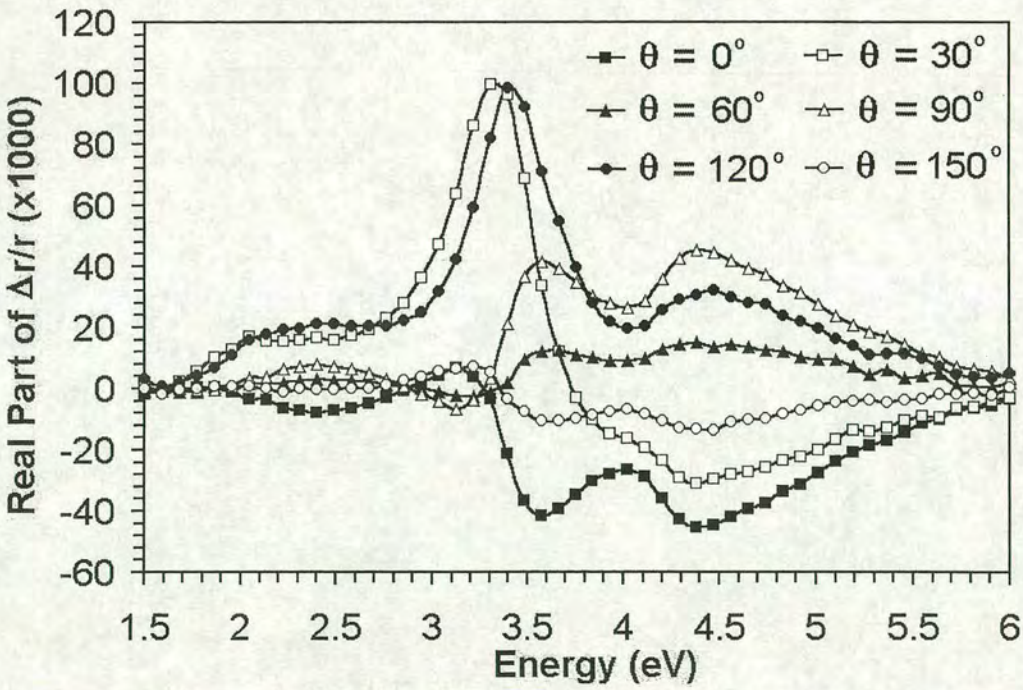

Figure 5.5 *RAS of a rubbed and squeezed sample as a function of azimuthal angle.*

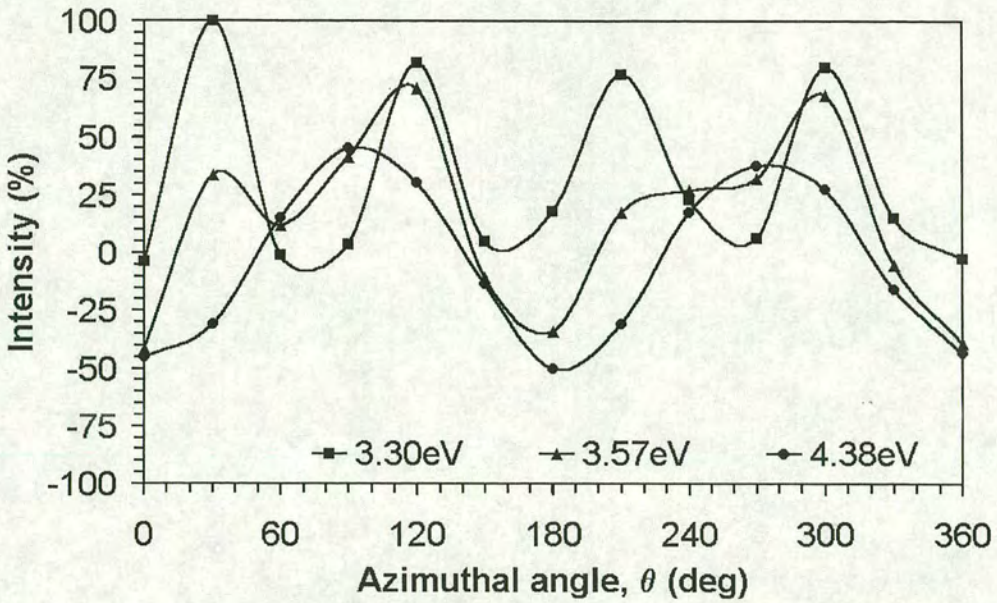

Figure 5.6 *ADRAS of a rubbed and squeezed sample at a selection of energies.*

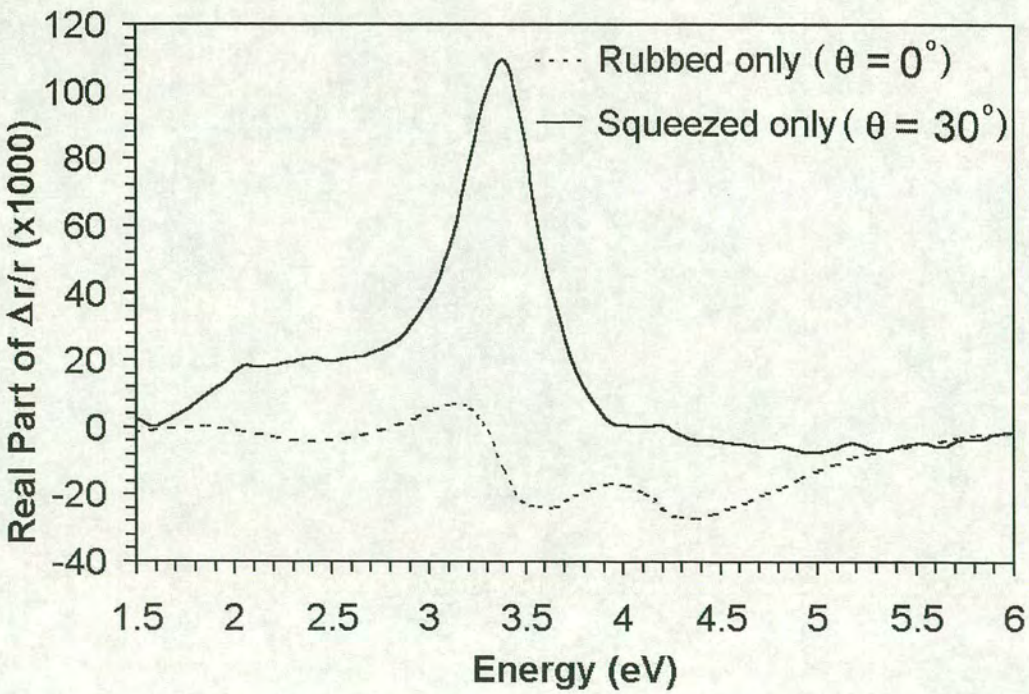

Figure 5.7 *RAS of the individual components of the rubbed and squeezed sample.*

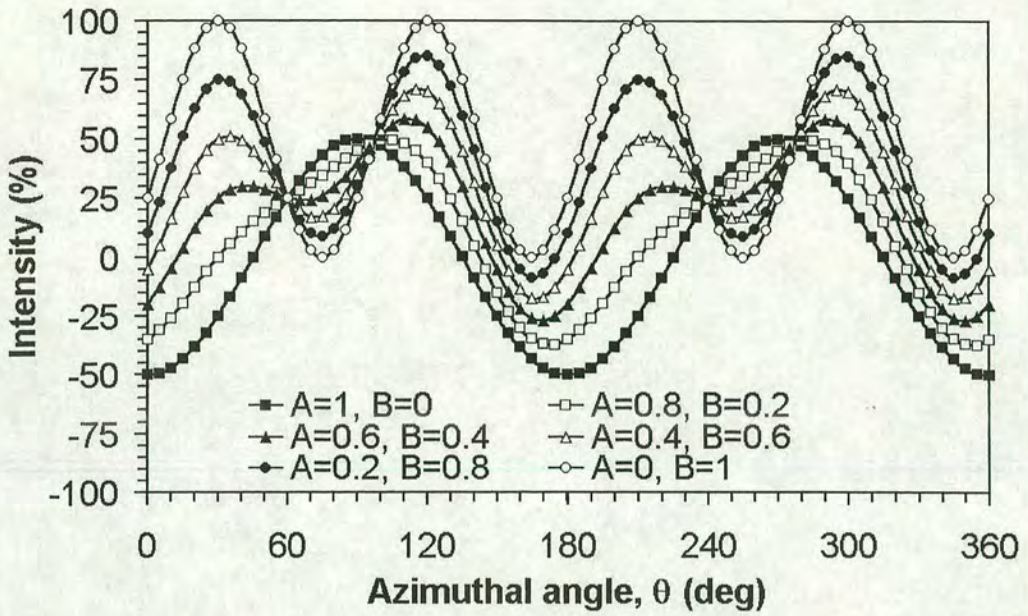

Figure 5.8 *ADRAS simulation using* $-A\cos(2\theta)+2B\sin^2(2(\theta-15))$ *demonstrating the addition of different anisotropic components.*

Double Sided Rubbing

Similar to the previous example, a sample with two sources of anisotropy resulting in two distinct spectra is studied. Since each source varies differently as a function of azimuthal angle, different information will be emphasised at particular angles depending on the configuration of the sample. As described in *Chapter 4*, PI samples of different film thickness can be characterised by their RA spectra. This difference can be seen as a multilayer interference effect in the RA spectra where the positions of the interference maxima can be predicted. Typical spectra for both standard (*sample 3a*) and thick (*sample 3b*) samples, as described in *Table 4.1*, can be seen in *Figures 5.9 & 5.10* which show the RA spectra as a function of energy as the azimuthal angle is rotated. As the thickness of the PI film is increased, the spacing of the interference patterns seen in the RA spectra decrease. In *Figure 5.9*, maxima can be seen at energies of approximately 2.0 eV, 3.1 eV and 4.2 eV, whilst in *Figure 5.10* the maxima appear as ripples in the energy range of 1.5 eV - 3.5 eV and with approximate periodicity of 0.2 eV. Here, the results of the previous section are built upon and further evidence of the way in which of optical anisotropies from different sources combine is presented.

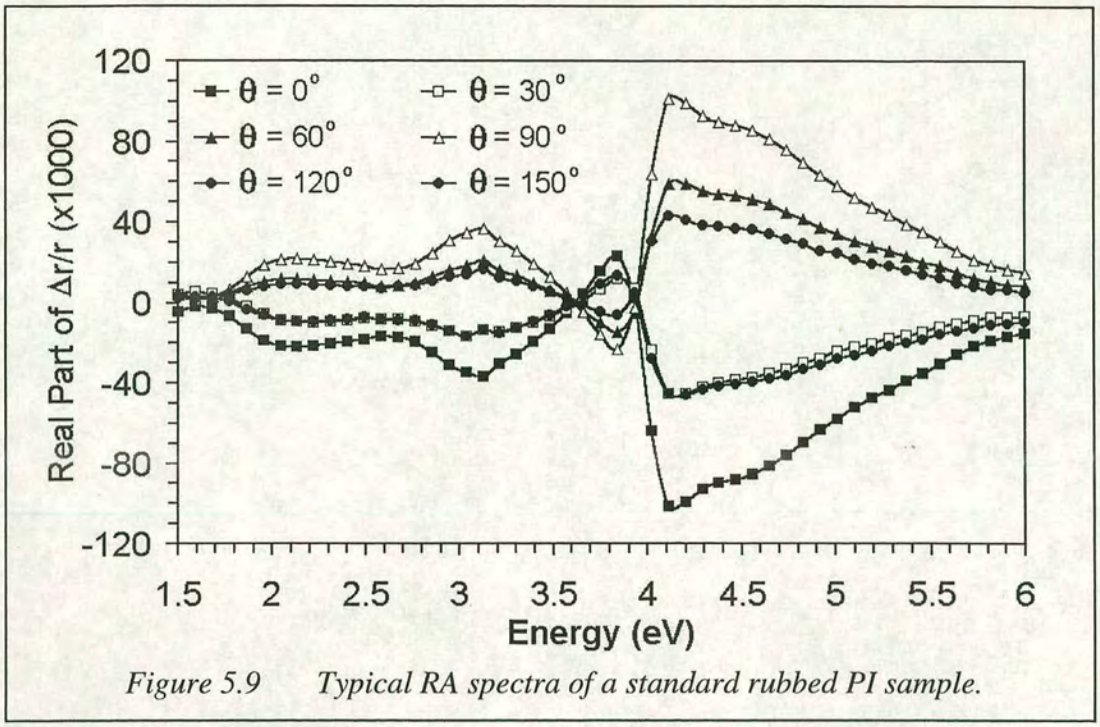

Figure 5.9 Typical RA spectra of a standard rubbed PI sample.

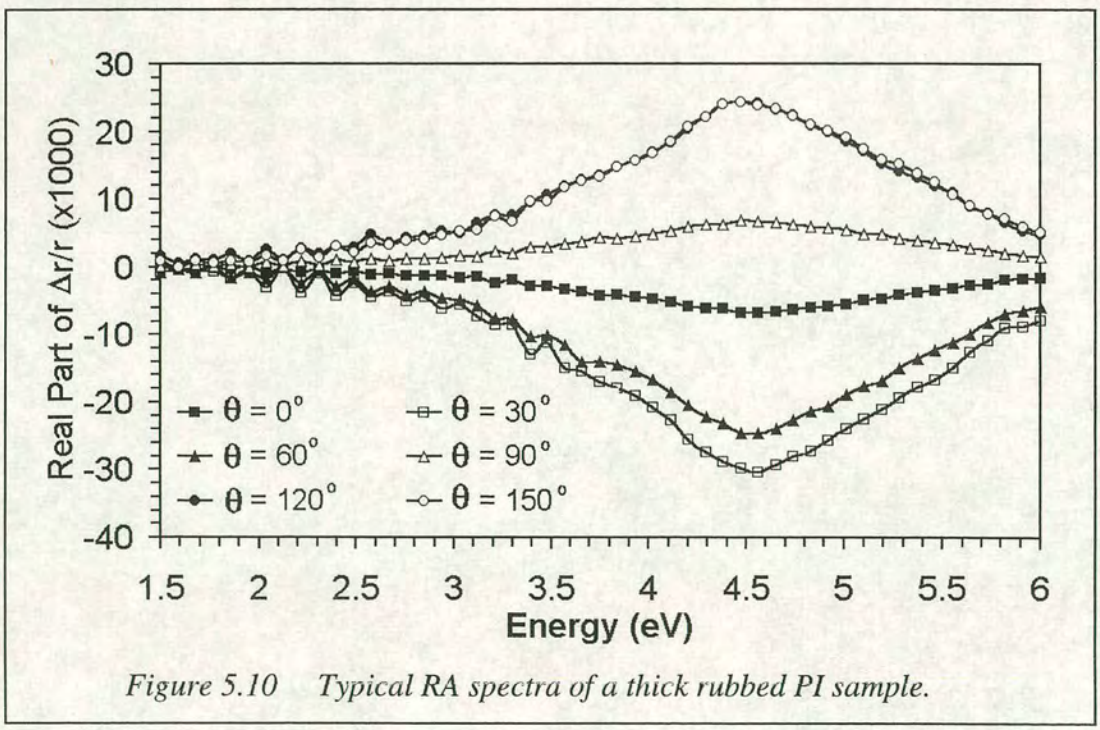

Figure 5.10 Typical RA spectra of a thick rubbed PI sample.

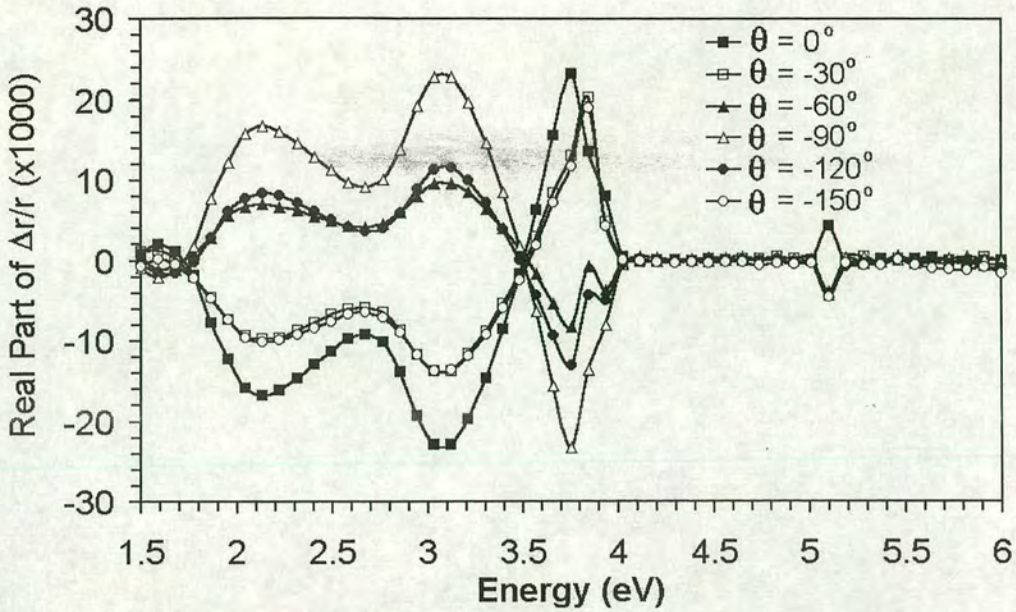

Figure 5.11 *Typical RA spectra from the reverse side of a standard rubbed PI sample.*

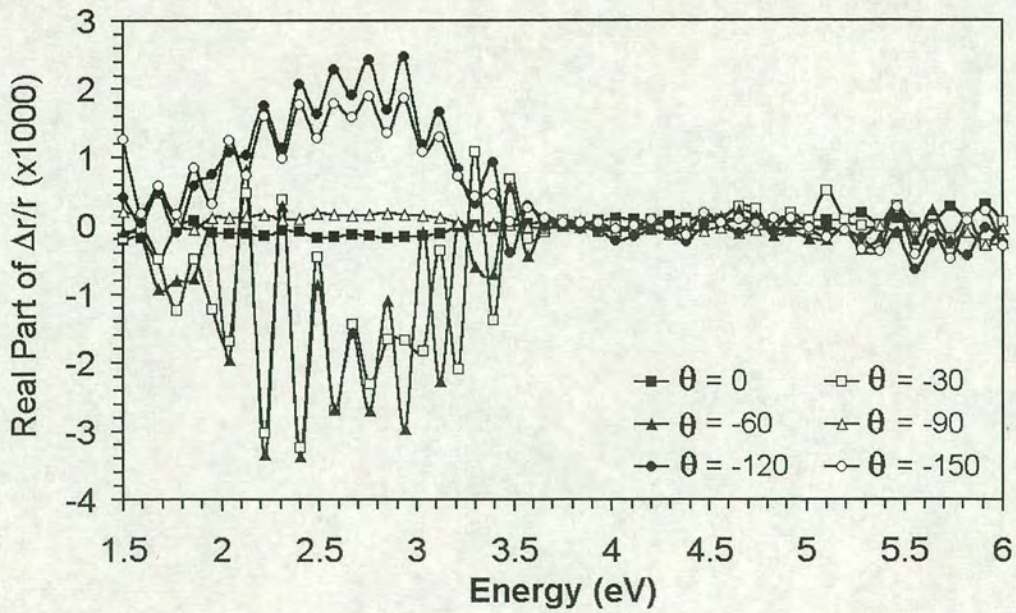

Figure 5.12 *Typical RA spectra from the reverse side of a thick rubbed PI sample. The difference in amplitude of interference peaks is due to sample misalignment.*

When the reverse side of these samples are studied, spectra similar to those obtained from the front surface are seen. Spectra from the front and rear surfaces differ as the latter is attenuated over the entire energy range, in particular in the UV area, as a result of optical absorption in the glass. *Figures 5.11 & 5.12* show the spectra from the reverse side of the standard and thick samples used in *Figures 5.9 & 5.10* respectively.

As expected, the amplitude of the anisotropy from each of the rubbed PI samples varies as a function of $\cos(2\theta - \varphi)$, where θ is the azimuth angle and φ is the angle parallel to the rubbing direction. *Figures 5.9 & 5.11* show the magnitude of the RA amplitude for the sample of standard thickness, which in this case has $\varphi=0°$, to have a maximum when $\theta = 0°, 90°, 180° \& 270°$. *Figures 5.10 & 5.12* show the magnitude of the RA amplitude for the thicker samples, which has $\varphi=45°$, to have a maximum when $\theta = 45°, 135°, 225° \& 315°$.

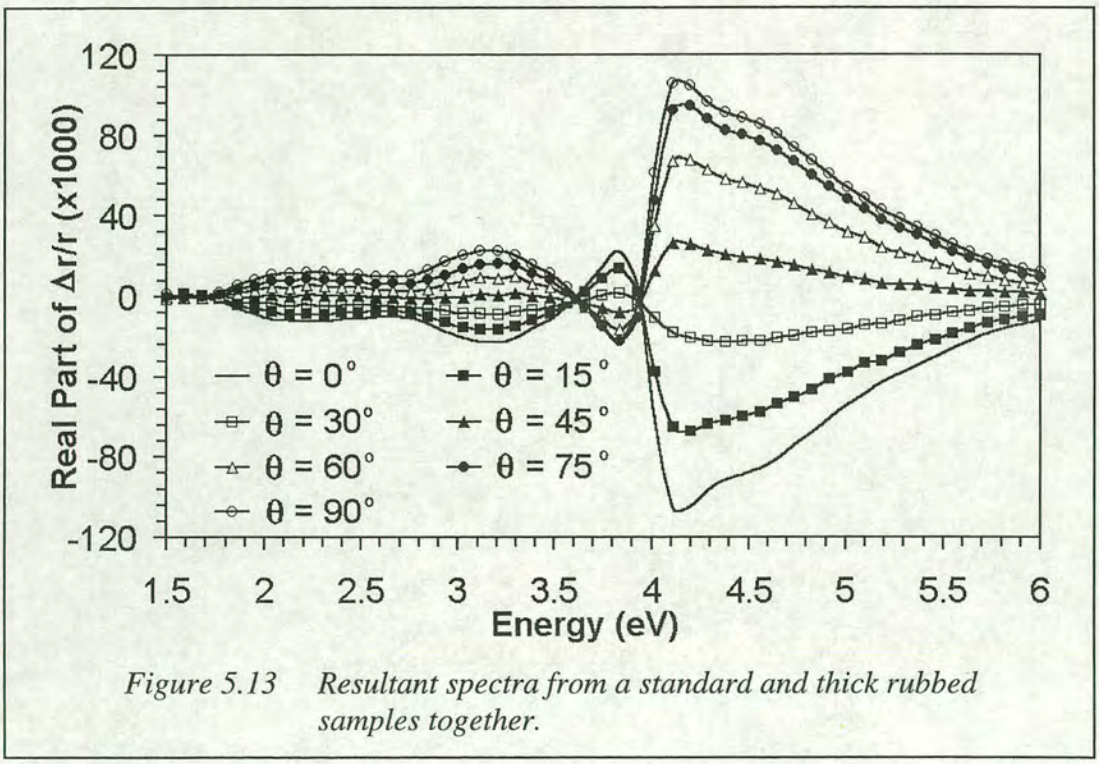

Figure 5.13 Resultant spectra from a standard and thick rubbed samples together.

These two samples are then studied at the same time, with both samples facing the beam, the standard sample in front of the thicker sample and with the rubbing directions at an angle of *45°* to each other. Initially the rubbing direction of the

standard sample is in the same direction as $\theta = 0°$. The resultant RAS is dominated by the signal from the standard sample and little evidence can be seen of the thicker sample behind. However, when the samples are rotated by $45°$ in azimuth, such that the signal from the standard sample is minimised, the signal from the thicker sample is maximised. The resultant spectra for this experiment is shown in *Figure 5.13* and a scaled version, clearly showing the interference from the thicker PI sample, can be seen in *Figure 5.14*.

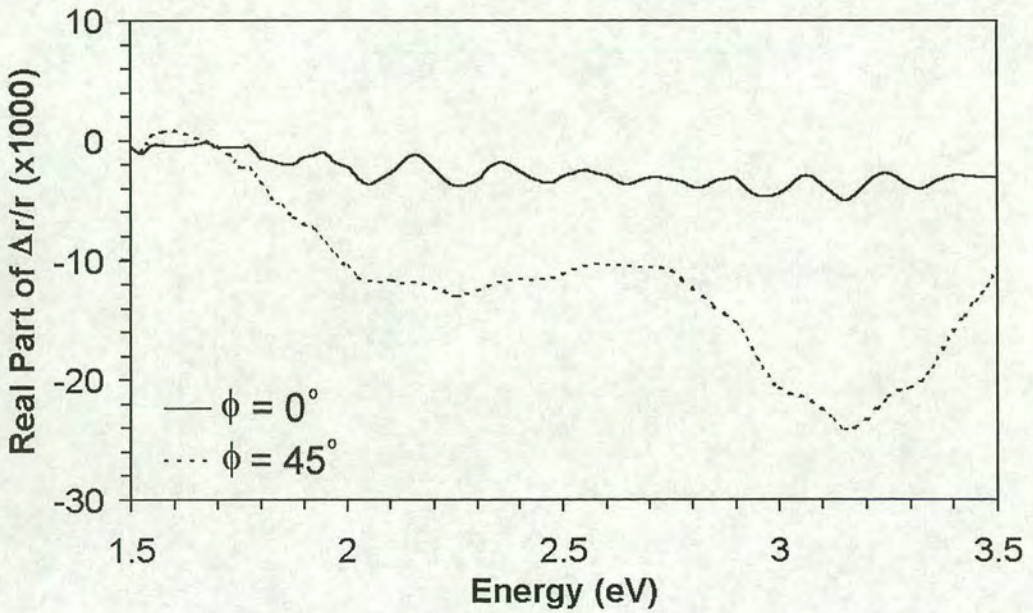

Figure 5.14 *Scaled version of Figure 5.13 highlighting the different interference effects seen by azimuth rotation.*

A good approximation to the spectra shown in *Figure 5.13* and *Figure 5.14* can be obtained by simply adding the data obtained from the front of the standard sample and the rear of the thick sample. Simulation of the absorption effect on the light as it passes through the ITO and glass components of the standard sample is made by using the data relating to the reverse side of the thicker sample. The spectra created as a result of this addition can be seen in *Figure 5.15* and is very similar to the spectra obtained experimentally in shape and in the behaviour as a function of azimuth angle. Again, as the component from the standard sample is minimised, the component from the thicker sample is maximised revealing the characteristic interference pattern. Although the simulated spectra does not have a 45° component

shown, the effect can clearly be seen in the 30° and 60° spectra which are less affected than the 45° spectra would be. This again demonstrates the addition of anisotropies from different sources and that by using ADRAS it may be possible to isolate these different sources of optical anisotropy.

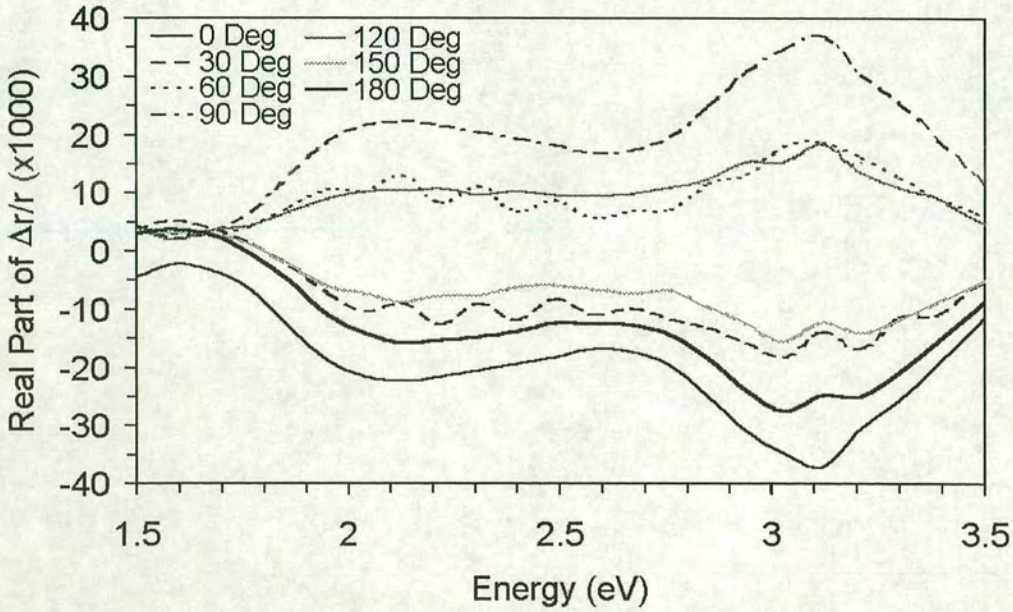

Figure 5.15 *Scaled resultant spectra obtained by adding Figures 5.9 and 5.12 giving a close approximation to Figure 5.14.*

Conclusions

Double rubbing of a polymer film with applications to LC alignment has been investigated using RAS and AFM. An angular dependent extension to RAS, was used to gauge the relative strength of rubbing in two different directions. Other examples used here to demonstrate ADRAS involved sources of optical anisotropy which had distinct spectra as well as distinct angular dependencies. For these cases, it has been shown that ADRAS is capable of isolating each independent source of optical anisotropy providing they have a distinct angular dependence. These measurements suggest ADRAS could allow sources of optical anisotropy such as microgrooves, surface steps, aligned molecules, stress and external fields, with a distinct θ dependence to be experimentally separated.

Recent work by Lorenzo [5.8] have shown that enantioselectivity (selective optical activity) can be induced in a heterogeneous catalytic system by the adsorption of chiral molecules, in this case R, R-Tartaric acid, onto a clean Cu (110) surface. These absorbed molecules have been shown to lie at an angle to the rows of copper atoms. Assuming the adsorbed molecules have a characteristic RAS spectra, by using ADRAS is will be possible to isolate this spectra from the Cu (110) spectra and provide important information about the system. This experiment will be discussed further in *Chapter 7*.

Chapter 6: Nanostructured Copper Surfaces

'Even when laws have been written down, they ought not to remain unaltered'
Aristotle (384BC - 322BC)

Summary

In the work presented in this chapter, RAS is applied to planar and vicinal copper surfaces under various processing techniques. The results from the vicinal surfaces represent another step forward in RAS studies of copper surfaces whilst the results from the plane surface further demonstrates the ability of RAS to monitor processes in real-time: a first for metal surfaces. These studies are used to gain information from 'simple' surfaces which can be applied to polymer alignment layers. The results are discussed in terms of surface state transitions, the temperature dependent diffusion of adatoms and vacancies and the corresponding energy barriers. The preliminary results of the real-time monitoring of Cu (110) surface processing have been published [6.1].

Introduction

Alignment layer fabrication using polymer films is known to have great potential and is one of the leading candidates to supersede the rubbing technique, yet relatively little is understood about the technique. Studying model systems will help to increase this knowledge. Cubic crystals, especially the *fcc* (110) surface, have been extensively studied in the past and are well understood, thus making them an ideal candidate for use with a new experimental technique such as RAS [6.2]. The electronic structure of metal surfaces is of fundamental interest [6.3] and in particular the symmetry of crystal surfaces has been shown to have a great influence on the chemical and physical properties of materials [6.4]. The most commonly studied metals are the noble metals (Cu, Ag and Au) as they have properties, such as resistance to contamination and the relative ease by which single-crystal surfaces can be prepared, which make them very important systems for understanding electronic structures [6.5].

Another virtue of these samples is that the form and structure of the surface can be significantly modified on the atomic and nano-scale by mis-cutting, thermal processing and ion bombardment. For example, the result of mis-cutting a metal crystal by a small angle can be the creation of a vicinal surface which may be considered analogous to the grooved PI surfaces studied in *Chapter 4*; the steps on the surface provide an atomic scale equivalent to the grooves. The introduction of defects (in this case steps) is a more realistic system; all commonly used materials have defects. By understanding the effect of atomic scale defects, advancements in 'bottom up' technology may be more forthcoming. The results of these experiments will therefore be of relevance to alignment layers, surface science and nano-technology in general.

RAS is used here as a non-destructive method to obtain spectroscopic information about the surface properties of these crystals. The technique has been used to study noble metal surfaces in the past but the origin of the spectra obtained from these surfaces is not wholly understood and attempts to simulate the spectra have not been

satisfactory. Suggested explanations for the features observed in the RA spectra from metal surfaces centre around two main mechanisms. Both of these are summarised briefly below.

Surface State Transitions

In bulk solids it is possible to find the allowed energies of the electrons within the crystal by finding the solutions to the three dimensional Schrödinger wave equation. The solutions to the wave equation highlight band gaps in the electronic structure of the solid. At the surface of a three dimensional solid, the previous periodicity is lost and so different solutions to the wave equation are found which results in the existence of energy states within the band gap of the bulk solid. These states are localised in the plane of the surface and are known are as *surface states*.

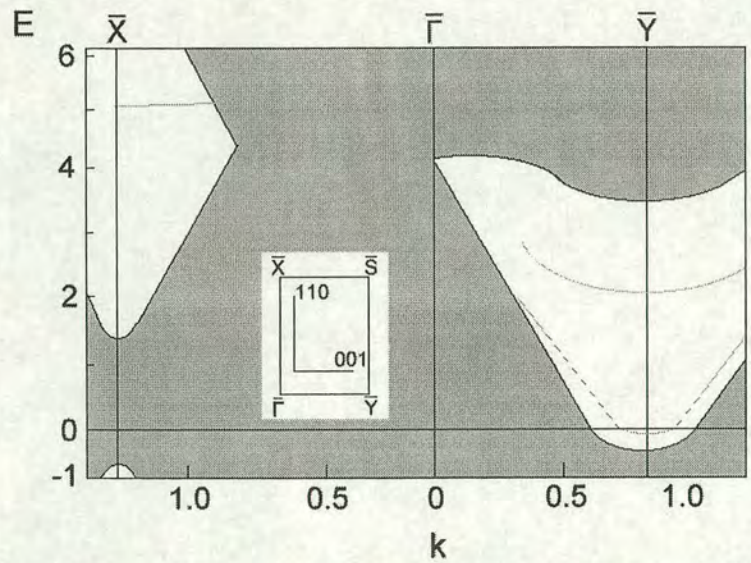

Figure 6.1 *Surface band structure of Cu (110) near the Fermi level. The intrinsic surface states are shown in light grey.*

Studies of the electronic structure of the surface of noble metals using both experimental and theoretical methods have revealed the existence of occupied and unoccupied surface bands within gaps near the Fermi surface at different points on the surface Brillouin zone (SBZ) for the various surfaces [6.6]. *Figure 6.1* shows a diagram indicating the location of these surface states. The main surface being studied here, Cu (110), possess two intrinsic surface bands that lie within the p-s band gap at the $\bar{Y}$ point of the (110) SBZ [6.6]. One of these is an occupied surface

band derived from the p-type band. The other is an unoccupied band derived from the s-type band. By using photoemission and inverse photoemission, it has been possible to identify these occupied and unoccupied states at ~0.4 eV below and ~2.0 eV above the Fermi level [6.5, 6.7-6.9]. The application of dipole selection rules indicates that transitions between these two states can only be induced by [001] polarized light [6.6]. The Cu (110) surface also possesses two unoccupied surface bands within the p-s band gap at the $\overline{X}$ point [6.6] with energies of ~2.0 eV above and ~1.0 eV below the Fermi level. This transition is not thought to contribute to the observed spectra [6.10].

Surface Local Field Effect

The electric fields in and around a surface are influential to the anisotropic reflectivity of a surface. Copper atoms have a shell structure of $1s^2 2s^2 2p^6 3s^2 3p^6 3d^{10} 4s^1$ which means the *3d* shell is complete while the *4s* is incomplete. By assuming the *3d* electrons are localised at lattice sites and the *4s* electrons are delocalised it is possible to model the anisotropy using the *Swiss cheese model* [6.11] depicted in *Figure 6.2*. The full *3d* shells are shown in this figure as ionic cores, represented here as small spheres with associated dipoles, and the space between the spheres is occupied by the delocalised *4s* electrons. Near the surface, the electron distribution is ordered to give an electric field the same as would be obtained if the lattice sites were mirrored.

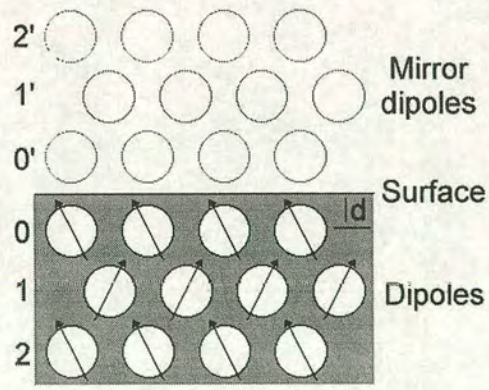

Figure 6.2 *Swiss cheese model.*

The dipole moment of each ionic core can be found by summing all the lattice and mirror dipoles which can then be broken down into orthogonal x and y components. These can then be used to calculate the surface conductivity in the orthogonal directions which is related to the measured RA by *Equation 6.1*, in which σ_x and σ_y is the surface conductivity in the x and y directions. A non-zero RAS is produced since the surface inter-band transitions in the x and y directions are not equal.

$$\frac{\Delta r}{r} = \frac{2(\sigma_x - \sigma_y)}{c\varepsilon_0(\varepsilon - 1)} \qquad \textit{Eq. 6.1}$$

Due to the design of the vacuum chamber used in conjunction with these experiments, it has been possible to obtain RAS measurements from Cu surfaces during processing (i.e. during etching and annealing). This gives the significant advantage of real time *in-situ* RAS measurements, for the first time. Prior to these experiments measurements were only *in-situ* as it would have been necessary to continuously re-orientate the sample being studied between the etching and RAS positions.

Cu (110)

The first measurement of Cu (110) using RAS was reported in 1995 [6.10] in which the now well known Cu (110) spectrum was presented along with a possible explanation for the main features, seen at 2.1 eV and around 4.0 eV. The lower energy peak was attributed to a transition between occupied and unoccupied surface states found at 0.4 eV below the Fermi level and ~2.0 eV above the Fermi level respectively. This explanation is based on predictions made by Jiang *et al.* [6.6] who also described that the indication of dipole selection rules is to only allow a transition between the two surface states when induced by [001] polarised light. Based on these selection rules, a resonance can be expected in the RA spectra. The higher energy features in the Cu (110) spectra consist of a double peak (at 3.9 eV and 4.2 eV). It was speculated that the latter of these results from transitions between the high density of states at the Fermi surface and the image potential state, and intrinsic anisotropy caused by the surface local field effect [6.3, 6.10]. The RA peak at 3.9 eV remains after the sample is exposed to adsorbates whereas the 4.2 eV peak appears unaffected by adsorption and reconstruction [6.11].

More recently, the possible explanation of the Cu (110) spectra was backed up to some extent [6.2, 6.3 & 6.12]. It originally was suggested that the 2.1 eV peak mainly due to surface state transitions. However, a peak at around the same energy can still be seen after the sample has been exposed to air, highly suggestive of another factor being involved. It is proposed the additional contribution to the 2.1 eV peak is the surface local field effect that gives a feature centred around 2.2eV [6.3].

The structure of the Cu (110) surface is shown by the model seen in *Figure 6.3* and clearly shows the surface to be anisotropic. The axes of symmetry of this surface are in the $[1\bar{1}0]$ and [001] directions, corresponding to the directions parallel and perpendicular to the orientation of the close packed row of atoms. In these studies it is desirable to obtain a copper surface as similar to the model surface as possible. To do this, single crystals of mechanically polished Cu (110), aligned using Laue x-ray diffraction to <0.5°, are inserted into the vacuum chamber for processing. By

repeated cycles of ion bombardment and annealing it is possible to obtain the desired periodic clean surface. These cycles typically consist of bombarding the sample, at room temperature, with ~18 μA of 0.5 KeV Ar^+ ions for approximately 30 minutes before annealing the sample at ~840 K for a further 30 minutes. The sample is then left to cool radiatively before the cycle is repeated.

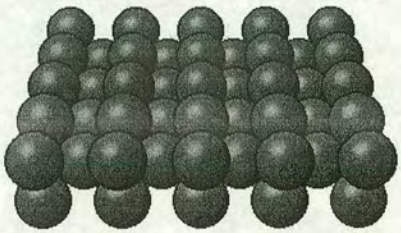

Figure 6.3 Model of the Cu (110) surface.

The periodicity of the sample can be confirmed using LEED, which, if the sample has been prepared successfully, will give a sharp 1x1 pattern. *Figure 6.4* shows the LEED pattern obtained from the Cu (110) surface after repeated bombard/anneal cycles and confirms the surface to be periodic. The LEED image presented here does not give an accurate representation of a sharp LEED pattern as the sample being studied was not optimally ordered at the time of the image being taken. As mentioned in *Chapter 2*, the position and distances between the spots in the LEED pattern are the reciprocal of the position and distances between the atoms on the surface of the crystal. In this LEED pattern the spots form rectangles that have their long axis in the horizontal direction. From this it is possible to determine the orientation of the sample: in this case, the long axis of the crystal, the [001] axis, is in the vertical direction with respect to the LEED apparatus. The cleanliness and periodicity of the surface are confirmed by the comparison of the RA spectrum to previously published spectra. The characteristic spectra reported in these other papers are known to correspond to the clean Cu (110) surface as several other techniques, for example x-ray photoelectron spectroscopy (XPS), Auger electron spectroscopy and STM, have been used in conjunction with RAS to determine the condition of the surface.

Figure 6.5 shows an STM image of the Cu (110) surface under vacuum conditions after it has been cleaned using the procedure described above. This confirms that the sample is clean as the image appears atomically flat and ordered as shown in the model of *Figure 6.3*.

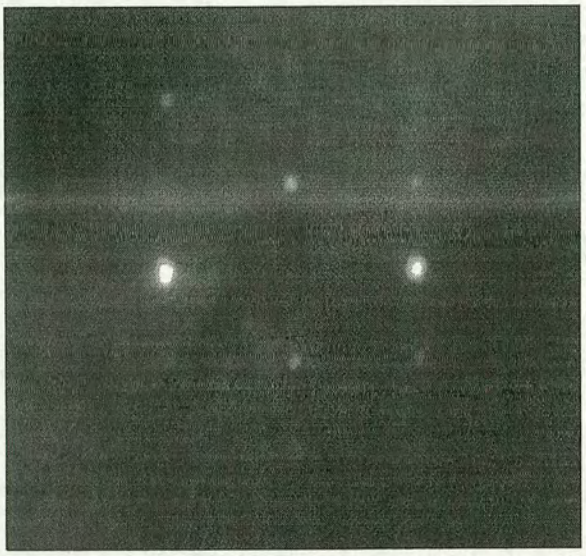

Figure 6.4 *LEED of the clean Cu (110) surface.*

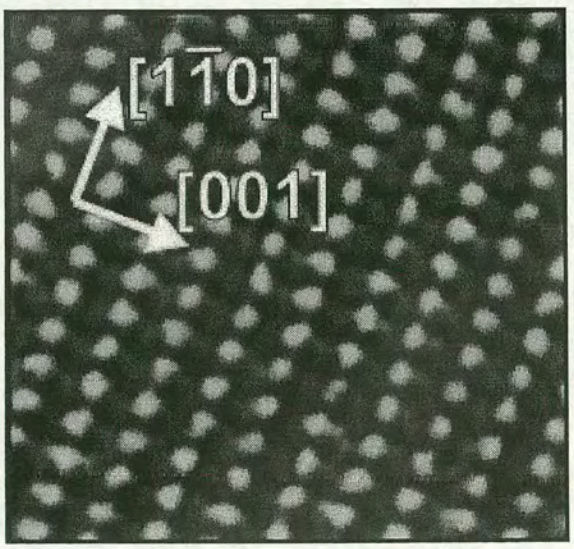

Figure 6.5 *STM of the clean Cu (110) surface. Image from www.dfi.aau.dk/camp.*

Clean Cu (110)

Figure 6.6 shows the RA spectra obtained from the clean Cu (110) crystal mounted within the vacuum chamber at room temperature. In *Equation 2.12*, the quantity measured by RAS was given in terms of the orientation of the spectrometer axes. As the crystal is orientated with the $[1\bar{1}0]$ direction parallel to the x-axis of the spectrometer (the same orientation is used throughout this chapter for each of the crystals studied) the quantity measured by RAS here can be written as,

$$\frac{\Delta r}{r} = 2\frac{r_{[1\bar{1}0]} - r_{[001]}}{r_{[1\bar{1}0]} + r_{[001]}}. \qquad \textit{Eq. 6.2}$$

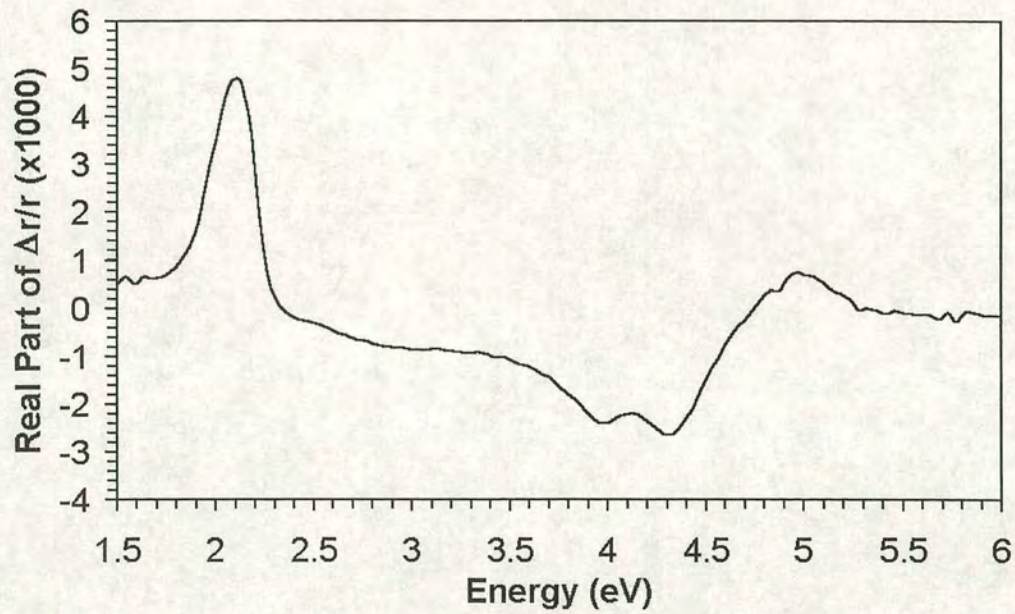

Figure 6.6 *RAS of the clean Cu (110) surface.*

The overall appearance of the spectra, including the amplitude and energy of the features observed, tie in well with previous reports of the surface [6.2, 6.3, 6.10 - 6.12]. This confirms the equipment used here is of a high standard, comparable to spectrometers used elsewhere and that the preparation of the sample surface is good. As described previously, the most significant features of the RA spectra from the Cu (110) surface are the peaks at 2.1 eV and around 4.0 eV. As the clean Cu (110) surface is exposed to contaminants, for example oxygen from ambient conditions, the 2.1 eV peak is reduced in intensity. This reduction is to be expected if the current

theory on the origin of this feature is correct. When the sample is exposed, an oxygen adlayer will form on the copper surface resulting in a reduction of the number of unoccupied surface states. A corresponding reduction in the number of surface state transitions will result in the reduced intensity of the feature [6.3]. Similar to the 2.1 eV feature, one of the double peaks (the 3.9 eV peak) is reduced in intensity because of contamination. This behaviour suggests that the origin of this feature is the same as the origin of the 2.1 eV peak. The contaminated spectrum also has an additional feature at 3.1 eV. The RA spectra taken from a contaminated Cu (110) surface is shown in *Figure 6.7* and appears almost identical to a Cu (110) spectrum under the same conditions reported elsewhere [6.2]. These can be used to gain further information as to the cleanliness of the experimental system and sample surface.

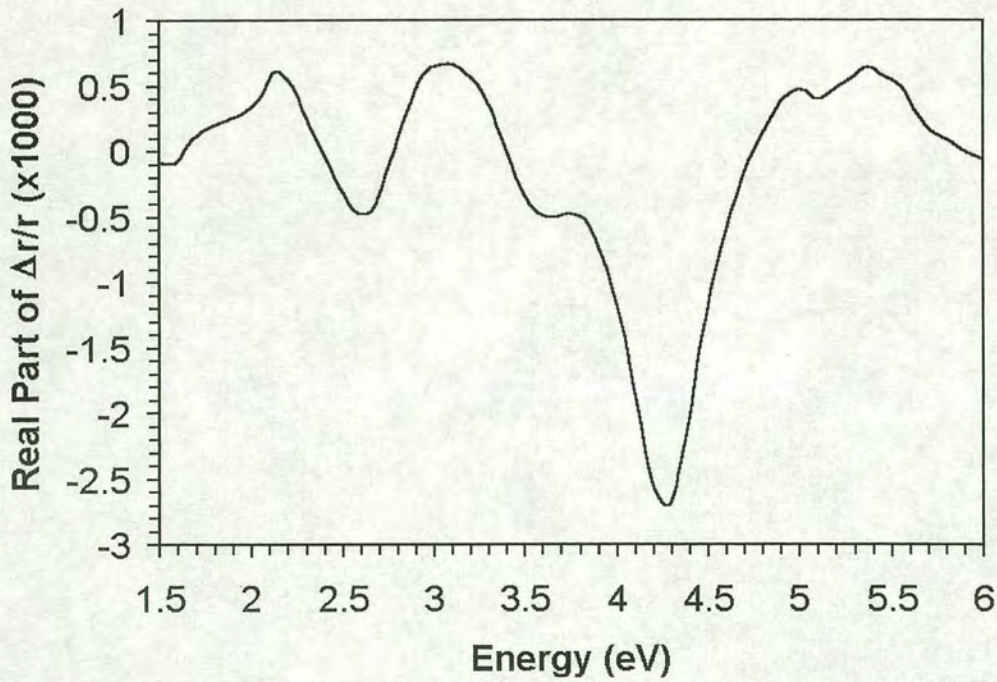

Figure 6.7 RAS of the contaminated Cu (110) surface.

Heating of Cu (110)

The RA spectra from Cu (110) are known to vary as a function of temperature and have been reported along with a possible explanation [6.13]. These experiments were repeated here over a lower temperature range and the results, which are found to be very similar to those previously reported, will be briefly discussed for completeness.

As the temperature of the sample is increased, the 2.1 eV peak is reduced in intensity, broadened and shifted to a slightly higher energy. The reduction in intensity is thought to be a result of thermal depopulation of the occupied surface state due to a gain in thermal energy. This can also be used to explain the broadening effect [6.13]. The shift in energy has been partially attributed to the increasing importance of the contribution of the surface local field effect peak, thought to exist at 2.2 eV, as the 2.1 eV peak reduces in intensity. Another contribution to the shift in energy may be the occupied surface state which photoemission studies have shown to have a linear shift in energy as a function of temperature [6.7]. The 3.9 eV peak is found to be independent of temperature in the range studied here whilst the 4.2 eV peak is reduced in intensity with increasing temperature. The temperature independence of the 3.9 eV peak does not seem consistent with the possible origin of the feature being the same as the 2.1 eV feature as the latter is temperature dependent.

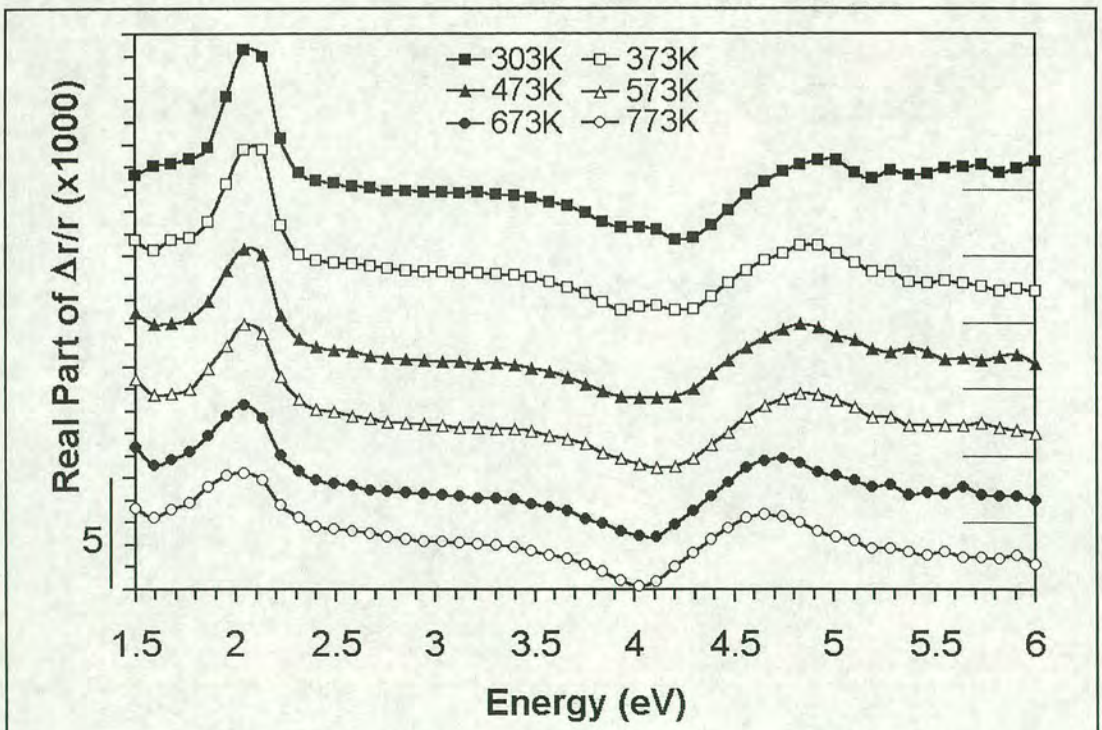

Figure 6.8 *RAS of the clean Cu (110) surface studied as a function of temperature.*

At temperatures outwith the range studied here, from ~730 K to ~1060 K, the RA spectra from the Cu (110) changes further because of irreversible thermal roughening of the surface [6.13]. The roughening transition causes the creation of atomic steps

on the surface as the temperature exceeds a threshold value [6.14]. In the work presented here, the experiments are concentrated on the temperature range of up to 773 K which simplifies the experiments as the roughening transition will not be a consideration.

Cleaning Cycle of Cu (110)

The cleaning cycle used to prepare the Cu samples *in-situ,* involves two distinct processes: ion bombardment (etching or sputtering) and annealing to 'repair' the damage done to the sample by the bombardment process.

Etching

The development of RA spectra from the clean Cu (110) surface at room temperature as the sample is bombarded with 0.5 KeV Ar^+ ions has been studied. This experiment has been reported previously, for example [6.13, 6.15]. The results presented here are similar to those previously presented but are the first to show the effect of etching, as studied by RAS, in real-time. Although the previous reports have been *in-situ* studies, it would have been necessary to re-orientate the sample from the etching position to allow RAS measurements to be taken and so are not real-time measurements. The need to re-orientate the sample results from the limitations of the vacuum chamber used in the past, which have been overcome here by the design discussed in *Chapter 2*.

In *Figure 6.9* the peak at 2.1 eV can be seen to remain unchanged during the bombardment process whilst the features at ~4 eV becomes less pronounced and grows7 into a single peak, orientated in the same direction as the 2.1 eV feature, centred at 4.1 eV. The growth of this feature (at 4.1 eV) is thought to be a result of an increased quantity of vacancies and steps on the surface [6.15]. As a function of time, this feature increases approximately linearly before saturation (after ~30 min under these conditions). It is possible that the intensity of this feature gives a direct measure of the number of vacancies. Each impinging ion is thought to have a sputtering yield of up to 5 vacancies [6.16], therefore the number of vacancies on the surface will be proportional to the incident number of ions. Adatoms are also created as an ion impacts on a surface but as atoms are ejected from the surface (etching is an erosive

technique) the number of adatoms created will be less than the number of vacancies. However, as the surface is eroded, vacancies will be destroyed. The increase in the number of vacancies will saturate when the number of vacancies being created and destroyed, either by erosion of the surface or recombination, is in equilibrium. These results support the view that the peak at ~4 eV is sensitive to atomic disorder at the surface [6.13].

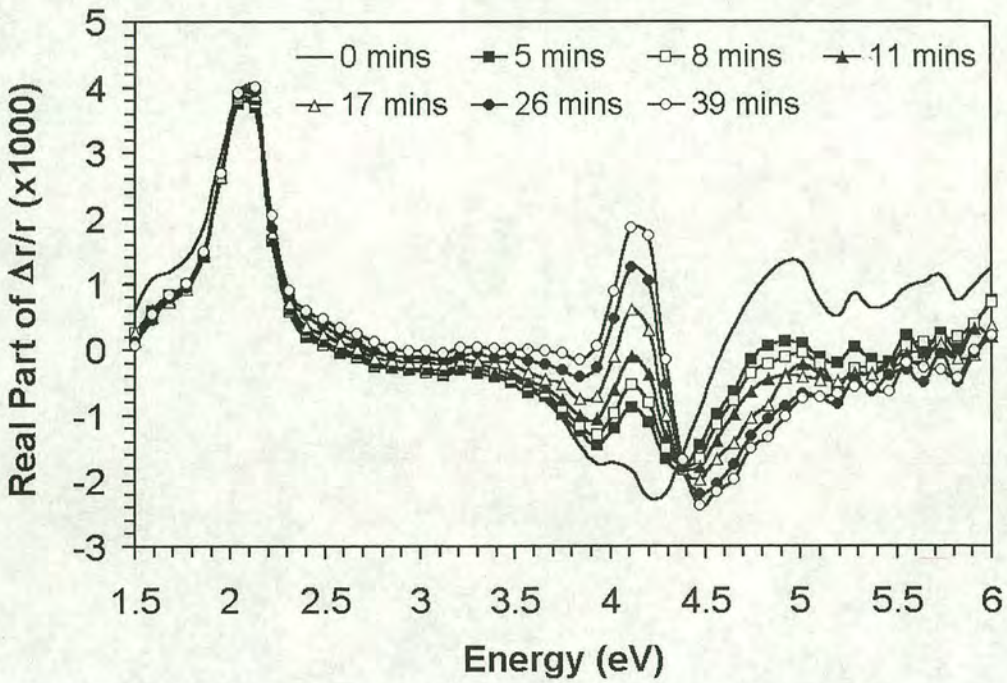

Figure 6.9 *RAS of the clean Cu (110) surface studied during bombardment by 0.5 KeV Ar^+ ions at ~300 K.*

As the etching process proceeds, the RA measured in the UV region decreases. It was demonstrated in *Chapter 4* that this sort of behaviour may be a result of the roughness of the surface increasing. AFM images of the copper surface shortly after etching show some roughness and surface structure. Although these surfaces were imaged *ex situ*, and are likely be oxidised, the observed topography should give a good indication of the underlying copper surface. The AFM image (*Figure 6.10*) shows the surface to be heavily stepped, which appear, in general, to have a preferred orientation. This result is similar to previous findings using *in-situ* STM to study ion bombarded Cu (110) [6.17] and Ag (110) [6.18] surfaces in which the steps are found to lie in $[1\,\bar{1}\,0]$ direction. The orientation and periodicity of the steps observed

on the silver surface were found to be independent of the angle of incidence of the ions [6.18]. In a similar manner, as part of this project, the Cu (110) surface was studied under etching at azimuthal angles of 0°, 45° and 90° at ~300 K. RAS is used to provide indirect information by revealing the symmetrical spectra for 0° and 90° and null spectra for 45°. This implies that the directional properties of the anisotropic topographic surface features, in this case steps, are orientated depending of the crystallographic axes of the sample during etching and do not depend on the angle of incidence of the ions.

Figure 6.10 *Ex-situ AFM of a Cu (110) surface after exposure to 500 eV Ar^+ ions at ~300 K. The image is 2 x 2 μm, has a maximum height of 2.4 nm and step heights of ~1.0 nm.*

The steps seen after etching have been suggested [6.18] to result from competition between the erosion rate cause by the impinging ions and the surface diffusion rate of the adatoms, which is believed to be different for each principle crystallographic axis of the sample. The probability of an adatom moving from one site to another is given by the equation,

$$\rho = Ae^{\frac{E}{kT}} \qquad \text{Eq. 6.3}$$

in which ρ is hopping frequency (s^{-1}), E is the diffusion energy barrier (eV), T is the temperature (K), k is Boltzmanns constant (eVK^{-1}) and A is a constant (s^{-1}) [6.19]. Presented in reference [6.19] is a table of energy barriers for some hopping processes

on a selection of *fcc* surfaces. Although energy barrier values relating to the Cu (110) surface are not specified, these are expected be comparable to the Ag (110) values as the (001) energies for each metal are very similar. In this section, the Cu (110) energy barrier values are assumed to be the same as the Ag (110) values. *Equation 6.3* implies an increased probability of hopping, resulting in a higher rate of diffusion, will occur if the energy barrier is decreased or if the temperature is increased. For the (110) surface, both adatoms and vacancies preferentially move in the $[1\bar{1}0]$ direction. However, the rate at which they diffuse is different. The probability of recombination in the $[1\bar{1}0]$ direction is therefore going to be higher than in the [001] direction. Also, in this temperature range, an adatom which reaches a step may move along its edge. Due to the very high energy barrier, it is highly improbable for adatoms to detach from $[1\bar{1}0]$ steps and so the formation of ripples in this direction should be favoured [6.18].

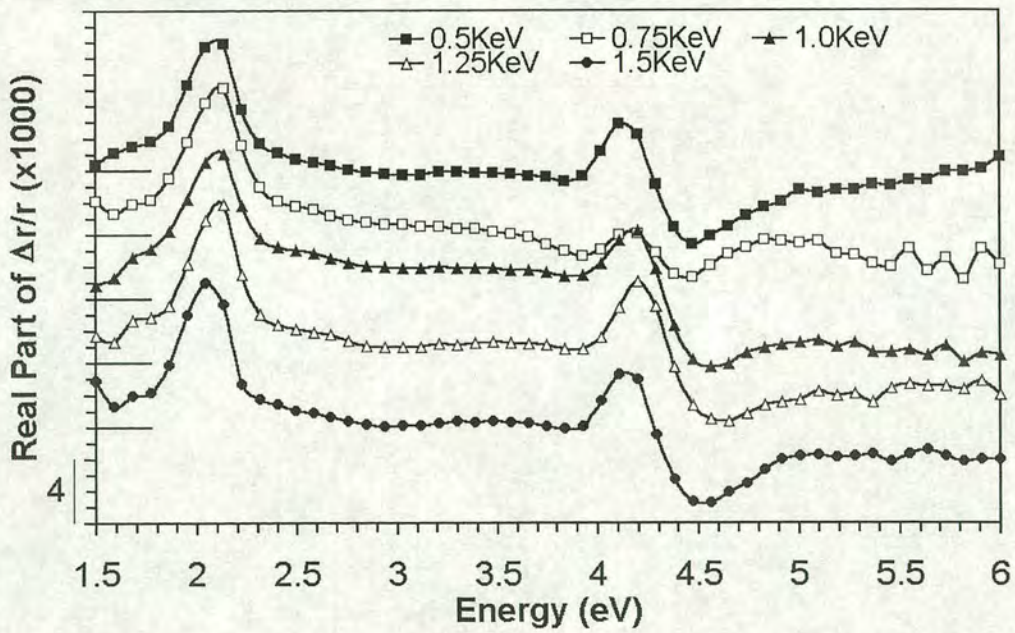

Figure 6.11 *RAS of a clean Cu (110) surface etched over a range of incident ion energies at room temperature.*

It is possible that the size of the features created by the argon ions as they impact into the copper surface is dependent on the energy and mass of the incident ions. The effect on the RA spectra from etching over a range of different ion energies (from 0.5 KeV to 1.5 KeV) is shown in *Figure 6.11*. No significant differences can be seen between the spectra except in the UV region where the intensity decreases with

increasing ion energy. This is not unexpected as the sputtering yield is thought to be approximately constant in the energy range considered here [6.18].

Annealing

After etching it is necessary to anneal the surface to remove the defects and re-obtain surface order and periodicity. By heating the sample, the constituent atoms gain enough energy to increase their mobility and 'repair' the damage done to the surface by recombining with vacancies. RAS data obtained from a Cu (110) surface after the completion of the etching cycle and during the annealing phase can be seen in *Figure 6.12*. The surface appears to 'heal' as the RA spectra gradually changes from the etched RA spectrum into the elevated temperature RA spectrum. As the temperature of the surface is increased, the feature at 2.1 eV decreases in intensity, moves to higher energy and broadens in the same way as in the elevated temperature spectra of *Figure 6.8*. The feature at 4.1 eV is reduced in intensity although it does not return to its initial state because of the influence of the temperature dependent 4.2 eV feature. As the sample cools back to room temperature the RA spectra behave in a similar way to the elevated temperature spectra, shown in *Figure 6.8*, except in reverse.

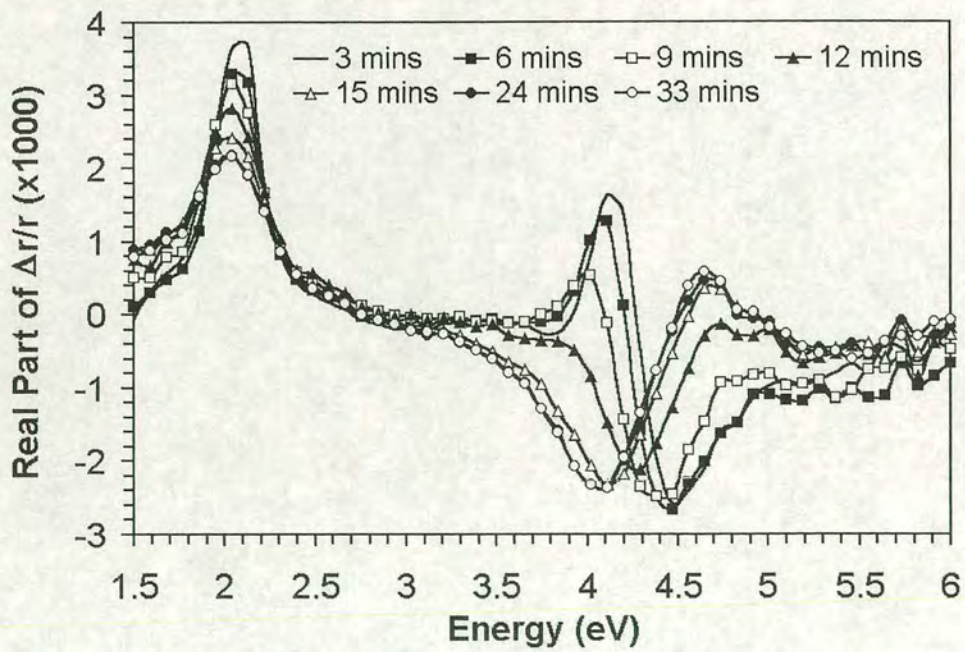

Figure 6.12 RAS of the etched Cu (110) surface studied during annealing to ~840 K.

Elevated Temperature Etching of Cu (110)

The effect of ion bombarding surfaces decreases with increasing temperature. Studies on similar surfaces have shown mobility in both the vacancies and adatoms created during etching. As more energy is given to these 'particles' the probability of them overcoming the energy barrier and moving to new location is increased, resulting in a higher rate of diffusion and an increased rate of recombination. Once enough energy has been given to the substrate, the effect of bombarding the surface cannot be seen at all due to the speed at which the surface heals. In this situation the rate of creation of vacancies is in a steady state with the recombination caused by diffusion. For the Cu (110) surface this appears to be at a temperature of between 600 K and 700 K. Spectra taken from the Cu (110) surface after exposure to 0.5 KeV argon ions for 30 minutes, over a range of substrate temperatures are shown in *Figure 6.13*. In each case the copper surface had been etched, annealed and cooled, to reveal the characteristic clean copper RA spectra directly before being heated to a specific experimental temperature. For comparative purposes, a spectrum from the Cu (110) which has not been etched, taken at 773 K, is plotted in the same figure and is practically identical to its etched counterpart.

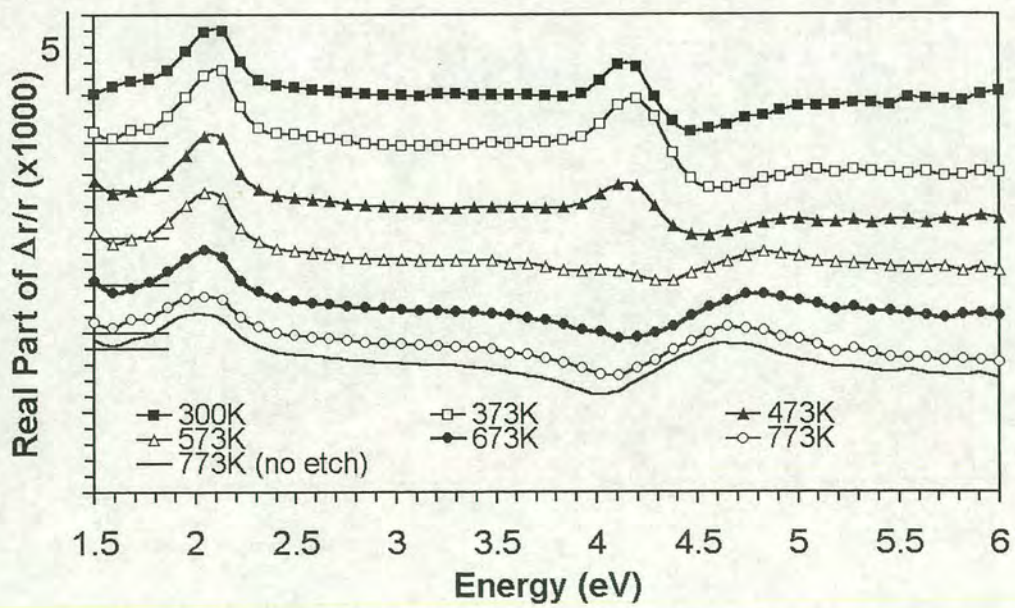

Figure 6.13 *RAS of the Cu (110) surface after ion bombardment at elevated temperature.*

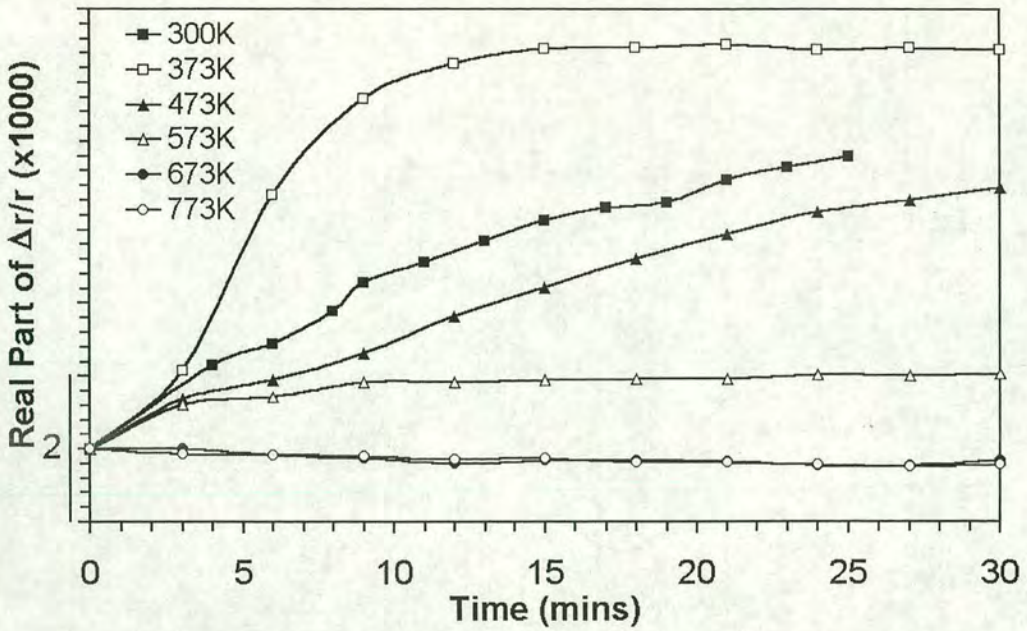

Figure 6.14 *RAS of the 4.2 eV peak from the Cu (110) surface after ion bombardment at elevated temperatures as a function of time.*

The change of intensity of the 4.2 eV peak is initially greatest at a temperature of ~400 K and saturates after ~30 minutes exposure to the incident ions with an ion flux of ~1.3×10^{14} ions cm^{-2} s^{-1}. At temperatures above this value, the rate of increase is lower and the peak does not reach saturation point within the time scale shown. This behaviour is expected for the higher temperatures but not for the lower temperatures. As the temperature of the etched surface is increased, the rate of diffusion of the vacancies and adatoms increases proportionally (*from Equation 6.3*), increasing the rate of recombination and so decreasing the effect of etching. Conversely, at lower temperatures the rate of diffusion is low and so the time required by the surface to reorder is long compared to the time scale of ion bombardment. This is consistent with data presented in *Figure 6.14* and implies that the 4.2 eV feature will reach saturation point for etching at higher temperature but the time scale *will* be increasing large. The question of why the effect of etching is maximised at around 400 K still remains. Costantini *at al.* [6.19] have shown that the surface roughness of Ag (001) caused by ion bombardment is temperature dependent and also peaks at ~400 K. As with the etching results presented in this thesis, this is somewhat surprising as an increased rate of surface diffusion should result in a smoother surface. The explanation of this phenomenon presented by Costantini *et al.* should apply for the

elevated temperature etching results of this thesis and is as follows. For temperatures below ~440 K, the adatoms produced from ion impacts cannot balance the effect of etching because there are less of them (etching is an erosive technique and so atoms will be ejected from the surface upon impact). Additionally, because of the high energy required to remove an adatom from a step, they predominantly contribute to structure formation of straight edges. For the lowest energies, the rate of diffusion is very low and so adatoms and vacancies remain localised to the impact site which results in a layer by layer diffusion. Erosion to an underlying layer only begins when the upper layer is nearly all gone giving little roughness. With a slight increase in energy, the adatoms and vacancies are not so localised and so deeper etched features result. At temperatures greater than ~440 K, adatom evaporation occurs more readily from the steps leading to an increased adatom density on the terraces that eventually exceeds the number of vacancies.

Conclusions on RAS of Cu (110)

The results of these experiments match those already reported by several other groups examining the same surface. This gives a very good indication that our RA spectrometer is working well and is capable of producing high quality results. A new feature of these results, in particular for the etching experiments, is that the RAS results are taken in real-time, allowing continuous processing and monitoring. This compares favourably to previous studies which could only monitor intermittently.

A significant new result presented here regarding the Cu (110) crystal is found whilst etching the crystal at elevated temperatures. As the temperature of the substrate is increased the effect of etching visible by RAS and therefore the damage done to the surface of the sample diminishes. This continues until ~570 K after which damage induced by ion impacts are no longer visible. It has also been found that the effect of etching is maximised at a temperature of ~400 K. A likely explanation for both these observations stem from the energy barriers of the created adatoms and the subsequent adatom terrace densities and rates of diffusion. This means that below a certain temperature the movement of the adatoms is restricted to step edges. Above this temperature the probability of an adatom being on a terrace is increased allowing a greater number of vacancies to be annihilated.

Vicinal Cu (110)

The next step in these studies is to increase the complexity of the substrate surface by the introduction of vicinal copper surfaces. Although there have been some previous reports of RAS studies of vicinal surfaces [6.20, 6.21], there has been none on copper. The surface used is Cu (771) which is a Cu (110) surface mis-cut by an angle of 5.8° ± 0.5°. This should result in a stepped surface with (110) terraces 4 atoms wide (~12.6 Å) and (111) step edge facets of height ~1.8 Å. The steps run parallel to the close packed row of atoms in the $[1\bar{1}0]$ direction. A model of the surface can be seen in *Figure 6.15.*

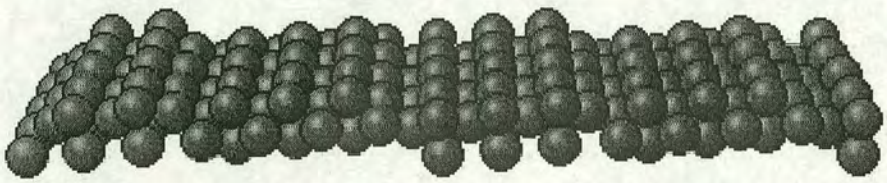

Figure 6.15 Model of the Cu (771) surface.

Following the success of the surface preparation for the Cu (110) crystal, exactly the same procedure is used again for the Cu (771) surface. LEED of the surface taken at room temperature after the sample has been etched and annealed shows the expected contribution from the (110) surface plus additional spots from the steps. The sharpness of the features confirms the surface is ordered. This is in contrast to an etched Cu (110) surface which is also known to have steps in the $[1\bar{1}0]$ direction but does not produce a sharp LEED pattern. The difference between the two is that the Cu (771) surface is ordered and periodic whilst the etched Cu (110) surface is not. *Figure 6.16* shows the Cu (771) LEED pattern and confirms the steps to be along $[1\bar{1}0]$. The unit cell of the stepped surface appears about four times wider indicating monatomic height steps and a terrace width of ~12 Å.

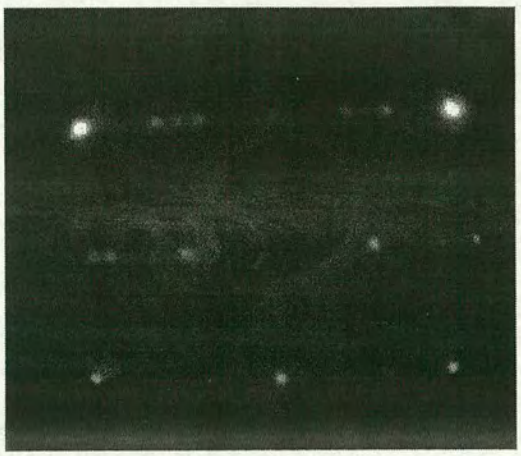

Figure 6.16 LEED of the Cu (771) surface.

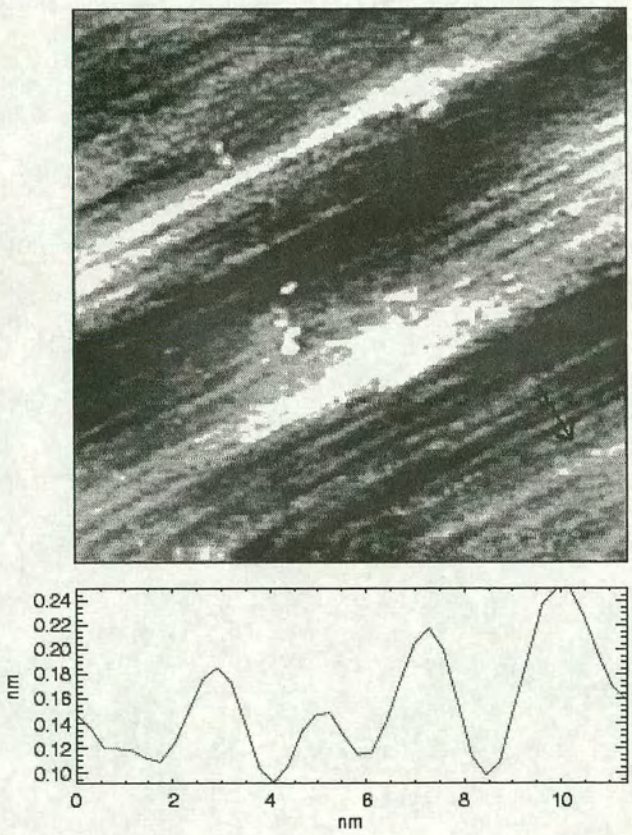

Figure 6.17 STM of the clean Cu (771) surface showing monatomic height steps in the [1$\bar{1}$0] direction. The cross-section corresponds to the black arrow in bottom right-hand of the image which is ~100 x 100 nm and was provided by Dr Martin of the University of Liverpool.

STM of the surface corroborate with the LEED images in showing the surface has the expected structure. The STM images of the Cu (771) surface, *Figure 6.17*, shows a number of steps, all in the $[1\bar{1}0]$ direction. The surface has a range of terrace widths from ~7 Å to ~3 nm giving a strong indication the surface is not optimally ordered. However, several regions can be found, for the example the region indicated by the arrow in *Figure 6.17*, in which a clear (771) surface is found.

Clean Cu (771)

RAS of the clean Cu (771) surface is shown in *Figure 6.18* and is plotted alongside the RAS of the clean Cu (110) for comparison. Unexpectedly, there appears to be no anisotropic contribution from the steps. While the overall shapes of the two spectra are similar, there are two main distinct differences; the 2.1 eV feature and the 3.9 eV feature are reduced in intensity. These features have previously been assigned to surface state transitions at $\bar{Y}$. A recent study by Heskett *et al.* [6.22] of the intensity of the 2 eV $\bar{Y}$ unoccupied surface state of the Cu (110) surface provides a significant insight into a connection between the electronic surface state and the surface order. By using inverse photoemission spectroscopy and Monte Carlo simulations Heskett *et al.* have shown that an area of 12 x 12 atoms (~25 x 25 Å for the Cu (110) surface) is needed to support the 2 eV Cu (110) $\bar{Y}$ surface state. In a similar manner, the STM measurements of Li *et al.* [6.23] have shown the existence of surface states, by measuring $^{dI}/_{dV}$, on a silver surface. These surface states are prominent on large terraces but diminished on smaller areas to the extent that they are not observed in an area of 10 x 15 Å. The STM image of the Cu (771) surface, *Figure 6.17*, shows that for well ordered areas of the surface, the terraces have a width ~12 Å. Using the argument of Heskett *et al.*, this area is not large enough to support the 2 eV surface state. The number of transitions and hence the contribution to the 2.1 eV RAS feature will be reduced. As the STM of the Cu (771) surface shows a range of terrace widths of up to ~3 nm, a limited number of surface states will be supported and will give rise to the measured intensity of the 2.1 eV RAS feature.

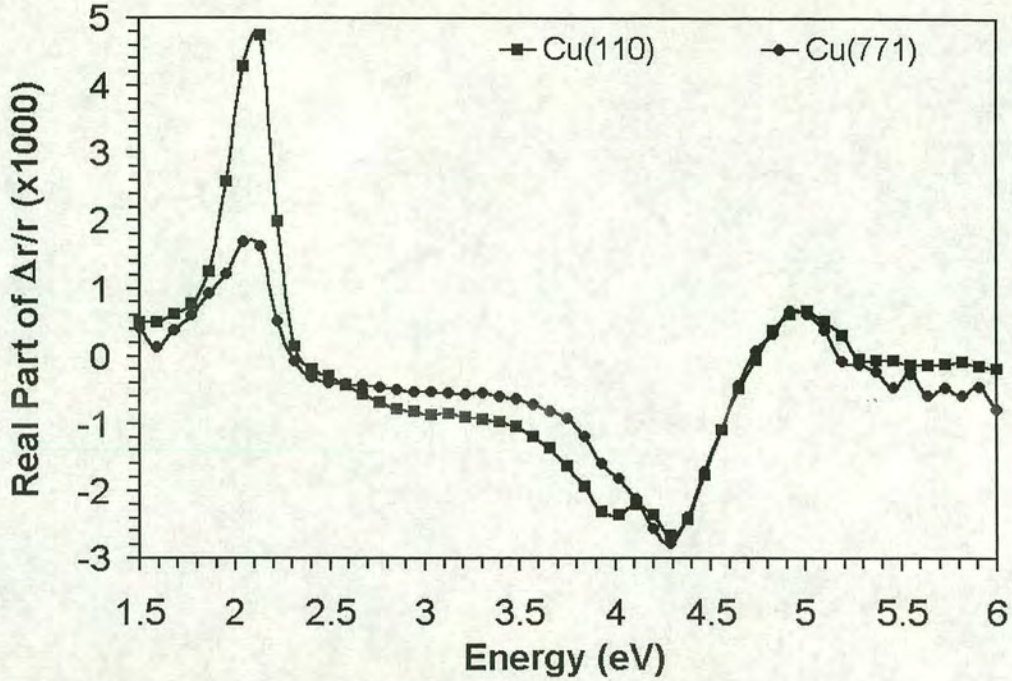

Figure 6.18 RAS of the clean Cu (771) and Cu (110) surfaces.

Heating of Cu (771)

The temperature dependence of the Cu (771) surface, shown in *Figure 6.19*, is essentially the same as the temperature dependence of the Cu (110) surface, shown in *Figure 6.8*. The difference between the two sets of spectra relate to the differences seen in the clean RA spectra from these samples: the reduction of the features at 2.1 eV and 3.9 eV. These differences are highlighted in *Figure 6.20* which shows a comparison of the spectra obtained from the two samples at a temperature of 773 K. A new difference between these spectra not apparent in the room temperature measurements is the intensity in the UV region of the spectra. The UV component of the RAS is significantly higher from the Cu (771) surface. As with the Cu (110) surface, the 2.1 eV peak from the Cu (771) is reduced in intensity, broadened and shifted to a slightly higher energy as the temperature is increased for the same reasons as previously discussed. Similarly, there is no evidence of change from the 3.9 eV peak whilst the position of the 4.2 eV peak is reduced in energy to 4.1 eV in the same way as was observed from this feature from the Cu (110) surface.

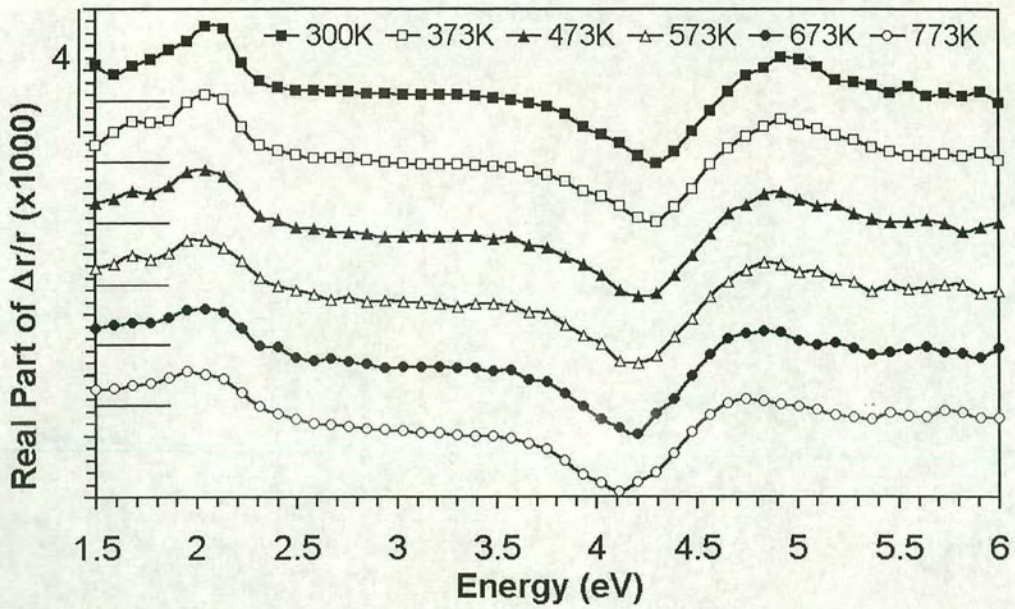

Figure 6.19 *RAS of the clean Cu (771) surface as a function of temperature.*

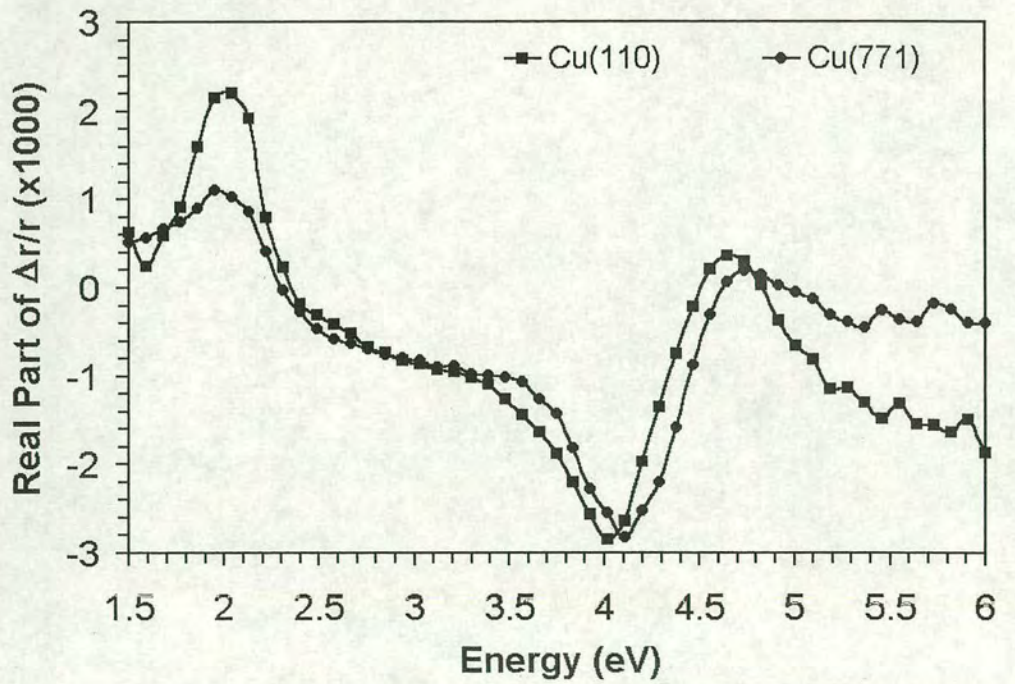

Figure 6.20 *Comparison of the clean RAS spectra for the Cu (110) and Cu (771) surfaces taken at 773K.*

Cleaning Cycle of Cu (771)

Etching

The change in the RA from the Cu (771) surface shown in *Figure 6.21* is essentially the same as the equivalent results from the Cu (110) surface. A comparison of the saturated RA spectra can be seen in *Figure 6.22*, this again highlights the differences in the two surfaces at 2.1 eV and 3.9 eV. In this case the effect of a having a reduced 3.9 eV peak is to give a broader peak at 4.1 eV which reveals more of the true shape of the 4.1 eV feature. In the RA from the Cu (110) surface, the shape of this feature has been disguised by the contribution at 3.9 eV. One significant difference between the Cu (110) and Cu (771) surfaces under etching is the rate at which they reach saturation point. The Cu (110) surface typically takes ~30 minutes whilst the Cu (771) surface typically takes ~20 minutes. The latter is quicker to saturate as etching has a greater effect on this surface. The reason for this difference relates to the number of steps on the surface. As discussed in the Cu (110) section, the adatoms created from ion impacts, which can annihilate vacancies, cannot be easily detached from steps. On the Cu (771) surface there are many more steps, if the surface is optimally ordered then there should a step every 4 atoms. This means there is a lower density of adatoms on the terraces as more are attached to the steps, therefore the relative number of vacancies is higher.

Annealing

As with the Cu (110) surface, the 4.1 eV feature is reduced in intensity and the RA changes from the characteristic etched RA to the characteristic elevated temperature RA (*Figure 6.23).* However, the rate at which the Cu (771) surface heals is higher. As the Cu (771) surface has more steps, there is a larger supply of adatoms that can repair the surface. Overcoming the adatom detachment energy barrier is not thought to be a concern in this situation, at a temperature of ~800 K, there is an abundant supply of energy.

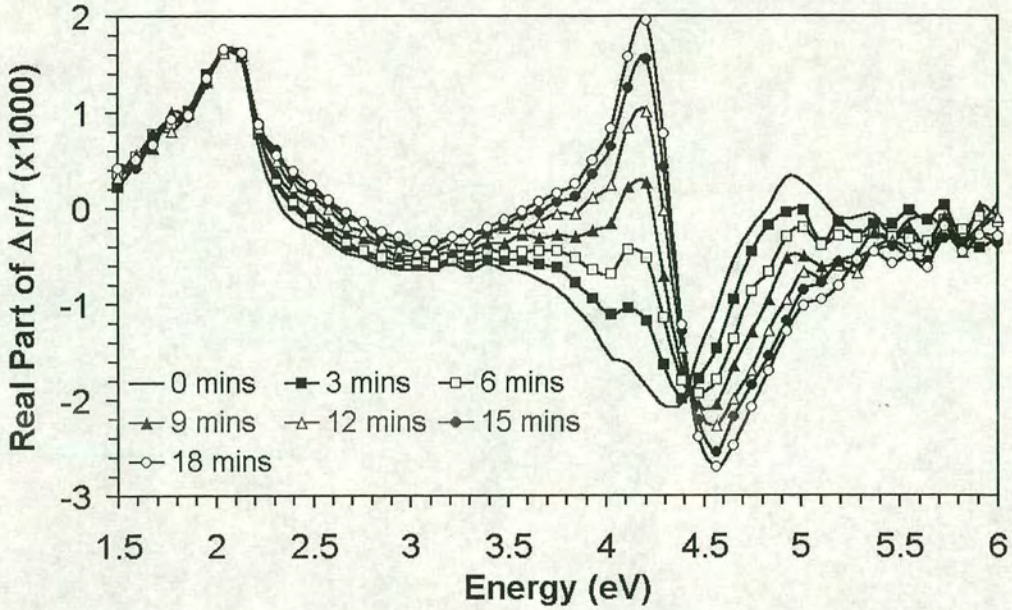

Figure 6.21 *RAS of the clean Cu (771) surface studied during bombardment by 0.5 KeV Ar^+ ions at ~300 K.*

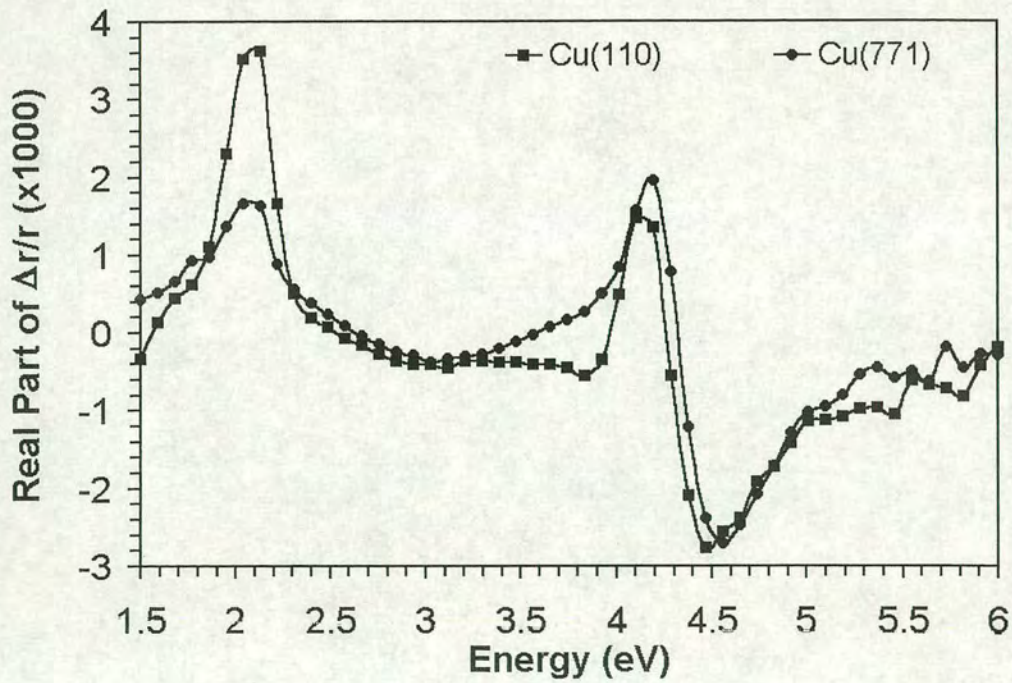

Figure 6.22 *Comparison of the clean RA spectra for the Cu (110) and Cu (771) surfaces taken after 30 minutes Ar^+ ion bombardment at ~300 K*

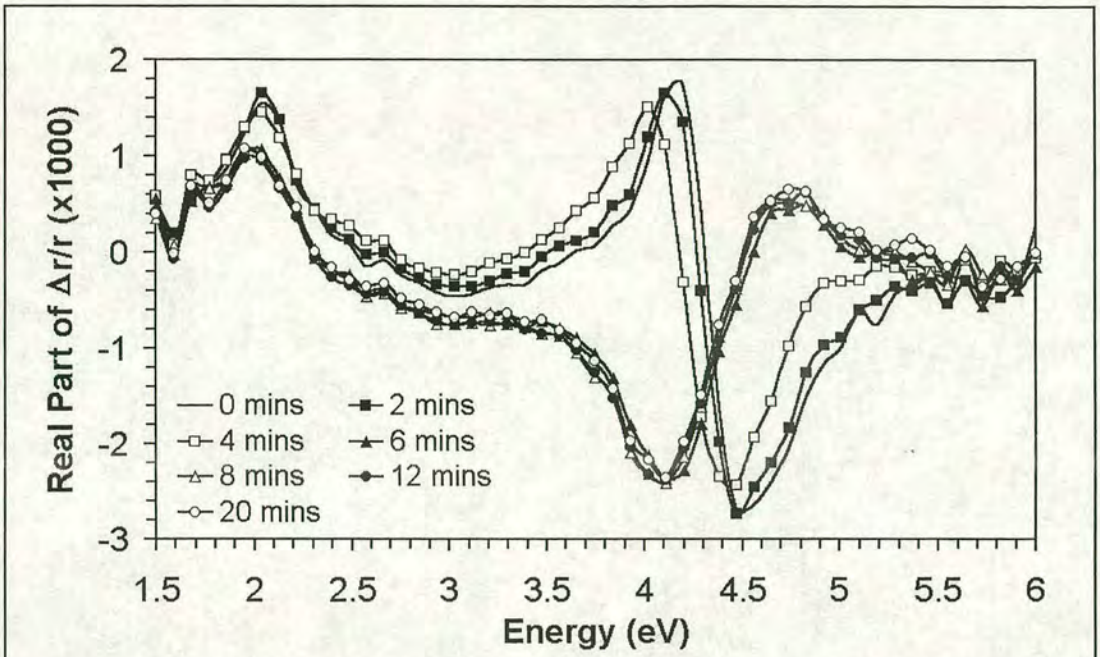

Figure 6.23 *RAS of the etched Cu (771) surface studied during annealing to ~840 K.*

Etching at Elevated Temperatures

Similar to Cu (110), the RA measured from the Cu (771) surface shows that the damage done to the surface by etching decreases with increasing temperature (*Figure 6.23*). This will happen for the same reasons. A comparison of the two figures which show the RA spectra after etching over a range for temperatures for the two surfaces, *Figures 6.13* and *6.24*, do not clearly show which surface is affected more during by temperature during etching. Neither surface shows evidence of damage to the surface whilst being etched at temperatures greater than ~673 K although the Cu (771) surface has more evidence of etching at a temperature of 573 K. This implies that the Cu (771) is slightly less effective in counteracting the effect of etching than the Cu (110) surface. The energy barrier and diffusion rate discussion of before is still valid for this situation. As the Cu (771) surface has more steps than the Cu (110) surface, a greater number of adatoms are attached to steps instead of being on the terraces, where they can recombine with vacancies. In order to obtain the situation for the Cu (771) where the number of adatoms is in equilibrium with the number of vacancies, it is necessary to apply more energy than is required for the Cu (110) surface. The difference in energy required will be proportional to the difference in number of steps and is a direct result of the adatom detachment energy barrier being very high.

The values of these energy barriers are given in *Table 1* of reference [6.19] and show that the detachment energy for the (110) surface is different by a factor of two in the [001] and [1 $\bar{1}$ 0] directions, the higher energy barrier being in the [1 $\bar{1}$ 0] direction. It would be possible to confirm the validity of the previous argument by studying a surface which had steps running in the [001] direction. If this theory is correct, it should require a significantly lower energy to detach adatoms from the steps onto the terraces. A higher density of adatoms on the terraces would counter act the effect of etching at a lower temperature. Preliminary studies of the Cu (1090) surface as it is etched at various temperatures (*Figure 6.25*) show no evidence of damage to the surface at temperatures above ~473 K, ~100 K lower than the equivalent result from both Cu (110) and Cu (771) surfaces.

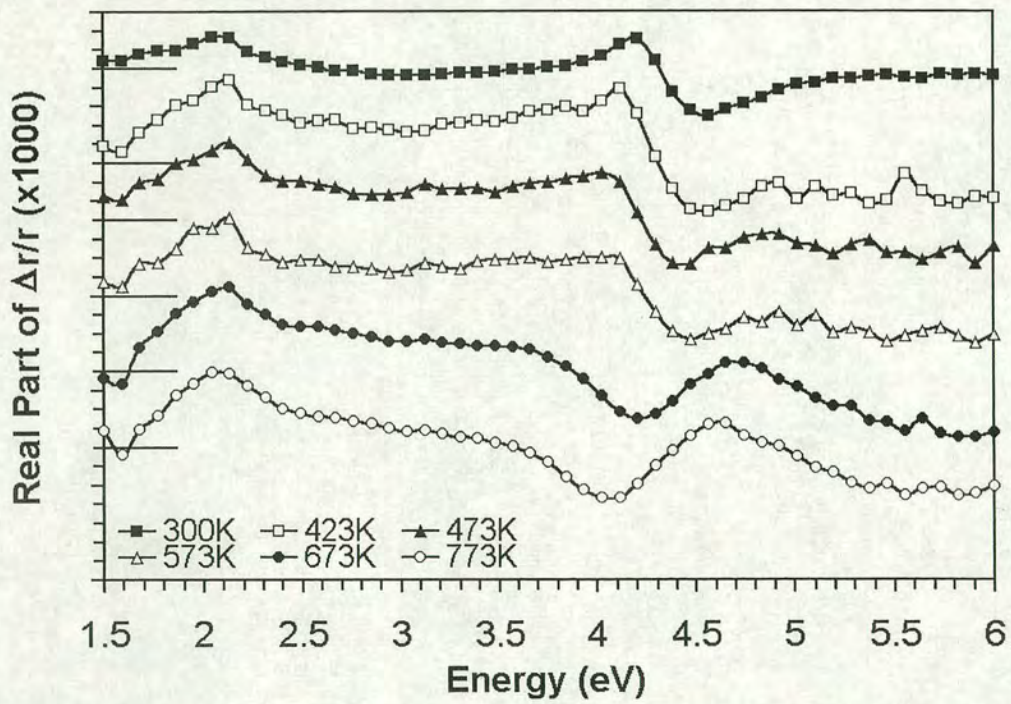

Figure 6.24 *RAS of the Cu (771) surface after ion bombardment at elevated temperatures.*

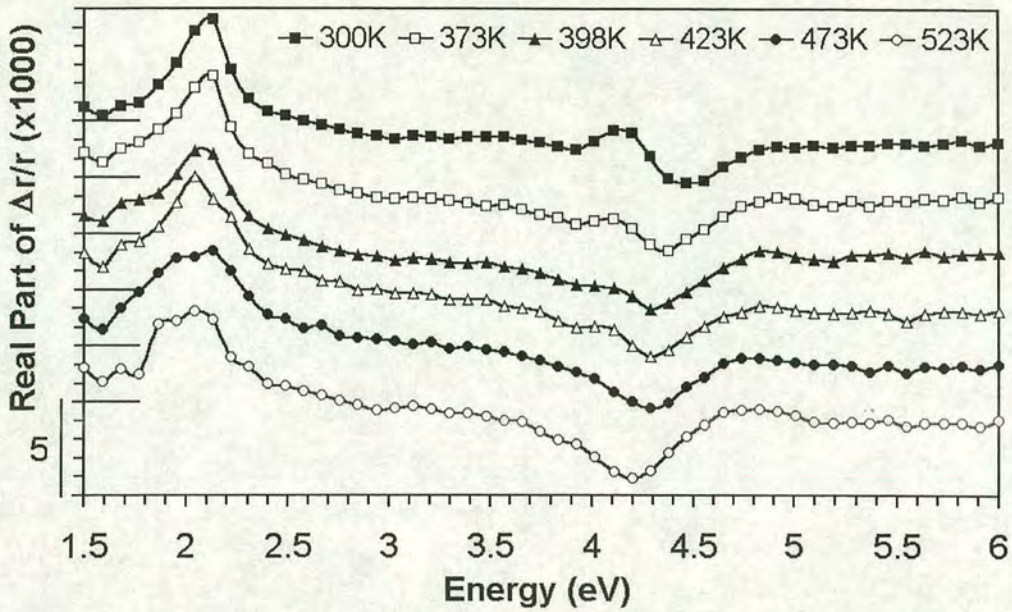

Figure 6.25 RAS of the Cu (1090) surface after ion bombardment at elevated temperatures.

Conclusions on RAS of Cu (771)

The RA measured from the Cu (771) surface are essentially the same as the Cu (110) spectra. No additional contribution to the measured RA from the steps has been observed. The main difference between the spectra is the reduced intensity of the 2.1 eV and 3.9 eV features which is thought to be caused by the narrow terraces that are not able to support surface states. As the Cu (771) surface is etched, damage is caused to the surface at a faster rate because a higher number of adatoms are attached to the steps, reducing the rate of annihilation of vacancies. When the Cu (771) surface is etched at elevated temperatures, it is suspected that evidence of etching will be seen at a higher temperature than for the Cu (110) surface. This is because of the higher number of steps which would need a greater amount of energy to allow the same number of adatoms to be detached from the steps onto the terraces as compared to the Cu (110) surface. Confirmation of this has been found from preliminary studies of the Cu (1090) surface which has steps running in the [001] direction and requires a significantly lower amount of energy to detach adatoms from steps.

Conclusions

The study of metal crystals is used to gain 'background' information which is relevant to many applications. In particular, the morphology of polymer alignment layers can be simulated by ion bombarding and mis-cutting these crystals. The form and effect of these surfaces on the RAS is studied over a range of processes.

The Cu (110) and Cu (771) surfaces have been studied for the first time by RAS in real-time during etch and anneal cycles. The final result of these processes are clean ordered surfaces. A comparison of the RA measured from each surface indicates differences only in the features at 2.1 eV and 3.9 eV, both of which have been attributed to surface state transitions. The intensity of these features are reduced in the RA from the Cu (771) surface. STM images of this surface show narrow terraces which may not be able to support surface states and would therefore result in a reduced intensity at 2.1 eV and 3.9 eV.

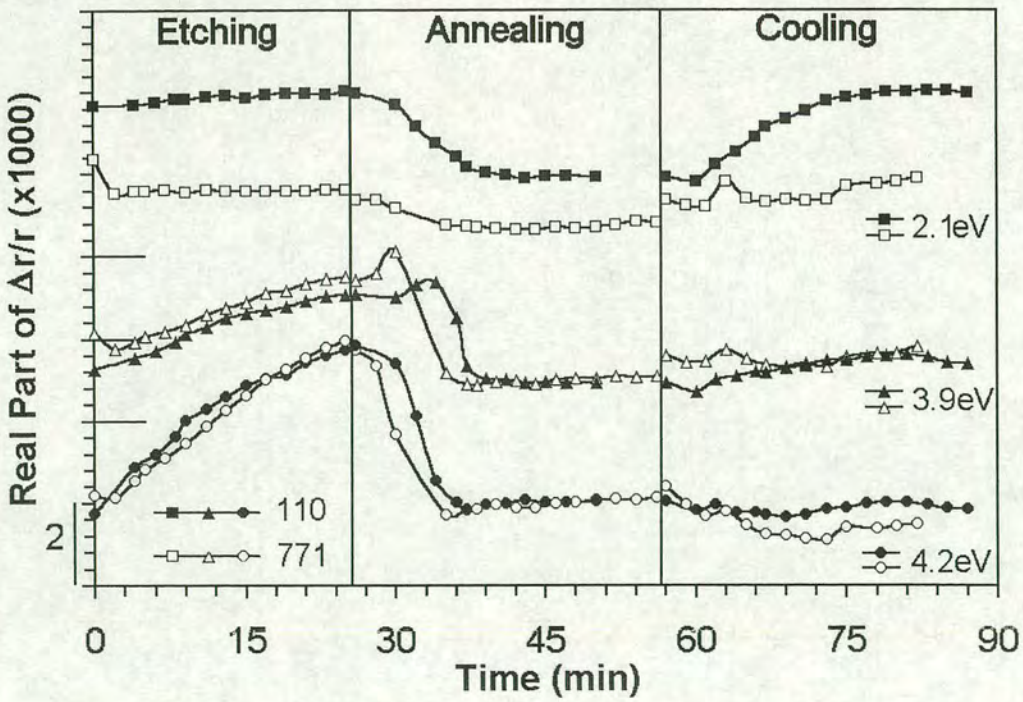

Figure 6.26 *Time dependence of the main RAS features from the Cu(110) and Cu(771) surfaces studied during etching, annealing and cooling.*

Differences in the behaviour of the main features of these surfaces during the bombard/anneal cycle are illustrated in *Figure 6.26* as a function of time. Although not clearly shown in this figure because saturation is not reached, the effect of etching is slightly different for the two surfaces. As the Cu (771) has a greater number of steps, more energy is required to get a specific number of adatoms from the steps onto the terraces as compared to the Cu (110) surface. When the amount of energy is limited, for example in this situation when etching occurs at room temperature, the Cu (771) surface is less capable of overcoming the effect of etching than the Cu (110) surface as it has less adatoms available. Although during etching at lower temperatures the steps are detrimental to the effect of adatoms annihilating vacancies, the opposite is true at high temperature when the surface is annealed. *Figure 6.26* shows the Cu (771) surface to heal quicker as there are more adatoms available due to the higher number of steps.

Studies of the effect of etching at elevated temperatures shows several things. For the Cu (110) surface, the effect of etching maximised at ~400 K and cannot be seen above ~573 K although it is thought the exact value may be somewhat lower. Similarly for the Cu (771), the effect of etching cannot be seen above ~573 K. A possible explanation has been given in terms of the rate of diffusion of adatoms and the adatom step detachment energy barrier. Further evidence in favour of the explanation is found in preliminary results of RA measurements from the Cu (1090) surface.

Etching these copper surfaces at room temperature has shown grooves to form in a direction that is dependent on the orientation of the crystallographic axes of the substrate and independent of the azimuthal orientation of the substrate with respect to the incident ions. This occurs because of the rates of diffusion of the vacancies and adatoms created during the etching. The diffusion process is highly temperature dependent and so at high temperatures, when the rate of diffusion is high, the effect of etching is reduced. This is different from what was found in *Chapter 4* when the polymer surfaces where bombarded in a similar manner. In the case of the polymers, because of the random orientation of the polymer chains, there is no intrinsic surface

Chapter 7: ADRAS of Organic Molecules

'If I have ever made any valuable discoveries, it has been owing more to patient attention, than to any other talent'
Sir Isaac Newton (1642 - 1727)

Summary

A potentially important experiment, based around the previously introduced ADRAS technique, is discussed in this chapter. The example considered involves adsorbing chiral molecules on to the Cu (110) surface. Information contained at different azimuthal angles of this sample, which has distinct orientation directions for the substrate surface and adsorbate, could be exploited using ADRAS and have applications to enantiomeric catalysis and biomolecular adsorption.

Introduction to RAS Studies of Adsorbates on Copper

Following the studies of copper surfaces in the previous chapter, the next logical step to replicate a liquid crystal/alignment layer system is to deposit organic molecules on the Cu (110) surface. This could then be followed by deposition of organic molecules onto the more complex stepped and kinked Cu (110) surfaces. These systems will be studied using the same techniques as before: RAS and LEED. Although, ideally a combination of RAS and LEED in addition to other surface sensitive techniques, for example STM, would be used.

Previous RAS studies of adsorbates on copper systems include the original experiments used to determine the origin of the characteristic 'clean' copper spectrum. This spectrum, which was introduced in *Chapter 6*, has its main features located around 2.1eV and 4.0eV. When the clean surface is covered with an adsorbate, the peak at 2.1eV is reduced in intensity. This behaviour has been attributed to the reduced number of unoccupied surface states on the copper surface as a result of the adsorbate [7.1] and ties in well with previous work on the same sample which used inverse photoemission to observe these states at around the same energy [7.2]. The existence of these unoccupied surface states had been predicted in an earlier report by Jiang *et al.* [7.3]. Many experiments have been reported in which the adsorption of contaminants onto the copper surface have caused a change in the measured anisotropy [7.1, 7.4, 7.5] but it was Frederick *et al.* [7.6] who first reported the observation of RA originating from the intermolecular transitions within an organic compound adsorbed onto the copper surface. By studying an adsorbate that has electronic transitions within the spectral range of the RA spectrometer, Frederick *at al.* showed it was possible to use RAS to obtain information about the orientation of the adsorbate. A very recent report by Martin *et al.* further demonstrates the use of RAS in this manner and is used in conjunction with IR measurements and STM to study the orientation of adsorbed molecules on the copper surface [7.7]. The ability to obtain this type of information is only going to become more important in the future as the applications and uses of molecular and sub-nanometer scale engineering are increased.

Introduction to Chirotechnology [7.8]

The basis of chirotechnology dates back to around the 19th century to Jean–Baptiste Biot and his once student Louis Pasteur. Pasteur introduced the concept that the optical activity of certain organic substances occurs as a direct consequence of its molecular structure. To be precise, he observed that the optical activity of a molecule varied with its 'chirality'. A molecule is said to be 'chiral' when it is not superimposable on its mirror image and 'enantiomers' are the isomers of a molecule that are chiral. An example of a chiral molecule is tartaric acid, the isomers of which can be seen in *Figure 7.1*. The nomenclature of these isomers is based around the tetrahedral bonding of the carbon atoms. By prioritising the groups bound to the carbon atom it is possible to denote that atom as being either left (denoted *S*, from the Latin *'sinister'*) or right handed (denoted *R*, from the Latin *'rectus'*) [7.9]. In his work, Pasteur studied solutions of tartaric acid and found the polarisation of the light to be rotated clockwise or not at all. He later found that a solution of a single enantiomer would rotate the polarisation of light in one particular direction whilst a solution containing a equal mixture of opposite enantiomers (a racemic solution) would not, as the effect of the isomers cancelled each other out. In the case of tartaric acid, the *R, R* enantiomer rotates the polarisation clockwise whilst the *S, S* enantiomer rotates its anti-clockwise.

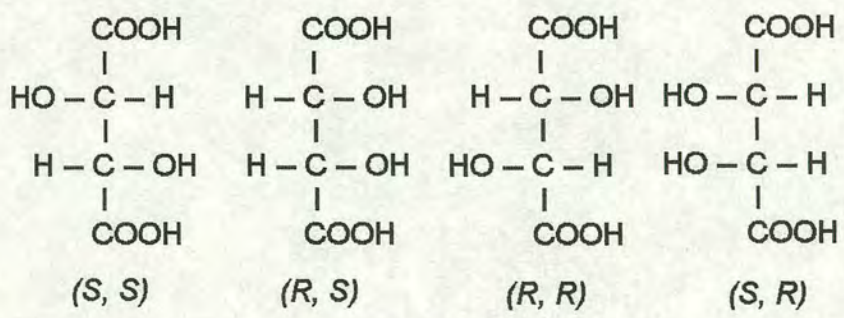

Figure 7.1 The isomers of the chiral molecule tartaric acid.

The applications of chirotechnology are wide and range from the preparation of new drugs to catalysis. An example of the importance of chirality is the synthesis of the thalidomide compound [7.10]. The left handed compound can be used as a tranquilliser whilst the right handed version can cause severe disabilities.

ADRAS and Chirotechnology

The initial examples of ADRAS given in *Chapter 5* were devised to demonstrate that RA spectra do not always obey the predicted $\cos(2\theta)$ dependency and can change shape as well as amplitude as the azimuthal angle is varied. It was shown that the information contained within the ADRAS curves could enable independent sources of optical anisotropy to be separated, provided they have a distinct angular dependence. The previous examples used well-understood samples and confirmation of the separation of the optical anisotropy was obtained by switching off each particular contribution in turn. Obviously, the control of the sources of optical anisotropy is not always possible and so ADRAS could prove invaluable when characterising unknown samples for the first time. Here, the potential of ADRAS is emphasised further when it is applied to the chiral modification of surfaces for enantio-selective catalysis and biomolecular adsorption studies.

Ortega Lorenzo *et al.* [7.11, 7.12] have shown *R,R*-tartaric acid can adsorb onto the Cu (110) surface to form extended hydrogen bonded domains with a distinct orientation to the axes of underlying substrate. As the equivalent counter-rotation domain cannot be formed the surface is rendered chiral. This has also been shown to be the case for the same chiral molecule on a Ni (110) surface [7.13]. Through experiment and simulations, ADRAS will be shown to be well suited to detecting chiral surface modification. It is expected that the RA spectra taken at $\theta=0°$ will show a typical copper spectra containing a strong component from the adsorbate. At an angle corresponding to the axis of symmetry of the adsorbate, the RA spectra should again be comprised of information from both the sources of optical anisotropy. However, when the system is studied at an azimuth angle of $\theta=45°$, the amplitude of the RA from the copper surface will be zero, therefore the total measured RA will be solely due to the adsorbate. From the work of Ortega Lorenzo *et al.* it is known that the axis of symmetry of the adsorbate is at ~20° to the [001] direction of the substrate and so the RA spectra measured at $\theta=45°$ will be a scaled by the known factor of $\cos(2\theta)$.

Experiment

These experiments were carried out using a Cu (110) single crystal which was prepared in the same manner as described in *Chapter 6*. Due to the detrimental effect of the high number of experiments conducted using this crystal in the past, some of which have involved the deposition of large quantities of organic compounds at high temperatures, the surface has become contaminated. Numerous cleaning cycles have been unsuccessful in resolving this issue. A remedy for this would be to have the sample re-cut and re-polished, however, the sample is still suitable for use to obtain preliminary measurements and information regarding the deposition procedure and the suitability of *R, R*-tartaric acid to this experiment. The 'clean' spectrum obtained from this crystal can be seen in *Figure 7.2* and appears slightly different to those found previously and those which have been reported numerous times before (see *Chapter 6* for details). Certain similarities can be seen between this spectrum and the spectrum from a copper sample exposed to ambient conditions [7.15], in particular the reduced size of the 2.1 eV feature. The figure shown has not had the window correction function applied to it, explaining why the spectrum appears to slope upwards at higher energies. The remaining features can be considered to be 'real' as they vary with $\cos(2\theta)$, as expected.

The deposition of the tartaric acid molecules onto the copper surface was carried out using the sublimation apparatus described in the *Vacuum Chamber* section of *Chapter 3* and using the same method as Ortega Lorenzo *et al.* [7.11]. That is, firstly out-gassing the tartaric acid at 300 K and then heating the acid to 370 K whilst exposing the copper surface. During the sublimation, the pressure in the main chamber was ~1×10^{-9} mbar. As the copper was exposed to the sublimated acid, RA spectra were taken, the change in the RA of the copper spectra can be seen in *Figure 7.3*. As expected the 2.1 eV feature is diminished, corresponding to a reduction in unoccupied surface states as the acid bonds to the surface. Additionally, the centre of the contaminant peak appears to shift to a lower energy, as does the feature normally observed around 4.0 eV. These results strongly indicate the suitability of this acid for these experiments as the RA from the molecule falls within the energy range of the spectrometer.

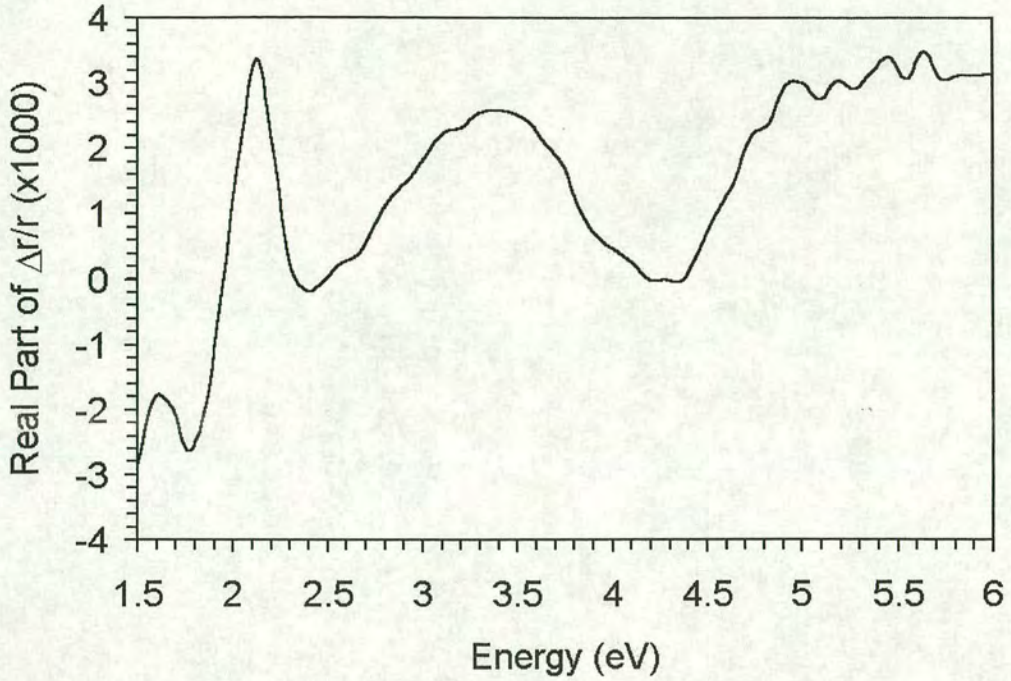

Figure 7.2 The contaminated Cu (110) spectra.

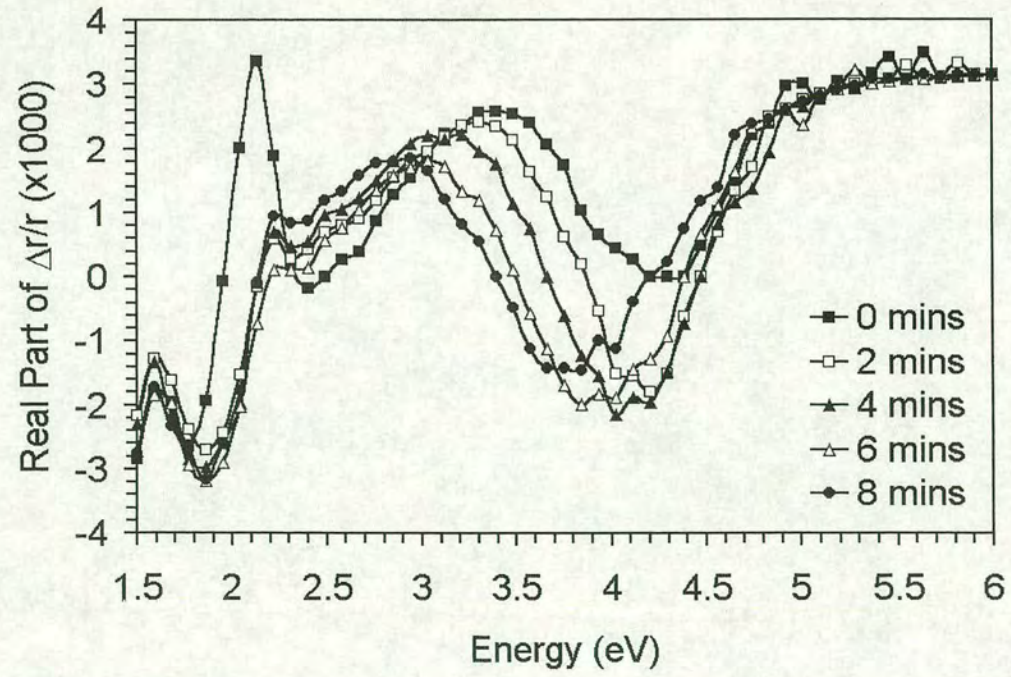

Figure 7.3 Development of the Cu (110) RA spectra upon adsorption of R, R - tartaric acid.

Upon completion of the sublimation, the copper surface was examined using LEED. Initially the LEED pattern appeared very similar to that reported by

Ortega Lorenzo *et al.* suggesting the molecules had been successfully adsorbed on the surface in an ordered fashion. This pattern disappeared within seconds to leave only a poor 1x1 pattern, which is attributed to the substrate surface being covered with a disordered over-layer. It is not surprising that these preliminary experiments should suffer from such problems as Ortega Lorenzo *et al.* have shown the ordering of the surface to be very sensitive to temperature and time [7.11]. From this it can be concluded that in principle the sublimation was a success but needs more time spent on it to perfect the technique and to obtain the necessary orientated adsorbate layer. An ADRAS study of the surface at this stage revealed only the $\cos(2\theta)$ azimuth dependence associated with the copper surface which is to be expected as a disordered overlayer would have no net effect on the angular variation.

Simulations

Simulations of this experiment were made using the Berreman 4x4 matrix method. The RA spectra from the clean Cu (110) surface is simulated by allowing the adsorption of [001] polarised light at 2.1 eV which reproduces one of the main features of this surface. The simulated Cu (110) RA spectra at azimuth angles of 0°, 30°, 45° and 75° can be seen in *Figure 7.4* and follow the $\cos(2\theta)$ angular dependency. The adsorption of the tartaric acid is modelled by reducing the intensity of the 2.1 eV feature and by adding a new adsorption at 3.5 eV. The feature was added at this energy to correspond with the peak seen in *Figure 7.3*. Although the orientation of the adsorbed molecule is known to lie at about 20° to the substrate [7.13, 7.14], for simplicity in the analysis of these simulations it is set to lie at 30° to the [001] direction. The RA from the molecule due to optical absorption will be maximised at this angle. The simulated Cu (110) spectra with the tartaric acid adsorbed on the surface is shown for azimuthal angles of 0°, 30°, 45° and 75°, in *Figure 7.5*. At 45°, the amplitude of the intrinsic optical anisotropy from the copper surface is reduced to zero and so does not contribute to the spectra. The signal seen arises only from the adsorbed over-layer. Similarly at 75° the spectra is solely from the copper surface as the optical anisotropy from the adsorbate has been extinguished. Comparison of the simulated adsorbate spectra at 0° and 30° show that standard RAS measurements would be very similar and would not reveal much new

information. In fact as the sample is rotated from 0° to 30°, the 2.1 eV will only be reduced in intensity by a factor of ½ and so the standard RAS measurements may not be able to determine if either one were chiral in nature. However, adsorption geometry permitting, a racemic mixture of enatiomeric domains would leave the optical axis parallel to the mirror planes of the Cu (110) surface, giving a null RAS spectra for 45°.

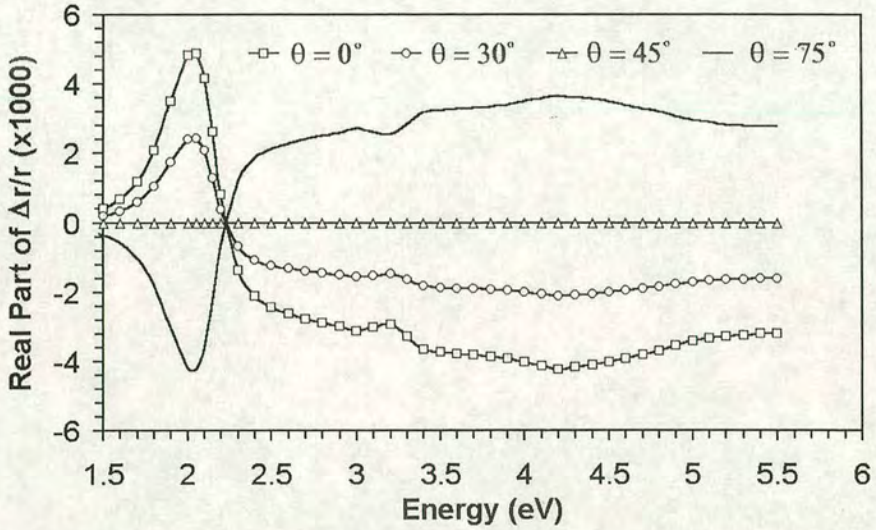

Figure 7.4 *Simulation of the clean Cu (110) surface at azimuthal angles of 0°, 30°, 45° and 75°.*

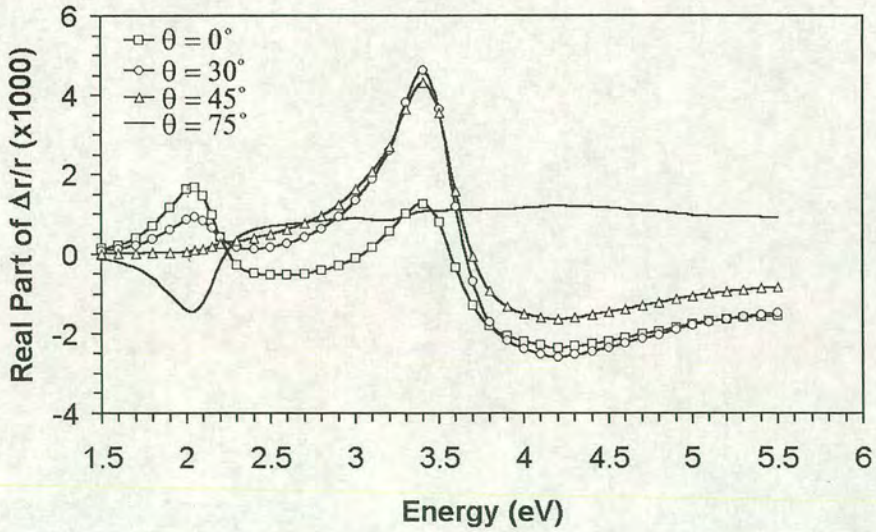

Figure 7.5 *Simulation of the Cu (110) covered with a chiral absorbate aligned at 30° to the substrate axis shown at azimuthal angles of 0°, 30°,45° and 75°.*

Conclusions

The extension to the normal RAS technique, ADRAS, which was introduced in *Chapter 5* has been shown here to have potential applications in the currently topical areas of research of enatiomeric catalysis and biomolecular adsorption. The example considered here involves the adsorption of the chiral tartaric acid on the clean Cu (110) surface. It is known that the optical axis of the adsorbate lies at an angle of approximately 20° to the optical axes of the substrate surface. By using ADRAS it is possible to extinguish the contribution of the copper surface to the measured RA and hence isolate the RA from the adsorbate molecule. ADRAS also has the potential to determine the quantity of enantiomers in a racemic mixture.

In this chapter, details of the experiment have been given although it has not been successfully completed due to time constraints. Simulations of the adsorbate covered copper surface at a selection of azimuthal angles have been presented here to demonstrate the principle of the experiment.

Chapter 8: Dodecane on Graphite

'The difference between the impossible and the possible lies in determination'
Tommy Lasorda (1927-)

Summary

For the optimal alignment of LCs, a uniform surface is desirable. *Chapter 4* has shown that as polymers are put onto a substrate some structures can be formed during drying. In this chapter the evaporation of dodecane from a highly ordered pyrolytic graphite surface is used as a model system to study the drying and dewetting processes which are found to result in the formation of interesting nanoscale patterns and stable structures. The formation of these structures has been studied as a function of evaporation time and temperature using AFM. At low times and temperatures, the general structure of the patterns on the surface is comprised of sub-micron sized holes and nano-scale ripple structures. As the time and temperature are increased, these holes grow into micron sized features by two independent mechanisms. The work presented in this chapter has been submitted for publication [8.1].

Introduction to Dewetting and Drying

The drying and dewetting of liquid films is of fundamental importance to many aspects of science and technology. Numerous applications exist, for example the drying of ink and the lubrication of engines, which would benefit from a deeper understanding of the mechanisms involved in dewetting and drying. Obtaining this knowledge could lead to the prevention of dewetting and allow the formation of homogeneous films. For the particular application of liquid crystal alignment layers, as studied in this thesis, a greater understanding of these processes could allow more uniform polymer films to be created. This could result in the removal of the drying structures seen in *Figures 4.7 & 4.11 (a)* and create better alignment layers. It may also be possible to apply the same principles to the LC molecules themselves. Although drying and dewetting has been the subject of much interest over the last decade, a complete understanding is yet to be achieved. In this work the patterning of an n-alkane on a highly ordered pyrolytic graphite (HOPG) surface after drying and dewetting is studied using AFM.

Previous work on these samples has shown the existence of stable nanoscale features on the 'dry' surface. The dimensions of these are thought to be dependent on the size of the alkane used [8.2, 8.3]. The stability of these structures is believed to arise from the absorption of the bottom n-alkane layer onto the graphite surface with the carbon chain lying parallel to the surface and with the hydrogen atoms fitting into the centres of the hexagonal structures formed by the carbon atoms of the graphite [8.4].

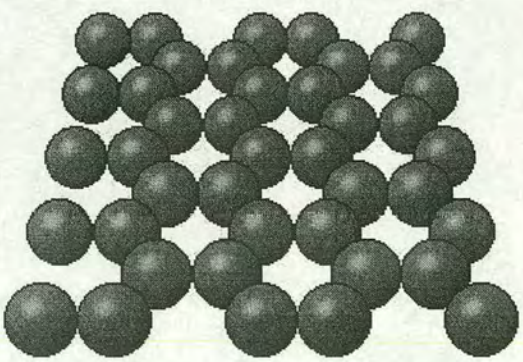

Figure 8.1 Model of the HOPG surface.

A model of the HOPG surface can be seen in *Figure 8.1.* With alkanes, and other materials, for example liquid crystals, this absorption can result in domains of aligned molecules [8.5]. At the meeting point of such domains, the formation of a characteristic chevron type structure is possible and has been observed for some materials by scanning tunnelling microscopy [8.6, 8.7].

Dewetting has been characterised by three stages, the rupture of a film leading to the formation of holes, the growth of the holes resulting in a network structure and then the aggregation of material causing the formation of structures on the substrate [8.8]. Two mechanisms of triggering film rupture have been suggested [8.9], nucleation and spinodal dewetting. The first results from the nucleation of dry spots which are caused by defects/heterogeneities or thermal activation [8.10]. The second is due to long range molecular forces [8.11] destabilising the film and causing the exponential growth of surface fluctuations resulting in spontaneous rupture of the film.

Drying can be described as the removal of liquid material from a surface due to evaporation. The rate at which material is removed from the surface is dependent on factors such as surface area, temperature, humidity and air velocity and can be described on the basis of kinetic theory. If the liquid film wets the solid surface (this corresponds to this experimental system) there are two options: (i) the thickness of the film remains uniform and decreases continuously until total evaporation has occurred; or (ii) for a specific range of film thickness uniform films are unstable and rupture into two different phases (thickness'). This second scenario is more complicated and it has been shown to produce pattern formation in case of water on cleaved mica [8.12].

Sample Preparation

Samples are created by depositing 1.0 μl of $C_{12}H_{26}$ onto the freshly cleaved HOPG surface at ~295 K. The samples are then heated to temperatures of 373 K, 398 K, 423 K, 448 K or 473 K for either 5, 10 or 15 minutes before being left to cool naturally to ~295 K for imaging. Temperature measurements are taken from the surface of the sample heater; it is therefore expected that the temperature of the surface of the HOPG will be lower than the measured value. Several different areas of the same samples have been studied and although they are found to be inhomogeneous, certain similarities do exist between the observed patterns. *Figure 8.2* shows three different areas of a sample prepared by heating to 373 K for 10 minutes after the alkane is deposited onto the HOPG surface. Images (a) and (b) appear very similar to each other as they have roughly the same patterns formed on the surface, except with a minor discrepancy in the size of the holes. Although the appearance of the structures shown in image (c) are marginally different to the other areas of the sample; the periphery of the holes tend to be not as smooth, the overall surface coverage is similar and appears to be at roughly the same stage of evaporation.

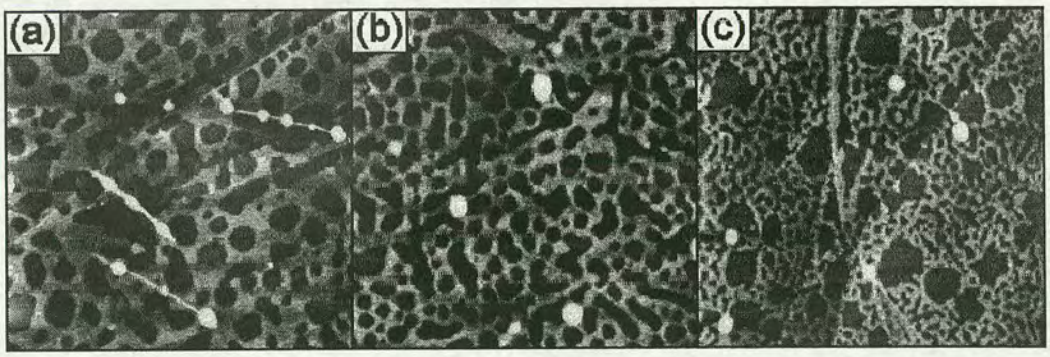

Figure 8.2 *AFM of three different areas of a single sample prepared at 373 K for 10 min. Each image shows an area of 5 x 5 μm with maximum heights of 5.5 nm, 6.2 nm and 5.0 nm respectively.*

Dewetting and Drying of Dodecane on Graphite

Results

All experiments were carried out using the AFM operating in intermittent contact mode. The cantilevers used have a spring constant of 1.2 - 5.5 N/m (typically 2.8 N/m), a resonant frequency of 60 - 100 kHz (typically 75 kHz) and nominal tip radius of ~10 nm. The HOPG surface (AGAR) was initially examined directly after cleaving and found to have similar characteristics to those reported by Martin *et al.* [8.2]. The alkane used for these experiments is n-dodecane ($C_{12}H_{26}$) which has dimensions of 1.85 nm in length, ~0.4 nm in width and a boiling point of 469 K. A gas chromatograph mass spectrometry analysis of the alkane gives strong evidence to the purity being over 99%. This analysis was carried out by Ms S. Shirran of the School of Chemistry at the University of Edinburgh.

Figures 8.3 – 8.8 show the drying and dewetting patterns which have been observed at various heating times and temperatures. For each permutation of heating time and temperature, sizeable quantities of dodecane remained on the HOPG surface to form patterns. These have been found to remain on the surface for many hours after the samples are prepared. Cross-sectional AFM images of the samples at different heating times and temperatures can be seen in *Figure 8.9* and show the patterns to have a preferential thickness of ~2.5 nm of dodecane on the HOPG surface. This thickness approximately corresponds to either six layers of dodecane lying flat on the surface or two layers lying flat and one layer perpendicular to the surface. The latter formation is similar to the structures observed by Martin *et al.* [8.2, 8.3] who reported HOPG surfaces decorated with irregularly shaped features, some with sharp peaks. Martin proposed these features were formed by two layers of alkane orientated parallel to the HOPG and another layer orientated perpendicular, on top of the first two. The AFM images shown here also reveal larger features along the step edges where material has aggregated. An interesting point to be noted is that the rims of the holes do not have the aggregation of material normally associated with the drying process as a result of the 'coffee stain' effect (giving indirect proof of the high purity of the liquid).

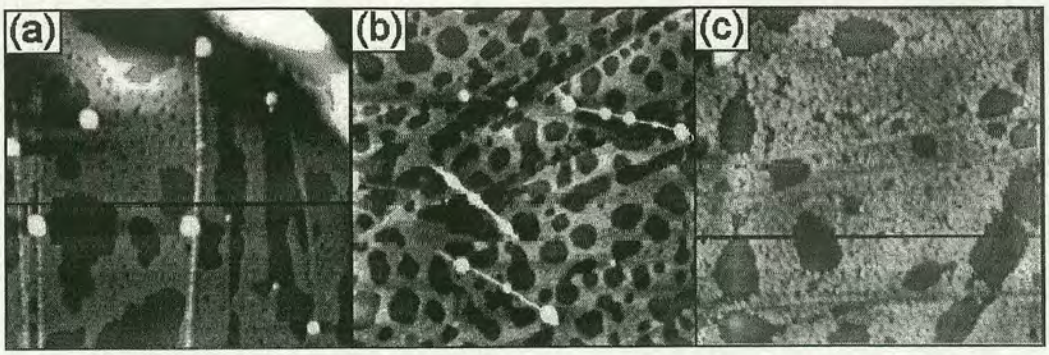

Figure 8.3 *AFM of samples prepared at 373 K for 5, 10 and 15 min. Each image shows an area of 5 x 5 μm with maximum heights of 8.7 nm, 6.2 nm and 5.0 nm respectively.*

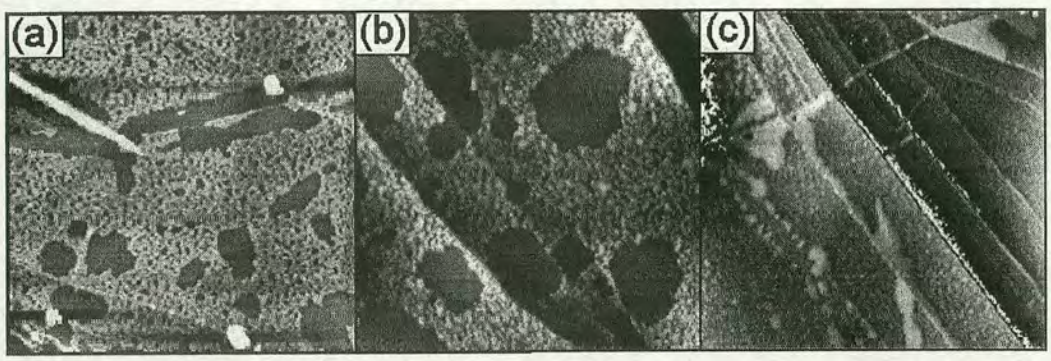

Figure 8.4 *AFM of samples prepared at 398 K for 5, 10 and 15 min. Each image shows an area of 5 x 5 μm with maximum heights of 5.0 nm, 5.4 nm and 7.7 nm respectively.*

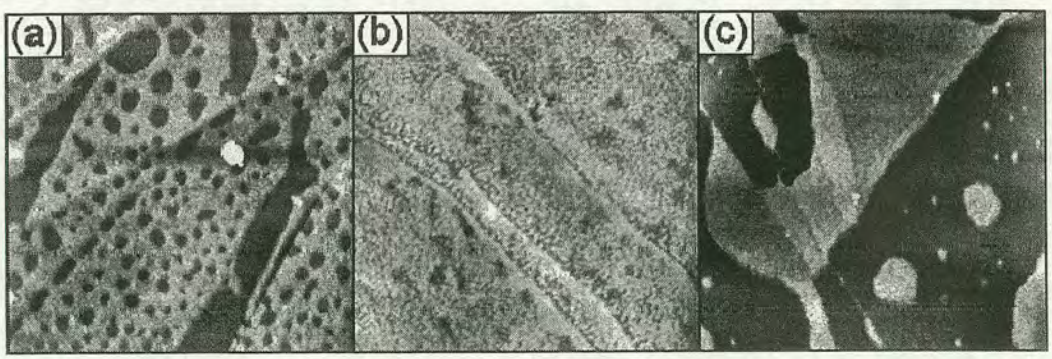

Figure 8.5 *AFM of samples prepared at 423 K for 5, 10 and 15 min. Each image shows an area of 5 x 5 μm with maximum heights of 5.0 nm, 5.0 nm and 5.7 nm respectively.*

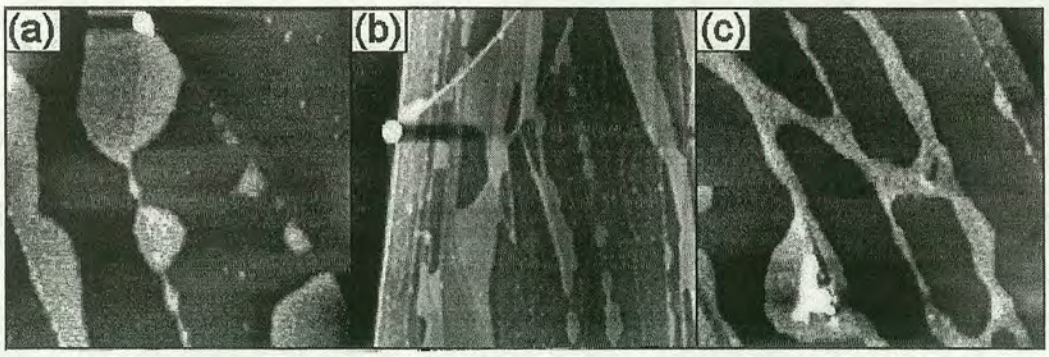

Figure 8.6 *AFM of samples prepared at 448 K for 5, 10 and 15 min. Each image shows an area of 5 x 5 μm with maximum heights of 6.0 nm, 10.6 nm and 5.7 nm respectively.*

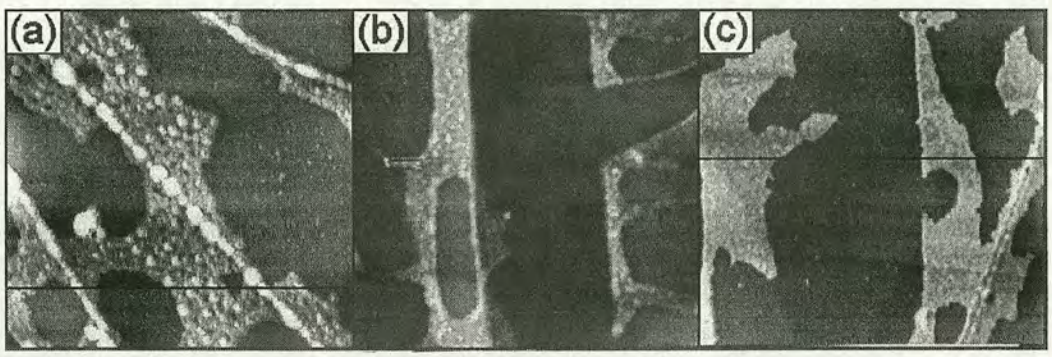

Figure 8.7 *AFM of samples prepared at 473 K for 5, 10 and 15 min. Each image shows an area of 5 x 5 μm with maximum heights of 5.0 nm, 6.0 nm and 5.0 nm respectively.*

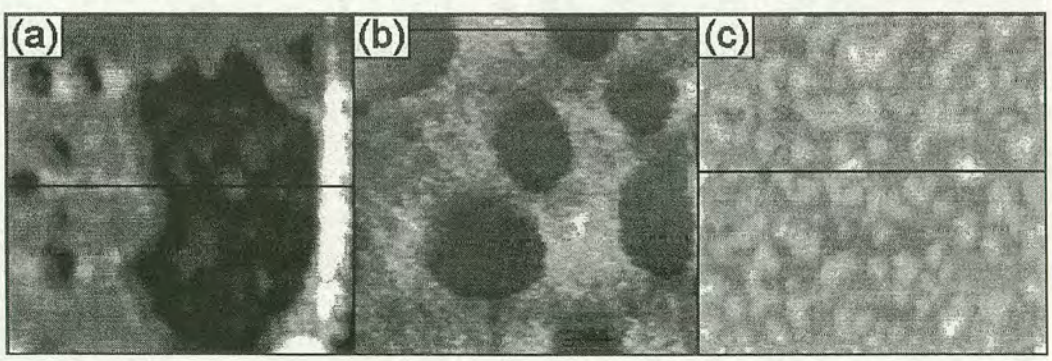

Figure 8.8 *AFM images samples prepared at (a) 373 K for 5 min, (b) 423 K for 5 min and (c) 473 K for 15 min corresponding to Figures 8.3 (a), 8.5 (a) and 8.7 (c). Each image is 1 μm^2 and has maximum heights of 6.0 nm, 5.0 nm and 5.0 nm respectively.*

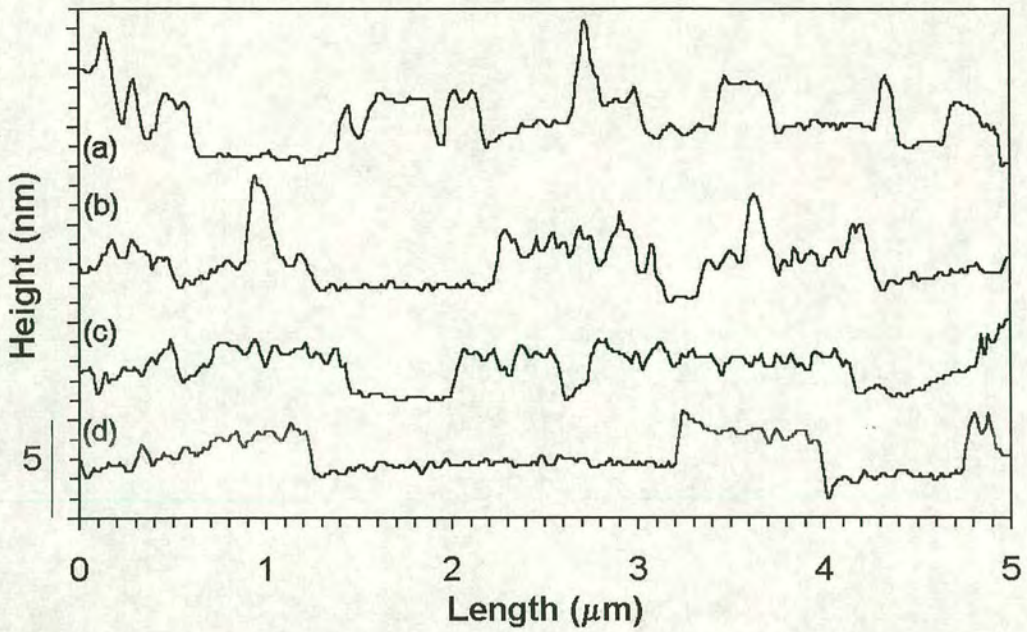

Figure 8.9 *AFM cross-sections of samples prepared at (a) 373 K for 5 min, (b) 473 K for 5 min, (c) 373 K for 15 min and (d) 473 K for 15 min. The cross sections correspond to the horizontal lines shown on Figures 8.3 (a), 8.3 (c), 8.7 (a) & 8.7 (c).*

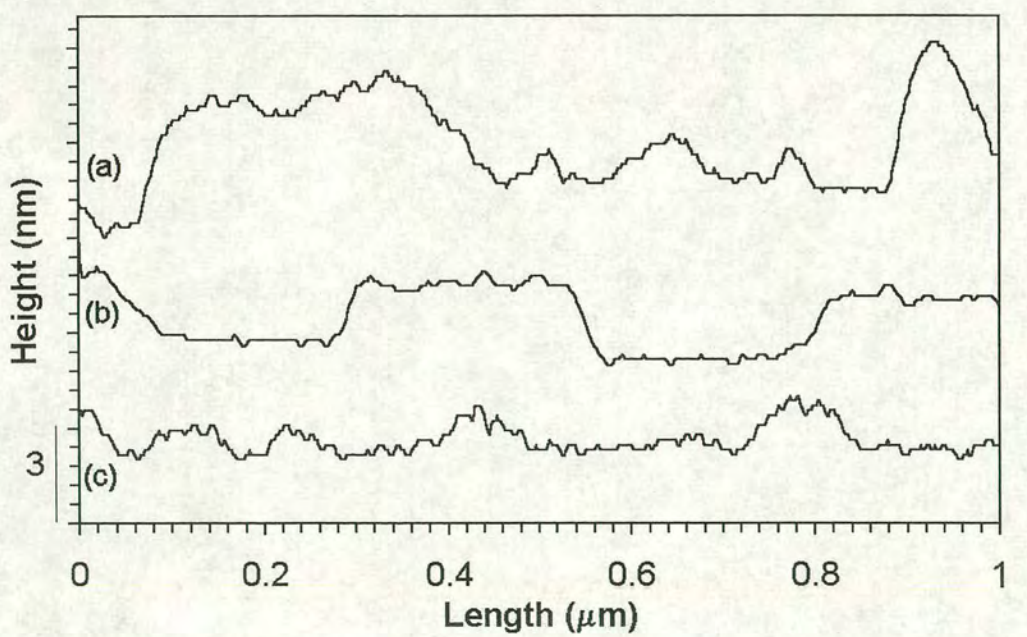

Figure 8.10 *Cross-sections of the AFM images of the dodecane on HOPG samples corresponding to Figure 8.8 showing the relative scales of the preferred film thickness and the residual debris.*

As would be expected, at low heating times and temperatures the coverage was far greater than compared to higher heating times and temperatures. In general, two different types of patterns were observed at low heating times and temperatures. The first of these is a ripple structure which has large ruptures randomly spread out over the surface (*Figures 8.3 (a), 8.4 (a) & 8.5 (b)*), the typical size of the large ruptures is initially about 1μm. The second is a 'Swiss cheese' pattern formed from a network of small holes in the film (*Figure 8.3 (b) & 8.5 (a)*). An additional feature is the numerous large globules clearly seen in *Figure 8.3 (a),* for example. These are thought to occur due to the accumulation of the alkane and are deemed inconsequential with regards to the formation of the patterns as they do not appear at the increased temperatures and times. We define large holes as having dimensions over ~1 μm, small holes having dimensions of ~100 nm to ~1 μm and the ripple structure having typical dimensions of less than ~100 nm. These two different structures appear to tie in well with the two dewetting mechanisms mentioned previously, that is, (i) heterogeneous nucleation (due to defects and possibly contaminants) and thermally activated dewetting and (ii) long range molecular forces destabilising a film resulting in film rupture. However, dynamic effects during drying could be causing variations in the patterns within the same sample and their influence on pattern formation cannot be excluded.

At high heating times and temperatures, the overall coverage of the surface is low and the patterns formed on the surface typically appear long and thin (*Figure 8.5 (c), 8.6 (b), 8.6 (c), 8.7 (b) & 8.7 (c)*). These features are formed from the coalescence of the ruptures in the film as a result of the evaporation of the liquid, which is known to occur faster at the edges of liquid films. Interestingly, in this case, as the film gradually evaporates over time, the preferential film thickness remains. Instead of a decrease in the film thickness as the material is removed from the surface we see either an increase in the surface area of the ruptures or a decrease in the density of the ripple structure. In the cases where the bulk of the material has been removed from the surface to leave a 'dry' HOPG area, residual debris remains. This occurs at high heating times and temperatures when the coverage is low and also at low heating times and temperatures in the large holes formed within the ripple structure

but not in the holes of 'Swiss cheese' pattern. *Figure 8.10* shows smaller area AFM scans of the patterns formed and include some 'dry' areas of the graphite surface. Within the 'dry' areas residual structures can be seen in images (a) and (c) but not in image (b) which corresponds to a 'dry' area (a hole) within the 'Swiss cheese' structure. The height of these residual features is constant at ~1.1 nm, as shown in *Figure 8.10.* More structural information could be obtained by examining the surface with a smaller range/higher resolution piezo than was used here.

There appears to be two general mechanisms for the dodecane covered HOPG surface to get from the high coverage state to the lower coverage state. These mechanisms appear to be dependent on the starting pattern (either a 'Swiss cheese' structure or a ripple structure) although the end result is largely the same. The only difference being the presence of the ~1.1 nm sized debris left on the surface in the case of the ripple structure. In the case of the 'Swiss cheese' system, the holes continue to grow in size, coalescing with each other to form larger holes. This process is thought to continue until the surface is dry. The series of images; *Figure 8.3 (b), 8.5 (a)* and *8.6 (c)* show a possible reconstruction of this dewetting/drying mechanism and results in a surface which is free of the ~1.1 nm sized residual debris. If the starting structure has a ripple effect then over time, as the dewetting/drying proceeds, the ripple structure appears to thin out. Additionally, in a similar manner to the previous mechanism, larger holes can nucleate out of the ripple structure which will then grow and coalesce as before. A possible reconstruction of this dewetting/drying mechanism can be seen in the series of the images of *Figure 8.3 (a), 8.4 (a), 8.4 (b), 8.7 (a)* and 8.7 *(c)* and results in debris on the 'dry' graphite surface.

Figure 8.11 shows a series of consecutive elevated temperature AFM images, taken *in-situ,* which clearly show the drying/dewetting of the dodecane from the HOPG surface as a function of time. This series demonstrates nucleation due to both defects and thermal activation. As a direct consequence of imaging at elevated temperatures over a larger area, the initial ripple structure (which has dimensions of less than ~100 nm) and the larger holes which appear at this early stage cannot be clearly

distinguished. These images show that over time, as previously described, the holes nucleate and then grow into each other leaving large dry areas speckled with residual debris. As before, the aggregation of material along the step edges gives the patterns an elongated appearance.

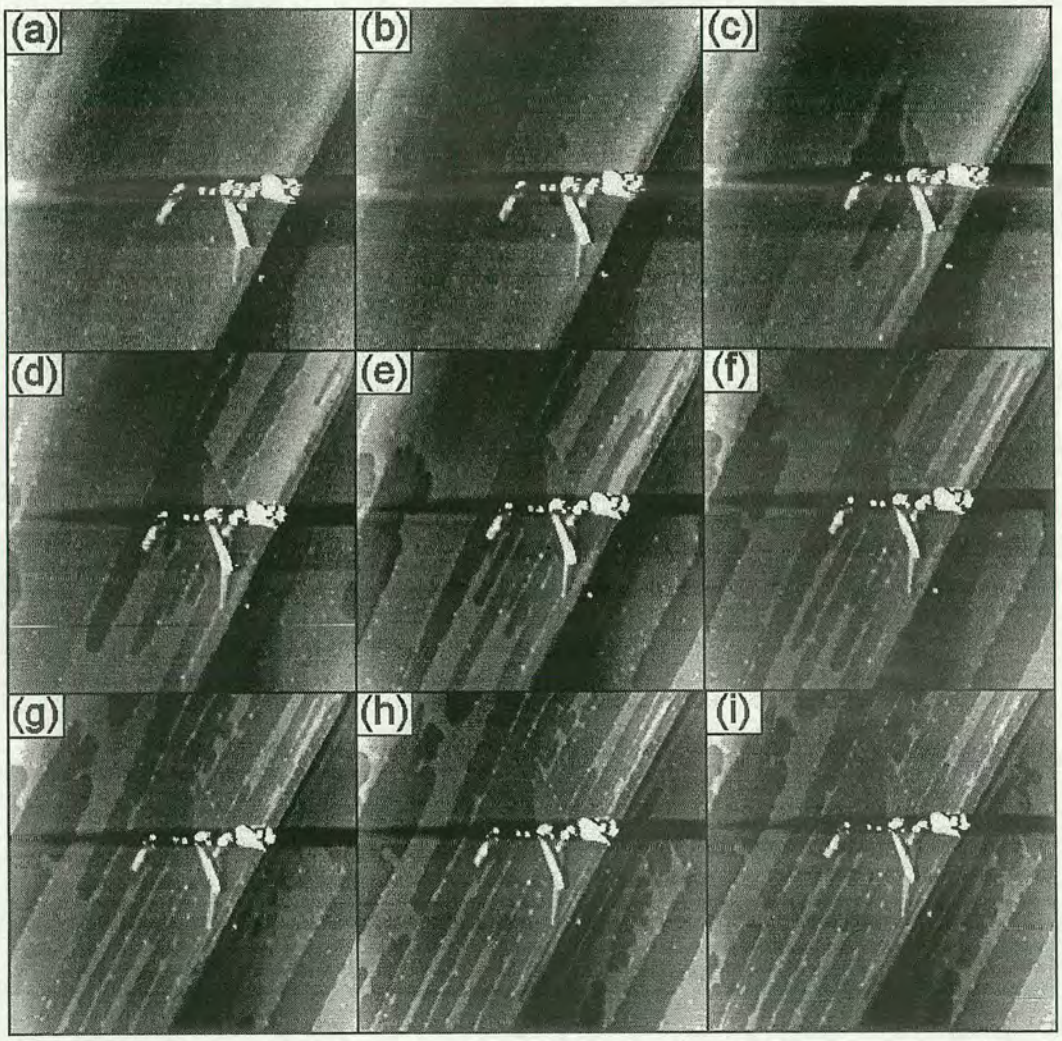

Figure 8.11 *A series of AFM images taken in-situ at an elevated temperature of ~340 K. Each image is 20 x 20 μm and has a maximum height of ~32 nm. The time difference between each image is ~3 min.*

The structures reported by Martin *et al.* [8.2, 8.3] are also observed in some of the figures presented here, for example in *Figures 8.6 (a) & 8.5 (c).* Similarly, some of the patterns reported here can be seen in *Figure 11* of reference [8.2]. This image shows the slightly different system of n-pentane on HOPG in which a 'Swiss cheese'

type structure is visible. Although an in-depth discussion of this structure was not given by Martin *et al.*, we refer to it here to show the close similarities between the two systems. This figure is also used to emphasise the new results we have obtained by studying this system at earlier stages of evaporation, when more material is on the surface, by the use of lower HOPG surface temperatures than Martin.

Discussion

In this system, there are two competing phenomena occurring at the same time: drying and dewetting. As they occur simultaneously and since the majority of our AFM measurements are snapshots of an evolving system, it is difficult to judge their individual contributions to the observed structures.

A variety of patterns of various length scales have been observed previously in drying drops of colloid solutions [8.13] and have been associated with the antagonistic effects of flow during drying and pinning of surface heterogeneities and irregularities. Although the patterns presented here are on a much smaller scale than those observed by Deegan *et al.*, one could argue that the fundamental ingredients for pattern formation due to drying are present in our system: nanometer-size irregularities and pinning effects could arise from preferential alignment and adsorption of the dodecane molecules on the graphite surface, as observed previously [8.5 - 8.7]. The small differences between the patterns observed at different areas of the same sample may arise from the rapid and far-from-equilibrium drying process.

However, the appearance of holes of several sizes and of the rippled structure is reminiscent of well-known dewetting mechanisms: large holes of different sizes are very common features in our measurements. The variety of their size indicates a thermal activation process. It is well-known that thermal nucleation initiates the continuous formation of ruptures leading to holes of different sizes [8.8, 8.10]. The ripple structure is reminiscent of the spinodal dewetting process known to occur as the thickness of the liquid layer becomes sub-microscopic in size. Our system can be categorised as a "Type IV" system [8.14] the thin alkane film experiences a long range van der Waals repulsion combined with a short range attraction resulting in a metastable interface potential (stable for sufficiently thick films but unstable for

films below a limiting thickness which is usually at the nanometer scale) [8.8, 8.10]. A thin liquid film becomes unstable if the effective interfacial potential exhibits negative curvature at a range of thickness'. In many situations this arises from long-range attractive forces (positive Hamaker constant). In type IV systems the negative curvature appears from the combination of long-range repulsion and short-range attraction. For a detailed discussion of the phenomenon and the connection of the interfacial potential and the resulting dewetting patterns see ref. [8.8], [8.10], [8.14]. The long range repulsion is associated with a negative effective Hamaker constant: $A = A_{ll} - A_{sl} = 5 \times 10^{-20} - 15.3 \times 10^{-20}$ J < 0 ($A_{ll} = A_{dodecane} = 5 \times 10^{-20}$ J , $A_{ss} = A_{graphite} = 47 \times 10^{-20}$ J, $A_{sl} = A_{graphite\text{-}dodecane} = (A_{dodecane}A_{graphite})^{1/2} = 15.3 \times 10^{-20}$ J) [8.15] and stabilises the films above the limiting thickness. The short range attraction can originate from packing or steric effects: it has been shown that there are situations where a liquid cannot spread on its own monolayer resulting in "autophobic" behaviour at sufficiently low thicknesses [8.16]. The aligned adsorption of alkanes on the graphite surface is well-known from STM measurements [8.5 - 8.7]: ultra-thin alkane monolayers seem to form "crystallised" regions on the graphite surface.

Conclusion

In this chapter it has been shown that the evaporation of n-dodecane on graphite results in the formation of patterns which are tentatively attributed to two different dewetting scenarios: (i) heterogeneous and thermal nucleation of "dry" spots and (ii) spinodal dewetting at nanometer-size film thickness' due to combination of long-range repulsive and short range attractive forces. It is possible that the resulting patterns give an indication of the effective interface potential of n-dodecane films on graphite surfaces.

The drying and dewetting behaviour observed here and the formation of structures in this relatively simple situation may give an insight into more complex systems with 'real' applications, the relevant example being LC alignment layers. By having knowledge of why these structures and patterns are formed, it should be possible to minimise and perhaps eradicate this effect as the substrates are coated with polymers. This would allow more uniform flatter alignment layers to be made which would increase the device quality. In a similar manner, this knowledge may also be advantageous to the deposition of the LC molecules onto the alignment layer.

Chapter 9: Conclusions

'If we know what we were doing it would not be called research would it!'
Albert Einstein (1879 - 1955)

Summary

In this final chapter, a summary of the results from each chapter is given. This is followed by suggestions of work that could be done to improve and further the results obtained in this project. Final conclusions of the completed project are given.

Summary of Results

By using RAS it has been possible to monitor the fabrication of LC alignment layers both *in-situ* and real-time. This has been done extensively for the rubbing technique and on a preliminarily basis for the non-contact alignment techniques of photopolymerisation and atomic beam etching.

The results obtained from the rubbing technique clearly demonstrate that RAS can monitor the growth, saturation and reduction of optical anisotropy that results from processing and in the latter case, over processing. The ability of RAS to monitor these enables it to be used as a quality control tool which has the potential to reduce the high waste currently associated with the rubbing technique. Information contained within the measured reflectivity, later replicated using the multilayer simulations, has proved to be invaluable to these studies even though this information is normally overlooked by RAS practitioners. The variation of the optical anisotropy with the number of rubs (amount of rubbing) can be partially explained by analysis of the topographic AFM images of the surface. These have helped to show that reductions in the anisotropy, after saturation, are due to a degradation of the surface caused by over-rubbing. Further understanding of the spectra has emerged from simulations based on Berreman's stratified media matrix formalism. These simulations have confirmed that the main features of the RAS spectra result from multilayer interference and a difference in the surface optical properties in the directions parallel and perpendicular to the rubbing direction, most probably due to the alignment of the polymer chains. The interference patterns appear at low energies, up to ~4.0 eV but are extinguished at higher energies due to absorption of the light as it propagates through the media. Another feature common to all RAS measurements of rubbed polymers appears around 4.5 eV and has not been replicated by simulations. A possible source of this feature is induced surface dichroism.

By constructing operational LC cells it has been possible to assess the effect of rubbing and over rubbing on the performance of these devices. Whilst it is necessary

to promote the alignment capability by surface processing, over-rubbing can have the opposite effect as it creates a high amount of contamination. Non-contact alignment techniques are a possible solution to this problem and here, RAS studies have been carried out on two possible candidates. Although RAS is capable of measuring the optical anisotropy in a photoaligned sample, the power output of the probe light source is comparable to the alignment method itself. A consequence of this is the modification of the photosensitive polymer by the RAS probe whilst measurements are taken. However, RAS measurements show anisotropy in the IR and visible regions and so non-destructive monitoring of this technique is possible providing an UV filter is used.

LC cells constructed from alignment layers created by the etching process are shown to be superior to the rubbing equivalent as they are less susceptible to contamination. Again, RAS is found capable of monitoring the changes in optical anisotropy as the alignment layer is etched even though AFM show negligible signs of surface modification at the nano-scale. The fundamental reasons behind the optical anisotropy of the rubbing and etching techniques is suggested to be the same as similarities exist between the measured spectra. This proposition could be tested by increasing the topographical effect of ion bombardment to try to replicate the surface corrugation and therefore depth of molecular alignment caused by the rubbing process.

Several question marks remain with regard to the use of RAS as a monitor in this manner but the potential of this technique has been demonstrated and it has been proven a suitable technique to study such systems. The use of RAS as a quality control monitor could result in increased production yields, lower waste and therefore lower manufacturing costs. In fact, further simulations have shown RAS to be far better suited to the study of transparent thin films than the transmissive equivalent, TAS. To help solve some of the remaining problems: the increased anisotropy at 4.5 eV, the contribution to the anisotropy from molecular alignment and the behaviour of surface optical properties under various conditions, further RAS studies are carried out on model surfaces.

In a slight tangent to the main goal of the project, the PI/ITO/glass substrates from the alignment layers studies were used to introduce a new extension to the typical RAS technique. By studying the RA of a sample over a range of sample azimuthal angles, angular dependent RAS (ADRAS) can yield additional information. In the first example considered, ADRAS was used to determine the relative strength of rubbing in each direction of a doubly rubbed sample. Other examples, a stressed rubbed sample and a double sided rubbed sample, are used to show ADRAS is capable of isolating each independent source of optical anisotropy providing they have a distinct angular dependence. This new technique has the potential to be invaluable to applications involving, for example, microgrooves, stress and aligned molecules.

Noble metal crystals have been studied by RAS to gain information relevant to polymer alignment layers as their morphology can be controlled by ion bombardment and mis-cutting. These properties allow them to simulate polymers surfaces and the effect of processing these surfaces. The first real-time RAS study of the Cu (110) and Cu (771) surfaces during etching and annealing has been presented. The spectra obtained from these surfaces are very similar and the differences have been explained by considering the terrace widths and the minimum width required to support a surface state. Differences in the behaviour of the main features of these surfaces during the bombard/anneal cycles have been observed. By considering the adatom diffusion energy barriers it has been possible to explain the observed behaviour in terms of the rate of diffusion of the adatoms. The same argument has been applied to the situation of elevated temperature etching of the surfaces which has revealed the effect of etching is maximised at ~400 K and cannot be seen above ~573 K. The results of the copper bombardment experiments have been applied to the bombardment of the polymer surfaces for use in creating alignment layers by ion bombardment.

It has been possible to continue the studies of the copper surfaces whist continuously advancing towards the goal of understanding more about liquid crystal alignment layers. By increasing the complexity of the sample again, by the deposition of

organic molecules onto the copper surfaces, a further step towards the alignment layers is taken. The tangent of ADRAS is brought into context as it is the primary tool used in these advanced studies. The example considered involves the adsorption of a chiral molecule onto a clean Cu (110) surface. As the optical axis of the adsorbate is known to lie at a different angle to the optical axis of the substrate surface, it should be possible to use ADRAS to exploit the angular dependence and gain additional information. The preliminary work presented here confirms R, R-tartaric acid is suitable for use in this experiment as changes are seen in the RA as it is deposited onto a copper surface. When the precise deposition conditions have been established and a suitably orientated sample produced, it will be possible to extinguish the anisotropic contribution of the substrate and study the adsorbate anisotropic spectrum in isolation. Simulations of these experiments successfully demonstrate the potential of ADRAS to be used in this way and highlight the potential of ADRAS in applications such as enatiomeric catalysis and biomolecular adsorption. Using ADRAS may also allow the quantity of enantiomers in a racemic mixture to be determined.

Studies of the relatively simple system of an alkane on graphite as a function of time and temperature have revealed stable nano-scale patterns and structures formed on the graphite surface. *In-situ* AFM images show these structures to result primarily from dewetting although drying may also be a contributing factor. From these results a greater understanding of the mechanisms involved in the formation of such features has been obtained. This information is of potential use in many areas, in particular the application of polymer coatings for use as liquid crystal alignment layers. AFM images of current polymer alignment layer surfaces show evidence of drying induced structures and a degree of surface roughness. Homogeneous orientation of the LC molecules on the polymer surface will be encouraged by having a uniformly flat polymer film and hence improved device quality will result.

Future Work

Experimental Apparatus

A significant improvement in the versatility and accuracy of the apparatus used throughout this project, giving improved results and greater time efficiency, would be possible by upgrading some of the experimental apparatus. The design and the components used in the RA spectrometer do not need improvements and in general the same can be said about the vacuum system. However, an improved sample heater, with a temperature range of up to ~1300° K would allow the roughening transition to be studied. Also, in having the ability to cool the sample, either by using a Peltier or preferably by using liquid nitrogen, would give far more flexibility over the current radiative method. These improvements would allow the clean surface to be studied at room temperature without having to wait several hours for the sample to cool naturally, in which time the surface becomes slightly contaminated. Ideally, information about the quantities and types of contaminants on the surface should be known. This information could be obtained by using Auger analysis. Although this technique has recently been added to system, it is not yet operational.

The idea of using a transfer mechanism to exchange the samples without venting the entire chamber has been found to be excellent. However, the current design is somewhat temperamental and can result in the sample being dropped or getting stuck within the chamber. An improved design would save time and effort by allowing easy (and safe) transfers of samples.

The addition of one final experimental technique, an STM capable of operating under vacuum, would allow extremely useful, almost necessary, data to be obtained. Unfortunately, the cost of this type of STM is high, as would be the necessary changes to pumping system to reduce vibrations.

In *Chapter 5* ADRAS was introduced, this new technique proved to be a useful extension and gave additional information about the samples. The data acquired in these experiments was obtained by taking a series of RAS spectra at different sample azimuthal angles. The individual ADRAS data at specific energies was then

extracted from each data set to form the complete set. The collection of ADRAS data could be simplified by alterations to the experimental set-up. One possibility is to use a double modulated RA spectrometer, similar to that reported by Aspnes [9.1]. In Aspnes' alternative system, the azimuth angle of the sample is slowly rotated at a rate that allows the axes of the sample to interchange twice during a single measurement cycle. This system allows the 'window correction', as given in *Equation 3.3,* to be automatically accounted for and could be adapted to automatically acquire data over a range of azimuthal angles, both spectroscopically and at single energies. A second, more complex suggestion, would allow greater versatility in situations where the sample cannot be rotated. The same angular information could be obtained by rotating the polarisation of the light incident upon the sample. Correlating the alignment of the polariser with the PEM and analyser would be extremely difficult but it may be simplified if these components were replaced by a rotating analyser as in original design of Aspnes [9.2]. In theory these suggestion would allow ADRAS data to be taken at a higher speed and with greater ease without losing the original features of RAS. The reduction in the signal to noise ratio in the case of the latter suggestion would have to be considered [9.3].

Experiments

Throughout this project it has become apparent that the number of possible new experiments in the same general areas covered by this thesis is huge. Whilst this project has been kept relatively strictly to the main goal, several related avenues of work have been investigated on a preliminary basis. The result of one these experiments in particular, shown in *Figure 2.12*, has shown great promise to produce further scientific insight and another useful application of RAS. In this experiment a stretching device, which is compatible with RAS and AFM, has been built to apply a force to samples, causing elastic and plastic deformations in the sample, whilst monitoring the extension and force applied. This device has been designed and constructed by Mr D. Higgins of the Centre for Material Science and Engineering at the University of Edinburgh as part of his MSc project. The preliminary results concern only the use of RAS and show the anisotropy (which will be stress induced anisotropy) to increase proportionally with the force applied. Evidence of a plastic deformation can be seen as the anisotropy does not return to the initial value (of zero)

after the sample fractures. The fluctuations seen in the RAS result from the flexibility of the sample. Varying the sample thickness to reduce these deviations whilst still allowing the sample to be stretched would be a very worthwhile task in the future. It is hoped that after compiling RA and force data from a number of samples it may be possible to apply RAS to gauge how much stress an object is subjected to. An example of a suitable application could be to monitor the stress in a car window as the glass is struck by flying objects.

In addition to perfecting some of the tangents which have been explored, the main experiments of this project could be studied further. Regarding the experiments presented in *Chapter 4* which presented studies of the fabrication of LC alignment layers, an even stronger case advocating the use of RAS in for this purpose could be made if it were possible to correlate the measured RA to a property of the completed devices. Although this could be done using any of the fabrication techniques studied here, it is suggested that the etching technique is concentrated on. Although it is thought that the mechanisms for promoting the alignment of LCs are the same for the rubbing and etching techniques, the etching technique is new and so warrants further investigation. Experiments to correlate with device properties could be tied in with investigations of the etching technique itself, for example a study of the effects of etching on the anisotropy as a function of etch energy, time, current, angle or temperature.

Although some differences were observed between the RA spectra of plane and vicinal surfaces, a larger contribution to the anisotropy was expected from the steps. Further work needs to be done to confirm these findings, in particular completing the studies of the Cu (1090) surface. A conclusive experiment would be to study an isotropic surface, for example Cu (100), which has steps. Studying more vicinal surfaces with a range of terrace widths may confirm the suggested explanations regarding terraces supporting surface states. It may also be interesting to study a stepped surface after undergoing the roughening transition, particularly if the roughening features are in the direction perpendicular to the vicinal steps.

Further work should be done on the temperature dependent experiments to allow more precise values of the temperature dependent transitions to be established. An interesting experiment derived from [9.4] would be to etch the Cu (110) surface at low temperature. Although the 2.1 eV feature is normally stable under etching, it is expected to be reduced in intensity if etched at a temperature of ~180 K. If this proved to be the case it would be direct evidence of this feature stemming from surface states.

The preliminary results of the chiral molecule experiments presented in *Chapter 7* have clearly shown the high potential of these experiments. To complete this study it is necessary to redo the experiment using a clean Cu (110) surface. It is expected that a significant amount of time will be needed to perfect the deposition of the molecules onto the copper surface. Once this has been achieved, it is then straightforward to obtain the ADRAS data. This experiment could be repeated for different molecules and different surfaces to give a range of information for use in catalysis or bimolecular adsorption.

The experiments of *Chapter 8* provide an almost endless list of possible future experiments by making subtle changes to the current experiments. An example would be to use other long-chain hydrocarbons such as alkenes to study the affect of the double bond. It would be worth while to redo the alkane on HOPG experiments presented here whilst measuring the temperature at the surface of the graphite instead of at the surface of the heater. The important thing would be to study shorter times/lower temperature to prevent any new work from being a repetition of the work by Martin *et al.* [9.5]. Although incredibly hard to do, further elevated temperature *in-situ* AFM measurements of the drying/dewetting processes could provide further interesting results. Crucial information about the material left on the on the surface of the graphite could be obtained by repeating the experiments in a vacuum chamber. By using mass spectroscopy it would be possible to monitor the material evaporated from the surface at the same time as an AFM study. Once an equilibrium situation has been reached, a further increase in the temperature of the substrate would reveal the identity of the molecules remaining of the surface to form the observed

structures. Using the same systems of alkanes on HOPG, friction measurements of the surface using AFM could reveal some very interesting and useful information.

Conclusions

The goal at the outset of this project was to study and improve the fabrication process of alignment layers for use in LCDs. This was to be done by applying an optical technique, initially conceived to monitor semiconductor growth, to monitor the process *in-situ*.

After the successful construction of the optical spectrometer, the technique was applied to study all of the most common commercially used alignment techniques. RAS measurements, supported by AFM images and simulations, have allowed not only a tool for empirically monitoring the quality of alignment layers as they are produced but has also given an insight into the mechanisms which create surface optical anisotropy and promote LC alignment.

Although not directly related to the study of LC alignment layers, a new technique which has the potential to make a significant impact in the fields of surface science and chirotechnology has been introduced. The ability of ADRAS is demonstrated using polymer coated substrates. Preliminary measurements and simulations are used to study the adsorption of a chiral molecule on a copper surface which has applications in catalysis.

Further information about the optical properties of surfaces, in particular the effect of ion beam etching a surface, was found by replacing the complex systems of before with a model substrate. Experiments were carried out on a Cu (110) surface and then on vicinal copper surfaces. RAS measurements highlighted differences in the electronic structure and morphology of the crystals. These properties were studied in real-time and were found to be highly temperature dependent.

AFM images of an alkane on graphite have shown the unusual patterns and structures which can be formed on a surface as a result of the dewetting and drying mechanisms.

Appendix A: Fresnel Coefficients

Two Phase System

An incident wave polarised with its E vector normal to the plane of incidence is shown in *Figure A.1*. The interface is defined at $z = 0$ where θ_i, θ_t and θ_r are the angles of incidence, transmission and reflection respectively.

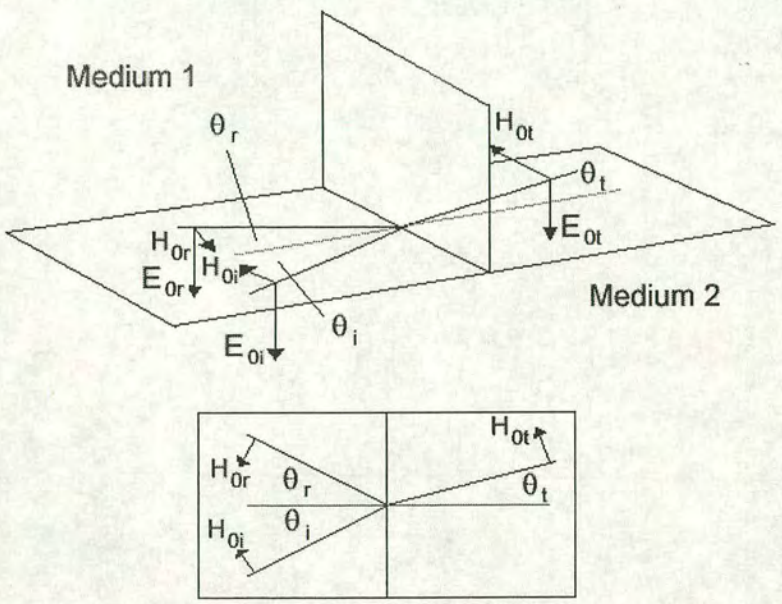

Figure A.1 *An incident wave polarised with its E vector normal to the plane of incidence.*

For any medium,

$$\frac{E_{0x}}{H_{0x}} = \frac{\omega\mu_x}{k_x} \qquad \textit{Eq. A.1}$$

Continuity of the tangential components of both E and H leads to:

$$E_{0i} + E_{0r} = E_{0t} \qquad \textit{Eq. A.2}$$
$$H_{0i}\cos\theta_i - H_{0r}\cos\theta_r = H_{0t}\cos\theta_t$$

And then using *Equation A.1*,

$$\frac{k_1}{\omega\mu_1}(E_{0i}\cos\theta_i - E_{0r}\cos\theta_r) = \frac{k_2}{\omega\mu_2}E_{0t}\cos\theta_t \qquad \textit{Eq. A.3}$$

But $\theta_i = \theta_r$ and from *Eq. A.2*,

$$E_{0t} = E_{0i} + E_{0r}$$

$$\therefore \frac{k_1}{\mu_1}\cos\theta_i(E_{0i} - E_{0r}) = \frac{k_2}{\mu_2}\cos\theta_t(E_{0i} + E_{0r})$$

$$\therefore E_{0i}\left\{\frac{k_1}{\mu_1}\cos\theta_i - \frac{k2}{\mu2}\cos\theta_t\right\} = E_{0r}\left\{\frac{k_1}{\mu_1}\cos\theta_i + \frac{k2}{\mu2}\cos\theta_t\right\}$$

$$\therefore \frac{E_{0r}}{E_{0i}} = \frac{\frac{k_1}{\mu_1}\cos\theta_i - \frac{k_2}{\mu_2}\cos\theta_t}{\frac{k_1}{\mu_1}\cos\theta_i + \frac{k_2}{\mu_2}\cos\theta_t} \qquad \textit{Eq. A.4}$$

Similarly, starting with *Eq. A.3* and solving for E_{0i} and E_{0t} this time,

$$\frac{k_1}{\mu_1}(E_{0i}\cos\theta_i - (E_{0t} - E_{0i})\cos\theta_i) = \frac{k_2}{\mu_2}E_{0t}\cos\theta_t$$

$$\therefore E_{0i}\left\{\frac{2k_1}{\mu_1}\cos\theta_i\right\} = E_{0t}\left\{\frac{k_1}{\mu_1}\cos\theta_i + \frac{k_2}{\mu_2}\cos\theta_t\right\}$$

$$\therefore \frac{E_{0t}}{E_{0i}} = \frac{\frac{2k_1}{\mu_1}\cos\theta_i}{\frac{k_1}{\mu_1}\cos\theta_i + \frac{k_2}{\mu_2}\cos\theta_t} \qquad \textit{Eq. A.5}$$

As,

$$k = \frac{2\pi}{\lambda} = \frac{2\pi f}{v} = \frac{2\pi fN}{c} = \frac{2\pi N}{\lambda_0}$$

Equation A.4 & *A.5* become,

$$\frac{E_{0r}}{E_{0i}} = \frac{\frac{N_1}{\mu_1}\cos\theta_i - \frac{N_2}{\mu_2}\cos\theta_t}{\frac{N_1}{\mu_1}\cos\theta_i + \frac{N_2}{\mu_2}\cos\theta_t}$$

&

$$\frac{E_{0t}}{E_{0i}} = \frac{\frac{2N_1}{\mu_1}\cos\theta_i}{\frac{N_1}{\mu_1}\cos\theta_i + \frac{N_2}{\mu_2}\cos\theta_t}$$

These equations apply to any isotropic media. However, for non-magnetic media, $\mu_1 = \mu_2 = \mu_0$, and the equations become,

$$\frac{E_{0r}}{E_{0i}} = \frac{N_1\cos\theta_i - N_2\cos\theta_t}{N_1\cos\theta_i + N_2\cos\theta_t}$$

&

$$\frac{E_{0t}}{E_{0i}} = \frac{2N_1\cos\theta_i}{N_1\cos\theta_i + N_2\cos\theta_t}$$

Another pair of similar equations can be obtained by considering the incident wave with E polarised parallel to the plane of incidence. Each pair of equations, at normal incidence $\theta_i = \theta_t = 0$, reduce to the form,

$$r_{12} = \frac{E_{0r}}{E_{0i}} = \frac{N_1 - N_2}{N_1 + N_2} \qquad \textit{Eq. A.6}$$

&

$$t_{12} = \frac{E_{0t}}{E_{0i}} = \frac{2N_1}{N_1 + N_2} \qquad \textit{Eq. A.7}$$

These are the Fresnel reflection and transmission coefficients for a two phase system. The subscripts, e.g. r_{12}, denote the propagation of light from medium 1 (N_1) to medium 2 (N_2).

Three Phase System [A.1]

The results of the two phase system can be used to determine the Fresnel coefficients of the three phase system. Similar to the previous situation, light incident on an interface is spilt into the reflected and transmitted components. For multiple layer systems, each time the light is incident at an interface it is divided further, as illustrated in *Figure A.2*. As before, θ_i, θ_r & θ_t are the angles of incidence, reflection and transmission respectively.

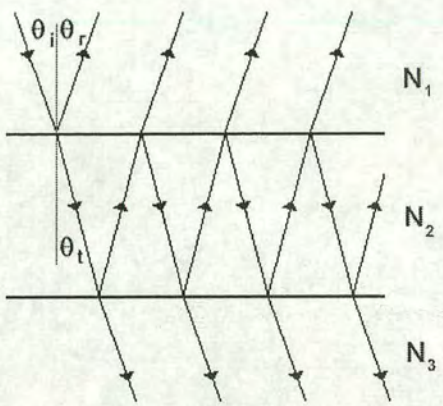

Figure A.2 *Splitting of light at an interface into reflected and transmitted components.*

The resultant reflected and transmitted beams, which are the equivalent Fresnel coefficients for a three phase system (r_{123} & t_{123}), are obtained by the addition of all of the reflected components and all of the transmitted components. Here, the Fresnel reflection and transmission coefficients for light incident at the interface between N_1 and N_2 are denoted r_{12} & t_{12}, at the interface between N_2 and N_1 they are r_{21} & t_{21} and at the interface between N_2 and N_3 they are r_{23} & t_{23}. Summing all of the reflected components gives,

$$r_{123} = r_{12} + t_{12}t_{21}r_{23} + t_{12}t_{21}r_{21}r_{23}^2 + t_{12}t_{21}r_{21}^2r_{23}^3 + ...$$

As $r_{21} = -r_{12}$,

$$r_{123} = r_{12} + t_{12}t_{21}r_{23} - t_{12}t_{21}r_{12}r_{23}^2 + t_{12}t_{21}r_{12}^2r_{23}^3 + ...$$

The change in phase of light after each propagation through medium 2 is given by,

$$\beta_2 = \frac{2\pi N_2 d_2 \cos\theta_t}{\lambda}$$

As RAS is a near-normal incidence technique, this simplifies to,

$$\beta_2 = \frac{\omega N_2 d_2}{c} \qquad \textit{Eq. A.8}$$

After consideration of the phase changes, the resulting reflection coefficient is,

$$r_{123} = r_{12} + t_{12}t_{21}r_{23}e^{-2i\beta_2} - t_{12}t_{21}r_{12}r_{23}^2 e^{-2i\beta_2} + t_{12}t_{21}r_{12}^2 r_{23}^3 e^{-2i\beta_2} + ...$$

$$\therefore r_{123} = r_{12} + \frac{t_{12}t_{21}r_{23}e^{-2i\beta_2}}{1 + r_{12}r_{23}e^{-2i\beta_2}}$$

Using the thin film approximation, $d << \lambda$ and $t_{12}t_{21} = 1 - r_{12}^2$,

$$r_{123} = \frac{r_{12} + r_{23}(1 - 2i\beta_2)}{1 + r_{12}r_{23}(1 - 2i\beta_2)} \qquad \textit{Eq. A.9}$$

which is the Fresnel reflection coefficient of a three phase system.

2 x 2 Matrix Method For Isotropic Stratified Media

The method of addition of multiple reflections becomes extremely impractical when considering systems with higher numbers of layers. A more suitable approach for considering the reflection and transmission of polarised light from isotropic stratified media uses 2 x 2 linear matrix transformations which were developed by Abelès [A.2]. A full account is given by Azzam and Bashara [A.3].

If the complex amplitudes of the incident and reflected waves at an arbitrary interface z are defined as $E_+(z)$ and $E_-(z)$ then the total field at z, $E(z)$, can be expressed as a 2 x 1 matrix. It should be noted in these equations that the $\pm$ subscripts are used to give the direction in which the wave is travelling.

$$E(z) = \begin{bmatrix} E_+(z) \\ E_-(z) \end{bmatrix}$$

By considering the total fields found at planes parallel to z (z' and z''), a relation between the fields can be found. The relation has the form of a 2 x 2 matrix transformation and is called the *general transform matrix (T)*.

$$\begin{bmatrix} E_+(z') \\ E_-(z') \end{bmatrix} = \begin{bmatrix} T_{11} & T_{12} \\ T_{21} & T_{22} \end{bmatrix} \begin{bmatrix} E_+(z'') \\ E_-(z'') \end{bmatrix}$$

$$\begin{bmatrix} E_+(z') \\ E_-(z') \end{bmatrix} = T \begin{bmatrix} E_+(z'') \\ E_-(z'') \end{bmatrix} \qquad \textit{Eq. A.10}$$

The general transfer matrix is used to represent the overall reflection and transmission properties of the stratified media between z' and z'' and can be expressed as the product of the interface (*transition*) matrices (L) and layer (*partial transfer*) matrices (T_P) that lie within these bounds.

$$T = L_{12} T_{P2} L_{23} T_{P3} \ldots\ldots T_{Pm-1} L_{(m-1)m} \qquad \textit{Eq. A.11}$$

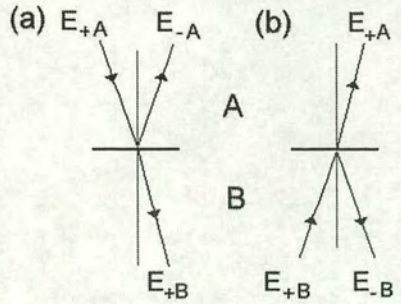

Figure A.3 *The interface between two media, A and B, showing (a) light incident from medium A and (b) light incident from medium B.*

A typical interface between two media (*A* and *B*) is shown in *Figure A.3*. *L* is used to relate the electric fields of a wave at either side of an interface to each other. The subscripts *A* and *B* relate to the medium being considered and r_{AB} and t_{AB} are the Fresnel reflection and transmission coefficients for the *AB* interface.

$$\begin{bmatrix} E_{+A} \\ E_{-A} \end{bmatrix} = \begin{bmatrix} L_{11} & L_{12} \\ L_{21} & L_{22} \end{bmatrix} \begin{bmatrix} E_{+B} \\ E_{-B} \end{bmatrix}$$

For light incident from medium *A* on the interface (*AB*), shown in *Figure A.3 (a)*, it is known that,

$$\begin{aligned} E_{+B} &= t_{AB} E_{+A} \\ E_{-A} &= r_{AB} E_{+A} \\ E_{-B} &= 0 \end{aligned}$$

Therefore,

$$\begin{bmatrix} E_{+A} \\ E_{-A} \end{bmatrix} = \begin{bmatrix} \dfrac{1}{t_{AB}} & L_{12} \\ \dfrac{r_{AB}}{t_{AB}} & L_{22} \end{bmatrix} \begin{bmatrix} E_{+B} \\ 0 \end{bmatrix}$$

Similarly for light incident from medium *B* on the interface (*BA*), shown in *Figure A.3 (b)*, it is known that,

$$E_{+A} = 0$$
$$E_{-A} = t_{BA} E_{-B}$$
$$E_{+B} = r_{BA} E_{-B}$$

Therefore,

$$\begin{bmatrix} 0 \\ E_{-A} \end{bmatrix} = \begin{bmatrix} L_{11} & -\dfrac{r_{BA}}{t_{AB}} \\ L_{21} & \dfrac{(t_{AB}t_{BA} - r_{AB}r_{BA})}{t_{AB}} \end{bmatrix} \begin{bmatrix} E_{+B} \\ 0 \end{bmatrix}$$

And so after manipulation using Fresnel interface coefficients for both propagation directions,

$$L_{AB} = \frac{1}{t_{AB}} \begin{bmatrix} 1 & r_{AB} \\ r_{AB} & 1 \end{bmatrix} \qquad \textit{Eq. A.12}$$

The result of propagation through a homogeneous medium is a phase change in the direction of travel. This is dependent on the complex index of refraction and thickness of the medium, the wavelength of light and the angle of incidence. The partial transfer matrix is therefore,

$$T_P = \begin{bmatrix} e^{i\beta} & 0 \\ 0 & e^{-i\beta} \end{bmatrix} \qquad \textit{Eq. A.13}$$

With β as defined before,

$$\beta = \frac{2\pi dN}{\lambda} \cos\theta$$

Knowing that $E_{-B} = 0$, *Equation A.10* applied to the *AB* interface becomes,

$$\begin{bmatrix} E_{+A} \\ E_{-A} \end{bmatrix} = \begin{bmatrix} T_{11} & T_{12} \\ T_{21} & T_{22} \end{bmatrix} \begin{bmatrix} E_{+B} \\ 0 \end{bmatrix}$$

By expanding this equation the reflection (r) coefficient can be found to be,

$$r = \frac{E_{-A}}{E_{+A}} = \frac{T_{21}}{T_{11}} \qquad \textit{Eq A.14}$$

The general transfer matrix can be obtained, as described in *Equation A.11*, by matrix multiplication and when used in conjunction with *Equation A.10* provides a simple method of studying the reflection and transmission of stratified media. As an example of this technique, the three-phase system previously discussed is considered again and by using *Equation A.11* the general transfer matrix is found to be,

$$T = L_{12} T_{P2} L_{23} \qquad \textit{Eq. A.15}$$

By applying *Equations A.12 & A.13* the T matrix becomes,

$$T = \left(\frac{1}{t_{12}t_{23}}\right)\begin{bmatrix} 1 & r_{12} \\ r_{12} & 1 \end{bmatrix}\begin{bmatrix} e^{i\beta_2} & 0 \\ 0 & e^{-i\beta_2} \end{bmatrix}\begin{bmatrix} 1 & r_{23} \\ r_{23} & 1 \end{bmatrix}$$

$$T = \left(\frac{e^{i\beta_2}}{t_{12}t_{23}}\right)\begin{bmatrix} \left(1 + r_{12}r_{23}e^{-i2\beta_2}\right) & \left(r_{23} + r_{12}e^{-i2\beta_2}\right) \\ \left(r_{12} + r_{23}e^{-i2\beta_2}\right) & \left(r_{12}r_{23} + e^{-i2\beta_2}\right) \end{bmatrix} \qquad \textit{Eq. A.16}$$

By substituting the values of T_{11} and T_{21} from *Equation A.16* into *Equation A.14*, it is possible to obtain the reflection coefficient for a three-phase system which can be seen to the same as previously found (*Equation A.9*).

$$r_{123} = \frac{r_{12} + r_{23}(1 - 2i\beta_2)}{1 + r_{12}r_{23}(1 - 2i\beta_2)} \qquad \textit{Eq. A.17}$$

In isotropic systems the s and p polarisation components are uncoupled making it possible to treat each separately. To calculate the reflection and transmission coefficients for each polarisation it is necessary to apply the 2 x 2 matrix technique twice.

4 x 4 Matrix Method For Anisotropic Stratified Media

To allow calculations of the reflection and transmission coefficients from an anisotropic stratified media it is necessary to use a higher rank matrix system as the *p* and *s* components of the electric and magnetic fields are no longer uncoupled. This technique was originally introduced by Teitler and Henvis [A.4] although it is more commonly known for the development by Berreman [A.5] and it has been recently refined by Schubert [A.6]. A very good overview of this technique, prior to Schubert's contribution is given by Azzam and Bashara [A.3].

By assuming $e^{i\omega t}$ time dependence, Maxwell's first order equations can be represented as a matrix of rank 6.

$$\begin{bmatrix} 0 & 0 & 0 & 0 & -\frac{\partial}{\partial z} & \frac{\partial}{\partial y} \\ 0 & 0 & 0 & \frac{\partial}{\partial z} & 0 & -\frac{\partial}{\partial x} \\ 0 & 0 & 0 & -\frac{\partial}{\partial y} & \frac{\partial}{\partial x} & 0 \\ 0 & \frac{\partial}{\partial z} & -\frac{\partial}{\partial y} & 0 & 0 & 0 \\ -\frac{\partial}{\partial z} & 0 & \frac{\partial}{\partial x} & 0 & 0 & 0 \\ \frac{\partial}{\partial y} & -\frac{\partial}{\partial x} & 0 & 0 & 0 & 0 \end{bmatrix} \begin{bmatrix} E_x \\ E_y \\ E_z \\ H_x \\ H_y \\ H_z \end{bmatrix} = i\omega \begin{bmatrix} D_x \\ D_y \\ D_z \\ B_x \\ B_y \\ B_z \end{bmatrix} \qquad \textit{Eq. A.18}$$

This can be abbreviated to,

$$\begin{bmatrix} 0 & curl \\ -curl & 0 \end{bmatrix} \begin{bmatrix} E \\ H \end{bmatrix} = i\omega \begin{bmatrix} D \\ B \end{bmatrix} \qquad \textit{Eq. A.19}$$

$$RG = i\omega C \qquad \textit{Eq. A.20}$$

Ignoring non-linear effects there is a linear relation between G and C,

$$C = MG \qquad \textit{Eq. A.21}$$

The matrix M is known as the *optical matrix* as it contains all of the information about the optical properties of a medium and has the form,

$$M = \begin{bmatrix} Dielectric & Rotation \\ Rotation & Permeability \end{bmatrix} = \begin{bmatrix} \varepsilon & \rho \\ \rho' & \mu \end{bmatrix} \qquad Eq.\ A.22$$

where each quadrant represents a 3 x 3 matrix corresponding to the properties in the x, y and z directions. Substituting *Equation A.21* into *Equation A.20* gives,

$$RG = i\omega MG$$

or

$$R\Gamma = i\omega M\Gamma \qquad Eq.\ A.23$$

where Γ is the spatial part of G ($G = e^{i\omega t}\Gamma$).

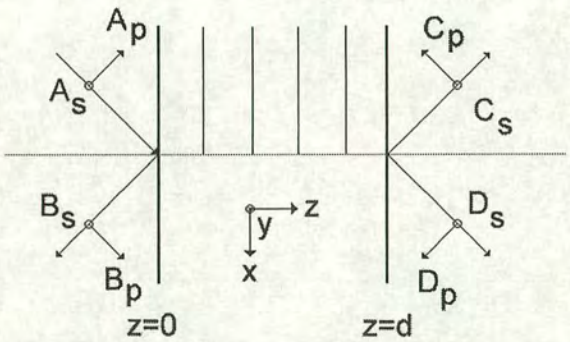

Figure A.4 *s and p polarised components of the incident, reflected and transmitted electromagnetic wave at an anisotropic stratified media.*

By assuming the geometry of the system is the same as shown in *Figure A.4* with the z-axis orthogonal to the plane of the substrate, the symmetry dictates that there is no variation in the y-direction of any of the field components.

$$\frac{\partial}{\partial y} = 0$$

For continuity of the tangential fields at the z=0 boundary all fields in the x-direction should vary as $e^{-i\xi x}$, where ξ denotes the x component of the wave vector of the incident wave. ξ can also be written in terms of the refractive index and the angle of incident of the ambient material, $\xi = \frac{\omega}{c} N_0 \sin\theta_i$. Therefore the *curl* operator can be simplified to,

$$curl = \begin{bmatrix} 0 & -\frac{\partial}{\partial z} & 0 \\ \frac{\partial}{\partial z} & 0 & i\xi \\ 0 & -i\xi & 0 \end{bmatrix} \qquad \textit{Eq. A.24}$$

By substituting *Equation A.24* into the matrix R (as defined in *Equation A.20*), two linear equations and four first order differential equations can be obtained by expanding *Equation A.23*. Solving the two linear components for E_z and H_z in terms of E_x, E_y, H_x and H_y and then substituting these into the four differential equations gives a 4 x 4 matrix of the field variables E_x, E_y, H_x and H_y.

$$\frac{\partial}{\partial z}\begin{bmatrix} E_x \\ H_y \\ E_y \\ -H_x \end{bmatrix} = -i\omega \begin{bmatrix} \Delta_{11} & \Delta_{12} & \Delta_{13} & \Delta_{14} \\ \Delta_{21} & \Delta_{22} & \Delta_{23} & \Delta_{24} \\ \Delta_{31} & \Delta_{24} & \Delta_{33} & \Delta_{34} \\ \Delta_{41} & \Delta_{42} & \Delta_{43} & \Delta_{44} \end{bmatrix} \begin{bmatrix} E_x \\ H_y \\ E_y \\ -H_x \end{bmatrix}$$

or

$$\frac{\partial}{\partial z}\psi = -i\omega\Delta\psi \qquad \textit{Eq. A.25}$$

The Δ matrix is a *differential propagation matrix* from which the propagation of the generalised field vector (ψ) can be specified. The definition of each of the components of the Δ matrix can found on *p344* of reference [A.3] and the value of each component is comprised of ε, μ, ρ and ρ', from *Equation A.22*, and η which can be defined as,

$$\eta = \frac{\xi}{\omega} = \frac{N_0}{c}\sin\theta_i$$

The differential propagation matrix is used to obtain *a partial transfer matrix (T_P or T_P')* for each layer of the stratified media. These matrices connect the in-plane components of the electric and magnetic fields at interfaces separated by a distance d, in a manner similar to the 2 x 2 isotropic method [A.6].

$$\psi(z+d) = \exp(-i\omega\Delta d)\psi(z) = T_P'\psi(z) \qquad \textit{Eq. A.26}$$

$$T_P' = \exp(-i\omega\Delta d)$$

$$T_P' = \left\{ I - i\omega\Delta d - \frac{(\omega d)^2}{2!}\Delta^2 + i\frac{(\omega d)^3}{3!}\Delta^3 + ... \right\}$$

For heterogeneous anisotropic media in which M is dependent on z, by dividing the media into thin slices, such that M is independent of z for each slice, and repeatedly applying *Equation A.26*, it is possible to relate the field at either side of a layered structure. In this case,

$$\psi(z+d) = T_P(z,d)\psi(z)$$

where,

$$T_P(z,d) = T_P'(z+d-h_m, h_m)....T_P'(z+h_1+h_2, h_3)T_P'(z+h_1, h_2)T_P'(z, h_1)$$

The sum of the distances between each of the thin layers (h_1, h_2, ...h_m) equals the total thickness (d). These partial transfer matrices can in turn be used to calculate the *general transfer matrix (T)* when considered with the *transition matrices*. The *transitions matrices* are required to project the tangential parts of the wave existing in the incident medium through to the first interface and then to project the tangential electric and magnetic fields from the last interface back to the exit medium. The *general transfer matrix* is defined as the product of the *incident transition matrix* (L_I), the *partial transfer matrix* for each layer (T_P') and the *exit transition matrix* (L_E).

$$T = L_I^{-1}\prod_{i=1}^{N} T_{iP}(-d_i)L_E. \qquad \textit{Eq. A.27}$$

The final result is the definition of a *general transfer matrix* (T) for any stratified media. A, B, C and D are as depicted in *Figure A.4*.

$$\begin{bmatrix} A_S \\ B_S \\ A_P \\ B_P \end{bmatrix} = T \begin{bmatrix} C_S \\ D_S \\ C_P \\ D_P \end{bmatrix} = \begin{bmatrix} T_{11} & T_{12} & T_{13} & T_{14} \\ T_{21} & T_{22} & T_{23} & T_{24} \\ T_{31} & T_{32} & T_{33} & T_{34} \\ T_{41} & T_{42} & T_{43} & T_{44} \end{bmatrix} \begin{bmatrix} C_S \\ 0 \\ C_P \\ 0 \end{bmatrix} \qquad \textit{Eq. A.28}$$

The coefficients of reflection and transmission for stratified media can be defined as the ratio of the amplitudes of the incident and reflected or transmitted waves and can expressed in terms of the elements of the general transfer matrix. *Equation A.28* gives the relationship between the polarised components on either side of *Figure A.4* The Jones reflection and transmission coefficients, which relate the amplitude of electromagnetic waves before and after an optical component, can be expressed in terms of the elements of the general transfer matrix.

$$r_{ss} = \left(\frac{B_s}{A_s}\right)_{A_p=0} = \frac{T_{21}T_{33} - T_{23}T_{31}}{T_{11}T_{33} - T_{13}T_{31}} \qquad t_{ss} = \left(\frac{C_s}{A_s}\right)_{A_p=0} = \frac{T_{33}}{T_{11}T_{33} - T_{13}T_{31}}$$

$$r_{sp} = \left(\frac{B_p}{A_s}\right)_{A_p=0} = \frac{T_{33}T_{41} - T_{31}T_{43}}{T_{11}T_{33} - T_{13}T_{31}} \qquad t_{sp} = \left(\frac{C_p}{A_s}\right)_{A_p=0} = \frac{-T_{31}}{T_{11}T_{33} - T_{13}T_{31}}$$

$$r_{pp} = \left(\frac{B_p}{A_p}\right)_{A_s=0} = \frac{T_{11}T_{43} - T_{13}T_{41}}{T_{11}T_{33} - T_{13}T_{31}} \qquad t_{pp} = \left(\frac{C_p}{A_p}\right)_{A_s=0} = \frac{T_{11}}{T_{11}T_{33} - T_{13}T_{31}}$$

$$r_{ps} = \left(\frac{B_s}{A_p}\right)_{A_s=0} = \frac{T_{11}T_{23} - T_{13}T_{21}}{T_{11}T_{33} - T_{13}T_{31}} \qquad t_{ps} = \left(\frac{C_s}{A_p}\right)_{A_s=0} = \frac{-T_{13}}{T_{11}T_{33} - T_{13}T_{31}}$$

In comparison to the 2 x 2 matrix method, the uncoupled components r_{pp}, r_{ss}, t_{pp} and t_{ss} are equivalent to *Equations A.14 & A.15*. If the reflection and transmission coefficients were to be calculated for *s* and *p* polarised light for the 2 x 2 system, the results would be denoted r_s and r_p. Using the 4 x 4 matrix system they would be denoted r_{ss} and r_{pp}. The 4 x 4 matrix coupled components r_{sp}, r_{ps}, t_{sp} and t_{ps} do not exist in the 2 x 2 matrix system.

To demonstrate this technique the reflection coefficients are calculated for the simple example of the single interface as used for the calculation of the Fresnel reflection and transmission coefficients. In this case no partial transfer matrix is needed as there is no layers between the incident and exit interfaces. The light is propagating from

medium 1 (N_1) to medium 2 (N_2) with the angles of incidence and transmission given by θ_i and θ_t. The general transfer matrix is the product of the incident and exit transition matrices with,

$$L_I^{-1} = \frac{1}{2}\begin{bmatrix} 0 & 1 & -\frac{1}{N_1\cos\theta_i} & 0 \\ 0 & 1 & \frac{1}{N_1\cos\theta_i} & 0 \\ \frac{1}{\cos\theta_i} & 0 & 0 & \frac{1}{N_1} \\ -\frac{1}{\cos\theta_i} & 0 & 0 & \frac{1}{N_1} \end{bmatrix} \quad L_E = \begin{bmatrix} 0 & 0 & \cos\theta_t & 0 \\ 1 & 0 & 0 & 0 \\ -N_2\cos\theta_t & 0 & 0 & 0 \\ 0 & 0 & N_2 & 0 \end{bmatrix}$$

The origin of these matrices can be found in [A.6].

Therefore from *Equation A.27*,

$$T = \frac{1}{2}\begin{bmatrix} 1+\frac{N_2\cos\theta_t}{N_1\cos\theta_i} & 0 & 0 & 0 \\ 1-\frac{N_2\cos\theta_t}{N_1\cos\theta_i} & 0 & 0 & 0 \\ 0 & 0 & \frac{\cos\theta_t}{\cos\theta_i}+\frac{N_2}{N_1} & 0 \\ 0 & 0 & -\frac{\cos\theta_t}{\cos\theta_i}+\frac{N_2}{N_1} & 0 \end{bmatrix}$$

By using *Equation A.28* and the definitions of the reflection and transmission coefficients for the various polarisation combinations, it is possible to obtain,

$$r_{ss} = \frac{T_{21}T_{33}-T_{23}T_{31}}{T_{11}T_{33}-T_{13}T_{31}} = \frac{\left(1-\frac{N_2\cos\theta_t}{N_1\cos\theta_i}\right)\left(1+\frac{N_2\cos\theta_t}{N_1\cos\theta_i}\right)}{\left(1+\frac{N_2\cos\theta_t}{N_1\cos\theta_i}\right)\left(1+\frac{N_2\cos\theta_t}{N_1\cos\theta_i}\right)} = \frac{N_1\cos\theta_i - N_2\cos\theta_t}{N_1\cos\theta_i + N_2\cos\theta_t}$$

$$r_{pp} = \frac{T_{11}T_{43}-T_{13}T_{41}}{T_{11}T_{33}-T_{13}T_{31}} = \frac{\left(1+\frac{N_2\cos\theta_t}{N_1\cos\theta_i}\right)\left(-\frac{\cos\theta_t}{\cos\theta_i}+\frac{N_2}{N_1}\right)}{\left(1+\frac{N_2\cos\theta_t}{N_1\cos\theta_i}\right)\left(\frac{\cos\theta_t}{\cos\theta_i}+\frac{N_2}{N_1}\right)} = \frac{-N_1\cos\theta_i + N_2\cos\theta_t}{N_1\cos\theta_i + N_2\cos\theta_t}$$

From these equations, under normal incidence conditions, the Fresnel reflection coefficient (*Equation A.6*) can be obtained. A factor of -1 resulting from the definition of the electric vector axis must be borne in mind when considering the r_{pp} case to obtain the same format as r_{ss} [A.7]

$$r_{12} = r_{ss} = r_{pp} = \frac{N_1 - N_2}{N_1 + N_2}.$$

Appendix B: Acronyms

ADC	Analogue to digital converter
ADRAS	Angular dependent RAS
AFM	Atomic force microscopy
CRT	Cathode ray tube
fcc	Face centred cubic
FLC	Ferroelectric liquid crystal
HOPG	Highly ordered pyrolytic graphite
IR	Infra-red
ITO	Indium tin oxide
LC	Liquid crystal
LCD	Liquid crystal display
LEED	Low energy electron diffraction
NMP	N-methyl-2-pyrrolidone
PEM	Photoelastic modulator
PI	Polyimide
PMT	Photo multiplier tube
PVA	Polyvinyl alcohol
PVCi	Polyvinyl cinnamate
RA	Reflection anisotropy
RAS	Reflection anisotropy spectroscopy
RD	Reflection difference
SBZ	Surface Brillouin zone
SEM	Scanning electron microscopy
SPM	Scanning probe microscopy
STM	Scanning tunnelling microscopy
TAS	Transmission anisotropy spectroscopy
TN	Twisted nematic
UHV	Ultra high vacuum
UV	Ultra-violet
XPS	X-ray photoemission spectroscopy

Appendix C: Equipment Photographs

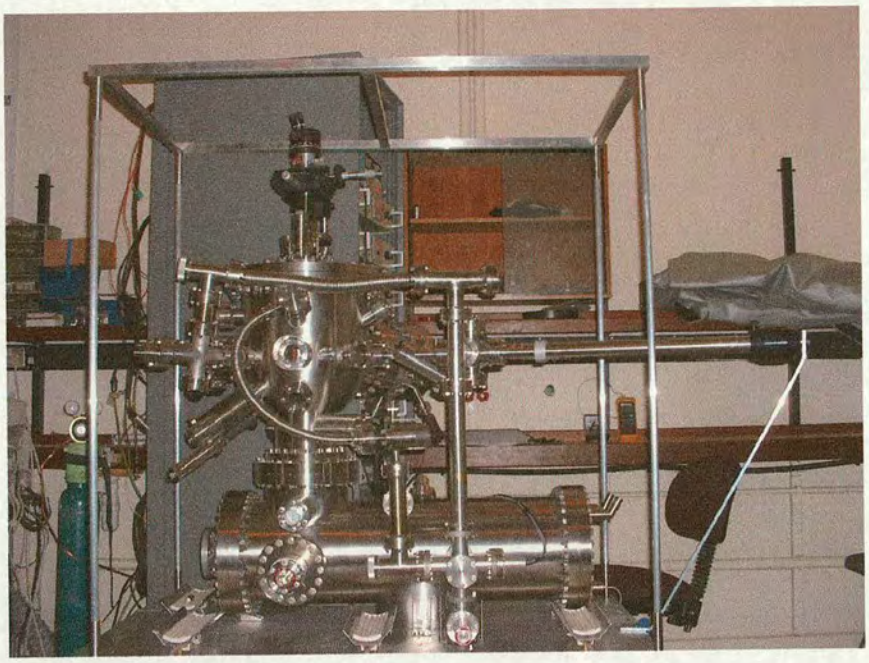

Figure C.1 *Photograph of the vacuum chamber that was constructed and used throughout this project.*

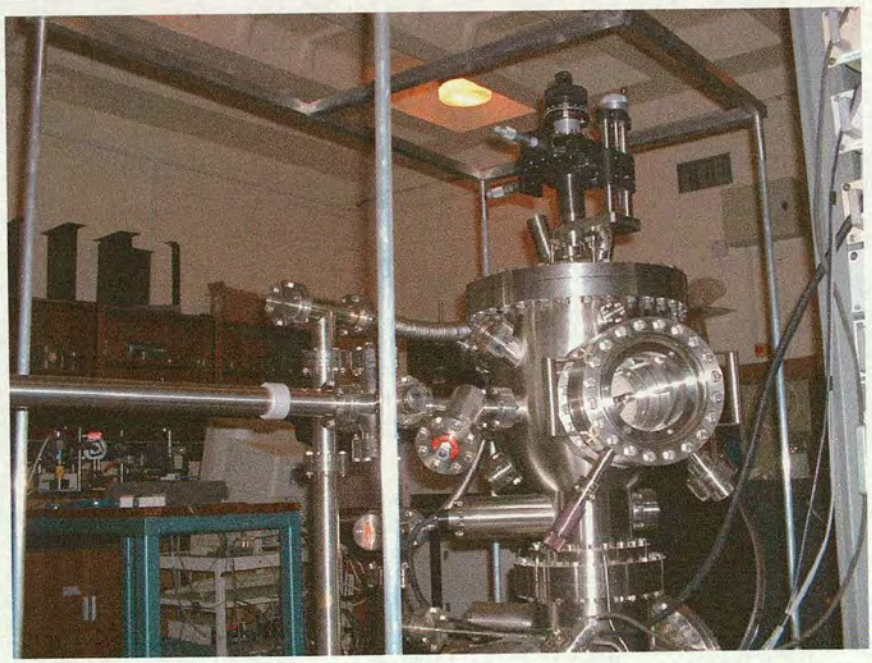

Figure C.2 *Photograph of the vacuum chamber that was constructed and used throughout this project.*

Figure C.3 *Photograph of the reflection anisotropic spectroscopy apparatus which was constructed and used throughout this project.*

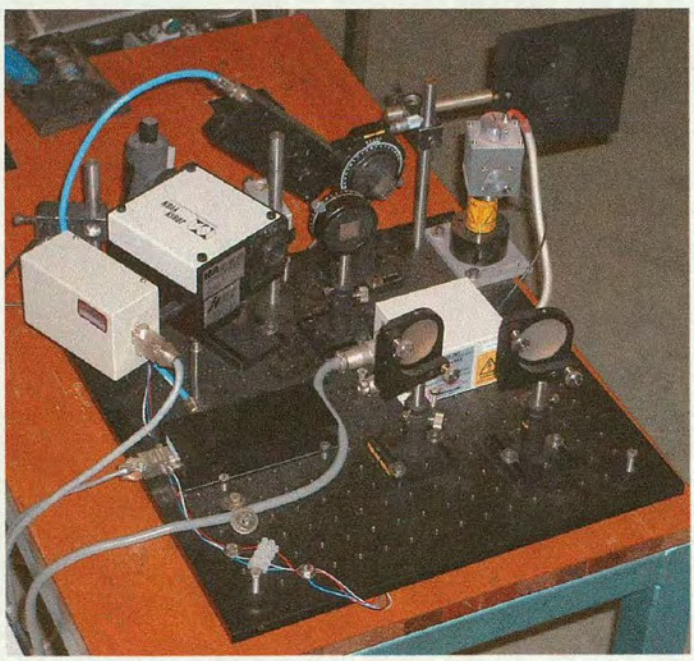

Figure C.4 *Photograph of the reflection anisotropic spectroscopy apparatus which was constructed and used throughout this project.*

Appendix D: Published Papers

phys. stat. sol. (a) **188**, No. 4, 1489–1493 (2001)

RAS as an in situ Monitor of Ion Bombardment

B. F. MACDONALD and R. J. COLE

Department of Physics and Astronomy and Centre for Materials Science and Engineering, University of Edinburgh, Edinburgh, Scotland, EH9 3JZ, UK

(Received July 20, 2001; in revised form August 14, 2001; accepted September 19, 2001)

Subject classification: 78.40.Kc; 78.68.+m; S1.3

RAS is used as a real time monitor of the bombarding of a surface by argon ions. Changing the reference frame of the spectrometer is found to give new insight into the competition between ion-induced and crystallographic anisotropy.

1. Introduction

The new range of surface optical spectroscopies, known collectively as "epioptics", offer *in situ* applicability combined with extremely good surface sensitivity (or even surface specificity). In particular these attributes have enabled reflectance anisotropy spectroscopy (RAS), which measures the difference in normal incidence reflection amplitude for light linearly polarised along two orthogonal directions as a function of photon energy, to make a significant impact in the field of semiconductor micro- and nano-fabrication. In contrast the surface optical anisotropy of metal surfaces has received much less attention, while *in situ* RAS monitoring of processes which *remove* material from surfaces remains largely unexplored, despite the fact that many commercially important processes (e.g. reactive ion etching) lack real time surface diagnostics. This preliminary study of ion bombardment of the Cu(110) surface is aimed at demonstrating the viability of RAS in this context.

Among metals the Group 1B elements (the noble metals) have been the most studied by RAS on account of the relative ease with which clean surfaces can be prepared, even in air. Three mechanisms for optical anisotropy of the (110) surfaces of these elements have been idenitifed: the surface local field effect [1, 2], polarisation selective optical transitions involving surface states [3, 4], and anisotropic surface modification of bulk states [5, 6]. Yet the supposed simplicity of clean noble metal surfaces has not been borne out by experimental results, and there has been some discussion as to what the "true" RA spectra of these elements actually are [2, 4]. The observed dependence of RA spectra on the details of surface preparation and surface history serves to emphasize the sensitivity of the technique to a wide range of surface properties, a fact yet to be exploited in real time monitoring of metals surfaces during processing. Here we extend previous similar studies [5, 7] by focussing on real time RAS measurements during a bombard–anneal cleaning cycle for a Cu(110) sample.

2. Experimental

A Cu(110) crystal was inserted into an ultra-high vacuum chamber (PSP Vacuum Technology) with a base pressure of 10^{-10} mbar and cleaned by cycles of room temperature bombardment by 500 eV Ar ions followed by annealing to 860 K. A phase modulating

 0031-8965/01/18812-1489 $ 17.50+.50/0

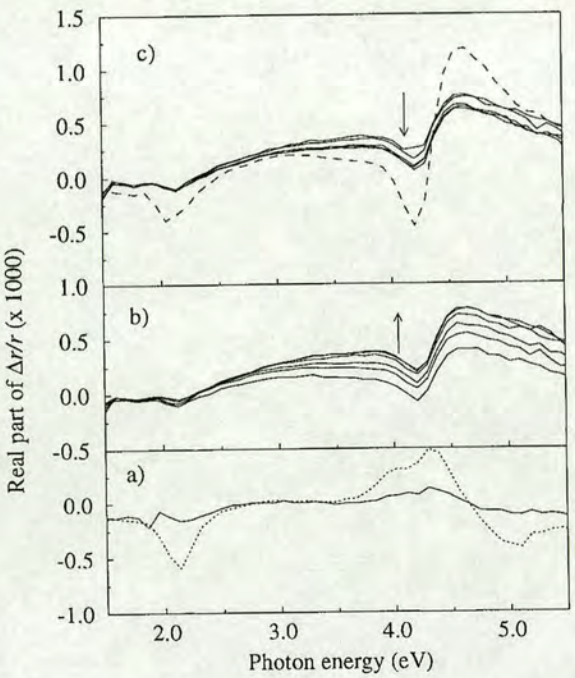

Fig. 1. a) RA spectra of a partially clean Cu(110) sample in the xy-frame (dotted line) and the $x'y'$-frame (solid line). b) Evolution of the RAS signature in the $x'y'$-frame during bombardment of the surface by Ar ions. The lower solid curve was taken after 3 min exposure to the ion beam while subsequent spectra are separated by increments of 9 min. The upward arrow indicates the trend. c) Post-bombardment $x'y'$-frame RA spectra (solid curves) for recovery times of 0, 4, 16, 28 and 40 min. The downward arrow indicates the direction of the trend while the dashed curve is the stabilised RA spectrum in the xy-frame

RA spectrometer following the design of Aspnes was coupled to the vacuum system using a low strain quartz window and could be used to acquire RA spectra in real time at any stage of the cleaning cycle. Experimental artefacts were removed from the experimental data by the standard procedure of determining a correction function from spectra obtained before and after a 90° sample rotation. Surface periodicity could be assessed using low energy electron diffraction (LEED).

The RAS spectrum of the Cu(110) sample 24 h after five bombard–anneal cycles had been performed is shown by the dotted curve in Fig. 1a. To be precise, the measured quantity is the real part of $\Delta r/r$ which is defined by

$$\frac{\Delta r}{r} = 2\,\frac{r_x - r_y}{r_x + r_y}\,, \tag{1}$$

where $r_x(r_y)$ is the complex Fresnel reflection amplitude for light polarised along the $x(y)$ direction. Here we define x to be the [001] direction while y is along [$\bar{1}$10] and we refer to this choice of axes, which are the mirror planes of the Cu(110) surface, as the "xy-frame". Comparison with previous work [3] shows that the prominent feature at 2.1 eV in this spectrum is rather weak, suggesting that the quality of the surface is poor, despite the observation of a relatively sharp 1×1 LEED pattern. Nonetheless, the primary features of the standard Cu(110) spectrum (the negative peak at 2.1 eV and the positive structure with clearly resolved peaks at 3.9 and 4.2 eV) are already well developed. Further cleaning cycles produced the much stronger RAS signature usually presented, but the aim here is to monitor in real time the modification of the surface during such a cycle.

Before resuming the ion bombardment, Ar was admitted into the vacuum chamber and its purity verified using a mass spectrometer. The presence of this gas was found to

have no discernible effect on the optical anisotropy of the partially cleaned Cu(110) surface. Rotating the sample by 36° yielded the RA spectrum shown by the solid curve in Fig. 1a. As expected the measured anisotropy is greatly reduced (by a factor of $\sim\cos(2 \times 36°)$) since the spectrometer is now comparing new directions in the surface ($x' = [\bar{1}1\bar{2}]$ and $y' = [\bar{1}11]$) which are almost equivalent. This sample orientation, which we refer to as the $x'y'$-frame, was chosen so that the $[\bar{1}11]$ azimuth was in the plane of incidence of the Ar ion beam, as in the previous study of Bremer et al. [5]. Contrary to previous work, however, RAS measurements were then performed in real time using the $x'y'$-frame during Ar ion bombarding. The ions impinged on the surface at 45° incidence and the beam density was 15 $\mu A/cm^2$.

3. Results and Discussion

RA spectra obtained during Ar bombardment of the Cu(110) surface as described above displayed a broad oscillatory structure centred on ~4.3 eV, as shown in Fig. 1b. The upward arrow indicates the evolutionary trend of the spectrum. The first spectrum of this series was acquired after 3 min exposure to the beam, while subsequent spectra are separated by 9 min. It can be seen that on this timescale the RAS signature (in the $x'y'$-frame) of the bombarded surface is established directly upon exposure to the ion beam. Only a gradual evolution of the surface optical anisotropy of the bombarded surface is observed in subsequent spectra. Stabilisation of the spectrum is observed at about 40 minutes, indicating that a steady state is achieved on this timescale. When the RAS spectrum of the bombarded surface had been stable for about 15 min the ion beam was shut down. Post-bombarding RAS spectra are shown in Fig. 1c for recovery times of 0, 4, 16, 28 and 40 min. The amplitude of the broad ion-induced feature between 3 and 6 eV can be seen to decay slightly over the first 4 min. It appears that the surface mobility of the Cu(110) surface at room temperature is sufficient to promote a degree of "healing" of the ion-induced surface damage. The RAS results indicate that no significant changes in the surface condition take place after about 20 min.

Consideration of the experimental geometry provokes two questions. Firstly, does the orientation of the reference frame of the RA spectrometer matter? And secondly, does the orientation of the plane of incidence of the ions matter? If the surface modification induced by the incident Ar ions were isotropic in character then the answer to the second question would be 'no' by definition, and similarly the dependence of the RA spectrum on the orientation of the spectrometer would be trivial; for a rotation of the spectrometer by ϑ, the RA spectrum will be scaled by $\cos 2\vartheta$, provided $|\Delta r/r| \ll 1$, but it will not change shape. In fact the RA spectra in Fig. 1b clearly show that the answer to the second question must be 'yes' since, in contrast to the starting surface, the x' and y' azimuths are rendered inequivalent by the bombardment of ions along y', just as one might expect. Given this fact, the answer to the first question may also be 'yes'. Since the ion beam imposes a directionality on the sample which is in general unrelated to the underlying crystallography, the Jones reflection matrix will not be diagonal in either the xy- or the $x'y'$-frame. A diagonal frame must exist, but the required transformation will in general be different for each photon energy, rather like the dielectric axes of a monoclinic crystal [8]. We conclude that in general the *shape* of the RA spectrum will be dependent on the choice of the reference frame, or to put it another way, the azimuthal dependence will furnish additional information.

The xy-frame RA spectrum of the bombarded sample is shown by the dashed curve in Fig. 1c. The anisotropy in this frame is considerably greater than in the $x'y'$-frame. Incidence of the ion beam incident along [$\bar{1}$11] strongly modifies the optical anisotropy along the eigen axes of the clean surface and this is to be expected since the surface crystallography will ensure both the etch rate and the atomic diffusion rate for this surface are anisotropic in the xy-frame. Similar post-bombarding xy-frame results have been observed by Bremer et al. [5] who have modelled the spectrum using the surface local field model which accounted for a surface vacancy fraction. Notice that the xy and $x'y'$ RA spectra of the bombarded sample are not simply related by a scaling factor. We conclude that the Jones matrix does indeed comprise off-diagonal elements and that in situ RAS measurements therefore offer new insight into the kinetic competition of ion-induced and crystallographic anisotropy.

Before moving on we should moderate our earlier statement that the azimuthal direction of the incident ions "does matter". We have found that bombarding along the [001] and [$\bar{1}$10] directions produces xy-frame RA spectra qualitatively similar to that shown in Fig. 1c (where the bombarding direction is [$\bar{1}$11]) but with varying relative intensities of the 2.1 and 4.5 eV structures. The RAS spectra were also distinguishable (both from each other and from an annealed surface) after exposure to air. *Ex situ* atomic force microscopy (AFM) was used to look for differences in morphology which could pinpoint the explanation for these differences. Preliminary results suggest that bombarding along [$\bar{1}$10] creates wide ($\sim 10^2$ nm) terraces with straight steps also running along [$\bar{1}$10]. On the other hand bombarding with a component of ion momentum transverse to the close-packed rows of copper atoms tended to produce less regular step edges which lacked a consistent orientation. While our results for the $x'y'$-frame demonstrate that

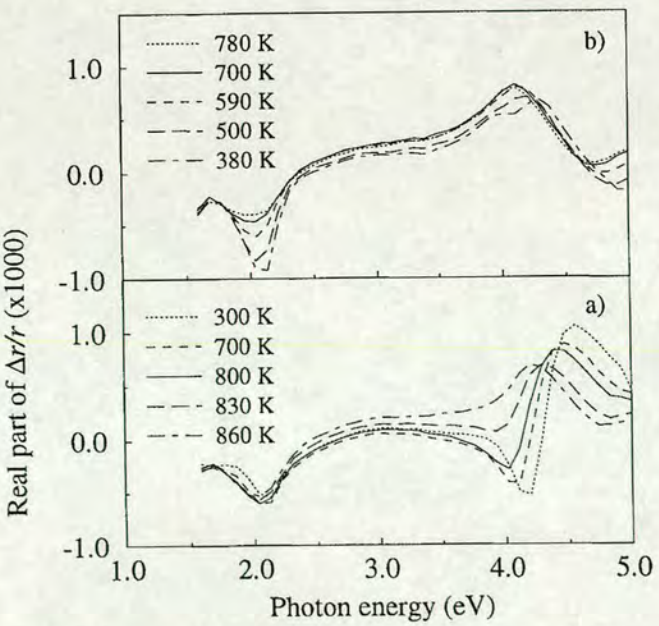

Fig. 2. RA spectra of the Cu(110) surface in the xy-frame a) during annealing and b) subsequent cooling

RAS is sensitive to the direction of the incident ions, we must also conclude that the *xy*-frame results show that the surface crystallography plays a decisive role in determining the structure of the bombarded surface.

Returning now to the dashed curve in Fig. 1c, it can clearly be seen that the RAS signal of the bombarded surface is somewhat further from the "target" spectrum than the spectrum we started with. In particular the feature at 2.1 eV, attributed to transitions between surface states at the $\bar{Y}$ point of the surface Brillouin zone and in some sense a measure of surface order, is seen to be weaker than before. The results in Fig. 2a show this feature is further weakened by annealing. As the temperature reaches 860 K spectral weight in the region 3–5 eV shows substantial redistribution, similar to that observed in the recent study of Martin et al. [8]. The spectra displayed in this sequence correspond to a sample continuously heated until a temperature of 860 K was reached and therefore do not indicate steady state surfaces (except at 860 K). Note that this temperature is somewhat below that required to produce a roughening transition on this surface.

The final stage of the standard cleaning cycle is sample cooling and representative RAS spectra for this process are shown in Fig. 2b. It can be seen that the 2.1 eV feature rises linearly between 800 and 300 K, as observed previously [8]. The positive feature centred on 4 eV does not change significantly until the temperature drops to $\sim$500 K whereupon it moves to slightly higher energy and weakens a little, eventually splitting into two resolved structures below $\sim$400 K.

4. Summary

RAS has been used as a real time monitor of the bombarding of a surface by argon ions. The aim of the present work was to investigate the evolution of surface optical anisotropy of the Cu(110) surface during a cleaning cycle but RAS could equally well be applied *in situ* to a range of conceptually similar processes such as reactive-ion or wet chemical etching. The surface energetics, dynamics and kinetics which determine the bombarding, healing, annealing and cooling steps studied here are relevant to many phenomena, such as epitaxial growth and surface reactivity for example. The value of the azimuthal dependence of RA spectra for systems with non-diagonal Jones matrices was briefly discussed.

Acknowledgements This work was supported by the EPSRC of the UK (GR/N02924), the Royal Society, and by the Nuffield Foundation.

References

[1] Y. Borensztein, W. L. Mochan, J. Tarriba, R. G. Barrera, and A. Tajeddine, Phys. Rev. Lett. **71**, 2334 (1993).
[2] J-K. Hansen, J. Bremer, and O. Hunderi, phys. stat. sol. (a) **170**, 271 (1998).
[3] Ph. Hofmann, K. C. Rose, V. Fernandez, A. M. Bradshaw, and W. Richter, Phys. Rev. Lett. **75**, 2039 (1995).
[4] K. Strahenberg, T. Herrmann, N. Esser, J. Sahm, W. Richter, S. V. Hoffmann, and Ph. Hofmann, Phys. Rev. B **58**, R10207 (1998).
[5] J. Bremer, J-K. Hansen, and O. Hunderi, Surf. Sci. **436**, L735 (1999).
[6] K. Strahenberg, T. Herrmann, N. Esser, and W. Richter, Phys. Rev. B **61**, 3043 (2000).
[7] D. S. Martin, A. Maunder, and P. Weightman, Phys. Rev. B **63**, 155403 (2001).
[8] See, for example, M. Born and E. Wolf, Principles of Optics, Cambridge University Press, Cambridge 1999 (p. 806).

phys. stat. sol. (a) **188**, No. 4, 1577–1581 (2001)

Reflection Anisotropic Spectroscopy as a Tool in the Fabrication of Liquid Crystal Devices

B. F. MACDONALD (a), R. J. COLE (a), W. ZHENG (b), and C. MIREMONT (b)

(a) Department of Physics and Astronomy, University of Edinburgh, Edinburgh, EH9 3JZ, UK

(b) Department of Electrical and Electronic Engineering, University of Edinburgh, Edinburgh, EH9 3JZ, UK

(Received July 12, 2001; accepted August 6, 2001)

Subject classification: 61.30.–v; 78.66.Qn; S12

We demonstrate the potential of Reflection Anisotropic Spectroscopy (RAS) as a new tool for predicting optical microelectronic device characteristics prior to assembly. The Reflection Anisotropy (RA) of polymer alignment layers has been studied as a function of rubbing. This data contains information about the suitability of the surface as an alignment layer as well as film thickness.

1. Introduction

Since its introduction, RAS has been widely used to provide *in-situ* monitoring of semiconductor growth. Since then it has been used to study model systems under ultra high vacuum conditions. Now, many new applications are being found. In this paper we present preliminary work which demonstrates RAS has applications to the fabrication of Liquid Crystal (LC) devices by the characterisation of the polymeric alignment layer. Topographical information of the surfaces is obtained using Atomic Force Microscopy (AFM).

Polymers are an important and commonly used material in the field of homogeneous alignment of LC molecules [1–5]. By unidirectionally rubbing a thin film of polymer with a fibrous material such as velvet, the molecular alignment for certain LCs can be promoted. It is thought [1, 2] alignment is produced by orientating the molecular chains of the polymer during the rubbing process. An alternative to this theory proposes the scratches and grooves on the surface of the polymer, induced by the rubbing process, may be the cause of the alignment [3]. Many different techniques have been used previously to study the effect of rubbing polymer surfaces [4, 5]. Here we show the possibility of using RAS to predict the alignment quality produced by a rubbed polymer film by measuring the RA of the alignment layer before the device is constructed.

2. Experimental Details

In these experiments two different polymers, Nylon 6,6 and LQ 1800, a Polyimide (PI) gratefully obtained from HD Microsystems Ltd, were studied on Indium Tin Oxide (ITO) coated glass slides. The slides were ultrasonically cleaned directly before spin coating. To prepare the Nylon samples, 1 mg of Nylon 6,6 was diluted in 20 ml of m-cresol and then spin coated onto the substrate at 3000 rpm for 1 min. The sample was then baked at 80 °C for 1 h. The polyimide samples were prepared by spin coating the substrate at 3000 rpm for 1 min with a 5% solution of LQ 1800 dissolved in NMP. The PI samples were cured

 0031-8965/01/18812-1577 $ 17.50+.50/0

initially by soft baking at 100 °C for 15–30 min followed by thermal curing at 250 °C for 100 min. The procedure used here for preparing both types of samples is the same used when preparing samples for the construction of LC devices.

The machine used to rub the samples has been custom made and is composed of a flat plate, housing the sample, which is moved laterally at a defined speed underneath a rotating velvet coated drum. We define one rubbing cycle, or one rub, as one pass through under the rotating drum. For the duration of the remainder of the experiment the surface rubbing procedure was continuously alternated with the data collection procedure. A correction function based upon RA data obtained at sample rotations of 0° and 90° was used to remove artefacts. Reproducibility of all data was obtained by repeating the experiment for several samples. Additionally, reproducibility of the AFM data was obtained by imaging several different areas of each sample.

RAS is a linear optical experimental method used to probe surface anisotropy as a function of photon energy incident upon a sample. The difference between the reflectivity for light linearly polarized along two perpendicular directions (a and b) at normal incidence is measured (Δr). The result is given in terms of the quotient of the change in the samples reflectivity and the average reflectivity (r),

$$\frac{\Delta r}{r} = 2\,\frac{(r_a - r_b)}{(r_a + r_b)}\,. \tag{1}$$

RA spectra and AFM images were taken of the prepared substrates before any surface modification. The RA analysis was carried out using apparatus with the same design as used by Aspnes et al. [6] incorporating a photoelastic modulator. The samples were studied with the rubbing direction in the same direction as b. All AFM measurements were obtained in contact mode using a Molecular Imaging PicoScan.

3. Results and Discussion

Figure 1 shows the development of the RA spectra obtained from a Nylon sample during the rubbing process. Individual spectra were taken after the completion of one rubbing cycle. It is apparent the amplitude of the RA signal prior to any rubbing shows little anisotropy. Topographical AFM images support this and can be seen in Fig. 2a. Also in Fig. 2a we can see some surface structure, probably due to the drying process, all of which appears isotropic. After one rub the anisotropy increases to its maximum

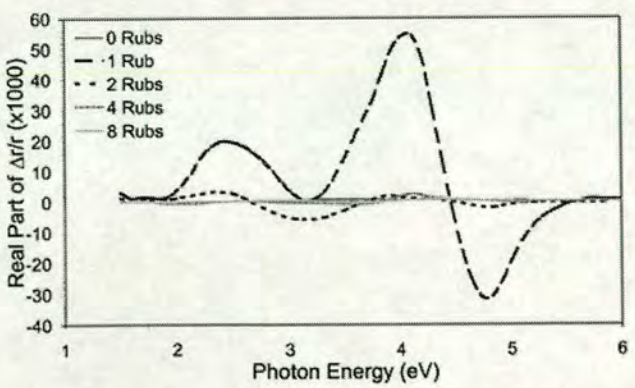

Fig. 1. RA spectra taken from an ITO/glass slide spin-coated with Nylon 6,6. The development of the signal for 0, 1, 2, 4 and 8 unidirectional rubs is shown to peak after one rub and then decrease back towards the initial value

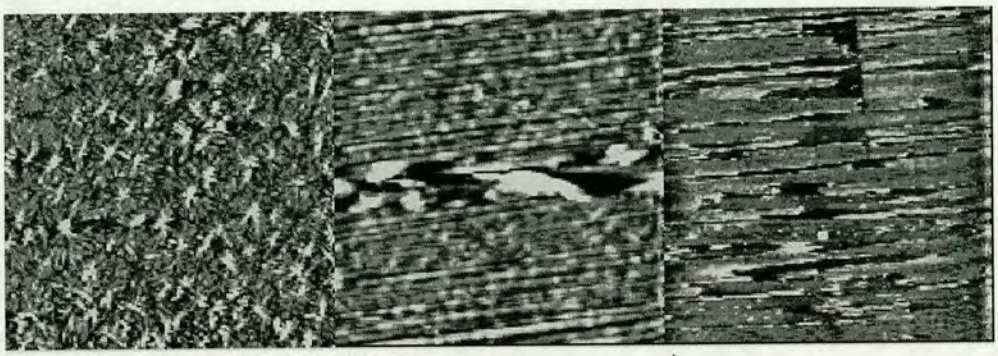

a) b) c)

Fig. 2. Contact mode AFM images, 30×30 μm^2, of a spin-coated film of Nylon 6,6 on an ITO coated glass substrate. Images taken a) prior to any surface treatment, b) after one rubbing cycle and c) after four rubbing cycles. The images show the modification and then damage to the surface after repeated rubbing. The z-scales of the images are 16 nm, 46 nm and 25 nm respectively, where the highest points are shown in white

value of ~6%. A reduction in amplitude can be seen after an additional rub. Subsequent rubbing of the sample reduces the RA spectra to levels comparable with the unrubbed sample with amplitudes at approximately 1/50th of the maximum value.

The large amplitude of the RA spectra after the initial rub may be explained by considering Fig. 2b. It can be seen the sample is clearly anisotropic having grooves at ~5 ° to the horizontal axis over the entire surface. Also to be noted on the same image is the uneven area approximately half way up the vertical axis which runs the full length of the image. It is likely this area has been created by the sample being over rubbed slightly, which for this material appears to cause significant damage to the surface. Additional rubbing reduces the RA amplitude further indicating more damage to the surface has occurred, Fig. 2c confirms this. It is probable the Nylon film is being gradually removed from the surface by continuous rubbing. The low dark areas visible on the AFM image of Fig. 2c are likely to be the ITO/glass substrate. It is very possible the entire surface has been worn to some degree.

The peaks seen in Fig. 1 and Fig. 3 are thought to be the result of a multilayer interference effect. The position and periodicity of the peaks in both figures can be pre-

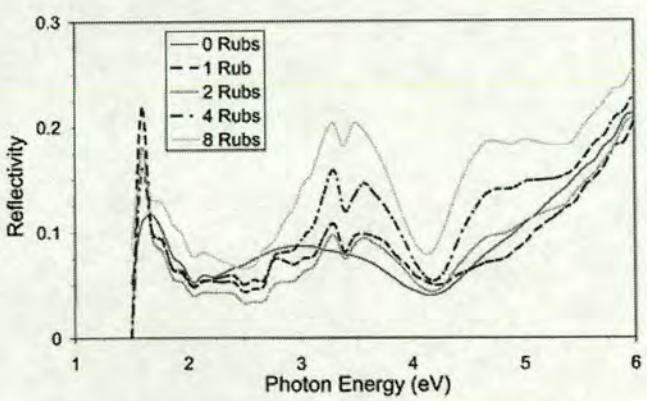

Fig. 3. The amplitude of the reflectivity, which is plotted as a function of energy, can be seen to increase with the number of rubs the sample has been subjected to. Periodicity due to multilayer interference effects can also be seen. The reflectivity data has been normalised using a silicon wafer and data from [7]

dicted using the simple relation for constructive interference, $2nd = m\lambda$. The predicted energies match almost exactly with the experimental results. The shape of RA spectra seen is the superposition of a multilayer interference effect onto the true RA spectra, specific to the polymer, which is centred around 3.2 eV. It is not necessary to have a more detailed explanation as our main interest is the increase and decrease of RA and how this is linked to alignment quality.

Figure 3 shows the amplitude of the reflected light is dependent on the number of rubs. The gradual removal of Nylon from the substrate by repeated rubbing, as suggested earlier, may be the explanation. Initially, before the sample has been rubbed, the reflectivity is low. As the sample is rubbed more, the reflectivity increases indicating more of the underlying ITO layer is exposed to the incident light.

Using the AFM data to back up the results of the RA spectra of the rubbed Nylon surfaces, it has been shown RAS can be used to predict the suitability of a surface to be used as an alignment layer. It is clear that Nylon is not suitable in this situation as the surface is very susceptible to be being damaged by over rubbing. To continue our studies, the experiment was repeated using the PI coated samples. Exactly the same procedure as used for the Nylon sample was repeated. In Fig. 4 the RA amplitude can be seen to increase as a function of the number of rubs. Even after 20 rubs the amplitude is still growing although the rate of growth is slow and appears to be heading for saturation shortly after the 20th rub.

AFM data not presented in this paper shows the initial PI surface to be flatter (PI maximum height of 10 nm compared to 16 nm for Nylon). The maximum height for the Nylon film was reached by over 100 peaks while the PI film showed only on average 3 peaks at the maximum height over a 30×30 μm^2 area. After the first rub the surface appears anisotropic with grooves similar to those found in the Nylon film. Continuous rubbing was found to increase the density of grooves and greatly increase the depth of a few grooves. After several rubs the surface becomes more abundant with defects, whether these are dirt or lumps of PI is not clear. It is clear however they result from the rubbing process.

The samples were made into simple LC cells by putting two substrates together, polymer surfaces facing each other, with the rubbing directions anti-parallel. The surfaces were separated by 2.4 μm spacers and the gap filled with LC. Observations of the cells between crossed polarisers under an optical microscope revealed the defects seen on

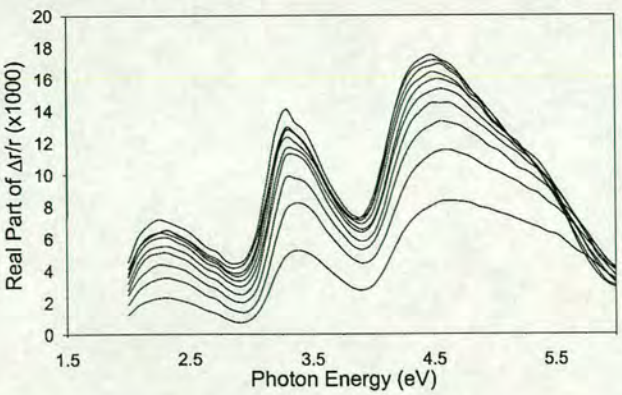

Fig. 4. The development of RA spectra as a function of rubbing on a PI coated ITO/glass slide. The lowest curve corresponds to 2 rubs, the highest curve to 20 rubs. Multilayer inference is clearly visible

the polymer surface lower the quality of the alignment. These observations suggest that in order to optimise the alignment of LCs between rubbed surfaces, a compromise must be reached between maximising the level of anisotropy and minimising the number of defects on the surface of the alignment layer. It may be necessary to find not only the minimum number of rubs required to saturate the anisotropy but to also find where the best alignment occurs in terms of a percentage of the maximum.

4. Summary

The results indicate the potential RAS has as a tool in characterising polymer alignment layers. The behaviour of RA spectra obtained from rubbed Nylon films can be explained by the removal of the Nylon from the substrate during the rubbing process. AFM images of the samples suggest the Nylon film is being removed from the surface. Studies of rubbed PI films show the anisotropy increases until saturation as a function of rubbing. Although the anisotropy is not a direct measure of the alignment quality of the polymer film, the RAS data from the film can be used as a guide to estimate alignment quality. Other work carried out in this field by the authors, as yet unpublished, suggest RAS would be better suited to study ultra-thin films of photoaligned surfaces which would utilise the higher sensitivity RAS has to offer.

Acknowledgements We acknowledge HD microsystems Ltd for supplying the polyimide, the EPSRC for the funding of BFM and grants GR/N02924 &GR/M13534/01, the Nuffield foundation for grant NAL/00073/9 and the Royal Society.

References

[1] J. M. Geary, J. W. Goodby, A. R. Kmetz, and J. S. Patel, J. Appl. Phys. **62**, 4100 (1987).
[2] S. Ishihara, H. Wakemoto, K. Nakazima, and Y. Matsuo, Liquid Cryst. **4**, 669 (1989).
[3] D. W. Berremann, Phys. Rev. Lett. **28**, 1683 (1972)
[4] X. Wei, X. Zhuang, S. Hong, T. Goto, and Y. Shen, Phys. Rev. Lett. **82**, 4256 (1999).
[5] C. L. H. Devlin, S. D. Glab, S. Chiang, and T. P. Russell, J. Appl. Polym. Sci. **80**, 1470 (2001).
[6] D. E. Aspnes, J. P. Harbison, A. A. Studna, and L. T. Florez, J. Vac. Sci. Technol. (A) **6**, 1327 (1988).
[7] D. F. Edwards, Handbook of Optical Constants for Solids, Ed. E. D. Palik, Academic Press, Orlando/London 1985 (p. 547).

Separation of optical anisotropies by angular dependent reflection anisotropy spectroscopy

B. F. Macdonald and R. J. Cole[a)]
Department of Physics and Astronomy and Centre for Materials Science and Engineering, University of Edinburgh, Edinburgh EH9 3JZ, United Kingdom

(Received 2 January 2002; accepted for publication 18 March 2002)

Double rubbing of polymer films, which finds applications in modern liquid crystal devices, has been investigated using reflection anisotropy spectroscopy (RAS) and atomic force microscopy. A method of gauging the relative strength of rubbing in two different directions, based upon the dependence of observed RAS signals on the sample azimuthal angle, has been found. Angular dependent measurements are shown to be a useful extension of the standard technique by allowing angular dependent sources of optical anisotropy to be separated experimentally. © *2002 American Institute of Physics.* [DOI: 10.1063/1.1478784]

Over the last decade we have seen the development of optical spectroscopies that offer real time *in situ* nanoscale surface characterization. One of these "epioptic" techniques, reflection anisotropy spectroscopy (RAS), also known as reflection difference spectroscopy (RDS), was conceived[1] as a nondestructive process control tool for commercial semiconductor epitaxy but the benefits of simplicity, speed and low cost have encouraged studies of diverse systems, such as molecular adsorbates,[2] catalysts,[3] Langmuir–Blodgett films,[4] solid–liquid interfaces[5] and surface-induced stress.[6] Here we demonstrate the viability of process control in liquid crystal device fabrication. In particular we show a simple extension of the standard RAS technique which allows convenient characterization of multidirectional overrubbed alignment layers, and hence how "azimuth-dependent" RAS can disentangle optical anisotropies derived from independent mechanisms.

Homogeneous alignment of liquid crystal (LC) molecules is essential to the fabrication and optimal operation of liquid crystal displays (LCDs), and can be promoted by a variety of means, including rubbing of a thin polymer film, oblique evaporation of a silicon oxide layer and photoalignment. Despite problems associated with charging and surface debris, rubbing is by far the dominant technique used in the commercial display industry. Accordingly, rubbed polymers continue to attract great scientific interest. A recent development is multidirectional rubbing in which a polymer film is first rubbed in one direction and then overrubbed in a different direction.[7–10] LC orientation on overrubbed polymer surfaces is believed to lie between two rubbing directions.[7,10] In recent reports it was suggested that overrubbing reduces the number of steps required to make multidomain displays which significantly increases the viewing angle, traditionally a weakness of LCD technology.[11] In this work we have combined RAS and atomic force microscopy (AFM) to investigate multidirectional overrubbing.

Indium–tin–oxide coated glass slides were ultrasonically cleaned before spin coating at 3000 rpm for 1 min with a 5% solution of the polyimide LQ 1800 (HD Microsystems Ltd.) dissolved in *N*-methyl-2-pyrollidinone. The samples were soft baked at 100 °C for 15–30 min followed by thermal curing at 250 °C for 100 min. This same procedure is used in the construction of LC devices. A correction function based upon RAS data obtained at perpendicular azimuthal angles was used to remove artifacts from the data, and the reproducibility of the results was checked by studying several samples.

RAS analysis of the unrubbed samples revealed negligible optical anisotropy. Corresponding topographic AFM images, obtained in contact mode using a Molecular Imaging PicoSPM, confirmed the samples to be isotropic. After mechanically rubbing the surface of the polyimide, microgrooves were observed along the rubbing direction, as can be seen in Fig. 1(a). The RAS spectrum after rubbing is shown in Fig. 2(a). To be precise the measured quantity is the real part of $\Delta r/r$ where

$$\frac{\Delta r}{r} = 2\frac{(r_{xx} - r_{yy} + r_{xy} - r_{yx})}{(r_{xx} + r_{yy} + r_{xy} + r_{yx})}, \tag{1}$$

and r_{ij} are the elements of the Jones matrix (i.e., the complex Fresnel amplitudes for converting i to j polarization) for normal incidence reflection. RAS spectra can in principle be simulated using phenomenological models to yield material parameters such as the composition, layer thicknesses and roughness.[12] However, we are primarily concerned here with

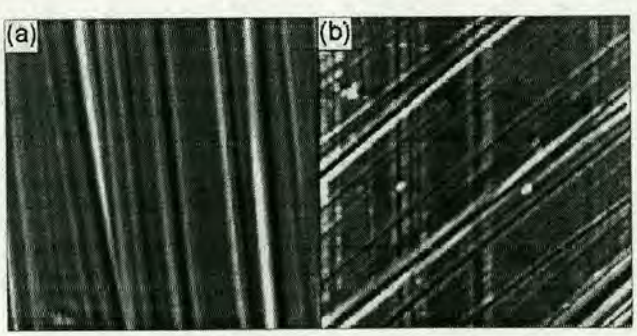

FIG. 1. Contact mode AFM images of (a) a typical rubbed polymer surface and (b) a rubbed polymer surface with a single overrub at an angle to the initial rubbing direction. Each image is ~10 μm^2 and the maximum heights are 35 and 25 nm, respectively.

a)Electronic mail: rjc@ph.ed.ac.uk

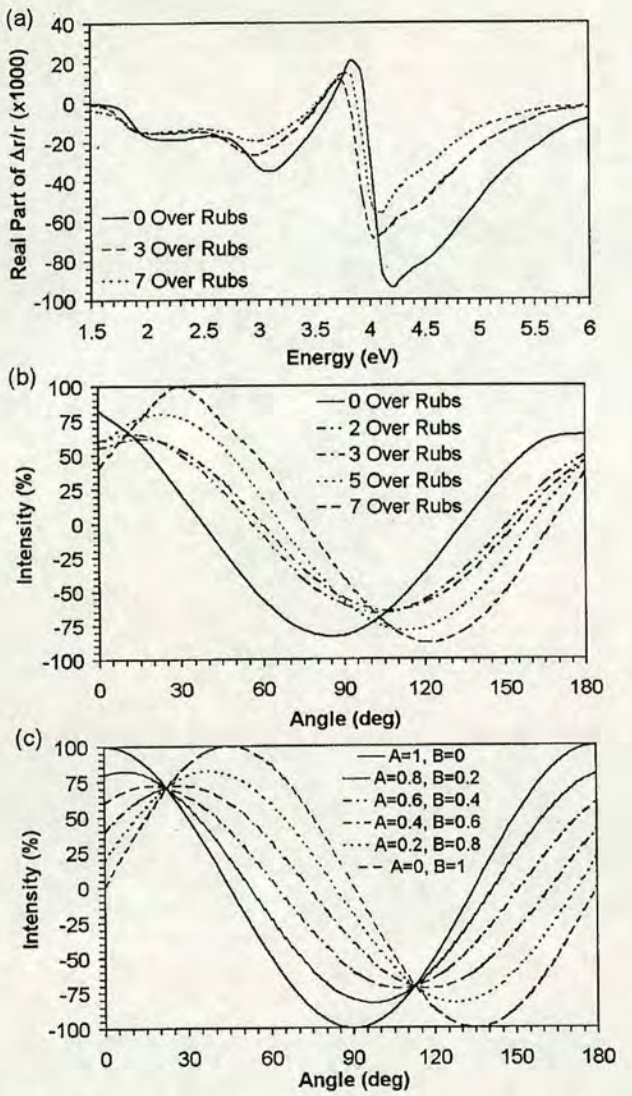

FIG. 2. (a) RAS of a singly rubbed sample with zero, three and seven overrubs at angle φ to the initial rub. In each case $\theta=0°$. (b) ADRAS curves at 3 eV for multiple overrubs. (c) Simulation of ADRAS based upon $A\cos(2\theta)+B\cos[2(\theta-\varphi)]$ where $B=1-A$.

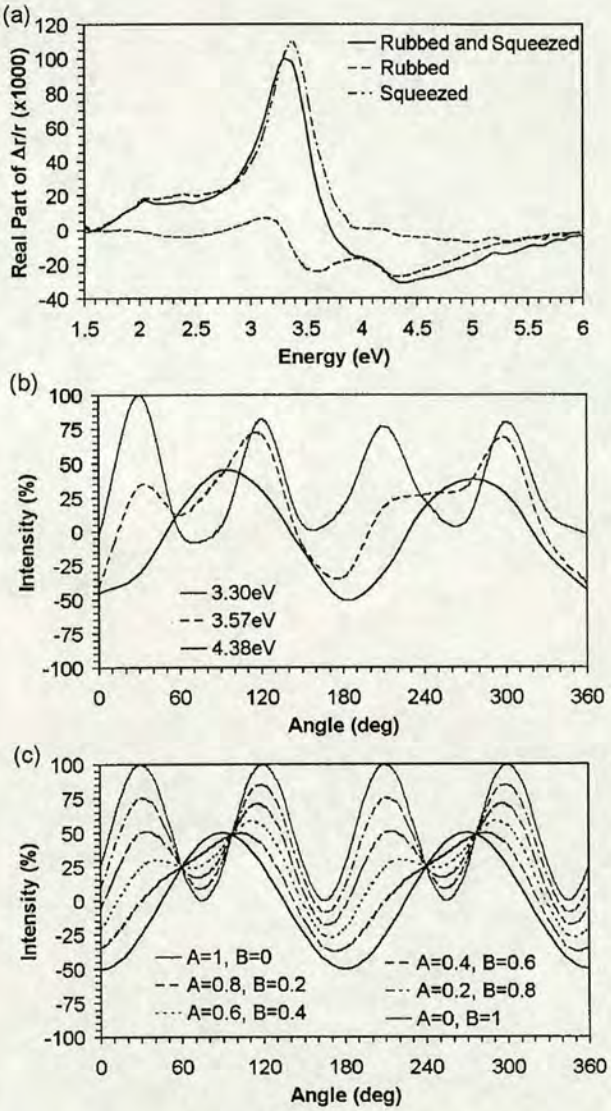

FIG. 3. (a) RAS spectra of a rubbed and squeezed sample. In each case $\theta=30°$. (b) ADRAS at a selection of energies demonstrating different angular variations of different anisotropic components. (c) ADRAS simulation using $-A\cos(2\theta)+2B\sin^2[2(\theta-15)]$, demonstrating the addition of different anisotropic components.

the dependence of RAS signals on the sample azimuthal angle θ, defined as the angle between the y axis of the spectrometer and the rubbing direction of the sample. This is shown for the 3 eV RAS signal of the rubbed polymer by the solid curve in Fig. 2(b). The same θ dependence was observed for all photon energies. For $\theta=0$, x and y are orthogonal linear polarizations, the off-diagonal elements r_{yx} and r_{xy} vanish, and Eq. (1) simplifies to the standard expression.[1] Introducing coordinate rotation should make the RAS signal vary as $\cos(2\theta)$ and this is what we see experimentally when the sample is rotated.

The polyimide surface was then overrubbed a number of times at an angle φ to the initial rubbing direction using the same rubbing parameters. RAS spectra after overrubbing are shown in Fig. 2(a), and AFM images of the surface, shown in Fig. 1(b), appear very similar to those previously reported[9] and clearly show the initial rubbing underlying the overrubbing. The RAS line shape is unchanged as expected but its angular dependence (ADRAS) is modified: Fig. 2(b) shows the ADRAS maximum moving towards higher θ with an increase in overrubbing. If the overrubbing completely replaces the original microgrooves one would expect $\cos[2(\theta-\varphi)]$ azimuthal dependence, but in general there will be two contributions: $A\cos(2\theta)+B\cos[2(\theta-\varphi)]$. For the present case where $\varphi\approx45°$, this expression can be rewritten as $C\cos[2(\theta-\delta)]$, where $2\delta=\arctan(B/A)$ and is therefore a measure of the *relative* residual anisotropy for the two rubbing directions, and $C=\sqrt{A^2+B^2}$ which is a measure of the total rubbing strength. Thus ADRAS measurements offer a direct means by which to characterize overrubbed samples and hence of predicting the behavior of the LC devices to be constructed with them.

The experimental results in Fig. 2(b) are qualitatively reproduced by the simulation in Fig. 2(c) which assumes $B=1-A$. However it is significant that even after seven overrubs we find that the ADRAS maximum does not reach $\theta=\varphi$. We note also that the ADRAS maximum for seven overrubs is stronger than that for the initial rub. Surprisingly the memory of the initial rub persists although $B>A$. These deductions are in agreement with the results of Kim *et al.*[7] and are further supported by AFM results. We observed for

repeated rubbing along φ that the corresponding microgrooves are enhanced but remnants of the initial microgrooves remain.

The angular dependent measurements considered here suggest ADRAS could be a useful extension of the standard technique by allowing sources of optical anisotropy such as microgrooves, surface steps, aligned molecules, stress and external fields with a distinct θ dependence to be experimentally separated. We now demonstrate this process using results obtained for a 10 mm^2 rubbed polymer coated indium–tin–oxide on glass sample subjected to mechanical stress applied 45° to the rubbing direction. The RAS spectrum of the rubbed and squeezed sample is shown by the solid curve in Fig. 3(a), while ADRAS curves for photon energies of 3.30, 3.57 and 4.38 eV can be seen in Fig. 3(b). The signal at 4.38 eV shows 180° periodicity while that at 3.30 eV has 90° periodicity indicating the presence of two distinct sources of anisotropy. The first is rub induced, as discussed earlier, while the second is stress-induced birefringence (the photoelastic effect). The 90° periodicity of the latter is due to reflections from the lower surface of the sample with polarization parallel and perpendicular to the stress combining *incoherently* on account of their large phase difference. The simulation in Fig. 3(c) shows that the ADRAS curves of all photon energies can be decomposed into weighted sums of the cosine and sine-squared contributions. Conversely, a numerical fit of each ADRAS curve allows the stress-induced and rub-induced optical anisotropy spectra to be separated. For the present case this can be achieved by relieving the external stress, but usually competing mechanisms cannot simply be "switched off." Various mechanisms, including surface-induced substrate strain,[6] have been proposed to explain the RAS of surfaces.[6] ADRAS may be a useful tool in clarifying the fundamental questions which still surround the nature of surface optical anisotropy, even for model systems.

In conclusion, double rubbing of a polymer film with applications to LC alignment was investigated using RAS and AFM. An angular-dependent extension to RAS, ADRAS, was used to gauge the relative strength of rubbing in two different directions.

This research was funded by The Royal Society, The Nuffield Foundation and EPSRC (GR/N02924/01). The authors wish to thank Dr. W. Zheng for preparing the polymer samples.

[1] See, for example D. E. Aspnes, J. P. Harbison, A. A. Studna, and L. T. Florez, Appl. Phys. Lett. **52**, 957 (1988).
[2] B. G. Frederick, J. R. Power, R. J. Cole, C. C. Perry, Q. Chen, S. Haq, Th. Bertrams, N. V. Richardson, and P. Weightman, Phys. Rev. Lett. **80**, 4490 (1998).
[3] S. M. Scholz, F. Mertens, K. Jacobi, R. Imbihl, and W. Richter, Surf. Sci. **340**, L945 (1995).
[4] C. Di Natale, C. Goletti, R. Paolesse, F. Della Sala, M. Drago, P. Chiaradia, P. Lugli, and A. C'Amico, Appl. Phys. Lett. **77**, 3164 (2000).
[5] B. Sheridan, D. S. Martin, J. R. Power, S. D. Barrett, C. I. Smith, C. A. Lucas, R. J. Nichols, and P. Weightman, Phys. Rev. Lett. **85**, 4618 (2000).
[6] R. E. Balderas-Navarro, K. Hingerl, A. Bonanni, H. Sitter, and D. Stifter, Appl. Phys. Lett. **78**, 3615 (2001).
[7] Y. J. Kim, Z. Zhuang, and J. S. Patel, Appl. Phys. Lett. **77**, 513 (2000).
[8] H. Kikuchi, J. A. Logan, and D. Y. Yoon, J. Appl. Phys. **79**, 6811 (1996).
[9] M. P. Mahajan and C. Rosenblatt, Appl. Phys. Lett. **75**, 3623 (1999).
[10] D.-H. Chung, Y. Takanishi, K. Ishikawa, H. Takezoe, and B. Park, Jpn. J. Appl. Phys., Part 1 **40**, 1342 (2001).
[11] P. Chaudhari, J. Lacey, J. Doyle, E. Galligan, S. C. A. Lien, A. Callegari, G. Hougham, N. D. Lang, P. S. Andry, R. John, K. H. Yang, M. H. Lu, C. Cai, J. Speidell, S. Purushothaman, J. Ritsko, M. Samant, J. Stohr, Y. Nakagawa, Y. Katoh, Y. Saitoh, K. Sakai, H. Satoh, S. Odahara, H. Nakano, J. Nakagaki, and Y. Shiota, Nature (London) **411**, 56 (2001).
[12] As described within the context of spectral ellipsometry by R. M. A. Azzam and N. M. Bahara, *Ellipsometry and Polarised Light* (North-Holland, Amsterdam, 1987).

INSTITUTE OF PHYSICS PUBLISHING JOURNAL OF PHYSICS D: APPLIED PHYSICS

J. Phys. D: Appl. Phys. **35** (2002) L41–L43 PII: S0022-3727(02)35460-3

RAPID COMMUNICATION

RAS—a new process control tool in liquid crystal device fabrication

B F Macdonald[1], W Zheng[2], R J Cole[1] and I Underwood[2]

[1] Department of Physics and Astronomy and Centre for Materials Science and Engineering, University of Edinburgh, Edinburgh, EH9 3JZ, UK

[2] Department of Electronics and Electrical Engineering, University of Edinburgh, Edinburgh, EH9 3JZ, UK

Received 4 April 2002
Published 21 May 2002
Online at stacks.iop.org/JPhysD/35/L41

Abstract

Ion beam etching of surfaces has recently been shown to be an attractive liquid crystal alignment technique for use in the commercial fabrication of liquid crystal displays. Reflectivity and atomic force microscopy measurements suggest the alignment ability of an ion-etched surface is promoted by modifications at the atomic scale. Reflection anisotropy spectroscopy is demonstrated as a real time monitor of the etching process, promising a process control tool for the next generation of liquid crystal devices.

The alignment of liquid crystal (LC) molecules is fundamental to the fabrication and optimum operation of liquid crystal displays (LCDs). While this can be engineered by a variety of means, it is the crude process of rubbing a polymer film with a piece of fabric that dominates in the commercial displays industry. Thus far the considerable inertia of sustained investment in the rubbing procedure has protected its pre-eminence, but with recent advances in resolution the limitations of rubbing are becoming increasingly troublesome. For example, degradation of the rubbing fabric can lead to non-uniformity of the alignment layer and streaking defects in completed displays, resulting in the rejection of entire batches, i.e. hundreds of displays [1]. This is a problem which will only be emphasized by the steady scaling up of substrate size [2] and whose occurrence highlights the need for both an improved alignment strategy and a real time diagnostic to monitor, and ideally control, LCD fabrication. The pioneering work of Sun *et al* [3] has shown that argon ions, when directed with oblique incidence, can induce anisotropic surface modifications capable of providing an alignment template for LC molecules. Very recently, Chaudhari *et al* have demonstrated this alignment technique to be well suited to the commercial production of LCDs and to be superior in several respects to rubbing [1]. The aim of this work is to extend our preliminary *ex situ* measurements in this field [4, 5] to demonstrate reflection anisotropy spectroscopy (RAS) in the role of a real time process control tool.

It has been suggested that homogeneous alignment of LC molecules is promoted by the orientation of polymer chains within the surface layer [6]. In general, the change in the reflectance of a material due to the modification of near nanoscale surface regions is small and therefore surface information contained within reflectance measurements is very difficult to extract. However RAS is an optical spectroscopy ideally suited to this purpose since it is surface *specific*, rather than simply surface *sensitive*, and furthermore isolates the *anisotropic* contribution to the optical response. To be precise, RAS measures

$$\frac{\Delta r}{r} = 2\frac{r_x - r_y}{r_x + r_y}, \tag{1}$$

the anisotropy in Fresnel complex reflection amplitudes for orthogonal polarizations at normal incidence. In addition to this intrinsic 'double discrimination', RAS offers submonolayer surface sensitivity. These points have previously been exploited in the context of process control in semiconductor epitaxy, and in fact RAS was conceived with this purpose in mind (see, e.g. [7]). We now demonstrate that it can play a similar role in LCD fabrication by offering the means to probe, in real time, the creation of alignment layers rather than making inferences based on the performance of completed devices.

The substrates used were ultrasonically cleaned 1 cm^2 indium tin oxide coated glass slides. A 100 nm polymer layer was deposited by spin coating at 3000 rpm for 1 min with a 5% solution of the polyimide LQ 1800 (HD Microsystems Ltd)

dissolved in *N*-methyl-2-pyrollidinone. The samples were soft baked at 100°C for 15–30 min followed by thermal curing at 250°C for 100 min. Before and after polymer coating, the samples were analysed using a phase modulating reflection anisotropy (RA) spectrometer and were studied using an atomic force microscope. In each case, negligible optical anisotropy was found before and after. To create an LC alignment template, samples were then exposed to a beam of argon ions with energy 500 eV and current density 15 μA cm^{-2} at 45° incidence while their RA spectra were continuously measured. The alignment effect was confirmed by constructing miniature LC cells using the nematic LC E49 (Merck) sandwiched between samples with orthogonal alignment directions which had been subjected to a dose of $\sim 1.3 \times 10^{17}$ ions cm^{-2}. Figure 1 shows dark-state photomicrographs of such a cell alongside that of a similar device constructed with conventional rubbed polyimide alignment layers. As has been previously reported [1, 8], we find that the ion-etched polymer layers produce more uniform devices with less debris and no evidence of streaking defects. In fact, the debris observed in the ion-etched cell, figure 1(*a*), is not intrinsic to the etching process itself but arises primarily because of atmospheric contamination when moving the samples into and out of the ion bombarding chamber which is housed out with of a clean room environment.

The RA spectra measured during 20 min of bombardment of a sample are shown in figure 2(*a*). Figure 2(*b*) illustrates the optical anisotropy, measured at 3.12 eV, initially increased before saturating after ~10 min, corresponding to a total dose of $\sim 7 \times 10^{16}$ ions cm^{-2}. It appears that RAS allows clear detection of the development of the anisotropic (i.e. LC aligning) surface. Comparing the RA spectra of ion-etched and rubbed polymer alignment layers, shown in figure 2, it is clear that the optical anisotropy of the latter is greater by approximately two orders of magnitude. This can be attributed to the large 'form birefringence' (see, e.g. [9]) associated with the relatively deep (~10–30 nm) grooves created by the rubbing process. Atomic force microscopy cross-sections of the untreated, etched and rubbed surfaces, shown in figure 3, illustrate the surface roughness of the ion-etched polymer to be determined essentially by the initial surface. This fact, together with our observation that the reflectivity of the sample was negligibly affected by the etching process, indicate that LC alignment on the etched polymer is promoted by surface modification at the atomic scale, in accordance with Geary *et al* [6]. In the regime considered here, the collision cascade caused by the incident ions transfers energy to atoms in the near-surface region, causing some of them to be ejected. This sputtering process tends to establish a steady state in which the surface damage usually extends less than a nanometre or so into the surface. In-plane anisotropy may also be produced, giving rise to a non-zero RAS signature and the LC alignment effect in the case of etched polyimide. In general ion beams can induce surface corrugation parallel or perpendicular to the plane of incidence (see, e.g. [10] and references within), but

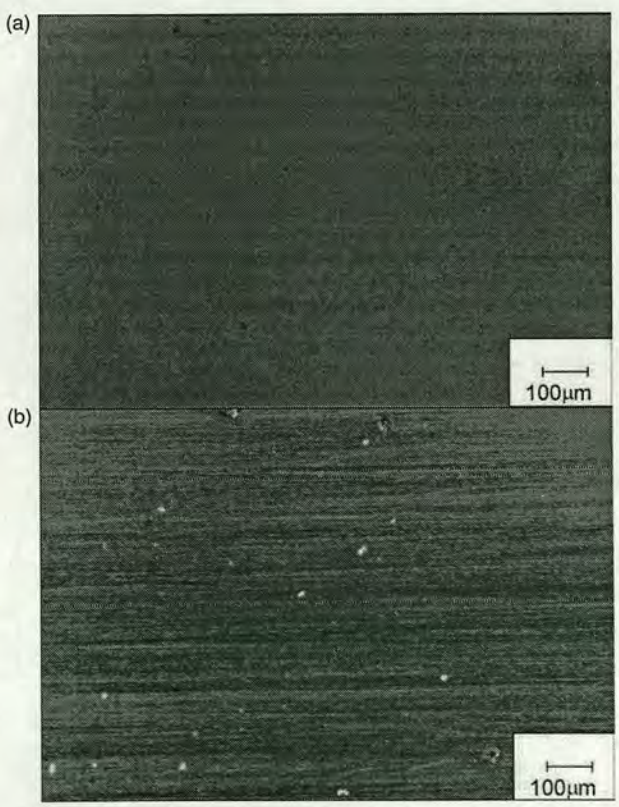

Figure 1. Dark-state photomicrographs of LC cells constructed using polymer alignment layers prepared by (*a*) the etching technique and (*b*) the rubbing technique.

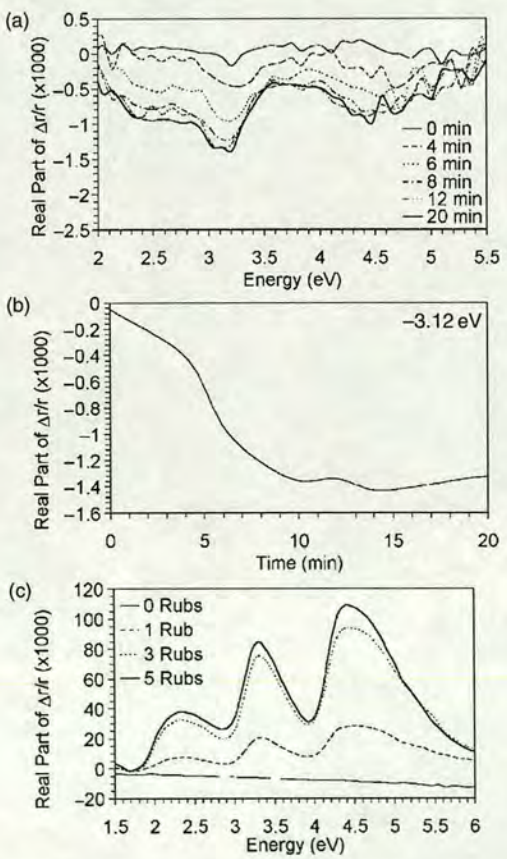

Figure 2. (*a*) RA spectra for an etched polyimide surface. The *y*-direction lies in the plane of incidence of the ion beam. (*b*) RAS signal as a function of time for an etched polyimide surface. (*c*) RA spectra of a polyimide surface rubbed along the *y*-direction.

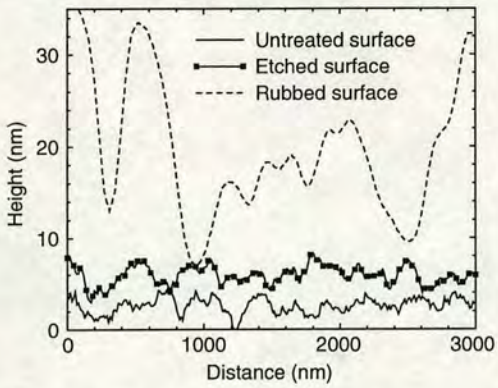

Figure 3. Cross-sectional atomic force microscopy images of an untreated polyimide surface, an etched polyimide surface and a rubbed polyimide surface. All cross-sections are from images 3 μm^2 and were taken in contact mode using a molecular imaging picoscan. The cross-sections have been displaced vertically for clarity.

for covalently bonded systems a simple picture in which bonds are preferentially broken in the plane of incidence of the ion beam seems appropriate [1]. Thus we expect polymer chains at the etched surface to be preferentially aligned along the etching direction. Since the dominant mechanisms for optical anisotropy are different for the ion-etched and rubbed polymer surfaces, it is not surprising that their RA spectra are quite different. In fact, figure 2 shows the spectra even have opposite *sign*, despite the fact that the rubbing direction was parallel to the plane of incidence of the ion beam. Further surface characterization is required for these differences to be clarified. Nevertheless, we have found that RAS can monitor in real time the creation of ion-etched polyimide LC alignment layers.

A key question is whether the RAS signal of the etched alignment layer can be related to some device characteristic. Chaudhari *et al* [1, 8] have previously observed the pretilt angle of LCs to vary not only with the ion dose of their alignment layers, but also with ion energy and angle of incidence. Indeed even changing the polyimide can affect the pretilt angle. Since it has been shown that a wide variety of surfaces, including diamond-like carbon and oxides as well as polymers, can be used to produce alignment layers by ion etching [1], it seems natural to investigate the fundamental physics of ion etching of surfaces and their subsequent interaction with LC thin films using model systems. By having the ability to determine the orientation of submonolayer adsorbed organic films [11], RAS promises to be a powerful tool in this field. Thus far both post-processing [12, 13] and real time [14] RAS studies have been performed for the ion bombarded Cu(110) surface. For this system it appears that the structure of the etched surface is determined predominantly by that of the starting surface, which is itself already anisotropic, and is insensitive to incidence angle and ion energy.

In conclusion, we have found RAS to provide a real time monitor of the production of LC alignment layers by ion bombardment, raising the prospect of feedback control in commercial device fabrication and increased production yields. We also note that the technique may also be operated in imaging mode [15] which could allow convenient screening for device uniformity.

Acknowledgments

R J C would like to thank the EPSRC (GR/NO2924), the Nuffield Foundation and the Royal Society for funding this work.

References

[1] Chaudhari P *et al* 2001 *Nature* **411** 56
[2] van Haaren J 2001 *Nature* **411** 29
[3] Sun Z M, Engels J M, Dozov I and Durand G 1994 *J. Phys.* II (France) **4** 59
[4] Macdonald B F, Cole R J, Zheng W and Miremont C 2001 *Phys. Status. Solidi.* a **188** 1577
[5] Macdonald B F and Cole R J 2002 *Appl. Phys. Lett.* **80** at press
[6] Geary J M, Goodby J W, Kmetz A R and Patel J S 1987 *J. Appl. Phys.* **62** 4100
[7] Aspnes D E, Harbison J P, Studna A A and Florez L T 1988 *Appl. Phys. Lett.* **52** 957
[8] Chaudhari P, Lacey J A, Lien S-C A and Speidell J L 1998 *Japan. J. Appl. Phys.* **37** L55
[9] Born M and Wolf E (ed) 1999 *p837 of Principles of optics* 7th edn (Cambridge: Cambridge University Press)
[10] Cuerno R, Makse H A, Tomassone S, Harrington S T and Stanley H E 1995 *Phys. Rev. Lett.* **75** 4464
[11] Frederick B G, Power J R, Cole R J, Perry C C, Chen Q, Haq S, Bertrams Th, Richardson N V and Weightman P 1998 *Phys. Rev. Lett.* **80** 4490
[12] Bremer J, Hansen J-K and Hunderi O 1999 *Surf. Sci.* **436** L735
[13] Martin D S, Maunder A and Weightman P 2001 *Phys. Rev.* B **63** 155403
[14] Macdonald B F and Cole R J 2001 *Phys. Status. Solidi.* a **188** 1489
[15] Rotermund H H, Haas G, Franz R U, Tromp R M and Ertl G 1995 *Science* **270** 608

INSTITUTE OF PHYSICS PUBLISHING JOURNAL OF PHYSICS D: APPLIED PHYSICS

J. Phys. D: Appl. Phys. **36** (2003) 142–145 PII: S0022-3727(03)54364-9

RAS measurements of optical retardation in rubbed polymer thin films

B F Macdonald and R J Cole

School of Physics and Centre for Materials Science and Engineering, University of Edinburgh, Edinburgh, Scotland, EH9 3JZ, UK

Received 7 October 2002
Published 30 December 2002
Online at stacks.iop.org/JPhysD/36/142

Abstract

Reflectance anisotropy spectroscopy (RAS) is used to study anisotropic polymer thin films. The measured spectra are interpreted in terms of molecular orientation at the polymer surface. It is shown that RAS spectra of thin transparent films resemble the logarithmic derivative of the corresponding polarization-averaged reflection spectra. The amplitudes of the spectra are found to be highly sensitive to the optical retardation in the anisotropic layer.

1. Introduction

Over the last decade reflection anisotropy spectroscopy (RAS), which measures anisotropy in the normal incidence reflectivity, has proved itself a powerful probe of semiconductor epilayers (see, e.g. [1]). Its ability to operate out-with of ultra-high vacuum conditions has stimulated RAS studies in a range of new fields, including solid–liquid electrochemistry [2], catalytic reactivity [3] and polymer thin films [4]. Underpinning these applications, there have been intensive studies of well controlled model systems such as clean and adsorbate covered semiconductor and metal single crystal surfaces (see the recent reviews in [5, 6]). These have shown that a detailed understanding of RAS spectra is rather hard to achieve, even for such 'simple' cases. Indeed, it is not even certain that the basic mechanisms of surface optical anisotropy have been correctly identified. While it is generally hard to relate optical anisotropy to more familiar surface properties (e.g. adsorption sites, surface symmetry, bond lengths, etc), RAS is inherently well suited to the study of systems and processes where the creation of surface anisotropy is the phenomenon of primary interest. Here, we consider one example: the anisotropic surface modification of polymer films for use in liquid crystal displays. Our preliminary work [7, 8] has shown that RAS can be used empirically to monitor the fabrication of such polymer alignment layers, demonstrating the potential for real time process control in a commercial environment. Here, we seek to establish an explicit link between the measured spectra and the molecular scale effects of processing the polymer films. We find that RAS is a very sensitive measure of birefringence in transparent media. It is readily demonstrated that for thin (of order 10^2 nm) birefringent films the observed spectra resemble the logarithmic derivative of the polarization-averaged reflectivity spectrum.

2. Experimental

The substrates used in this work were commercially obtained glass slides coated with a 120 nm indium tin oxide (ITO) film. These were spin coated at 3000 rpm for 1 min with a 5% solution of the polyimide (PI) LQ 1800 (HD Microsystems) dissolved in *n*-methyl-2-pyrrolidone. The samples were cured initially by soft baking at 100°C for 15–30 min followed by thermal curing at 250°C for 100 min. The PI film thickness could be controlled by varying the PI concentration. Since 120 nm PI films are routinely used in the manufacture of liquid crystal displays, we chose thicknesses of 80, 120 and 1400 nm to ensure relevance of this work to the fabrication of real devices. The samples were rubbed using a rotating velvet coated drum as described previously [7].

A home built phase modulating reflection anisotropy spectrometer following the design of Aspnes [1] was used in this work. For each photon energy, E, this instrument measures a DC voltage, V_0, and an AC voltage, $V_{2\omega}$, where ω is the modulation frequency, which are related to the optical properties of the sample by

$$V_0 = T|\bar{r}|^2, \qquad V_{2\omega} = \frac{T}{2}(\bar{r}\Delta^* + \bar{r}^*\Delta), \tag{1}$$

where asterisks denote complex conjugation,

$$\Delta = r_x - r_y, \qquad \bar{r} = \frac{r_x + r_y}{2}, \tag{2}$$

and r_x and r_y are the Fresnel reflection amplitudes for linear polarization along x and y (the horizontal and vertical axes of the spectrometer), respectively. T, the instrument transmission function, is not known precisely and so V_0 provides only an approximate measure of the absolute (polarization-averaged) reflectivity. Here, we have estimated T by measuring V_0 for materials with known optical constants (copper and silicon). The ratio $V_{2\omega}/V_0$ is proportional to the real part of the reflection anisotropy, $\Delta/\bar{r}$, and, being unaffected by temporal fluctuations and drifts in the light source and detector, is precisely measured. Optical measurements were made with the rubbing direction of the samples aligned with the x-axis of the RAS spectrometer.

3. Results and discussion

3.1. Reflectivity

While reflectivity measurements provided by V_0 are discarded in the majority of RAS studies, here they are a useful source of additional information. The measured reflectivity of an ITO/glass substrate prior to any surface treatment is shown in figure 1. The main features of the spectrum are broad thin film interference maxima centred on 1.8 and 3.7 eV. The ITO/glass reflectivity spectrum was simulated using the matrix method for isotropic stratified substrates described by Abelès [9], previously determined optical constants [10], and treating the ITO thickness as a free parameter. By varying the ITO thickness to reproduce the interference maxima of the experimental spectrum, we obtained an optimum thickness of 116 ± 5 nm, consistent with the manufacturer's specification. The simulated reflectivity spectrum for an ITO thickness of 116 nm is compared with the experimental data in figure 1. Given that the optical properties of ITO thin films are known to be somewhat variable [11], and that RAS spectrometers do not measure reflectivity with high accuracy, agreement with experiment was considered satisfactory. Improvements were apparent if the top 10–20 nm of ITO was modelled using the Bruggeman effective medium approximation [12], the standard approach for simulating surface roughness.

The measured reflectivity spectrum of the three PI/ITO/glass samples A, B and C are shown in figure 2.

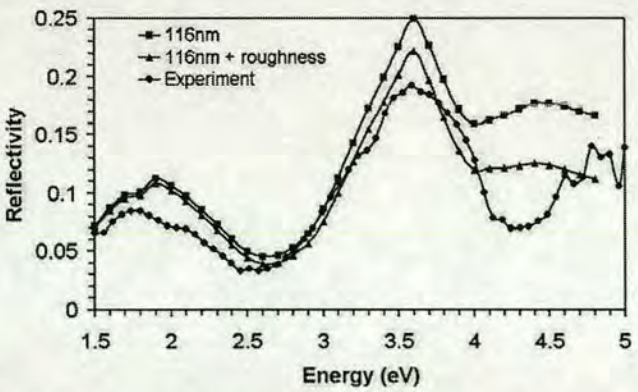

Figure 1. The solid circle data set shows the reflectivity from an ITO/glass substrate which has had its back surface frosted to suppress incoherent reflections from this surface. The simulated reflectivity for a 116 nm ITO layer on a glass substrate, with and without surface roughness, are also shown.

In each case oscillations are observed due to interference between the beams reflected from the air-PI, PI–ITO and ITO–glass interfaces. Simulation of these spectra is hampered by incomplete knowledge of the dielectric function of the particular PI used in this study. To allow simulations we have used measurements of the refractive index of this material in the visible region and extrapolated on the basis of data for similar systems. Using the Abelès method, and treating the PI thicknesses as free parameters, we found optimum agreement between simulated and experimental spectra for PI thicknesses of 80 nm, 120 nm and 1400 nm for samples A, B and C, respectively (figure 3). We estimate the uncertainty in these thickness measurements to be about 10%. Agreement between experiment and simulation can be considered satisfactory, given the uncertainties in each. We note that the central results of this work do not rely upon accurate knowledge of either the thickness or optical density of the PI films.

The reflectivity spectra measured after rubbing the PI surfaces are also shown in figure 2. While rubbing reduces the reflectivity in the UV region, consistent with surface roughening, it does not affect the general form of the reflectivity spectra, indicating that the PI film thicknesses do not change significantly.

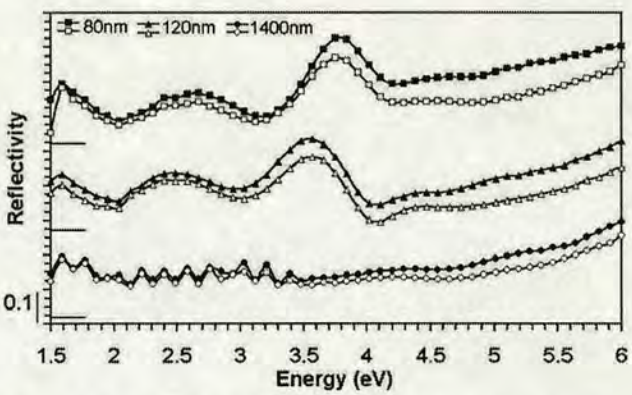

Figure 2. Solid data sets show the measured reflectivity spectra of unrubbed PI/ITO/glass samples. Hollow data sets are the spectra after rubbing the surfaces. Samples A, B and C are shown by squares, triangles and circles, respectively.

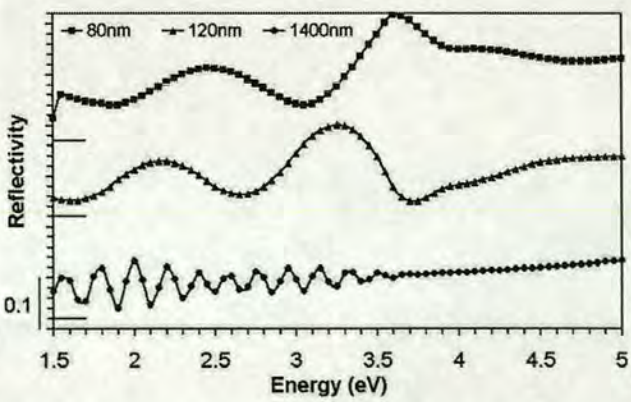

Figure 3. Reflectivity spectra simulated using the Abelès matrix method [10] for samples A, B and C. PI thicknesses of 80 nm, 120 nm and 1400 nm, respectively, have been assumed. In each case the ITO thickness was taken to be 116 nm.

3.2. RAS

RAS spectra of the three PI/ITO/glass samples after rubbing are shown as the solid data sets in figure 4. For all three samples a broad peak centred on $E \sim 4.5$ eV is observed. For sample C the oscillations in the reflectivity and RAS spectra die out abruptly at ~3.5 eV, indicating complete absorption within the PI layer for $E > 3.5$ eV. It follows that the 4.5 eV feature is derived purely from the upper surface of the PI, which is believed to be essentially the same for all the three samples. We consider first the visible region of the spectra. It is apparent from the RAS spectra of samples A and B that the interference related features in the region 1.5–3.5 eV are asymmetric, and that the photon energies of the maxima do not correspond with those of the reflectivity spectra. These observations can be explained as follows. It is widely accepted that rubbing causes a preferential alignment of polymer chains parallel to the rubbing direction [13] and it has been found that the refractive index for polarization parallel to this direction, n_x, exceeds that for perpendicular polarization, n_y, by typically 0.1 [14, 15]. This rub-induced birefringence, Δn, causes a slightly different optical thickness for x and y polarizations and so an energy shift, η, in the interference peaks of the reflectivity spectra for the two polarizations:

$$|r_x|^2(E) \approx |r_y|^2(E + \eta) \tag{3}$$

where

$$\eta \approx E\frac{d_1 \Delta n}{(d_1 + d_2)n} \tag{4}$$

and d_1 and d_2 are the thicknesses of the anisotropic surface layer and underlying polymer layer, respectively. It follows that

$$\mathrm{Re}\left[\frac{\Delta}{\bar{r}}\right] \approx \frac{|r_x|^2 - |r_y|^2}{|r_x|^2 + |r_y|^2} \approx \eta \frac{1}{2|\bar{r}|^2}\frac{\mathrm{d}}{\mathrm{d}E}(|\bar{r}|^2) \tag{5}$$

that is, the RAS spectrum is approximately proportional to the logarithmic derivative of the reflectivity spectrum, the constant of proportionality being determined by the optical retardation in the overlayer $d_1 \Delta n$. Our previous AFM measurements [8] on similar samples have revealed penetration of the fibres of the rubbing cloth to depths ~10 nm, so we estimate $d_1 \sim 10$ nm and hence $d_1 \Delta n \sim 1$ nm, a value consistent with previous retardation measurements [13, 16–19].

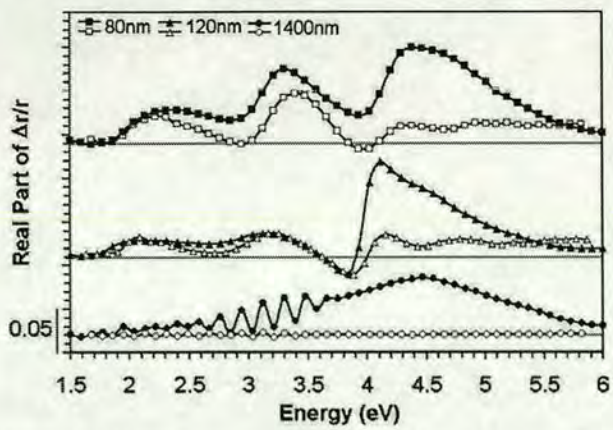

Figure 4. RAS measurements for samples A, B and C are shown as the solid data sets. The hollow data sets were obtained by applying equation (5) to the corresponding experimental reflectivity spectrum.

Before applying equation (5) to our experimental reflectivity data we first seek to establish its validity by comparing the simulations shown in figure 5. This figure reports results calculated for three different five-layer systems, each of the form sketched in figure 6 but with a different total PI thickness. In each case, a retardation of 1 nm was assumed for the anisotropic layer. It can clearly be seen that the exact RAS calculation for each system, shown by the solid data points, is very well reproduced by equation (5) using the calculated reflectivity for each system, shown by the hollow data points.

Having established the validity of equation (5), we now use it to simulate the experimental RAS spectra of samples A, B and C using only our estimate of $d_1 \Delta n \sim 1$ nm and the *experimental* reflectivity spectrum of each sample. This approach yields the hollow data sets in figure 4 which are clearly similar to the measured RAS spectra they are plotted against. This simple approach can be used to explain the asymmetry and peak positions in the measured spectra, as well as their approximate magnitude. Since $n_x > n_y$ we expect the reflectivity for x polarization to be slightly greater than that for y polarization, as well as being slightly shifted in energy. This would lead to a positive correction term to the right-hand side of equation (5), giving improved agreement with experiment.

As one would expect, the 4.5 eV RAS feature discussed above does not emerge from these simple considerations of rub-induced birefringence. In fact for sample C the large denominator in equation (4) ensures that birefringence makes only a minor contribution to the RAS spectrum. We speculate that, as well as birefringence, molecular alignment at the

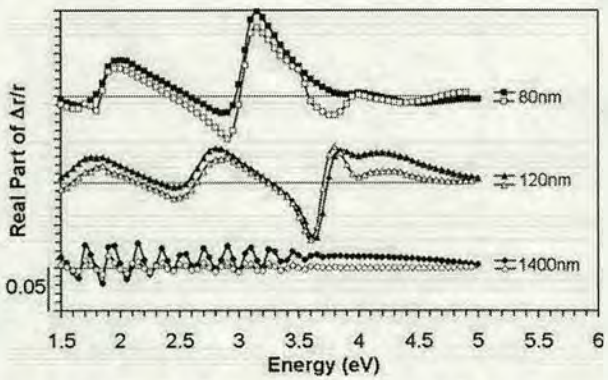

Figure 5. RAS simulations for samples A, B and C as shown as the solid data sets. The hollow data sets were obtained by applying equation (5) to the corresponding simulated reflectivity. The same thicknesses as used in figure 3 were used. In each case the upper 10 nm was assumed to have a birefringence of 0.1.

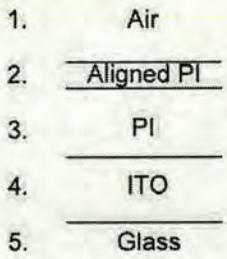

Figure 6. The five-layer model used in the simulations shown in figure 5.

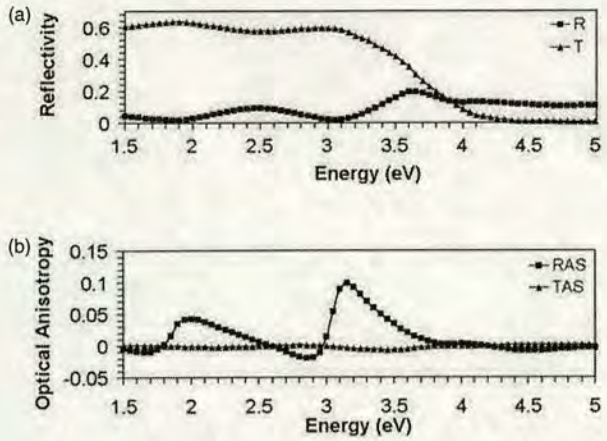

Figure 7. The comparison between the simulated reflectivity (R) and transmission (T) for a five-layer model with parameters corresponding to sample A is shown in (*a*). The comparison of the simulated RAS and simulated TAS for the same system is shown in (*b*).

surface would give rise to dichroic absorption, not included in the simulations in figure 5. The extinction above 3.5 eV of the thin film interference oscillations in the reflectivity spectra of our samples indicates strong absorption in this region. While we have not measured their dichroism spectra, strong dichroism would be consistent with the findings of Schadt *et al* [19] and Miller *et al* [20]. It is straightforward to show [20] that the RAS spectrum of a dichroic absorbing thin film reveals its dichroism spectrum, and we propose this as the origin of the 4.5 eV feature we observe. Miller *et al* [20] have previously used this effect to explain very similar RAS features for other oriented polymer films.

Previous measurements have established RAS to be capable of monitoring the orientation of molecules on surfaces [21] but it is not obvious that an optical reflection technique, such as RAS, will be a suitable probe of the surfaces of transparent thin films. In fact, the simulations for a five-layer model corresponding to Sample A, shown in figure 7, clearly demonstrate that while the reflected beam is much weaker than the transmitted beam, the reflection anisotropy is much more sensitive to the birefringence of the surface layer than the transmission anisotropy. This extra sensitivity makes the RAS technique much better suited for studying transparent thin films than transmission anisotropy spectroscopy (TAS). It is important to appreciate the large amplitude ($\sim 10^{-1}$) of the RAS spectra measured in this work compared to the experimental detection limit of standard spectrometers ($\sim 10^{-5}$). We deduce that retardations of order 10^{-4} nm should be measurable with a standard RAS spectrometer.

4. Conclusions

RAS has been used to characterize rubbed polymer alignment layers used in commercial liquid crystal display fabrication. Though usually discarded, the reflectivity spectra provided by the RAS instrument proved valuable in this study, enabling layer thicknesses to be deduced and providing a basis for interpreting the measured RAS spectra. The spectra were explained qualitatively using a simple birefringence model in terms of the logarithmic derivatives of the corresponding reflectivity spectra. Detailed RAS simulations using a five-layer model produced good agreement with experiment in the visible region and demonstrated the technique to be a sensitive probe of optical retardation. Although the RAS spectra of samples A, B and C are quite different, the simulations show that they are derived from essentially the same aligned overlayer. A feature in the UV region was observed in the RAS spectra of all samples studied. Though originating unambiguously from the rubbed PI surface, this feature and could not be explained by birefringence due to molecular alignment and has been attributed to dichroism arising from the same underlying mechanism. The development of a systematic approach to interpreting RAS spectra of anisotropic polymer thin films will greatly assist attempts to apply this technique to the real time monitoring and process control of liquid crystal device fabrication.

Acknowledgments

The funding for this work was provided by The Royal Society, The Nuffield Foundation and EPSRC. Assistance of Dr W Zheng in sample preparation is gratefully acknowledged.

References

[1] Aspnes D E, Harbison J P, Studna A A and Florez L T 1988 *Appl. Phys. Lett.* **52** 957
[2] Sheridan B, Martin D S, Power J R, Barrett S D, Smith C I, Lucas C A, Nichols R J and Weightman P 2000 *Phys. Rev. Lett.* **85** 4618
[3] Scholz S M, Mertens F, Jacobi K, Imbihl R and Richter W 1995 *Surf. Sci.* **340** L945
[4] Di Natale C, Goletti C, Paolesse R, Della Sala F, Drago M, Chiaradia P, Lugli P and D'Amico A 2000 *Appl. Phys. Lett.* **77** 3164
[5] Martin D S and Weightman P 2001 *Surf. Interface Anal.* **31** 915
[6] Sobiesierski Z, Westwood D I and Matthai C C 1998 *J. Phys.: Condens. Matter* **10** 1
[7] Macdonald B F, Cole R J, Zheng W and Miremont C 2001 *Phys. Status Solidi* a **188** 1577
[8] Macdonald B F, Zheng W, Cole R J and Underwood I 2002 *J. Phys. D: Appl. Phys.* **35** L41
[9] Abelès F 1950 *Ann. Phys.* (Paris) **5** 598
[10] Woollam J A, McGahan W A and Johs B 1994 *Thin Solid Films* **241** 44
[11] Synowicki R A 1998 *Thin Solid Films* **313** 394
[12] Bruggeman D A G 1935 *Ann. Phys.* (Leip.) **24** 636
[13] Geary J M, Goodby J W, Kmetz A R and Patel J S 1987 *J. Appl. Phys.* **62** 4100
[14] Sahre K, Eichhorn K J, Simon F, Pleul D, Janke A and Gerlach G 2001 *Surf. Coatings Technol.* **139** 257
[15] Hirosawa I 1996 *Japan. J. Appl. Phys.* **35** 5873
Hirosawa I 1997 *Japan. J. Appl. Phys.* **36** 6953
[16] van Aerle N A J M, Barmentlo M and Hollering R W J 1993 *J. Appl. Phys.* **74** 3111
[17] Kim J H and Rosenblatt C 2000 *J. Appl. Phys.* **87** 155
[18] Schwab A D, Agra D M G, Kim J H, Kumar S and Dhinojwala A 2000 *Macromolecules* **33** 4903
[19] Schadt M, Schmitt K, Kozinkov V and Chigrinov V 1992 *Japan. J. Appl. Phys.* **31** 2155
[20] Miller E K, Hingerl K, Brabec C J, Heeger A J and Sariciftci N S 2000 *J. Chem. Phys.* **113** 789
[21] Frederick B G, Power J R, Cole R J, Perry C C, Xhen Q, Haq S Bertrams Th, Richardson N V and Weightman P 1998 *Phys. Rev. Lett.* **80** 4490

Bibliography

Chapter 1

[1.1] B. Bahadur , Mol. Cryst. and Liq. Cryst. **109**, 3 (1984).

[1.2] P. Chaudhari, J. Lacey, J. Doyle, E. Galligan, S. C. A. Lien, A. Callegari, G. Hougham, N. D. Lang, P. S. Andry, R. John, K. H. Yang M. H. Lu, C. Cai, J. Speidell, S. Purushothaman, J. Ritsko, M. Samant, J. Stohr, Y. Nakagawa, Y. Katoh, Y. Saitoh, K. Sakai, H. Satoh, S. Odahara, H. Nakano, J. Nakagaki and Y. Shiota, Nature **411**, 56 (2001).

[1.3] J. van Haaren, Nature **392**, 332 (1998).

[1.4] *Introduction to Liquid Crystals*, P. J. Collings and M. Hird, Taylor and Francis, London (1997).

[1.5] http://www.atip.org/fpd/samples/flcd/flcd.htm.

Chapter 2

[2.1] G. Binnig, H. Rohrer, Ch. Gerber and E. Weibel, Appl. Phys. Lett **40**, 178 (1981).

[2.2] *Instructional Scanning Tunnelling Microscope* ^{TM} Users Manual by Burleigh Instruments Inc.

[2.3] *Scanning Probe Microscopy and Spectroscopy,* R. Wiesendanger, Cambridge University Press, Cambridge (1994).

[2.4] *Scanning Tunnelling Microscopy and its Applications,* C. Bai, Springer, Shanghai (1992).

[2.5] *Scanning Force Microscopy,* D. Sarid, Oxford University Press, Oxford (1994).

[2.6] *A Practical Guide to Scanning Probe Microscopy*, (Thermomicroscopes, 2000), http://www.tmmicro.com/spmguide/contents.htm).

[2.7] G. Binnig and C.F. Quate, Phys. Rev. Lett. **56**, 930 (1986).

[2.8] O. Marti, B. Drake and P.K. Hansma, Appl. Phys. Lett. **51**, 484 (1987).

[2.9] T. R. Albrecht and C. F. Quate, J. Appl. Phys **62**, 2599 (1987).

[2.10] T. R. Albrecht, S. Akamine, T. E. Carver and C.F. Quate, J. Vac. Sci. Technol. A **8**, 3386 (1990).

[2.11] http://www.di.com.

[2.12] *Low Energy Electron Diffraction*, J. B. Pendry, Academic Press, London (1974).

[2.13] http://www.chem.qmw.ac.uk/surfaces/scc/scat6_2.htm.

[2.14] M. Cardona, F. H. Pollak and K. L. Shaklee, J. Phys. Soc. Jap **21**, 89 (1968).

[2.15] J. D. E. McIntyre and D. E. Aspnes, Surf. Sci. **24**, 417 (1971).

[2.16] D. E. Aspnes and A. A. Studna, Phys. Rev. Lett. **54**, 1956 (1985).

[2.17] D. E. Aspnes, J. P. Harbison, A. A. Studna and L. T. Florez, Phys. Rev. Lett. **59**, 1687 (1987).

[2.18] J. P. Harbison, D. E. Aspnes, A. A. Studna and L. T. Florez, J. Vac. Sci. Technol. B **6**, 740 (1988).

[2.19] D. E. Aspnes, J. P. Harbison, A. A. Studna and L. T. Florez, Appl. Phys. Lett. **52**, 957 (1988).

[2.20] D. E. Aspnes, J. P. Harbison, A. A. Studna and L. T. Florez, J. Vac. Sci. Technol. A **6**, 1327 (1988).

[2.21] Y. Borensztein, W. L. Mochan, J. Tarriba, R. G. Barrera and A. Tadjeddine, Phys. Rev. Lett. **71**, 2334 (1993).

[2.22] P. Hofmann, K. C. Rose, V. Fernandez and A. M. Bradshaw, Phys. Rev. Lett. **75**, 2039 (1995).

[2.23] B. G. Frederick, J. R. Power, R. J. Cole, C. C. Perry, Q. Chen, S. Haq, Th. Bertrams, N. V. Richardson and P. Weightman, Phys. Rev. Lett. **80**, 4490 (1998).

[2.24] S. M. Scholz, F. Mertens, K. Jacobi, R. Imbihl and W. Richter, Surf. Sci. **340**, L945 (1995).

[2.25] C. Di Natale, C. Goletti, R. Paolesse, F. Della Sala, M. Drago, P. Chiaradia, P. Lugli and A. C'Amico, Appl. Phys. Lett. **77**, 3164 (2000).

[2.26] B. Sheridan, D. S. Martin, J. R. Power, S. D. Barrett, C. I. Smith, C. A. Lucas, R. J. Nichols and P. Weightman, Phys. Rev. Lett. **85**, 4618 (2000).

[2.27] R. E. Balderas-Navarro, K. Hingerl, A. Bonanni, H. Sitter, and D. Stifter, Appl. Phys. Lett. **78**, 3615 (2001).

[2.28] *Optical Properties of Thin Solid Films,* O. S. Heavens, Butterworths Scientific Publications, London (1955).

[2.29] *Epioptics: Linear and Nonlinear Optical Spectroscopy of Surfaces and Interfaces*, J. F. McGilp, D. Weaire and C. H. Patterson, Springer, London (1995).

[2.30] P. Gerber, Thesis: Development and Optimization of the Reflectance Anisotropy Spectroscopy (RAS) Technique with Respect to Online Growth Control, Institut für Festkörperphysik, Technische Universität Berlin (1996).

[2.31] J.-K. Hansen, PhD Thesis: Electronic and Optical Properties of Noble Metals Studied by Reflection Anisotropy Spectroscopy, Institutt for fysikk, Norges teknisk-naturvitenskapelige universitet Trondheim (2000).

Chapter 3

[3.1] *Handbook of Chemistry and Physics, 55th Edition*, R. C. Weast, E211 CRC Press, Ohio (1975).

[3.2] J. Rumberg, PhD Thesis: Development and Optimization of the Reflectance Anisotropy (RAS) Technique with Respect to Online Growth Control, Technische Universitat Berlin, Institus fur Festkorperphysik (1996).

[3.3] http://www.perkinelmer.com.

[3.4] *Handbook of Optical Constants of Solids,* E. D. Palik, Academic Press, London (1985).

[3.5] D. E. Aspnes, J. P. Harbison, A. A. Studna and L. T. Florez, J. Vac. Sci. Technol. A **6**, 1327 (1988).

Chapter 4

[4.1] B. F. Macdonald, R. J. Cole, W. Zheng and C. Miremont, Phys. Stat. Sol. (a), **188**, 1577 (2001).

[4.2] B. F. Macdonald, W. Zheng and R. J. Cole, submitted to J. Appl. Phys. September (2002).

[4.3] B. F. Macdonald and R. J. Cole, J. Phys. D: Appl. Phys. **36**, 142 (2003).

[4.4] W. Zheng, B. F. Macdonald and R. J. Cole, submitted to Mol. Cryst. And Liq. Cryst. June (2002).

[4.5] B. F. Macdonald, W. Zheng, R. J. Cole and I. Underwood, J. Phys. D: Appl. Phys. **35**, L41 (2002).

[4.6] B. F. Macdonald and R. J. Cole, submitted to Surf. Sci. May (2002)

[4.7] J. van Haaren, Nature **392**, 331 (1998).

[4.8] B. Bahadur, Mol. Cryst. and Liq. Cryst. **109**, 3 (1984).

[4.9] J. L. Janning, Appl. Phys. Lett. **21**, 173 (1972).

[4.10] L. A. Goodman, J. T. McGinn, C. H. Anderson and F. Digeronimo, IEEE Trans. Elec. Dev. **24**, 795 (1977).

[4.11] S. C. Jain and H-S. Kitzerow, Appl. Phys. Lett. **64**, 2946 (1994).

[4.12] I. Dierking, L. L. Kosbar, A. C. Lowe and G. A. Held, Liquid Crystals **24**, 397 (1998).

[4.13] G. Barbero and A. G. Petrov, J. Phys.: Condens. Matter **6,** 2291 (1994).

[4.14] T. Rupp, M. Eberhardt and H. Gruler, Jpn. J. Appl. Phys. **31**, 3636 (1992).

[4.15] A. J. Pidduck, S. D. Haslam, G. P. Bryan-Broan, R. Bannister and I. D. Kitely, Appl. Phys. Lett. **71,** 2907 (1997).

[4.16] A. Rastegar, M. Skarabot, B. Blij and Th. Rasing, J. Appl. Phys. **89**, 960 (2001).

[4.17] P. Chaudhari, J. Lacey, J. Doyle, E. Galligan, S. C. A. Lien, A. Callegari, G. Hougham, N. D. Lang, P. S. Andry, R. John, K. H. Yang M. H. Lu, C. Cai, J. Speidell, S. Purushothaman, J. Ritsko, M. Samant, J. Stohr, Y. Nakagawa, Y. Katoh, Y. Saitoh, K. Sakai, H. Satoh, S. Odahara, H. Nakano, J. Nakagaki and Y. Shiota, Nature **411**, 56 (2001).

[4.18] P. Chaudhari, J. A. Lacey, S.-C. A. Lien and J. Speidell, Jpn. J. Appl. Phys. **37,** L55 (1998).

[4.19] Z. M. Sun, J. M. Engels, I. Dozov and G. Durand, J. Phys. II France **4**, 59 (1994).

[4.20] J. van Haaren, Nature **411**, 29 (2001).

[4.21] T. Ito, K. Nakanishi, M. Nishikawa, Y. Yokoyama and Y. Takeuchi , Polymer Journal **27**, 240 (1995).

[4.22] D. S. Seo, T. Ohide, H. Matsuda, T. R. Isogami, K. I. Muroi, Y. Yabe and I. S. Kobatash, Mol. Cryst. Liq. Cryst. **231**, 95 (1992).

[4.23] Y. B. Kim, H. Olin, S. Y. Park, J. W. Choi, L. Komitov, M. Matuszczyk and S. T. Lagerwall, Appl. Phys. Lett. **66**, 2218 (1995).

[4.24] A. J. Pidduck, G. P. Bryan-Broan, S. Haslam, R. Bannister, I. Kitely, T. J. McMaster and L. Boogaard, J. Vac. Sci. Technol. A **14**, 1723 (1996).

[4.25] M. P. Mahajan and C. Rosenblatt, J. Appl. Phys. **83**, 7649 (1998).

[4.26] C. L. H. Devlin, S. D. Glab, S. Chang and T. P. Russell, J. Appl. Polym. Sci. **80**, 1470 (2001).

[4.27] X. Wei, X. Zhuang, S. -C. Hong, T. Goto and Y. R. Shen, Phys. Rev. Lett. **82**, 4256 (1999).

[4.28] X. Wei, S. - C. Hong, X. Zhuang, T. Goto and Y. R. Shen, Phys. Rev. E **62**, 5160 (2000).

[4.29] S.-C. Hong, M. Oh-e, X. Zhuang, Y. R. Shen, J. J. Ge, W. Harris and S. Z. D. Cheng, Phys. Rev. E **63**, 051706 (2001).

[4.30] T. Sakai, K. Ishikawa, H. Takezoe, N. Matsuie, Y. Yamamtò, H. Ishii, Y. Ouchi, H. Oji and K. Seki, J. Phys. Chem B **105**, 9191 (2001).

[4.31] I. Hirosawa, Jpn. J. Appl. Phys. Part 1 **35**, 5873 (1996).

[4.32] I. Hirosawa and N. Sasaki, Jpn. J. Appl. Phys. Part 1 **36**, 6953 (1997).

[4.33] S. Itoh and I. Hirosawa, Mol. Cryst. and Liq. Cryst. **367**, 745 (2001).

[4.34] I. Hirosawa, H. Miyairi, T. Matsushita and S. Saito, Mol. Cryst. and Liq. Cryst. **368**, 565 (2001).

[4.35] J.M. Geary, J.W. Goodby, A.R. Kmetz, and J.S. Patel, J. Appl. Phys. **62**, 4100 (1987).

[4.36] *Ellipsometry and Polarised Light,* R. M. A. Azzam and N. M. Bahara, North-Holland, Amsterdam (1987).

[4.37] D. E. Aspnes, J. P. Harbison, A. A. Studna and L. T. Florez, Appl. Phys. Lett. **52**, 957 (1988).

[4.38] D. W. Berreman, Phys. Rev. Lett. **28**, 1683 (1972).

[4.39] J. -H. Kim and C. Rosenblatt, J. Appl. Phys. **87**, 155 (2000).

[4.40] K. Sahre, K. J. Eichhorn, F. Simon, D. Pleul, A. Janke, G. Gerlach, Surface and Coatings Technol. **139,** 257 (2001).

[4.41] J. H. Kim and C. Rosenblatt, J. Appl. Phys. **87,** 155 (2000).

[4.42] A. D. Schwab, D. M. G. Agra, J.H. Kim, S. Kumar and A. Dhinojwala, Macromolecules **33,** 4903 (2000).

[4.43] D. W. Berreman, J. Opt. Soc. Am. **62**, 502 (1972).

[4.44] J. A. Woolam, W. A. McGahan and B. Johs, Thin Solid Films **241**, 44 (1994).

[4.45] R. A. Synowicki, Thin Solid Films **313**, 394 (1998).

[4.46] D. A. G. Bruggeman, Ann. Phys. (Leip.) **24**, 636 (1935).

[4.47] D. E. Aspnes and J. B. Theeten, Phys. Rev. B. **20**, 3292 (1979).

[4.48] E. K. Miller, K. Hingerl, C. J. Brabec, A. J. Heeger and N. S. Sariciftci, J. Chem. Phys. **113**, 789 (2000).

[4.49] D. -H. Chung, H. Takezoe, B. Park, Y Jung, H. -K. Heang, S. Lee, K. -J. Han, S. -H. Jang and H. Yoloyama, Jpn. J. Appl. Phys. **39**, 1252 (2000).

[4.50] M. Schadt, K. Schmitt, V. Kozinkov and V. Chigrinov, Jpn. J. Appl. Phys. **31**, 2155 (1992).

[4.51] B. F. Macdonald and R. J. Cole, Appl. Phys. Lett. **80**, 3527 (2002).

[4.52] R. Cuerno, H. A. Makse, S. Tomassone, S. T. Harrington and H. E. Stanley, Phys. Rev. Lett. **75**, 4464 (1995).

[4.53] S. Rusponi, G. Costantini, C. Boragno and U. Valbusa, Phys. Rev. Lett. **81**, 2735 (1998).

[4.54] H. H. Rotermund, G. Haas, R. U. Franz, R. M. Tromp and G. Ertl, Science **270**, 608 (1995).

[4.55] J. Bremer, J-K. Hansen and O. Hunderi, Surf. Sci. **436**, L735 (1999).

[4.56] D. S. Martin, A. Maunder and Weightman, Phys. Rev. B **63,** 155403 (2001).

[4.57] B. G. Frederick, J. R. Power, R. J. Cole, C. C. Perry, Q. Chen, S. Haq, Th. Bertrams, N. V. Richardson and P. Weightman, Phys. Rev. Lett. **80**, 4490 (1998).

Chapter 5

[5.1] B. F. Macdonald and R. J. Cole, Appl. Phys. Lett. **80**, 2002.

[5.2] B. F. Macdonald, J. S. Law and R. J. Cole, Accepted by J. Appl. Phys. January (2003).

[5.3] Y. J. Kim, Z. Zhuang and J. S. Patel, Appl. Phys. Lett. **77**, 513 (2000).

[5.4] H. Kikuchi, J. A. Logan and D. Y. Yoon, J. Appl. Phys. **79**, 6811 (1996).

[5.5] M. P. Mahajan and C. Rosenblatt, Appl. Phys. Lett. **75**, 3623 (1999).

[5.6] P. Chaudhari, J. Lacey, J. Doyle, E. Galligan, S. C. A. Lien, A. Callegari, G. Hougham, N. D. Lang, P. S. Andry, R. John, K. H. Yang M. H. Lu, C. Cai, J. Speidell, S. Purushothaman, J. Ritsko, M. Samant, J. Stohr, Y. Nakagawa, Y. Katoh, Y. Saitoh, K. Sakai, H. Satoh, S. Odahara, H. Nakano, J. Nakagaki and Y. Shiota, Nature **411**, 56 (2001).

[5.7] *Ellipsometry and Polarised Light,* R. M. A. Azzam and N. M. Bahara, North-Holland, Amsterdam (1987).

[5.8] M. Ortega Lorenzo, S. Haq, T. Bertrams, P. Murray, R. Ravel and C. J. Baddeley, J. Phys. Chem. B **103**, 10661 (1999).

Chapter 6

[6.1] B. F. Macdonald and R. J. Cole, Phys. Stat. Sol. A **188**, 1489 (2001).

[6.2] K. Stahrenberg, Th. Hermann, N. Esser and W. Richter, Phys. Rev. B **61**, 3042 (2000).

[6.3] J.-K. Hansen, J. Bremer and O. Hunderi, Surf. Sci. Lett. **418**, L58 (1998).

[6.4] Y. Borensztein, W. L. Mochan, J. Tarriba, R. G. Barrera and A. Tadjeddine, Phys. Rev. Lett. **71**, 2334 (1993).

[6.5] B. Reihl and K. H. Frank, Phys. Rev. B **31**, 8282 (1985).

[6.6] M. Y. Jiang, G. Pajer and E. Burstein, Surf. Sci. **242**, 306 (1991).

[6.7] P. Straube, F. Pforte, T. Michalke, K. Berge, A. Gerlach and A. Golman, Phys. Rev. B **61**, 14072 (2000).

[6.8] R. A. Bartynski and T. Gustafsson, Phys. Rev. B **33**, 6588 (1986).

[6.9] R. A. Bartynski, T. Gustafsson and P. Soven, Phys. Rev. B **31**, 4745 (1985).

[6.10] Ph. Hoffman, K. C. Rose, V. Fernandez and A. M. Bradshaw, Phys. Rev. Lett. **75**, 2039 (1995).

[6.11] J. -K. Hansen, J. Bremer and O. Hunderi, Phys. Stat. Sol. (a) **170**, 271 (1998)

[6.12] B. G. Frederick, J. R. Power, R. J. Cole, C. C. Perry, Q. Chen, S. Haq, Th. Bertrams, N. V. Richardson and P. Weightman, Phys. Rev. Lett. **80**, 4490 (1998).

[6.13] D. S. Martin, A. Maunder and P. Weightman, Phys. Rev. B **63**, 155403 (2001).

[6.14] S. G. J. Mochrie, Phys. Rev. Lett.**59**, 304 (1987).

[6.15] J. Bremer, J. –K. Hansen and O. Hunderi, Surf. Sci. **436**, L735 (1999).

[6.16] *Sputtering by Particle Bombardment I,* R. Behrisch, H. H. Anderson and H. L. Bay, Springer, Berlin (1991).

[6.17] S. Rusponi, G. Costantini, C. Boragno and U. Valbusa, Phys. Rev. Lett. **81**, 2735 (1998).

[6.18] S. Rusponi, C. Boragno and U. Valbusa, Phys. Rev. Lett. **78**, 2795 (1997).

[6.19] G. Constantini, S. Rusponi, R. Gianotti, C. Boragno and U. Valbusa, Surf. Sci. **416**, 245 (1998).

[6.20] W. G. Schmidt and J. Bernholc, Phys. Rev. B **61**, 7604 (2000).

[6.21] W. G. Schmidt and J. Bernholc, Phys. Rev. B **63**, 045322 (2001).

[6.22] D. Heskett, D. DePietro, G. Sabatino and M. Tammaro, Surf. Sci. **513**, 405 (2002).

[6.23] J. Li, W. –D. Schneider, S. Crampin and R. Berndt, Surf. Sci. **422**, 95 (1999).

Chapter 7

[7.1] Ph. Hoffman, K. C. Rose, V. Fernandez and A. M. Bradshaw, Phys. Rev. Lett. **75**, (1995).

[7.2] R. A. Bartynski, T. Gustasson and P. Soven, Phys. Rev. B **31**, 4745 (1985).

[7.3] M. Y. Jiang, G. Pajer and E. Burstein, Surf. Sci. **242**, 306 (1991).

[7.4] S. M. Scholz, F. Mertens, K. Jacobi, R. Imbihl and and W. Richter, Surf. Sci. **340**, L945 (1995).

[7.5] M. E. Pemble, N. Shukla, A. R. Turner, T. Bitzer, B. G. Frederick, K. J. Kitching, N. V. Richardson, J. Chem. Soc. Faraday Trans. **91**, 3627 (1995).

[7.6] B. G. Frederick, J. R. Power, R. J. Cole, C. C. Perry, Q. Chen, S. Haq, Th. Bertrams, N. V. Richardson and P. Weightman, Phys. Rev. Lett. **80**, 4490 (1998).

[7.7] D.S. Martin, R. J. Cole and P. Weightman, accepted for publication by Phys. Rev. E, August (2002).

[7.8] Chirotechnology, R. A. Sneldon, Marcel Dekker, New York (1993).

[7.9] C. F. McFadden, P. S. Cremer and A. J. Gellman, Langmuir **12**, 2483 (1996).

[7.10] J. M. Brown and S. G. Davies, Nature **342**, 631 (1989).

[7.11] M. Ortega Lorenzo, S. Haq, T. Bertrams, P. Murray, R. Ravel and C. J. Baddeley, J. Phys. Chem. B **103**, 10661 (1999).

[7.12] M. Ortega Lorenzo, C. J. Baddeley, C. Muryn and R. Ravel, Nature **404**, 376 (2002).

[7.13] V. Humblot, S. Haq, C. Muryn, W. A. Hofer and R. Raval, J. Am. Chem. Soc. **124**, 503 (2002).

[7.14] K. Stahrenberg, Th. Herrmann, N. Esser and W. Richter, Phys. Rev. B **61**, 3043 (2000).

Chapter 8

[8.1] B. F. Macdonald, R. J. Cole and V. Koutsous, submitted to Surf. Sci., (2002)

[8.2] D. S. Martin, P. Weightman and J. T. Gauntlett, Surface Science **424**, 187 (1997).

[8.3] D. S. Martin, P. Weightman and J. T. Gauntlett, Surface Science **398**, 308 (1998).

[8.4] A. J. Groszek, Proc. R. Soc. London Ser. A **314**, 473 (1970).

[8.5] R. Hentschke, B. L. Schürmann and J. P. Rabe, J. Chem. Phys. **96**, 6213 (1992)

[8.6] J. P. Rabe and S. Buchholz, Science **253**, 424 (1991).

[8.7] S. Buchholz and J. P. Rabe, J. Vac. Sci. Technol. B **9**, 1126 (1991).

[8.8] R. Seeman S. Herminghaus and K. Jacobs, Phys. Rev. Lett. **86**, 5534 (2001).

[8.9] U. Thiele, M. Mertig and W. Pompe, Phys. Rev. Lett. **80**, 2869 (1998).

[8.10] R. Seeman S. Herminghaus and K. Jacobs, J. Phys.:Condens. Matter **13**, 4925 (2001).

[8.11] E. Ruckenstein and R. K. Jain, J. Chem. Soc., Faraday Trans. 1 **70**, 132 (1974).

[8.12] N. Samid-Merzel, S. G. Lipson and D. S. Tannhauser, Phys. Rev. E 57, 2906 (1998)

[8.13] R.D. Deegan, Phys. Rev. E **61**, 475 (2000)

[8.14] A. Sharma and R. Khanna, J. Chem. Phys. **110**, 4929 (1999).

[8.15] J. Israelachvili, Intermolecular and Surface Forces, 2nd Edition, Academic Press, New York, 1992

[8.16] G. Reiter, P. Auroy, L. Auvray, Macromolecules **29**, 2150 (1996), E. F. Hare, W. A. Zisman, J. Phys. Chem. **59**, 335 (1955)

Chapter 9

[9.1] D. E. Aspnes, Y. C. Chang, A. A. Studna, L. T. Florez, H. H. Farrell and J. P. Harbison, Phys. Rev. Lett. **64**, 192 (1990).

[9.2] D. E. Aspnes, J. Vac. Sci. Technol. B **3**, 1498 (1985).

[9.3] D. E. Aspnes, J. P. Harbison, A. A. Studna and L. T. Florez, J. Vac. Sci. Technol. A **6**, 1327 (1988).

[9.4] D. Heskett, D. DePietro, G. Sabatino and M. Tammaro, Surf. Sci. **513**, 405 (2002).

[9.5] D. S. Martin, P. Weightman and J. T Gauntlett, Surf. Sci. **424**, 187 (1999).

Appendix A

[A.1] *Optical Properties of Thin Solid Films*, O. S. Heavens, Butterworths, London (1955).

[A.2] F. Abelés, Ann. Phys. (Paris) **5**, 596 (1950).

[A.3] *Ellipsometry and Polarised Light,* R. M. A. Azzam and N. M. Bahara, North-Holland, Amsterdam (1987).

[A.4] S. Teitler and B. W. Henvis, J. Opt. Soc. Am. **60**, 830 (1970).

[A.5] D. W. Berreman, J. Opt. Soc. Am. **62**, 502 (1972).

[A.6] M. Schubert, Phys. Rev. B. **53**, 4265 (1995).

[A.7] *Optics 2nd Edition*, E. Hecht, Addison-Weley, Massachusetts (1987).